DANISH METEOROLOGICAL INSTITUTE

¾ ¾ ¾ **SCIENTIFIC REPORT** ¾ ¾ ¾
98-7

GPS Atmosphere Profiling Methods and Error Assessments

By

Per Høeg
Georg Bergeton Larsen
Hans-Henrik Benzon
Jakob Grove-Rasmussen
Stig Syndergaard
Mette Dahl Mortensen
Jacob Christensen (SES)
Keld Schultz (TERMA)

Copenhagen 1998

Danish Meteorological Institute,
Atmosphere Ionosphere Remote Sensing Division,
Lyngbyvej 100, DK-2100 Copenhagen Ø, Denmark

ISBN 87-7478-374-2
ISSN 0905-3263

TABLE OF CONTENTS Page

1. INTRODUCTION

The document presents the functional design and analysis for the Global Positioning System Occultation Sensor (GPSOS) of the National Polar-orbiting Operational Environment Satellite System (NPOESS). Scope and methods of the observational technique together with a review of the Physics describe the capabilities of the satellite measurements. The detailed system error analysis completes the context of monitoring the atmosphere with remote sensing techniques from satellites using GPS/GLONASS signals.

The GPSOS makes observations of navigation signals from Global Positioning System (GPS) and GLONASS (the Russian Global Navigation Satellite System) by applying the limb sounding technique.

The principle of limb sounding has been used for at least 25 years for determining the properties of the atmosphere of other planets in our solar system. Some 10 years ago it was suggested that global navigation satellite systems provide a sufficient number of signals to give a high-resolution measurement of the Earth's atmosphere using a receiver on a low earth orbiting satellite. In April 1995 a proof-of-concept mission (GPS/MET) was launched. Since then GPS/MET have given valuable observations of the ionosphere and neutral atmosphere (troposphere and stratosphere).

This document contains the definitions and the analysis results of the scientific algorithms used with the GPSOS sensor to extract Environmental Data Records (EDR). The dominant parts of these algorithms are used on ground to post process instrument observations.

2. References and abbreviations

2.1. Reference Documents

[Andrews] Andrews, D.G., J.R. Holton, and C.B. Leovy, "Middle Atmosphere Dynamics", *Academic Press*, 1987.

[Askne] Askne, J., and H. Nordius, "Estimation of Tropospheric Delay for Microwaves From Surface Weather Data", *Radio Science*, **22**, 379-386, 1987.

[Basu] Basu, S., E. MacKenzie, and Su. Basu, "Ionospheric Constraints on VHF/UHF Communication Links During Solar Maximum and Minimum Periods", *Radio Science*, **23**, 363-378, 1988.

[Basu85] Basu, Su., Basu S., "Equatorial scintillations: Advances since ISEA-6", *J. Atmos. Terr. Phys.*, **47**, 753-768, 1985.

[Bevis] Bevis, M., Businger S., Chiswell S., Herring T.A., Anthes R.A., Rocken C., Ware R.H., "GPS Meteorology: Mapping Zenith Wet Delays onto Precipitable Water", *Journal of Applied Meteorology*, **33**, 379-386, 1994.

[Bevis92] Bevis, M., S. Businger, T.A. Herring, C. Rocken, R. Anthes, and R.H. Ware, "GPS Meteorology: Remote Sensing of Atmospheric Water Vapor Using the Global Positioning System, *Journal Geophysical Research*, **97**, 15,787-15,801, 1992.

[Budden] Budden, K. G., "The Propagation of Radio Waves", *Cambridge University Press*, 1985.

[Fjeldbo] Fjeldbo, G., Kliore, A. J. and V.R. Eshleman, "The Neutral Atmosphere of Venus as Studied With the Mariner V Radio Occultation Experiment", *Astronomical Journal*, **76**, 123-140, 1971.

[FRE] Fremouw, E. J., "Early Results from the DNA Wideband Satellite Experiment – Complex Signal Scintillations", *Radio Science*, **13,** 167, 1978.

[GPSNav] Technical Characteristics of the Navstar GPS, *GPS Navstar Global Positioning System*, 1991.

[Hajj] Hajj, G. A. and L.J. Romans, "First Ionospheric Electron Density Profiles Obtained with the Global Positioning System", *Radio Science*, **33** number 1., 175-190, 1998.

[Hardy] Hardy, K.R., G.A. Hajj, E.R. Kursinski, and R. Ibanez-Meier, "Accuracies of Atmosphere Profiles Obtained from GPS Occultations", *ION-GPS 93 Proceedings*, 1993.

[Hargre] Hargreaves, J.K., "The Upper Atmosphere and Solar-Terrestrial Relations", *Van Nostrand Reinhold*, 1979.

[Hedin] Hedin, A. E., "Extension of the MSIS thermosphere model into the middle and lower atmosphere", *Journal of Geophysical Research*, **96**, 1159-1172, 1991.

[Hocke] Hocke, K., Kirchengast, G., and A.K. Steiner, "Ionospheric Correction and Inversion of GNSS Occultation Data: Problems and Solutions", *IMG/UoG Technical Report*, for ESA/ESTEC-No. **2**, 1997.

[Johnson] Johnson, F.S. (Ed.), "Satellite Environment Handbook", *Stanford University Press*, 1961.

[Kelley] Kelley, M.C., "The Earth's Ionosphere", *Academic Press*, 1989.

[Kelley80] Kelley, M.C., K.D. Baker, J.L. Ulwick, C.L. Rino, M.J. Baron, "Simultanous Rocket Probe Scintillation and Incoherent Scatter Radar Observations of Irregularities in the Auroral Zone Ionosphere", *Radio Science*, **15**, 491, 1980.

[Kohl] Kohl, H., R. Rüster, and K. Schlegel, (Eds.), "Modern Ionospheric Science", *European Geophysical Society*, 1996.

[KUR95] Kursinski, E. R., Hajj, G. A., Hardy, K. R., Romans, L., and J.T. Schofield, "Observing Tropospheric Water Vapor by Radio Occultation Using the Global Positioning System", *Geophysical Research Letters*, **22**, 2365-2368, 1995.

[KUR97] Kursinski, E. R., Hajj, G. A., Schofield, J. T., Linfield, R. P., and K. Hardy, "Observing Earth's Atmosphere with Radio Occultation Measurements Using the Global Positioning System", *Journal of Geophysical Research*, **102**, 23429-23465, 1997.

[LADR] Ladreiter, H. P., Kirchengast G., "GPS/GLONASS sensing of the neutral atmosphere: Model-independent correction of the ionospheric influences", *Radio Science*, **31,** 877-891, 1996.

[LEI96] Leitinger, R., Titheridge, J. E., Kirchengast, G., and Rothleitner, W., "A 'simple' global empirical model for the F layer of the ionosphere", available

as *Report at Univ. of Graz, Austria*, 1996.

[MEL94] Melbourne, W. G. (Ed.), "The Application of Spaceborne GPS to Atmospheric Limb Sounding and Global Change Monitoring." *JPL Publication*, **94-18**, *Pasadena, CA*, 1994.

[Mortensen] Mortensen, M. D, P. Høeg, "Resolution Properties in Atmospheric Profiling with GPS", Danish Meteorological Institute Scientific Report 98-4.

[Mort98] Mortensen, M. D, P. Høeg, "Inversion of GPS occultation measurements using Fresnel diffraction theory", accepted for publication in *Geophysical Research Letters*, 1998.

[Rob] Robinson, R.M., R. Vondrak, J. Craven, L. Frank and K. Miller, "Comparison of Dynamics Explorer auroral imaging data with Chatanika radar electron density measurements", *Journal of Geophysical Research*, 94 No A5, 5382-5396, 1989.

[SOK96] Sokolovskiy, S., and D. Hunt, "Statistical Optimization Approach for GPS/Met Data Inversions", *URSI GPS/Met Workshop, Tucson, Arizona*, 1996.

[SYN98] Syndergaard, S., "Modeling the impact of the Earth's oblateness on the retrieval of temperature and pressure profiles from limb sounding", *Journal of Atmospheric and Solar-Terrestrial Physics*, **60** No. 2, 171-180, 1998.

[Tsunoda] Tsunoda, R.T., R.C. Livingston, J.P. McClure, W.P. Hanson, "Equatorial plasma bubbles: vertically elongated wedges from the bottomside F layer", *J. Geophys. Res.*, **87**, 9171-9180, 1982.

[VOR94] Vorob'ev, V.V., and T.G. Krasil'nikova, "Estimation of the Accuracy of the Atmospheric Refractive Index Recovery from Doppler Shift Measurements at Frequencies Used in the NAVSTAR System", *Physics of the Atmosphere and Ocean*, **29**, 602-609, 1994.

[Ware] Ware R., M. Exner, D. Feng, M. Gorbunov, K. Hardy, B. Herman, Y. Kuo, T. Meehan, W. Melbourne, C. Rocken, W. Schreiner, S. Sokolovskiy, F. Solheim, X. Zou, R. Anthes, S. Businger, and K. Trenberth, "GPS Sounding of the Atmosphere from Low Earth Orbit: Preliminary Results", *Bulletin of the American Meteorological Society*, **77** number 1, 19-39, January, 1996.

[Zandt] Van Zandt, T.E., and R.W. Knecht, "Space Physics", LeGalley and Rosen (Eds.), *John Wiley & Sons*, 1964.

2.2. Abbreviations

AFSCN	Air Force Satellite Control Network
AFSPC	Air Force Space Command
AS	Anti-Spoofing
CDA	Command and Data Acquisition
CDMA	Code Division Multiple Access
DD	Double Differences
DMI	Danish Meteorological Institute
DoD	US Department of Defense
ECMWF	European Center for Medium Range Weather Forecasts
EDR	Environmental Data Record
EGOPS	End-to-end GNSS Occultation Performance Simulator
FDMA	Frequency Division Multiple Access
GDOP	Geometric Dilution Of Precision
GLONASS	Global Orbiting Navigation Satellite System
GNSS	Global Navigation Satellite Systems
GPS	Global Positioning System
GPSOS	GPS Occultation Sensor
GRAS	GNSS Receiver for Atmospheric Sounding
LEO	Low Earth Orbit
MSIS90	Atmosphere model
NOAA	National Oceanic and Atmospheric Administration
NPOESS	National Polar-orbiting Operational Environment Satellite System
NWP	Numerical Weather Prediction
POD	Precise Orbit Determination
PPS	Precise Positioning Service
RDR	Raw Data Records
ROSAP	Radio occultation ray tracing simulation tool for atmospheric profiling
SA	Selective Availability
SD	Single Differences
SDR	Sensor Data Records
SNR	Signal to Noise Ratio
SOC	Satellite Operations Center
SPS	Standard Positioning Service
TBC	To Be Confirmed
TBD	To Be Defined
TEC	Total Electron Content
TECU	Total Electron Content Unit
TRD	Thermal Data Records

2.3. Nomenclature

$\hat{L}$	measured carrier phase
$\hat{P}$	measured code phase
$\overline{R}_G$	position vector of the GPS satellite
$\overline{R}_L$	position vector of the low earth orbit (LEO) satellite
$\dot{\overline{R}}_G$	velocity vector of the GPS satellite
$\dot{\overline{R}}_L$	velocity vector of the low earth orbit (LEO) satellite
θ	angle between ray -and magnetic field directions
	clock errors
e_0	permittivity of free space
a	impact parameter
B	bias term
B	horizontal component of the earth's magnetic field
B_0	earth's magnetic field strength
a	bending angle
C	constant
D	distance from LEO satellite to thin screen
corr	correlation function
cov	covariance function
e	electron charge
f	carrier frequency
f_c	collision frequency
f_g	gyro frequency
f_p	plasma frequency
m	index of refraction
	the angle between incoming ray and the velocity of the LEO satellite
	the angle between outgoing ray and the velocity of the GPS satellite
	the angle between position and velocity of the GPS satellite
	the angle between position and velocity of the LEO satellite
	the angle between the two position vectors
λ	wavelength
K	constant factor
L	carrier phase
m	electron mass
N	refractivity
N_e	electron density
P	code phase
P	received signal power
R_{curve}	curvature radius at tangent point.
S	signal phase
SNR	signal to noise ratio
t	time

z height above earth's surface
Z_F diameter of the first Fresnel zone

2.5. Acknowledgement

The EGOPS simulation software package has been developed under ESA contract 12025/96/NL/CN by University of Graz and Terma Elektronik. A range of the routines in EGOPS has been developed by DMI under the ESA contracts, 11024/94/NL/CN, 11818/96/NL/CN and 11930/96/NL/CN.

We want to thank M. Exner, UCAR, and his team for realizing the GPS/MET mission. We also want to express our admiration for P. Silvestrin, ESTEC/ESA, having foresight in making ESA GPS occultation studies possible during times when nobody else believed in the technique in Europe.

3. Review of Physics Governing the Measurements

3.1. Physical fundamentals

Before the space age our concept of the outer space around the Earth was a very simple one. Space was assumed to be essentially a vacuum, where matter only consisted of extremely high-energy particles originating from cosmic radiation. It was further believed that the magnetostatic fields stemming from electric currents in the interior of planets and stars were the only existing electromagnetic fields in space.

Since magnetic fields from celestial bodies decrease as the inverse third power to the radial distance, no interaction took place among the planets and stars spanning our universe. This conception led to the conclusion that magnetic distributions around planets, as the Earth, had a structure similar to a dipole configuration. Thus it was a major surprise when the first satellites orbiting the Earth observed a strongly perturbed Earth magnetic field and a large variability in the radiation and particle distribution around the outer tenuous part of the Earth's atmosphere.

The magnetosphere confined by the deformed Earth magnetic field is strongly influenced by the dynamic coupling with the interplanetary plasma, and therefore determined by the characteristics of the solar wind. The source for the solar wind is the sun's outermost region, the corona, which by convection and radiative transport processes establishes the particle content and magnetic relations of the solar wind.

These solar processes have large variations in time, energy and orientation. Through the solar wind these processes also impinges on the structure and energy balance of the magnetosphere. The variations of the magnetosphere caused by the interaction with the solar wind are in turn also observed in the ionosphere, which constitute the upper ionized part of the atmosphere, tied by friction to the rotation of the Earth's neutral lower dense atmosphere.

The ionosphere is ionized mainly by the short wavelength part of the solar radiation (UV and soft X-ray) and to some extent also by particle precipitation. Thus this regions ionization state has large diurnal variations with maximum electron densities in the sunlit sector of the Earth. The strongest variations are monitored on the nightside of the Earth dominated by high-energy particle fluxes from the tail of the Earth's magnetic field and magnetic field reconfiguration phenomena as for example substorm events [Kohl].

Figure 3.1-1 shows the high latitude average electron concentration during a daytime and nighttime situation, respectively, for high and low solar activity. The regions of the lower ionosphere (E, F1, and F2) are clearly seen. They originate from the changes in the density and composition of the medium together with recombination processes related to the ionization caused by the solar radiation.

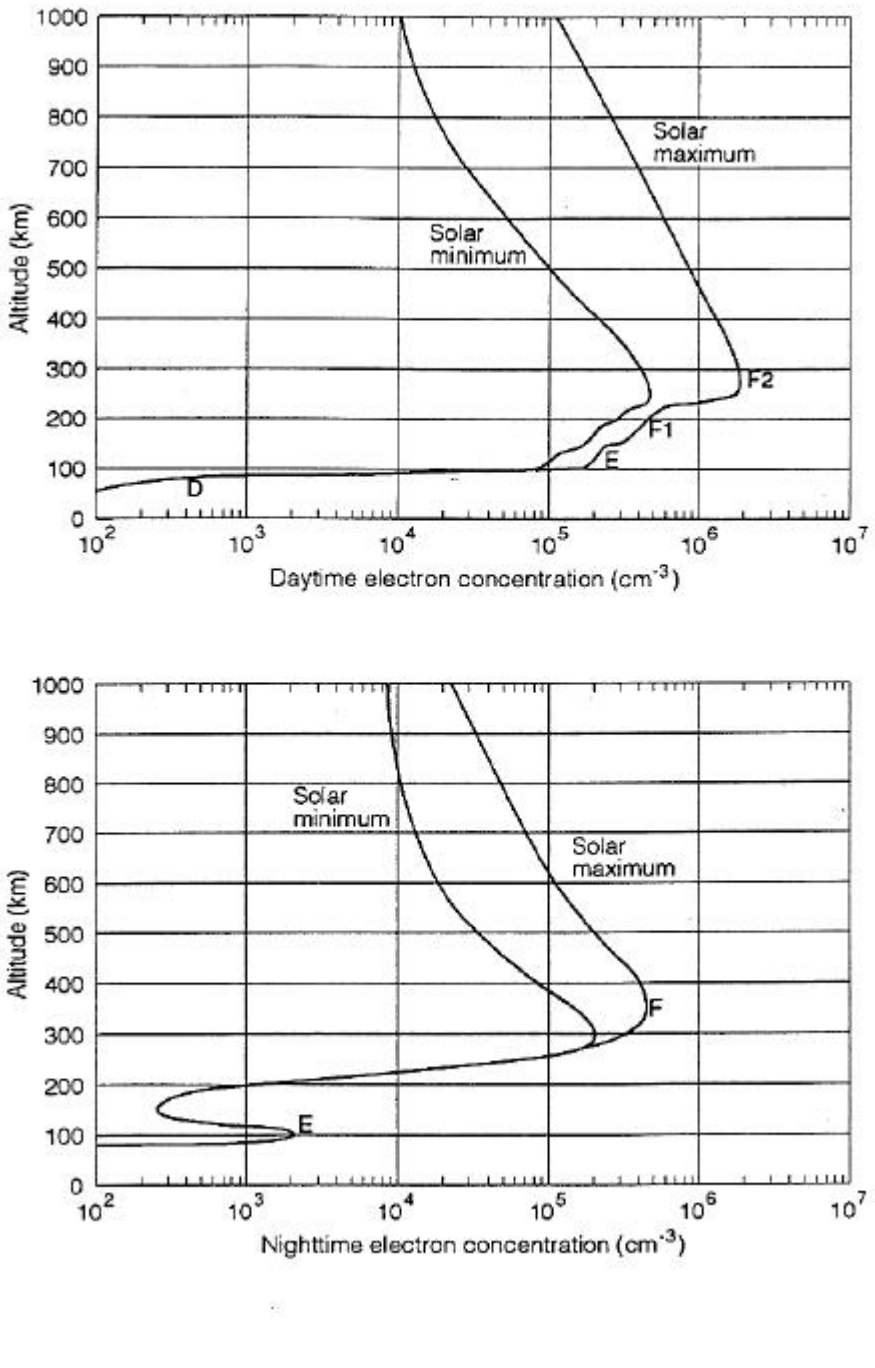

Figure 3.1-1 Altitude distribution of electron density in the ionosphere. The upper panel gives the situation in the daytime hours. While the bottom panel reveal the distribution at night [Johnson].

The F2 region is dominated by the atomic ion species O^+, He^+, and H^+ ionized by the UV solar radiation. While the E-region composition mostly consists of molecular ion species

as NO^+ and O_2^+, generated by the Lyman and X-ray solar radiation and collisions between electron, ions and neutral particles due to the more dense atmosphere in this altitude range [Kohl].

3.2. Atmospheric Conditions

The ionosphere regions structure according to the field line orientation of the Earth magnetic field. For invariant magnetic latitudes less than around 75 the closed field lines confine the ionosphere. While for latitudes larger than 75 the field lines are open and reconnected to the passing magnetic field of the solar wind.

Some of the effects of this plasma structuring are the major changes in the particle precipitation leading to the auroral regions, also associated with the intense upward and downward pair of field-aligned currents depositing major energy amounts in the lower ionosphere. Together with the polar cap potential drop across the magnetosphere current systems changes the convection flows in and around the auroral regions.

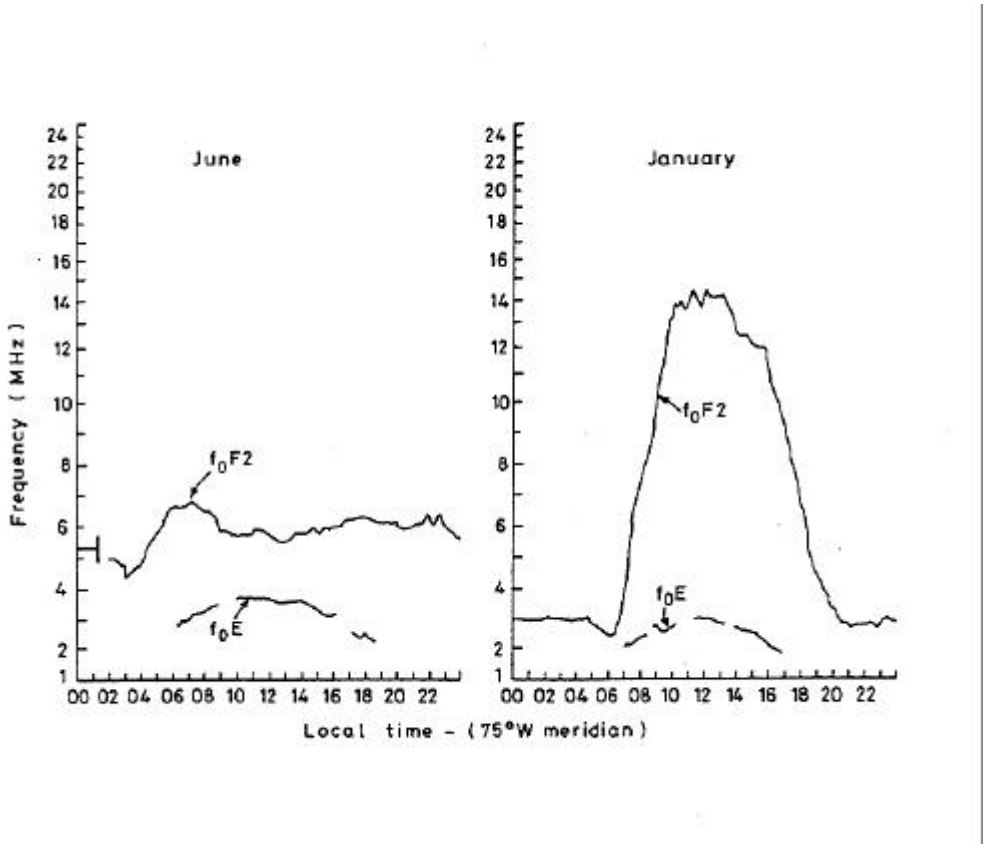

Figure 3.2-1. Diurnal change of foF2 and foE in summer and winter at a high latitude site in Alaska in the Northern Hemisphere [Zandt].

One of the prominent disturbances of the auroral oval is the magnetic substorm, which gives rise to major intensifications of the auroral activity and large variations in the ionospheric electron density distribution. As a result of this magnetosphere activity changes in the configuration of the nighttime convection cells are observed leading to drastic changes in the density structures of the ionized plasma.

The ionosphere conditions show also large latitudinal variations paired with seasonal changes. Figure 3.2-1 gives the daily observations of the peak electron densities of the E and the F2 region (f_oE and f_oF2) for high latitudes during summer and winter conditions. The right panel indicates an F-region winter situation, giving rise to large gradients in the refractive index around the terminator of the sunlit ionosphere. While the summer situation in the left panel shows a sunlit F region all through the day and most of the night. The large changes in the F region electron density results in major changes in the refractivity of radar observations and satellite communication through the medium.

The ordinate axis of the panels in Figure 3.2-1 is given in frequency units (MHz) related to the plasmafrequency (f_p) of the medium. The relation between the plasmafrequency and the electron density (N_e) can simply be approximated to be a function of the square root of N_e ($f_p^2 = 80.6 \cdot N_e$). Thus Figure 3.2-1 gives a good description of the high latitudinal diurnal changes in the ionosphere.

The tropical ionospheric effects arising from the equatorial electrodynamics lead to an enhanced electron density in the noon to afternoon sector local time. The upper panel in Figure 3.3-1 shows a contour plot of the enhancement in geomagnetic coordinates as function of local time. The phenomena occur when an eastward ambient electric field is enhanced and thereby drifting the F-region plasma to higher altitudes, where the recombination is slower. After sunset a combination of pressure forces and gravity start to drift the plasma along the magnetic field lines, which are almost horizontal, to the tropical regions leading to enhanced plasma densities here. This phenomenon is referred to as the equatorial anomaly.

The major daily changes associated with the equatorial anomaly is depicted in the upper panel of Figure 3.3-1 (the maximum F2 region electron density as function of the local time). While the lower left panel reveal the latitudinal variations as function of altitude in the F region. The curves have been offset on the ordinate axis for better to be able to see the variations. The enhancements north and south of the magnetic equator are most pronounced above the F-region peak. While the effects in the E region (lower right panel) are not so significant and sometimes not observable.

3.3. Atmospheric Effects on Electromagnetic Wave

The only way to efficiently observe the large ionosphere plasma region is by applying remote sensing techniques using electromagnetic radiation in the frequency domain from 1 MHz (MF and HF band.) to 40 GHz (SHF band). The propagation and energy flux re-

lation of the waves at these wavelengths are to a varying extent influenced by the natural frequencies of the plasma, characterizing the medium itself, and the scale sizes of the plasma physical processes.

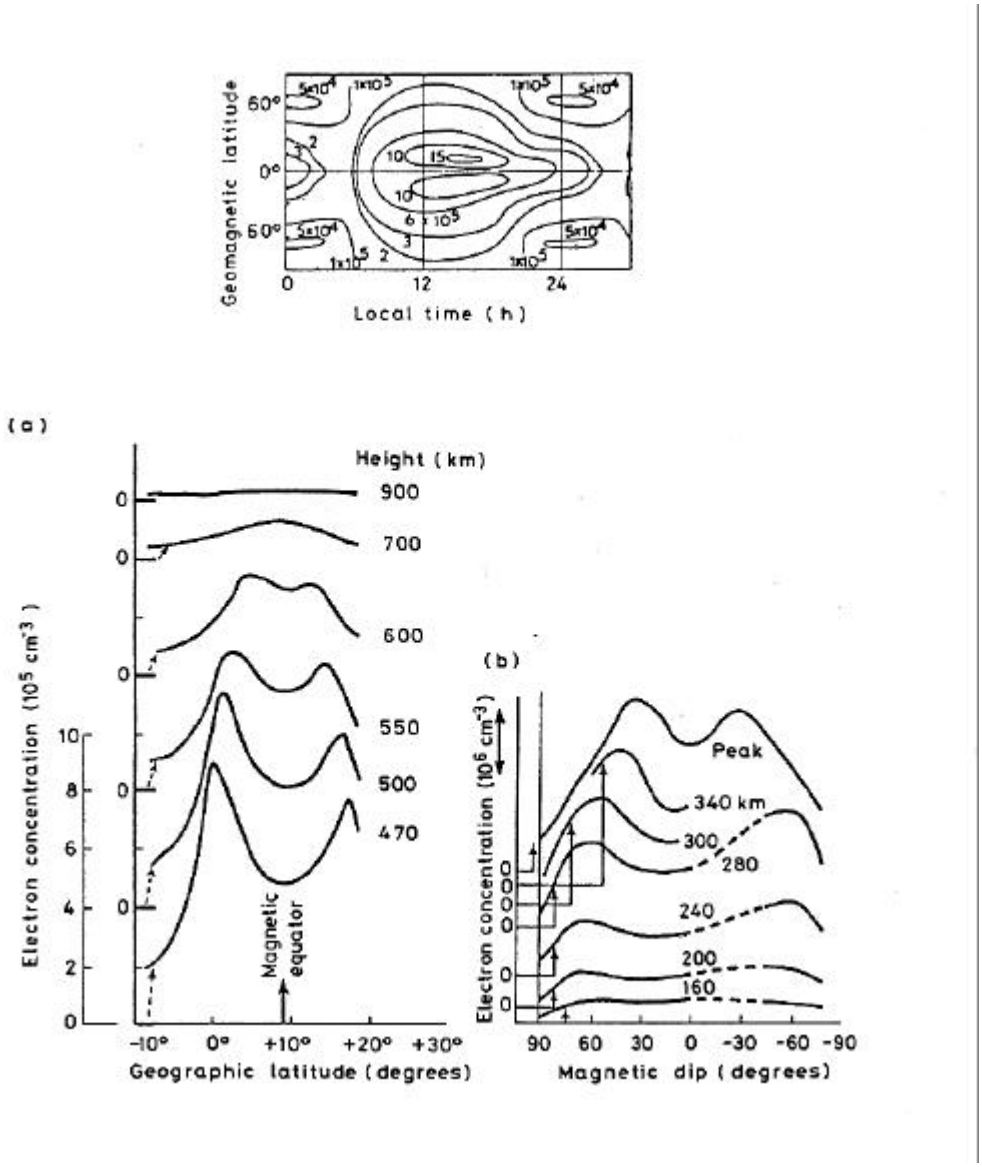

Figure 3.3-1. The top panel gives the equatorial anomaly outlined by the NmF2 contours (in electrons/cm^3). The lower panels show the latitudinal variation of the electron density across the equatorial anomaly at various altitudes. The lower left panel originates from topside ionograms above h_{max}. While the lower right panel gives the profiles below h_{max} observed from an ionosonde on ground [Hargre].

By combining information of the electromagnetic wave propagation direction and velocity, phase and amplitude changes, it is possible to monitor the dispersion relation governing the plasma.

In the ionosphere the direction of the ambient magnetic field of the Earth plays a crucial role in establishing the polarization characteristics of the wave probing the plasma. For planar high frequency electromagnetic waves the refractive relations are described by the Appleton-Hartree formulation, which expresses the wave field dependence of the characteristic frequencies of the medium. The refractive index [Budden] becomes,

$$m^2 = 1 - \frac{X(U-X)}{U(U-X) - \frac{1}{2}Y^2\sin^2 z \pm \sqrt{\frac{1}{4}Y^4\sin^4 z + Y^2\cos^2 z\,(U-X)^2}} \qquad (3.3.1)$$

where X, Y and U are dimensionless quantities relating the wave frequency with the plasmafrequency, gyrofrequency and collision frequency, respectively (see also chapter 6.3.4). ζ defines the angle between the direction of the constant ambient magnetic field and the wave number vector.

For the neutral part of the atmosphere consisting of the troposphere and stratosphere the refractive relation is dominated by the wave polarization from the atmospheric molecules together with the permanent dipole moment of water molecules related to the moisture content of the air mass. The refractive relation for L-band waves in the lower atmosphere [Bevis92] becomes,

$$m = 1 + k'_1\frac{P_d}{T} + k'_2\frac{P_w}{T^2} + k'_3\frac{P_w}{T} \qquad (3.3.2)$$

where P_d is the partial pressure of the dry air mass (in hPa), T the absolute temperature of the atmosphere (in Kelvin), and P_w the partial pressure of the water vapor content (in hPa). $k_{i,\,(i=1\text{-}3)}$ are constants of the neutral gas with evaluated values of, $k'_1 = 7{,}760\cdot10^{-5}$ K/hPa, $k'_2 = 3{,}739\cdot10^{-1}$ K^2/hPa, and $k'_3 = 7{,}040\cdot10^{-5}$ K/hPa [Bevis].

3.4. Model Validity

Monitoring the medium at GPS and GLONASS frequencies is an excellent way of measuring the integrated changes caused by the medium to the probing signal. The observing system is capable of accurately determining the important parameters of the ionosphere and the state of the neutral lower atmosphere together with information on geophysical phenomena as previously described. The simulation studies presented in chapter 7 underlines this conclusion.

For the total electron content observations and the electron density profile estimations the technique is able to give important global structural information on the state of the ionosphere and its interaction with the magnetosphere and the solar wind. Comparing the results from this technique with other ground-based radar TEC measurements reveals an accuracy of a few TECU [Kohl].

The scale sizes of the phenomena in the Earth's ionosphere favor occultation measurements to describe the differential vertical changes, either through profiles of the parameters or through a tomographic representation of the data distribution. Thus the above described understanding and model concept constitute an adequate method for observing a range of phenomena in the upper atmosphere.

Chapter 4 and 6 outline the methods and algorithms based on the above description of the physics of the ionosphere and the stratosphere/troposphere system. The chapters demonstrate too in detail the validity, capability and limitations of the technique probing the medium with GPS/GLONASS frequency waves. Additionally, chapter 7 gives the error analysis of the observations applying the system models and methods for best, nominal and worst conditions. The main conclusion of all the studies performed is that within the described limitations for the technique the suggested system is adequate to deliver the requested EDRs.

4. Scope and Methods

4.1. Ionospheric Measurements

The ionosphere is the region of the atmosphere covering the altitude range from roughly 80 km to 1500 km. Even though the neutral density is larger than the ionized portion of the gas, the latter determines the processes describing the medium in union with the external forces and the particle precipitation originating from the magnetosphere, the solar wind and the Earth's magnetic field.

The formation of layers or regions in the ionized part of the ionosphere is a result of the interplay between the incident radiation and particle precipitation and the occurrence of different atom and molecular species in the upper atmosphere. The complicated structure resembles a set of Chapman electron density distributions for most conditions with the E and F regions as the dominating layers.

The maximum electron density of the ionosphere is normally attributed to the F2 region. The height of the peak electron density varies from about 250 km to 400 km. While the maximum electron density for the E region covers altitudes from 100 km to 150 km.

The dispersive nature of the ionosphere plasma has a major impact on the electromagnetic wave characteristics and propagation. Thus the conditions in the ionosphere are important for the performance of all space-based communication, navigation, and surveillance systems.

Essentially only two methods exist to probe the physical parameters of the atmosphere. They are,

1. In-situ measurements

2. Remote sensing observations

Each of these techniques has its own advantages and disadvantages, and usually observations from both are required to provide a comprehensive understanding of the ionosphere and its physical processes.

In-situ measurements give information on the local environment of the ionosphere normally limited in spatial extent by the gyroradius of the ion species of the plasma. Thus these observations reveal the small scale phenomena in the ionosphere.

Due to the spatial large scale of the ionosphere these observations alone tell very little about the processes leading to the observed local phenomena. Thus model results or other types of observations from space and ground often complement in-situ measurements.

In-situ measurements are destined to follow certain observational constraints, as the orbit of the satellite. Therefore they will not always monitor the physical processes in question and their development, which again leads to problems in separating spatial and temporal phenomena and conditions for the observations.

Remote sensing methods can be divided into two groups. 1) backscatter radar techniques and 2) spatial separated transmitter-receiver methods for monitoring the impact on the probing signal. Backscatter methods give excellent observations of the atmosphere in local regions with high coverage. The major drawback of the technique is that normally it requires high-power transmitter and large receiving antennas or antenna arrays. Thus most measurements of this kind are done from ground.

The transmitter-receiver probing of the ionosphere has as one of its advantages that it can cover large parts of the ionosphere leading to a comprehensive understanding of the physics, taking place in the ionosphere. The GPSOS experiment is of this class. Since GPSOS uses an existing set of transmitters the cost of the mission is rather modest. Together with the long-term stability of the measurements the method has the potential of delivering a long-term monitoring of the ionosphere for space weather and climate change activities.

Due to the large number of high precision transmitters in the total GPS and GLONASS system (up to 48) the number of low Earth orbiting (LEO) satellites sets the limit for the spatial coverage.

It is possible with this technique to monitor the spatial and temporal development of the defined GPSOS observables, which consists of total electron density (TEC), slant-path TEC, electron density profiles, refractivity distribution, scintillations and their phase and amplitude spectra.

The major drawback of the technique is, that the observed parameters are integrated measurements through a medium, which sometimes at specific latitudes is highly variable. But the small relative vertical extent of the ionosphere compared to the radius of the Earth together with the radial structuring of the ionosphere lead to a highly detailed vertical information. This fact dissolves for a major part the intrinsic limitation of the technique.

Applying tomographic representation of the observations will result in further enhancements of the data products. Thus many LEO platforms performing GPSOS measurements can improve the accuracy of the description of the ionosphere state. This will also be the case when combining the GPSOS observations with GPS ground measurements of phase delays. The two data set represent scannings of the medium at different angles improving the total imaging reconstructions [Kohl]. The GPSOS measurements reveal the vertical changes and correlations in the atmosphere. While the ground observations gives information on the horizontal variability.

4.1.1. Scintillations

A radio wave traversing ionospheric irregularities consisting of unstable plasma waves or small-scale electron density gradients will experience phase and amplitude fluctuations. As long as the irregularities and the locations of transmitter and receiver do not change, a single receiver at a fixed location would detect a constant amplitude and phase.

Temporal or spatial changes of the irregularities as well as changes in the relative location of the transmitter/receiver system produce irregular temporal fluctuations of the received signal amplitude, phase and direction of arrival of the signal. For the GPSOS observations the temporal changes of the ionospheric irregularities plays a minor role, since the transmitter/receiver location velocity dominates over the time scale of the natural variability in the plasma caused by the irregularities.

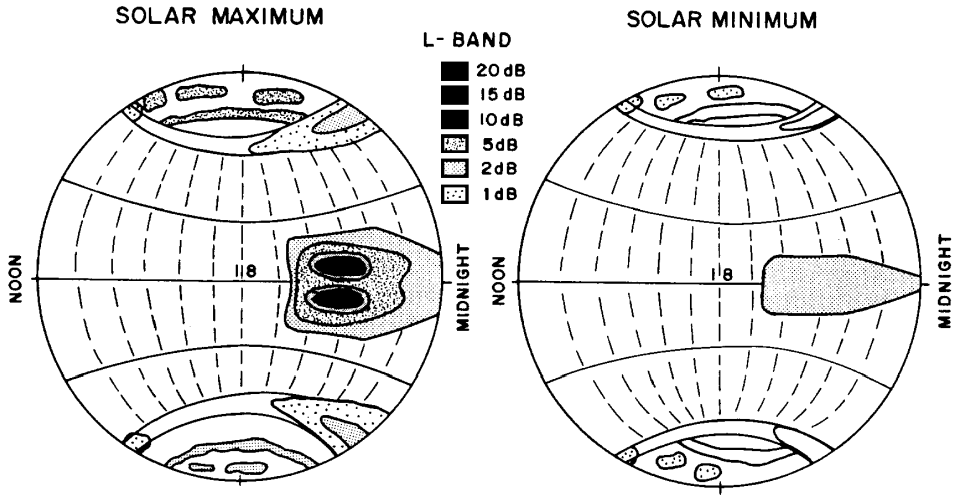

Figure 4.1.1-1. Global variations of amplitude fading in scintillations during solar maximum and minimum conditions [Basu].

The scintillations are predominantly observed in the F region of the ionosphere (spread-F irregularities). The altitudes, in which scintillations are observed, range from 200 km to 1000 km at high latitudes. At equatorial latitudes scintillations predominantly are observed between 250 km and 400 km. But also E region irregularities (particularly sporadic E and auroral E) produce scintillations, which at times is causing much larger phase scintillations than the F region perturbations.

The usual measure of the strength of amplitude scintillation is the S_4 index. S_4 is defined as the root mean square of the variance of the received power divided by the mean value. Phase scintillation strength is characterized by the standard deviation of the phase s_f over a given interval of fluctuation frequencies.

For S_4 less than 0.6, the amplitude scintillation has a frequency dependence of approximately $f^{-1.5}$ [Kelley]. Whereas s_f varies as f^{-1} for both weak and strong scintillation in the frequency range used by the GPS and GLONASS.

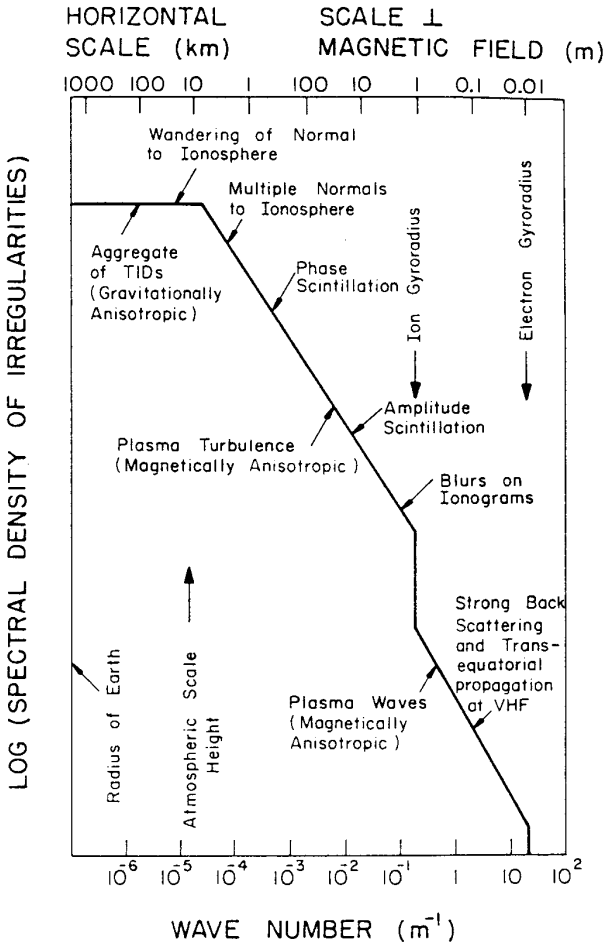

Figure 4.1.1-2. Spectra of ionosphere irregularities and their intensity as function of wave number over spatial scale sizes covering from the electron gyro-radius to the radius of the Earth (Booker, 1956).

The morphology of amplitude scintillations pinpoints two regions on the Earth with high probability of intense scintillations. They are, the high latitudinal auroral regions and the equatorial latitudes, both bounded by magnetic and not geographic latitudes (see Figure

4.1.1-1). For the high latitude regions the data representation are best treated when using invariant magnetic latitudes or magnetic dipole latitudes. While for equatorial latitudes scintillations are best described by using dip latitudes.

The most intense amplitude scintillations are expected to be for high solar activity in the region around the crests of the equatorial anomaly at equinox and in the evening hours in the local time sector from 20 to 24 hours. Figure 4.1.1-1 gives the global spatial variations in the amplitude fading during maximum and minimum solar activity conditions. Amplitude fading in the GPS frequency range can amount to 6 dB or more during high solar activity.

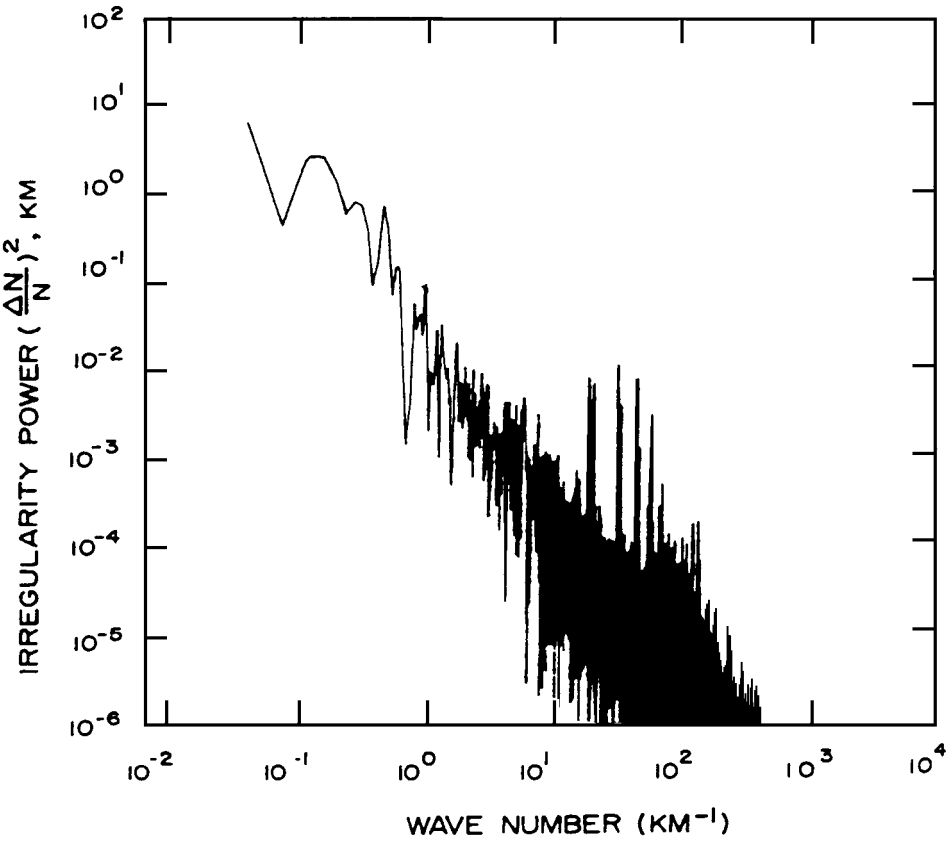

Figure 4.1.1-3. Rocket observations of the spectral horizontal variations in the electron density of the high latitude ionosphere [Kelley80]. The high frequency part of the power spectrum is cut off due to limitations in the instrumentation.

The observation of phase scintillation on a single GPS signal is difficult because of multipath problems and the fact that stronger amplitude scintillations couple to phase scintillations. Up to 8 radians of fluctuations have been observed in phase scintillations averaged

over the sampling frequency, with the strongest phase excursion reported on L_1-L_2 amounting to 14 radians for a period of 30 seconds.

Typical phase scintillation observations of the average phase change rate of L_1-L_2 are reported to happen for frequencies less than 1 Hz [Kelley]. Thus applying the frequency power law for 10 Hz phase scintillations leads to an estimate of the peak-to-peak fluctuations, which becomes less than 1 radian for highly disturbed conditions given above.

Power spectra of the upper ionosphere plasma density have been detected as well by in-situ measurements (rockets) and trans-ionospheric satellite measurements [Kelley]. The results show for both the auroral and equatorial electrojets a power law relation of the form k^{-n}, where k is the wave number of the scintillations and n a number varying from 1.5 to 5 depending on the geomagnetic conditions, latitude and scale size of the irregularities [Kohl].

A range of observations, simulations, and theoretical considerations indicate that for high k values the spectral shape is determined by the Kolmogorov turbulence theory. This theory states, that due to the conditions for the unstable waves the plasma structures will form in the region of k space close to the natural scale sizes in the plasma. Figure 4.1.1-2 shows a schematical representation of the scintillation spectrum including the dominant processes leading to the characteristics for the different regions in the spectrum. Energy cascades towards larger k values leading to a turbulence spectrum, which cease at a wave number, where energy dissipation occurs due to molecular viscosity. The turbulence theory indicate, that a more shallow spectral slope will be observed for wave numbers centered around k 30 m^{-1} (0.2 m, f 1.5 GHz), where the GPSOS system operates. Figure 4.1.1-3 shows a power spectrum measurement from a low latitude rocket experiment [Kelley80].

4.1.2. Total Electron Content

One of the basic observables of the GPSOS mission is the total electron content measurement (TEC), defined as the integrated electron density content along the ray path.

$$TEC = \int_{Path} N_e(s)ds \qquad (4.1.2.1)$$

Here $N_e(s)$ represents the electron density along the propagation path between the source and the detector.

TEC observations can be grouped into *vertical TEC* and *slant-path TEC* observations. Vertical TEC, normally given from the surface of the Earth and vertically upwards, are mostly done from ground in order to capture the total ionosphere contribution to the TEC observation. While slant-path TEC, defined as the total electron density along the

ray path between transmitter and receiver at angles deviating from the radial direction with respect to the center of the Earth, best is performed from satellites resulting in better global coverage.

Measurements of TEC are crucial for the derivation of the secondary EDRs too, since the retrieval process of the neutral atmosphere parameters need to correct for the ionosphere contribution to the measured refractivity. But TEC is also a good measure of the spatial changes in the global electron density structures of the ionosphere. TEC acts as an indicator of geographical, seasonal, and diurnal variations in the ionosphere, resulting from the combined effects of solar radiation and transport processes of electrons and ions from one region to another.

Vertical TEC show large spatial changes especially at high latitudes in the auroral regions. The magnitude can here increase to several hundreds TEC units (1 TEC unit = 1 TECU = 1 10^{16} electrons/m^2). In other regions of particular interest (the equatorial region) TEC is often quite large amounting up to 400 TECU for disturbed conditions.

The slant-path TEC can maximize during high sun spot numbers at values close to 1000 TECU (see chapter 7.2). The main reason for this is, that the signal passes through the ionosphere two times from the transmitter (GPS/GLONASS satellite) and to the receiver on the LEO satellite (NPOESS satellite).

TEC has been studied for many years using Faraday rotation and differential Doppler techniques. These measurements provide important information about the ionosphere variability through the measurements of the temporal and spatial variation of TEC. Simultaneous TEC data have been used to study horizontal (latitudinal as well as longitudinal) variations of ionospheric structures.

Since TEC is the line integral of the electron density along the ray path, the information about the spatial variation of the electron density along the path caused by irregular structures cannot be recovered using the conventional procedure to process TEC data. Therefore ionospheric imaging is applied when having many TEC measurements of the ionosphere. This method has the capability of producing a two-dimensional picture of the ionospheric electron density distribution by using the one-dimensional TEC information.

Two different techniques are normally used when measuring ionospheric TEC. The first method relies on the differences of the P-code measurements from the L1 and L2 frequencies in order to generate the TEC observations. While the second method uses the probing carrier phase differences to generate the biased TEC measurements. The latter is more precise than the code based method. But the technique contains an unknown bias, arising from the ambiguity of the phase measurements governed by the unknown TEC above the satellite orbit (see chapter 6.3). Normally both methods (code and phase measurements) are combined to generate a single TEC quantity, based on the precision of the phase measurement with the phase bias determined from either the code measurement or from a statistical optimized model of the upper part of the ionosphere.

The ionosphere as a dispersive medium leads to different phase delays as well as to different ray paths (bending) of the L1 and L2 frequencies. When passing through the ionosphere while approaching the closest distance to the surface of the Earth the L1 and L2 rays split and subsequently traverse the atmosphere at slightly different heights (up to one kilometer separation at the impact height is predicted during strong ionospheric disturbance conditions). After leaving the atmosphere and approaching the LEO the separated L1 and L2 rays are again subject to different bending.

The standard dual frequency range correction eliminates most of the ionospheric error by canceling the first order slant path TEC contribution, which would contribute to errors from the order of 1 meter at nighttime to the order of 100 meters at daytime during solar maximum conditions. However higher order effects (mainly the ray path splitting) lead to residual range errors of more than 0.3 meter, which if not corrected prevent accurate retrieval of secondary EDRs.

Improved correction of the above is a difficult task. But since the actual bending depends on both the asymmetry of the inbound and outbound ionosphere and on the actual ionospheric layering during the occultation events it is possible to include this knowledge into the correction method.

Bending angle correction is one of the techniques that result in better correction than range correction alone. This is a significant improvement with respect to the standard range corrections since it exploits the fact that most of the total bending is accumulated at grazing incidence near the ray perigee region in the atmosphere (see discussion in Appendix A).

Further theoretical studies show that also Doppler shift corrections instead of ranges or bending angles can nominally improve the accuracy of the achievable atmospheric parameters [LADR].

An approximation to the dispersion relation can be used to retrieve the EDR products for TEC. The refractive index is defined as,

$$|m|^2 = 1 - \left[\frac{f_p}{f}\right]^2 \qquad (4.1.2.2)$$

where f_p is the plasmafrequency of the electron gas in the ionosphere and f the probing electromagnetic wave frequency used by the GPS/GLONASS system. Equation (4.1.2.2) combines directly the electron density with the refractivity of the ionosphere plasma. This together with the relation for the excess phase change,

$$\Delta\Phi = l^{-1}\left(\int m(s)\,ds - R_L\right) \qquad (4.1.2.3)$$

where R_L is the line-of-sight distance between receiver and transmitter, λ the wavelength of the probing signal, and m the refractive index along the ray path, turns out to be a very good approximation for most ionospheric conditions.

Applying the full refractive index expression (see chapter 3 and 6) requires external knowledge of the Earth's magnetic fields magnitude and configuration. In chapter 6 we have assessed the error related to the higher order terms when applying different correction schemes.

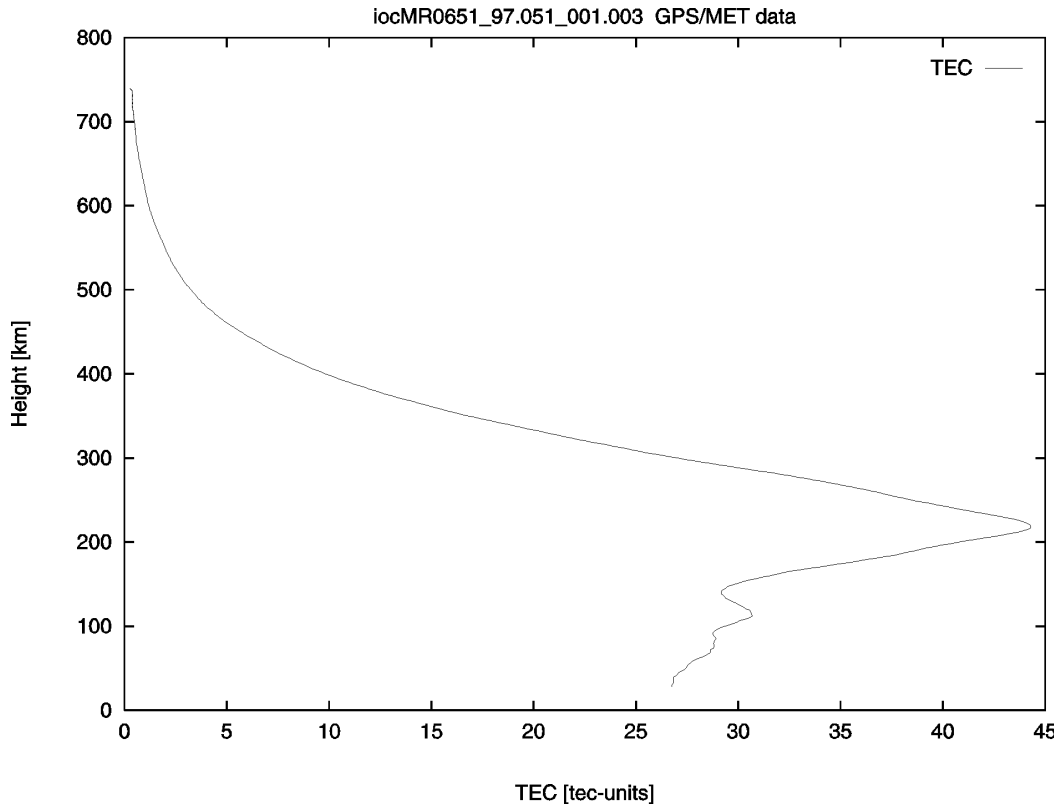

Figure 4.1.2-1. TEC retrieval from a GPS rising occultation observed by the GPS/MET experiment (Time: 22.20-22.30 UT; Date: 20. Feb. 1997). The latitude and longitude of the profile centers at 50 N and 80 W, respectively.

In the retrievals of the GPSOS data products we plan to use the simpler approximation above by combining the whole set of phase changes during an occultation to retrieve the variations in the refractive index. Chapter 6 and 7 describes in detail the applied developed methods.

Figure 4.1.2-1 shows an example of our retrieval software for TEC. The observations originate from the 'Prime Time 4' period of the GPS/MET experiment. This specific oc-

cultation data set is from the time period, 22.20-22.30 UT, on 20th February 1997, at latitudes of 50 N during a rising occultation. The E and F2 region is clearly depicted in the retrieval.

4.1.3. Ionospheric Refractivity

The ray path of the GPS/GLONASS signal is bent due to the dispersive nature of the ionospheric plasma. The bending angle a(r) is closely linked to the Doppler shift of the received signal. For a spherically symmetric atmosphere, assuming a layered model of the ionosphere, the ray path can be estimated analytically. A unique relationship is derived via the Abel integral transform between the bending angle a(r) and the refractive index m(r) as function of the distance from the center of Earth. The integral equation derived for the above assumption becomes,

$$m(r) = exp\left[p \int_{r}^{\infty} \frac{a(x)}{\sqrt{x^2 - r^2}}\, dx \right] \tag{4.1.3.4}$$

where

$$r = \frac{a}{m} \tag{4.1.3.5}$$

$$a = q - \arccos\left(\frac{a}{R_L}\right) - \arccos\left(\frac{a}{R_G}\right) \tag{4.1.3.6}$$

$$\dot{L}_C + \dot{R}_{LG} - (\dot{R}_L \cos f(a) - \dot{R}_G \cos c(a)) = 0 \tag{4.1.3.7}$$

Where q is the angle between the LEO and the GPS satellite, L_C is the corrected carrier phase, R_{LG} is the distance between the GPS and LEO satellite, χ is the angle between outgoing ray and the velocity vector of the GPS and finally φ is the angle between the incoming ray and the LEO velocity (See also Figure 6.3.2.5-1 in chapter 6).

Figure 4.1.3-1 gives the bending angle profile for the same data set used in obtaining the results presented in Figure 4.1.2-1. The bending angles at the highest altitudes show large variations due to low phase change caused by the ionosphere at these altitudes and the ambiguity in the TEC estimation here.

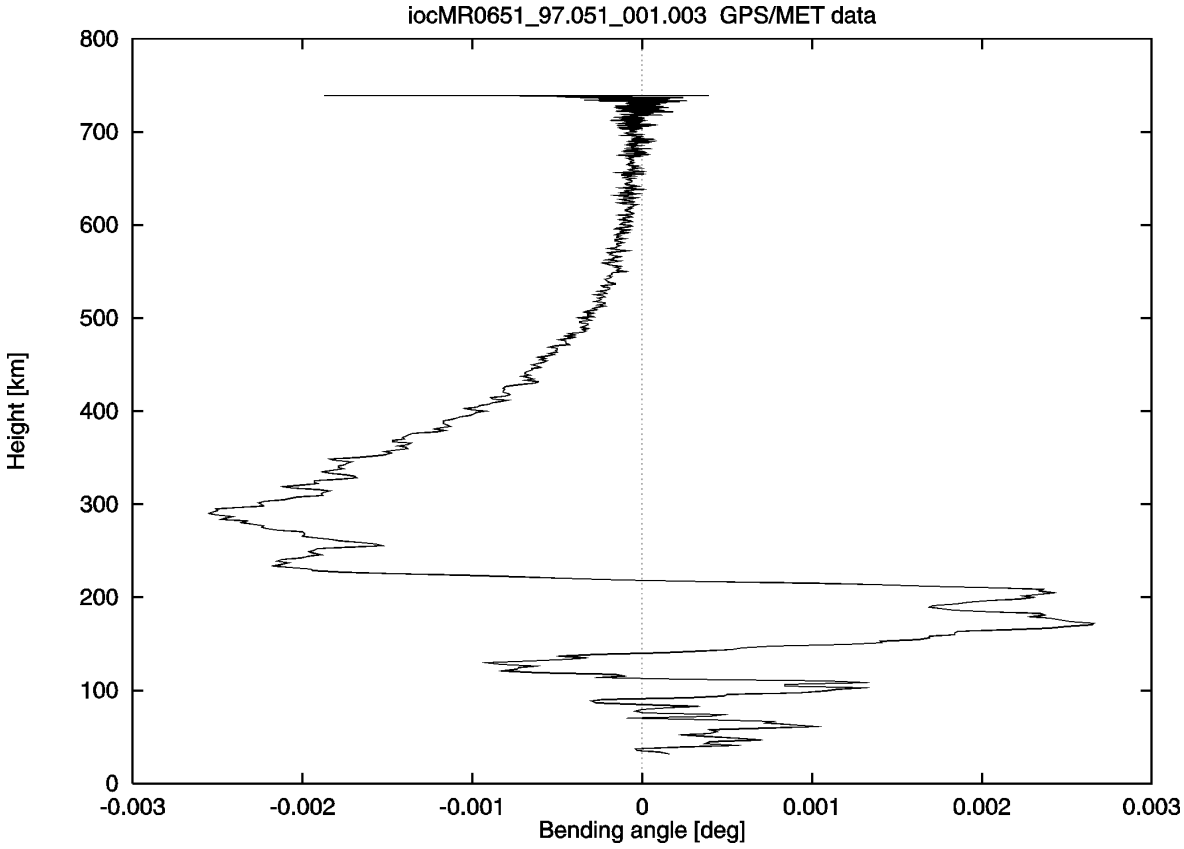

Figure 4.1.2-2. Bending angle retrieval as function of altitude for a GPS/MET occultation. The observations originate from 22.20-22.30 UT on 20th February 1997.

The magnitude of refractivity N (defined as $N = (\ -1)\ \ 10^6$) in the ionosphere is slightly negative having values down to -100 for the GPS/GLONASS frequency range. In the troposphere of the neutral atmosphere refractivity increase to values up to 450 leading to a major increase in the excess phase compared to the values observed in the ionosphere. Thus it is valuable to have the refractivity profile in the ionosphere to determine the errors in the retrieval of the other EDRs.

4.1.4. Electron Density

The electron density profile at the lowest impact height of the ionosphere gives a good measure of the characteristics of the layers in the ionosphere together with magnitudes and altitudes of the maximum electron densities.

The retrieval technique follows the following steps:

- Observations of the phase delays for L1 and L2

- Calculation of TEC
- Calculation of the bending angle profile
- Inversion of bending angles using the Abel transform
- Retrieval of the electron density profile

The input data are the positions and velocities of the two satellites performing the observation (GPS/GLONASS satellite and GPSOS LEO satellite) together with the phase delays of the two frequencies (L1 and L2). Only carrier phases are used.

TEC along the ray path through the ionosphere is calculated. TEC is obtained from the difference of the L1 and L2 phase delays. This difference cancels any clock errors between the transmitter and the receiver. Further, the sensitivity to the geometric variations is greatly reduced. The phase delays and thus the bending caused by the ionosphere are very small. So the ray path of the occulted beams can be assumed to be close to a straight line. With this assumption the phase delay can be calculated from the TEC (see also the detailed discussion in chapter 6).

$$\mathrm{TEC} = \frac{f_1^2 f_2^2}{C(f_1^2 - f_2^2)}\left[\mathrm{L}_1 - \mathrm{L}_2\right] \qquad (4.1.4.1)$$

C is a constant of the ionosphere, while f_1 and f_2 represent the two probing frequencies.

From the phase delay obtained this way, i.e. without clock errors or geometric Doppler, the bending angle as a function of impact parameter is calculated. This involves a differentiation of the phase with respect to time. Thus the sampling rate needs to be sufficiently high, preferable 1 Hz or higher.

For high impact parameters the bending angle is calculated using an exponential fit in order to eliminate errors introduced near the height of the LEO orbit. For the GPS/MET satellite observations we have used an exponential optimized method of the impact parameter between 550 km and 650 km (see chapter 6 and 7). This approach is needed when calculating the refractive index using the Abel transform since the integral goes to infinity.

Under the assumption that the electron density is spherically symmetric the refractive index (a) and the electron density can be obtained from the bending angles $\alpha(a)$ using the Abel transform.

$$\ln(m(\mathrm{a})) = \frac{1}{p}\int_{a}^{\infty} \frac{a(x)}{\sqrt{x^2 - a^2}} dx \qquad (4.1.4.2)$$

The electron density is finally obtained using the expression for the refractive index in the ionosphere to the first order. Effects originating from solar activity and the higher order terms from the magnetic field are neglected.

$$\mathrm{N_e}(a) = \frac{(1 - m(a))\, f_1^2}{C} \qquad (4.1.4.3)$$

When the assumption of spherical symmetry is violated the electron density calculated in this way can become negative. This is of course not real, but simply reflects, that horizontal data from for example tomography would be needed to construct the true electron density profile.

The above outlined procedure to calculate electron density profiles does not rely on an absolute determination of the TEC. The bending angle profile is obtained by differentiating the observed phases. So only the shape of the phase profile is important.

The absolute value of the horizontal TEC can be determined fitting an exponential function at high impact parameters and subtracting the offset. However the near zenith TEC must be determined by other means, i.e. calculating TEC using code phase information as earlier described.

The algorithms described above have been tested and validated on model data generated by a forward ray propagation simulator together with global models of the disturbed ionosphere. Comparing the electron density profile obtained using the Abel transform with the ‘true’ electron density from the input model ionosphere results in a near perfect match between retrieved profiles and the model ionosphere profiles.

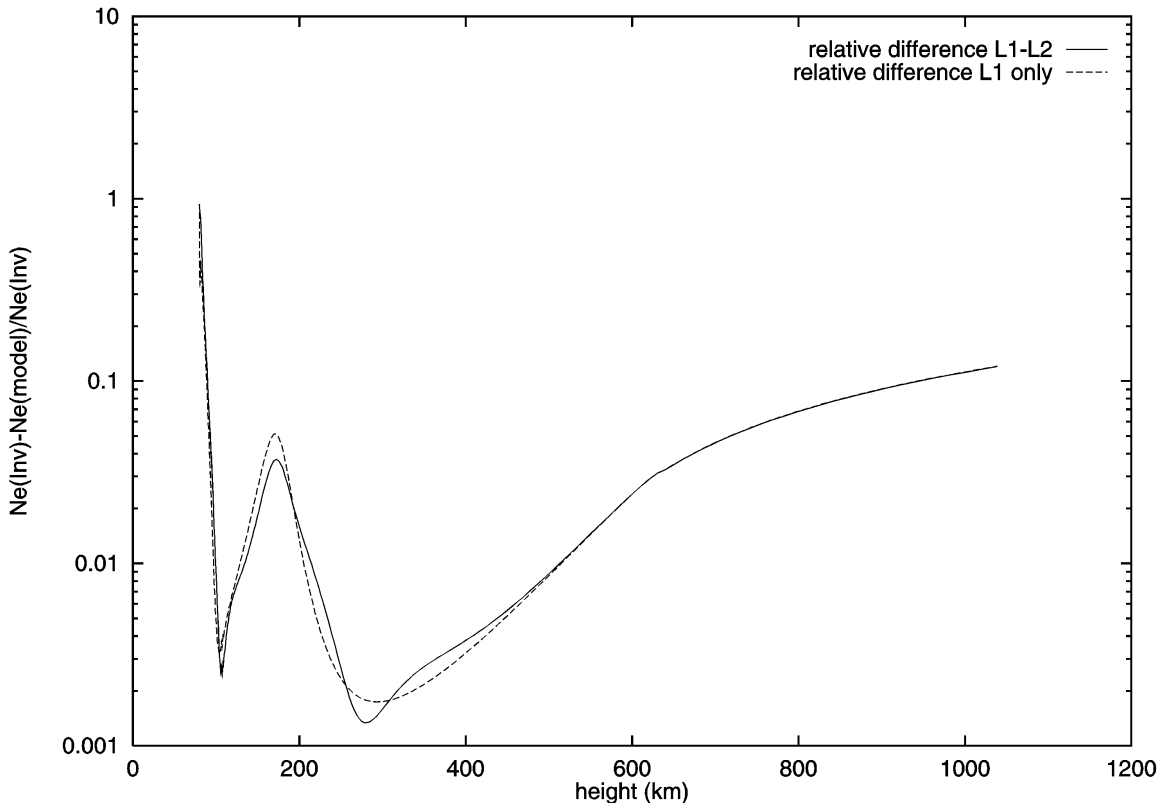

Figure 4.1.4-1. Simulations of the relative electron density profile errors using L1 without clock errors (dotted line) and the L1-L2 difference algorithm for the phase delay (full line) in order to eliminate the clock errors in the simulation.

Figure 4.1.4-1 shows the relative differences between the input electron density profile, applying Chapman layers for the E and F2 region, and the resulting retrieved electron density profile. The solid curve represents the inversion scheme, where the phase delay has been calculated from the L1-L2 difference as given above. The dashed curve represents the relative difference when using only using L1 and no clock errors. From the curves it is evident, that the relative difference is less than 1% near the peaks of the electron density profiles.

A small bias may be introduced at high impact parameters when the bending angles are fitted to an exponential expression. By subtracting this bias the errors reduce to below 0.5% for all heights.

Figure 4.1.4-2 shows the simulation results of the electron density errors of the retrieval technique when applying 1mm uncorrected Gaussian noise to both probing frequencies, L1 and L2, and applying the developed algorithms for the electron density retrieval described above. The experiment shows only minor errors between the undisturbed profile (dotted line) and the profile with the phase noises included (full line).

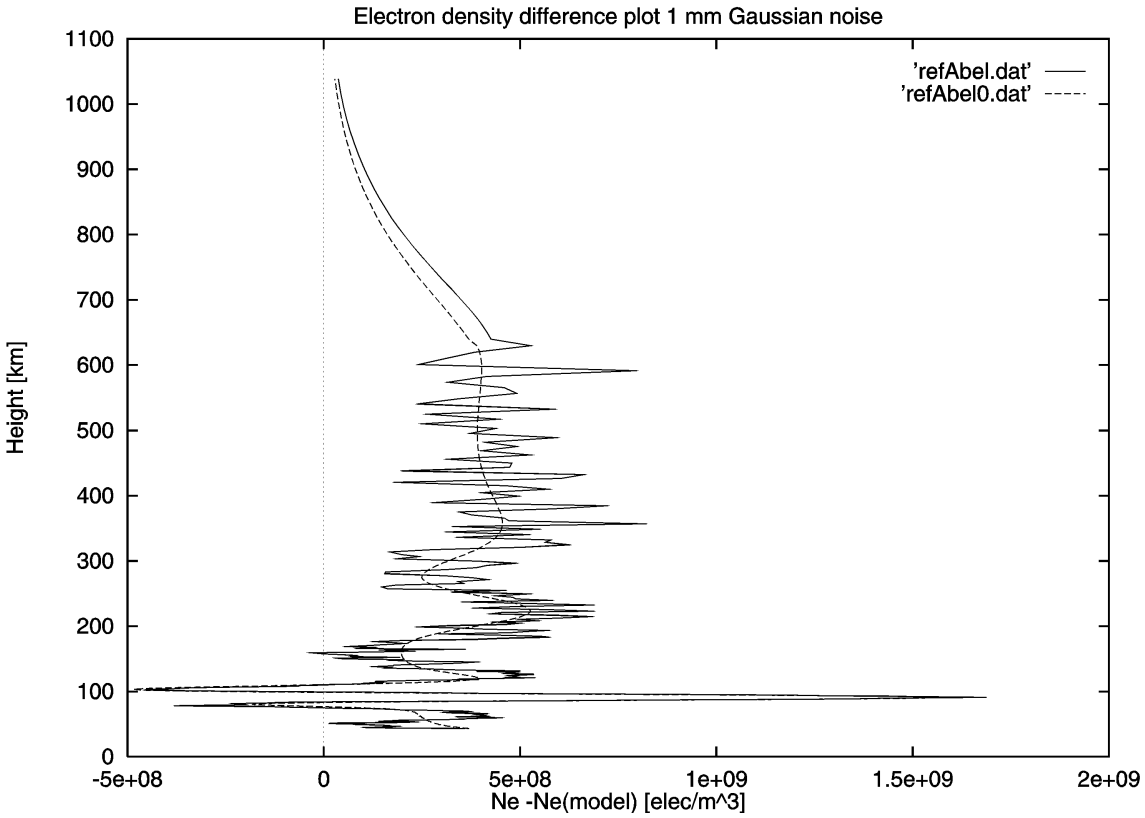

Figure 4.1.4-2. Retrieved ionospheric electron density profile differences when Gaussian noise of 1.0 mm has been added to the phase measurements (full line). The dotted line gives the unperturbed retrieved profile.

The algorithms have also been applied to ionosphere observations from the GPS/MET satellite. Figure 4.1.4-3 gives the estimated electron density profile from an GPS/MET occultation observation. Both the E and F2 region and their characteristics are clearly identified in the retrieval.

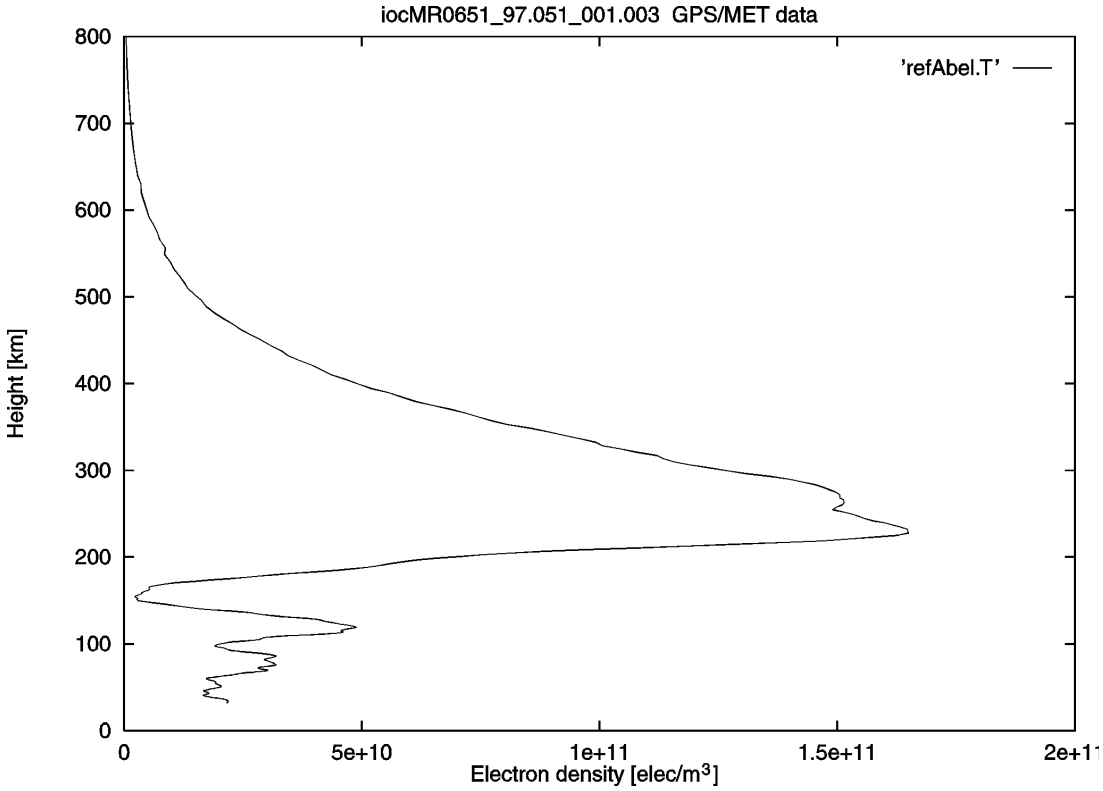

Figure 4.1.4-3. Calculated electron density profile for a GPS/MET occultation on 20th February 1997. The observations are the same as used in Figure 4.1.2-1 for the TEC profile.

4.2. Neutral Atmospheric Measurements

The atmospheric profiling technique provides measurements of the Doppler shift of the probing GPS/GLONASS signals that have passed through the limb of the atmosphere. The magnitude of the shift is related to the atmosphere's refractivity gradients along the path of the signal. These in turn are related to the neutral atmosphere's temperature, pressure and humidity fields.

Provided that the signal has sufficiently high quality (i.e. signal-to-noise ratio) and that other variables of the experiment (e.g. the positions of the transmitter and receiver, and the effects of the ionosphere) are known to sufficient accuracy, information on the temperature and humidity fields can be retrieved. More specifically, from series of measurements obtained during the occultation event, the profiles of temperature and humidity close to the tangent point of the signal path can be estimated.

The secondary EDRs relating to the stratosphere and troposphere retrievals are setting the highest demands on the accuracy of the observables and the POD estimates. To comply with these requirements the software algorithms follows two routes for determining

the dry state of the lower neutral atmosphere and the water vapor profile of the troposphere.

The occultation technique is defined by the geometry, where the transmitter and the receiver are positioned relative to the Earth in such an arrangement, that the radio wave signal traverses the atmosphere from the ionosphere to the limb of the Earth and back again towards the LEO satellite. The propagation path of the GPS/GLONASS electromagnetic wave through the atmosphere will be influenced by the dispersive characteristics of the medium, due to ionized and neutral part of the gas of the atmosphere. Ray bending and changes in the phase and amplitude of the transmitted signals, caused by the conditions in the ionosphere and troposphere/stratosphere, are the results.

The dispersion relation for the electromagnetic wave probing the atmosphere can be defined as the real part of the refractive index m, when discarding the absorption of the wave in the media (see also chapter 3.3). The relation expressing the total atmosphere refraction becomes,

$$N = k_1 \frac{P_d}{T} + k_2 \frac{P_w}{T^2} + k_3 \frac{P_w}{T} \qquad (4.1.4.5)$$

where $N = (m-1) \cdot 10^6$, P_d the partial pressure of the dry air mass (in hPa), T the absolute temperature of the atmosphere (in Kelvin), and P_w the partial pressure of the water vapor content (in hPa) [Bevis92], [Bevis]. The constants for each of the terms in (4.1.4.5) are evaluated to have the magnitudes, k_1 = 77,60 K/hPa; k_2 = $37{,}39 \cdot 10^4$ K^2/hPa; k_3 = 70,40 K/hPa.

The first term on the right-hand-side of the above equation is due to the dry part of the atmosphere, and is caused by the wave polarization of the molecules in the lower neutral atmosphere (troposphere and stratosphere). The second and third term relate to the moist atmosphere relation from the permanent dipole moment of water molecules. All these terms are independent of frequency. It is assumed that the ionosphere contribution can be estimated and removed, so that N only carries the neutral atmosphere contributions.

The moist terms have only a substantial impact on the magnitude of N in altitudes below 5 kilometer. Above altitudes of 7-10 kilometers the contribution to N from the water vapor terms is less than 2%. In the tropics the influence of water vapor has to be considered in the retrieval of the lowest part of the troposphere temperature profile. Thus, observations of refractivity itself is a measure of the combined effect of temperature and water vapor, and may ultimately be applied to weather and climate models as a consistent physical parameter describing the state of the atmosphere.

Taking account of the above considerations, N can be reduced to a function of only the dry term in the equation of refractivity. Combining this with the equation of state,

$$P = \frac{r\,RT}{m} \tag{4.1.4.6}$$

results in a directly proportional relation between the air mass density r and N. In other words, r(r) can be obtained from the values of the refractive index. Applying hydrostatic equilibrium,

$$dP = -gr\;dr \tag{4.1.4.7}$$

where g represents the acceleration of gravity, establishes a relation between the pressure P(r) at a certain height and the air mass density r(r). The temperature T(r) can now be obtained from P(r) and r(r). So in summary, vertical profiles of r, P, and T can be derived directly from the observed refractive index profile m(r).

The basic parts of this retrieval procedure can be synthesized in the below parameter and equation flow (see also section 4.1.3 and chapter 6).

Observables: $j = \int_{ray\,path} m\,ds - R_{LG}$ $\quad j_1$ and j_2

↓

Ionosphere correction: $j_C = \frac{f_1^2 j_1 - f_2^2 j_2}{f_1^2 - f_2^2}$ $\quad j_C$

↓

Doppler shift: $\frac{dj_C}{dt}$ $\quad \dot{j}_C$

↓

Impact height: $F(a) = \dot{j}_C + \dot{R}_{LG} - (\dot{R}_L \cos f(a) - \dot{R}_G \cos c(a)) = 0$ $\quad a$

↓ ↑

Bending angle: $a = q - \arccos(\frac{a}{R_L}) - \arccos(\frac{a}{R_G})$ $\quad a(a)$

↓

Abel transform: $\ln(m) = \frac{1}{p}\int_a^\infty \frac{a(x)dx}{\sqrt{x^2 - a^2}}, \quad r = \frac{a}{m}$ $\quad m(r)$

↓

Neutral density: $r = \frac{1}{k_1 R}(N - \frac{k_2 P_w + k_3 T P_w}{T^2}), \quad N = (m-1)\cdot 10^6$ $\quad r(r)$

↓

Hydrostatic equation: $$P = \int_{R_E+z}^{\infty} r(r)g(r)\,dr \qquad P(z)$$

$$\downarrow$$

Equation of state: $$T = \frac{P}{Rr} \qquad T(z)$$

4.2.1. Neutral Atmosphere Refractivity

The thermal noise and the ionosphere correction at altitudes above 30 km limit the refractivity measurements for the neutral atmosphere. While horizontal variations in the refractivity limit the accuracy of the measurements for altitudes less than 25 km. The mean error in the refractivity profile becomes less than 0.4% for altitudes between 5 km and 30 km.

In the lowest part of the troposphere refractivity suffers from increasing fluctuations due to the nonlinear character of the water vapor contribution in the refractivity expression. The variable spatial distribution of the water vapor additionally leads to higher uncertainties in the refractivity profile of the boundary layer. But in total it is possible to estimate the temperature and water vapor profile to the required accuracy when constraining the retrievals with external NWP predicted temperature fields. Chapter 6.3 gives a demonstrated of the potential of calculating the integrated troposphere water vapor based on this strategy.

4.2.2. Temperature Profiles

Figure 4.2.2-1 and 4.2.2-2 are examples of the possible accuracies in the temperature profiles for the stratosphere and troposphere when retrieving the profiles using the above algorithms.

The profiles are also compared with the Fresnel transform having a higher vertical resolution than the Abel transform. But because of the long computation time for this retrieval method we suggest to apply the above described inversion scheme. For a further discussion of the theory and the methods and their applications in temperature profile retrievals refer to [Mort98] and [Mortensen].

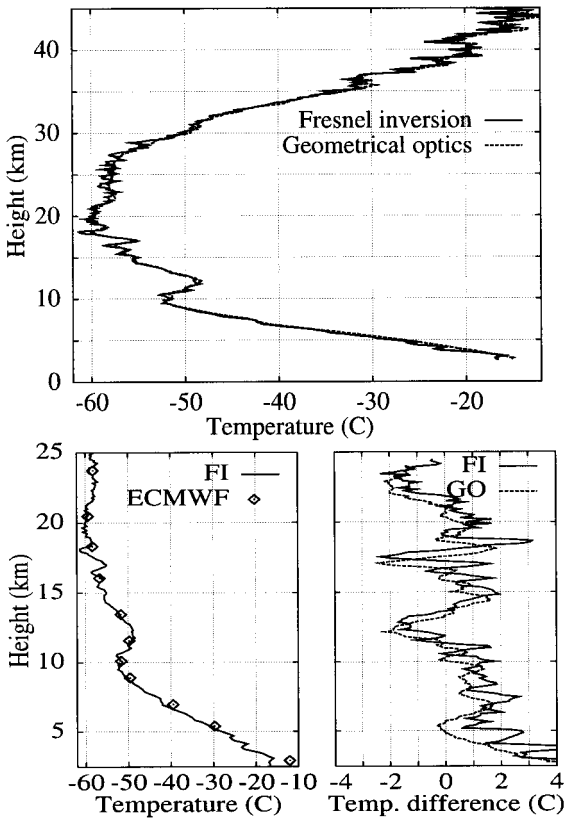

Figure 4.2.2-1. Temperature profile obtained from the GPS/MET occultation no. 256 on 4th February 1997. The upper panel shows the temperature profile based on the geometrical optics inversion (GO) using the Abel transform and the Fresnel inversion (FI). The lower left panel gives the comparison with the ECMWF analysis temperature fields. While the lower right panel show the temperature differences between the ECMWF data and the Abel transform inverted profile (GO) and the ECMWF data and the Fresnel transform inverted temperature profile [Mortensen].

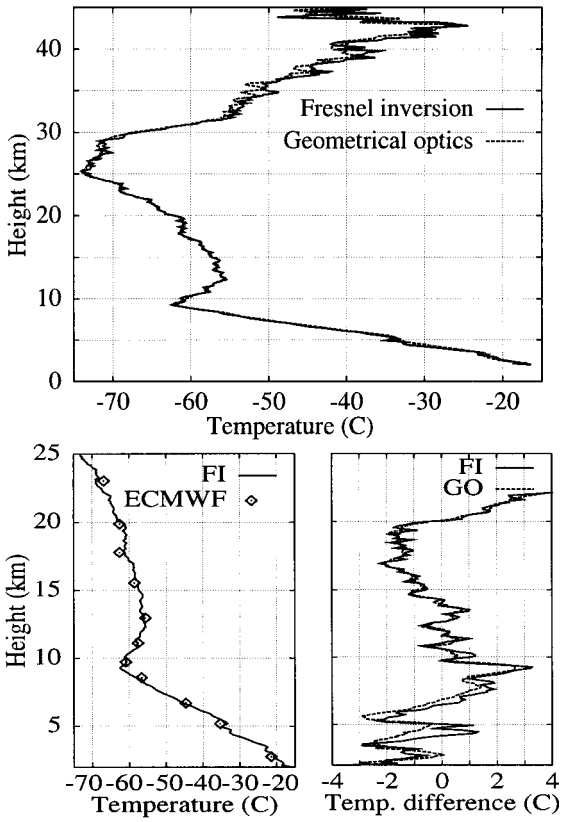

Figure 4.2.2-2. Temperature profile estimates resulting from GPS/MET occultation no. 70, 4th February 1997. The contents of the panels are similar to the content of Figure 4.2.2-1 [Mortensen].

4.2.3. Moisture Profiles

In the troposphere altitude range varying from 3 km to 8 km the water vapor term in the refractivity equation can be as large as 30% of the total refractivity. Especially in the tropics this term can locally dominate the vertical refractivity gradients and bending near the surface of the Earth.

The recovery of the water vapor profile from the measurements of the refractivity N can be estimated from the below expression.

$$P_w = \frac{NT^2 - k_1 PT}{k_2} \qquad (4.1.4.8)$$

The determination of P_w requires knowledge of the temperature profile derived from either climatological models, independent observations or from data fields from numerical weather prediction models. Since the vertical scale sizes of water vapor variability is

much smaller than for the dry atmosphere, this may be used to constrain the wet and the dry contributions to the refractivity profile. An iterative method is suggested where the profile of the temperature is determined initially leading to the derivation of the pressure and the water vapor profile.

4.2.4. Pressure Profiles

Due the processes in the atmosphere and the scale sizes in the troposphere the pressure profile is well defined throughout the lower neutral atmosphere. Thus the pressure profile exerts very small higher order vertical changes. This leads to a possibility to determine the pressure profile by having an initial guess of the temperature high up in the atmosphere. Initial pressure errors in the temperature guess decrease rapidly as the integration moves deeper into the troposphere.

The presence of significant amount of water vapor complicates the retrieval and the interpretation of the refractivity. However in the colder troposphere regions, where the water vapor plays a minor role, accurate profiles of the pressure can be retrieved with a high level of accuracy applying the above algorithms.

4.3. Definition of a Baseline Measurement System

The baseline observation system will consist of the high precision GPSOS receiver together with the antennas pointing in the fore and aft direction of the motion of the satellite and the zenith antenna.

The baseline EDR retrieval system will be founded on the above ideas (see also chapter 6) to live up to the operational constraints of the mission. The main parts can be synthesized in the following items.

The primary EDR retrieval method contains the following parts for TEC and N_e.

- Observations of phase and amplitude of two probing frequencies used by the GPS or GLONASS system.
- Calculation of TEC and ionosphere correction terms.
- Estimation of the bending angle profile.
- Inversion scheme using the Abel transform.
- Retrieval of the electron density.
- Calculation of the vertical TEC at the position for the lowest ionosphere impact height.

The retrieval of the secondary EDRs is described in the previous chapter with the most emphasis on the troposphere and lower stratosphere temperature profile.

4.4. System Extensions

The retrieval methods for the EDRs favor profile estimations. But the observations could also be used to determine the distribution functions of the parameters. In this case other techniques have to be applied.

Tomographic representations of the primary EDRs could result in improved information of the state of the ionosphere and lead to a more efficient exploitation of the observations. The latter since these techniques include measurements with a large ray path angle to the orbital plane of the satellite in the data representation.

Tomographic results would also be stabilized in space and time when combining NPOESS limb sounding observations with other GPS occultation measurement from other satellite platforms. The synergy of applying different data sources could result in better temporal solutions during disturbed conditions. At the same time due to the intrinsic accuracy of the technique merging different observations would not inflict on the accuracy of the EDR distribution functions.

The suggested baseline retrieval assumes spherical symmetry. This together with the vertical Fresnel zone limitation of the method might be seen as not the optimal solution. But for most cases this is a sufficient technique as has also been demonstrated in the EDR retrievals given in chapter 6 and in the error assessments of chapter 7. The stronghold of the suggested retrieval procedure is its capability to easily live up to the delivery times required for the EDR and still result in accurate EDRs.

But by applying the thin screen Fresnel transform in the data retrieval, as shown in the Figures 4.2.2-1 and 4.2.2-2, many more fine scale structures of the troposphere can be determined even during situations where multipath phenomena are dominant. Thus it is suggested to extend the system retrieval methods with a more advanced data transform once this can be done within the EDR delivery time limits.

5. Algorithm flowcharts

This chapter gives a quick introduction to the algorithms discussed in chapter 4 and presented in detail in chapter 6. The four flowcharts in figure 5-1 to 5-4 gives an overview of the algorithms used in the retrieval of the physical parameters in the ionosphere and in the neutral atmosphere. Figure 5-1 and 5-2 shows the structure of the two algorithms used to calculate the TEC and electron density profile in the ionosphere. Figure 5-3 presents the routine we use to find the E and F2 peaks in the electron density profile. Figure 5-4 shows the overall structure of the algorithms used in the neutral atmosphere to calculate the refractivity, pressure, temperature, water vapor pressure and the precipitable water. The different error sources are listed on the right side of the flowcharts. The position of an error source shows when it becomes important in the sequence of calculations that makes up the algorithm.

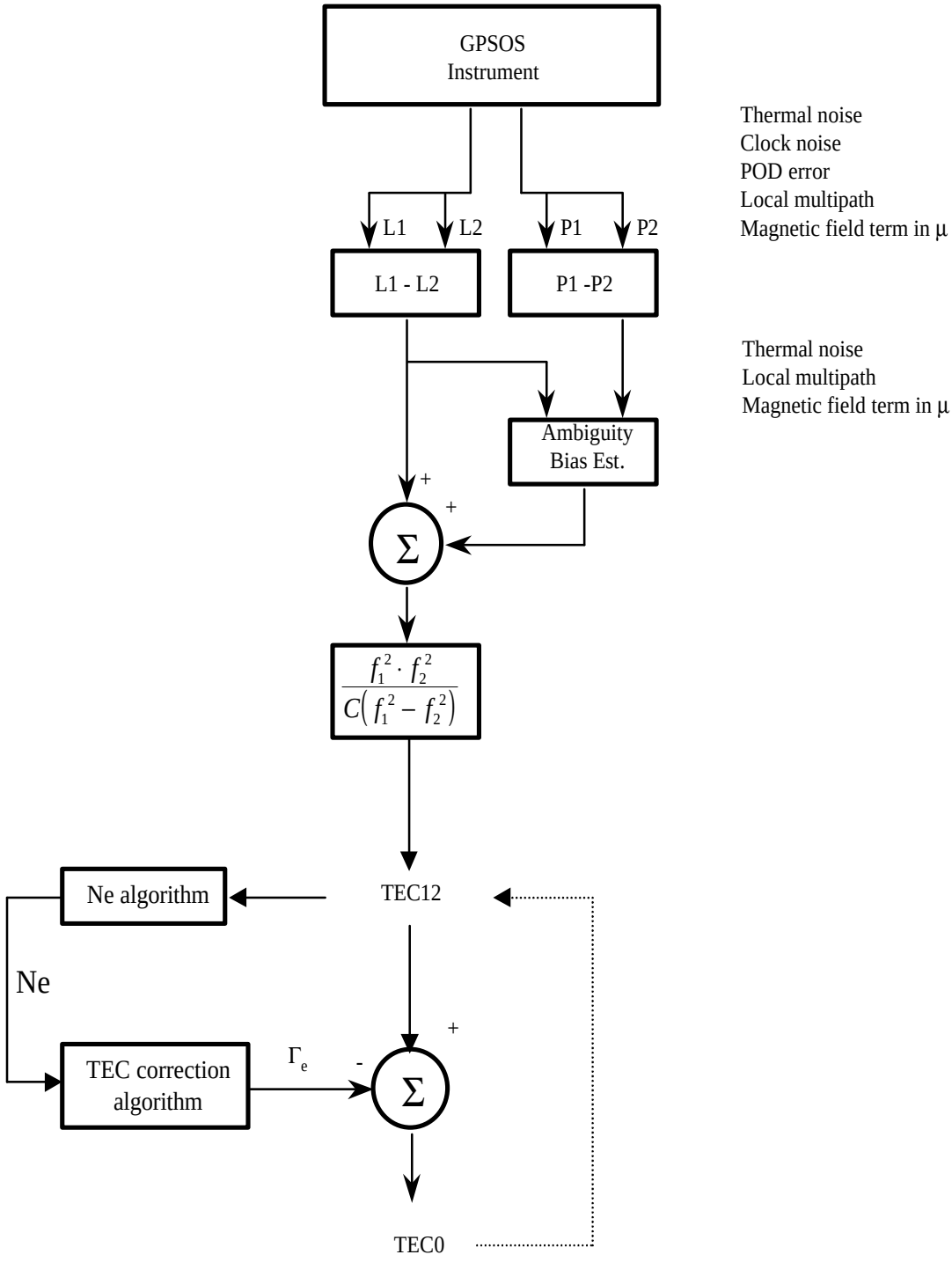

Figure 5-1 The overall structure of the TEC algorithm can be seen from the above TEC flowchart.

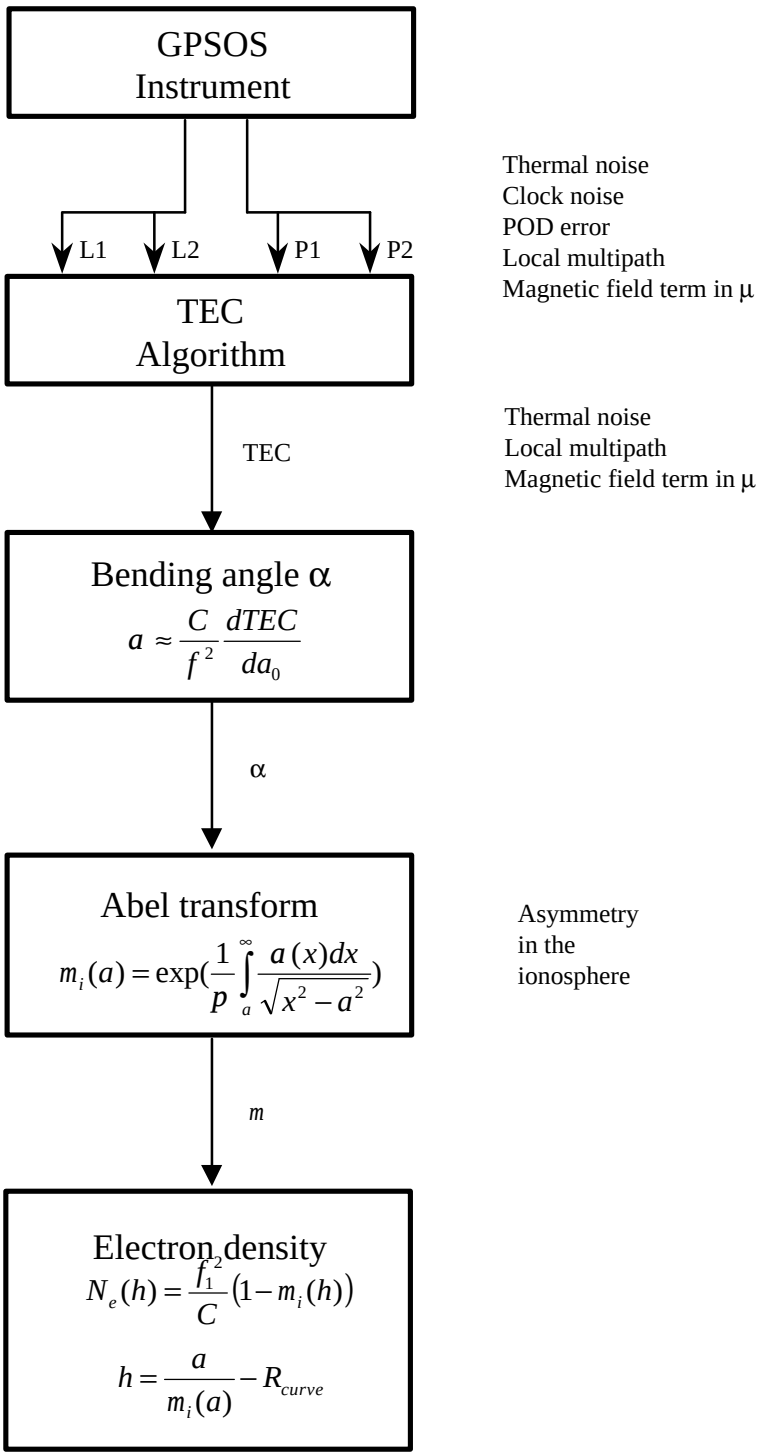

Figure 5-2 The overall structure of the electron density algorithm can be seen from the above electron density flowchart.

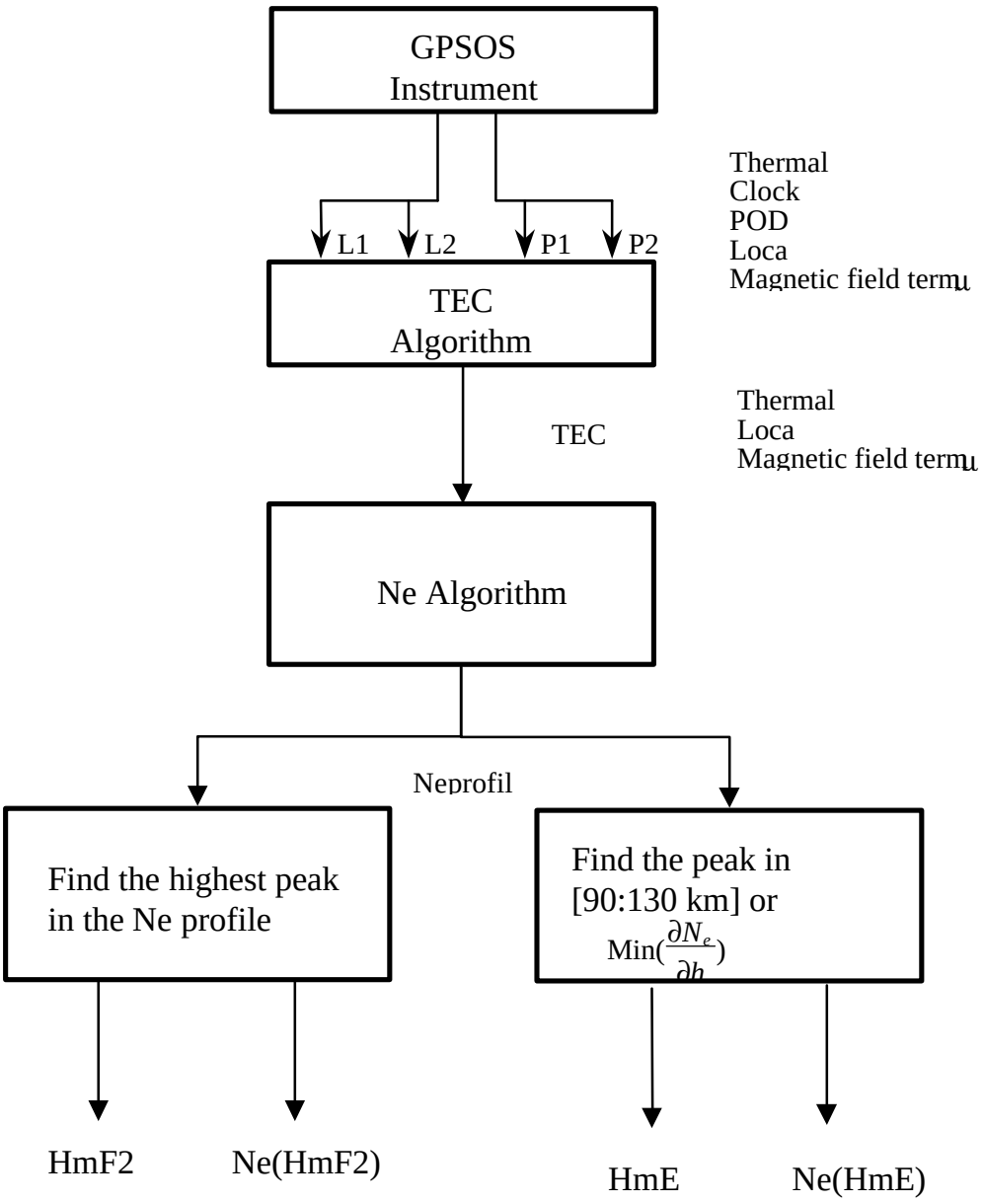

Figure 5-3 The overall structure of the electron density peak finding routine can be seen from the flowchart above.

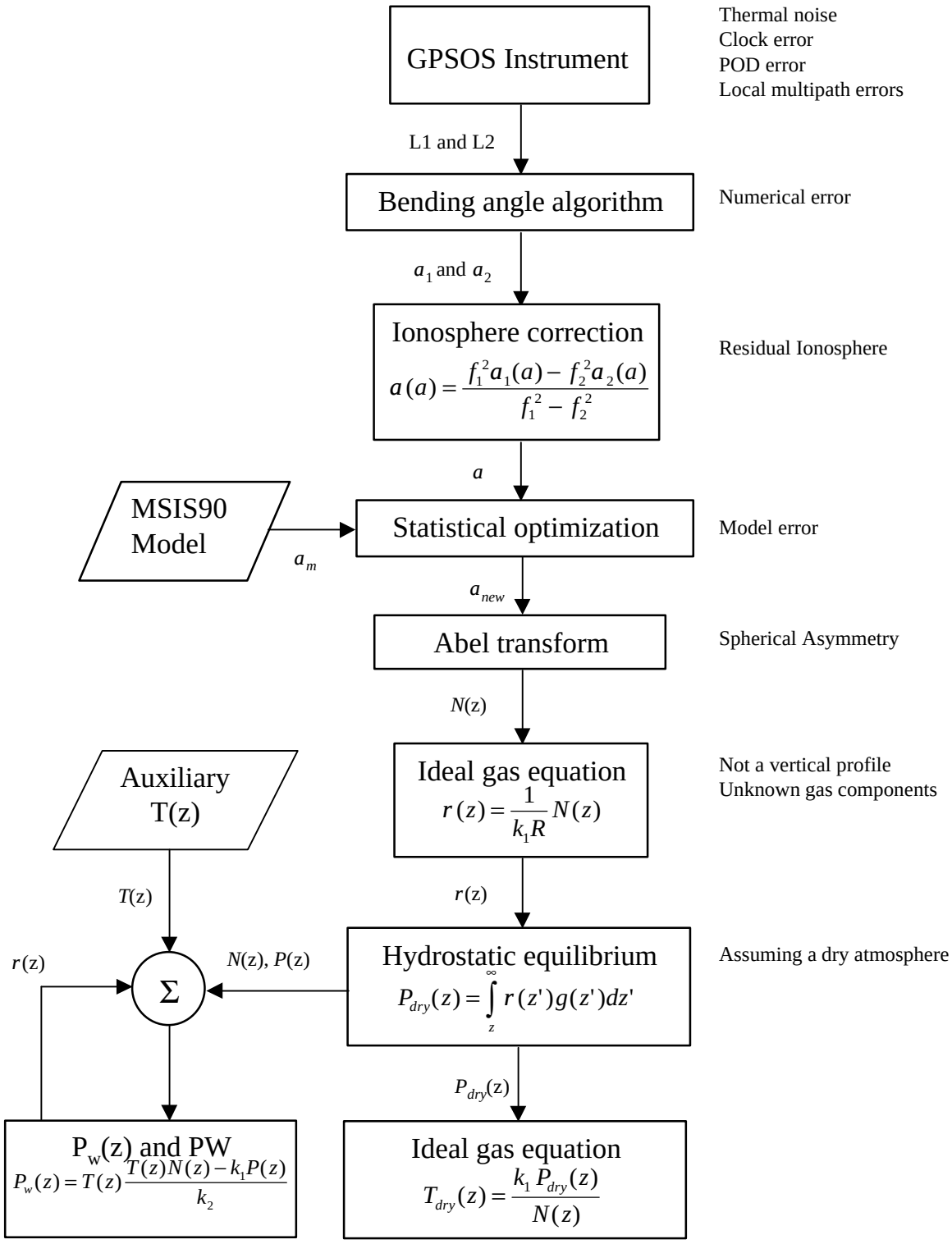

Figure 5-4 The overall structure of the algorithms used in the retrieval of the physical parameters in the neutral atmosphere can be seen from the flowchart above.

6. Algorithm Description

The description of algorithms is divided into two sections; on board algorithms related to scintillation measurements and EDR retrievals within the ground segment. Each section contains subsections on measured quantities EDR's and important parameters necessary to determine the EDR's. The algorithms are thought of as subroutines in the numerical code for retrieving the EDR's. They are described with input and output data format and with a detailed algorithm description. Important physical effects and correction methods are described within each subsection.

6.1. On board algorithms

Scintillation indices and power spectra of the phase and amplitude variations are calculated internally in the GPSOS receiver to monitor the upper ionosphere plasma density fluctuations.

6.1.1. Amplitude Scintillations

6.1.1.1. Input Data

The amplitude scintillation algorithm needs as input:

1. A set of measured power P samples for each frequency in the GPS/ GLONASS system.
2. The time interval over which the average values is calculated.
3. The number of samples used in the measurement.

6.1.1.2. Output Data

The amplitude scintillation algorithm gives as output:

1. The scintillation index S_4.

6.1.1.3. Algorithm

The strength of amplitude scintillation is given by the S_4 index, defined as the root mean square of the variance of received power P divided by the mean value of the received power P.

$$S_{4i}^2 = \frac{\overline{P_i^2} - \overline{P_i}^2}{\overline{P_i}^2} \qquad (6.1.1.1)$$

The suffix i indicates that the corresponding parameter can be evaluated for the two carrier frequencies f_1 and f_2.

6.1.2. Phase Scintillations

6.1.2.1. Input Data

The phase scintillation algorithm needs as input:

1. A set of measured samples of the signal phase j.
2. The time interval over which the average values is calculated.
3. The number of samples used in the measurement.

6.1.2.2. Output Data

The phase scintillation algorithm gives as output:

1. The phase scintillation strength s_j

6.1.2.3. Algorithm

The signal passing through the ionosphere from the GPS satellite to the LEO satellite suffers a number of phase shifts. The measured phase is obtained as,

$$j_r(t) = (w_T - w_R)t + \frac{2p}{l} L_G(t) + \frac{2pC}{cf} TEC(t) + j_S(t) + j_N(t) \qquad (6.1.2.1)$$

where w_T is the transmitter frequency and w_R is the receiver frequency. L_G(t) is the geometric phase shift, j_N(t) is the phase noise, and j_S(t) is the scintillation phase shift, which we are to measure. The *TEC*(t) term is the phase delay caused by the background electron density distribution without scintillations present. To measure j_S(t) we need to account for all the other terms in equation (6.1.2.1). The geometric phase shift is well defined and can be accounted for. The noise term j_N(t) depends on the receiver bandwidth and need to be sufficiently low. The real difficult term is the phase shift caused by the background electron density distribution, especially in the E-region where high gradients in the electron density are present. In figure 6.1.2.3-1 bellow we show an example of the Doppler shift on L_1 resulting from the *TEC* term in (6.1.2.1) and the derivatives here of.

The phase scintillation strength s_j is characterized by the standard deviation of the phase over a given interval of fluctuation frequencies. The bracket symbol, $\langle\rangle$, indicate the average value over some finite time interval 10 s, given by the number of samples and the time between two samples [FRE].

$$s_{fi} = \sqrt{\langle j_i^2 \rangle - \langle j_i \rangle^2} \qquad (6.1.2.2)$$

The suffix *i* indicates the corresponding parameter s_j evaluated for the i'th carrier frequency.

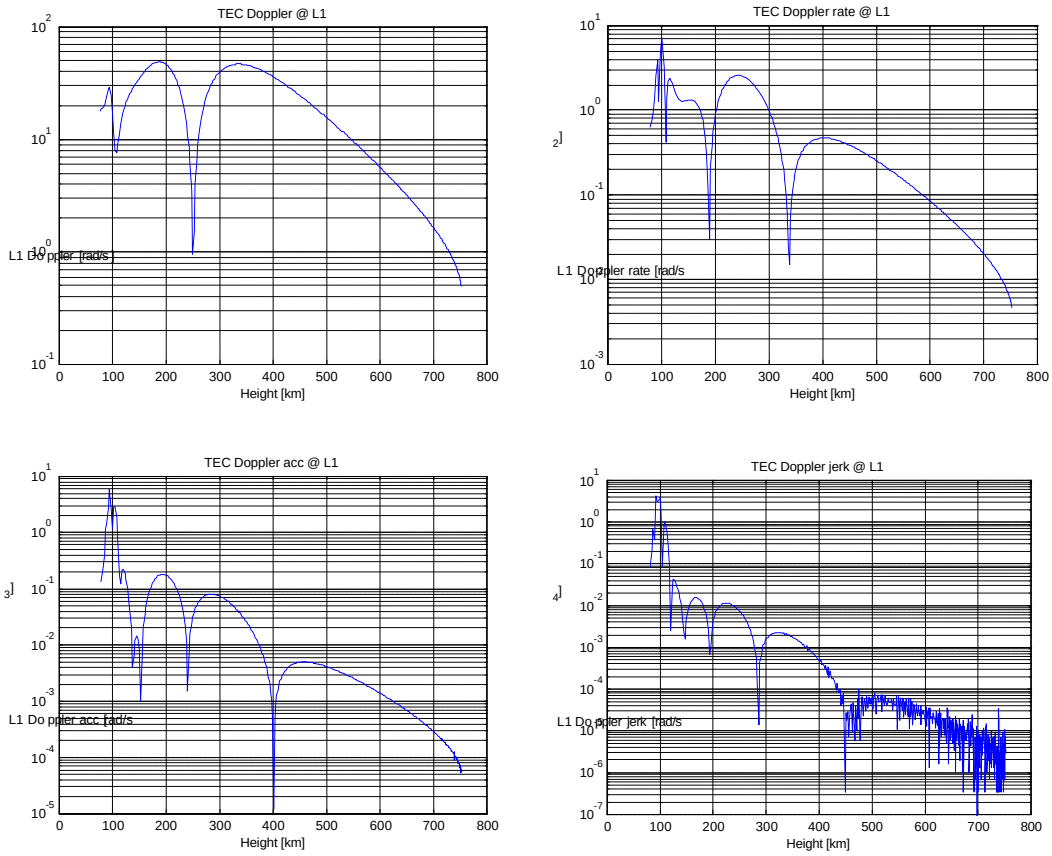

Figure 6.1.2.3-1 The derivatives of the phase delay resulting from the background electron density represented by the TEC term in equation (6.1.2.1). A double Chapman model of the ionosphere at solar maximum conditions is assumed. The occultation geometry is based on GPS/MET occultation 641 from Feb 20th 1997, the side-viewing angle is approximately 30° and the duration of the occultation is 7 minutes and 45 seconds. L1 Doppler denotes the derivative of the phase shift, Doppler rate equals the second derivative, Doppler acceleration (acc) is the third derivative, and the fourth derivative is denoted Doppler jerk.

6.1.3. Spectral Scintillation Processing

6.1.3.1. Input Data

The spectral scintillation algorithm needs as input:

1. An array of measured samples of the signal power P (and phase j).
2. The time interval over which the average values is calculated.
3. The number of samples used in the measurement.

6.1.3.2. Output Data

The spectral scintillation algorithm gives as output:

1. An array of spectral estimator samples.

6.1.3.3. Algorithm

A spectral estimator for the scintillations will exist on board the instrument. It will accept phase and amplitude data at up to 100 Hz sample rate and produce FFT spectrums for every 1 to 10s interval. The amplitude spectrum shall be the power spectral density of the amplitude samples.

6.2. Measurement Bias Corrections.

6.2.1 Input

1. The tracking signal carrier phase – L1 or L2 - received at a fiducial station referenced to a transmitting GNSS satellite during its occultation with the LEO carrying the GPSOS reveiver

2. The POD for the GNSS satellite

3. The precise location of the fiducial station

6.2.2 Output Data

The residual phase change between two consecutive carrier phase measurements having subtracted the POD based and calculated phase and corrected as required for ionosphere, and stratosphere. Thi residual phase will express the clock error originating from the GNSS and referenced to the GPSOS receiver under the assumption of stable clocks during the occultation for the GPSOS and fiducial station receivers.

6.2.3 Algorithm

$$\Delta j^{GNSS}_{fiducial}(t) = j^{GNSS}_{fiducial}(t) - j^{GNSS}_{fiducial,POD\,\exp ected}(t) = f(-dt^{GNSS}(t - t^{GNSS}_{GPSOS}))$$

where dt^{GNSS} is the GNSS clock error.

6.3. EDR Retrieval within the ground Segment

The order in which the ground segment EDR algorithms appear intend to show the flow of data in the calculations.

6.3.1. Total Electron Content (TEC)

6.3.1.1. Input Data

The slant path Total Electron Content (TEC) algorithm will use the following parameters as input:

1. The two carrier frequencies f_1 and f_2 (measured in MHz).
2. The carrier phases $L_1(t)$ and $L_2(t)$ (in mm) tracked by the GPSOS instrument with millimeter precision for each sample in time.
3. The two code phases $P_1(t)$ and $P_2(t)$, also named pseudo range (in mm) to determine the phase ambiguity as functions of time defined by the sampling rate.
4. The sampling rate *s* (in Hz) (In the ionosphere *s* will be equal to 1Hz).
5. Position vectors of both the LEO (NPOESS) satellite, $\overline{R}_L$, and the GNSS satellite, $\overline{R}_G$, (in km). Navigation solution is estimated to be adequate here. Thus POD solutions are not necessary for TEC retrieval.

6.3.1.2. Output Data

The output of the TEC algorithm will be:

1. The total electron content along the slant path traveled by the signal going from the GNSS satellite to the GPSOS receiver as a function of impact parameter, *TEC(a)*, measured in TECU (1 TECU = 10^{16} electrons/m^2)
2. The impact parameter *a* (in km).

6.3.1.3. Algorithm

The measurement is based on both carrier and code phase. Carrier phase is used to record the fine structure and the development of the profile, while the code phase is used to determine the absolute level of the profile. This level can not be determined from carrier phase measurements alone unless the ambiguities on L_1 and L_2 are resolved.

The total electron density along the ray path from a dual frequency measurement, TEC_{12}, is given by the following equation, assuming that only the first order terms of the refractive index are important,

$$TEC_{12} = \frac{f_1^2 f_2^2 (\hat{L}_1 - \hat{L}_2 - \hat{B}_L)}{C(f_1^2 - f_2^2)} \tag{6.3.1.1}$$

where

$$\hat{B}_L = \frac{\sum_i w_i (\hat{L}_1 - \hat{L}_2 + \hat{P}_1 - \hat{P}_2)_i}{\sum_i w_i} \tag{6.3.1.2}$$

The subscripts refers to the dual GPS/GLONASS signals, f is the carrier frequency, C equals 40.3082 $m^3 s^{-2}$ in the applied expression for the dispersion relation. The signal quality weighting factors w_i are implemented to compute the ambiguity bias using only the phase delay data with high SNR. (For the occultation measurements, this may involve selecting data recorded in the lower ionosphere where the antenna gain and SNR are high and multipath errors are expected to be lower than in the upper ionosphere). See also chapter 7 where a detailed evaluation of the measurement and instrument errors is presented. In this chapter only the algorithm errors for the *TEC* measurement are considered.

The slant path *TEC* is in this context defined as the total electron content along the straight line connecting the two satellites. The ray path bending is very small, thus only a small difference exists between this definition and the TEC_{12} measured along the ray path. However, in order to estimate errors of measured *TEC*, it is necessary to work with a definition, which do not depend on the actual path followed by the signal.

We define the straight line connecting the occultating satellites as our reference when estimating the error due to ray path bending and splitting. Without such a reference we can not estimate this error, hence on TEC_{12} per definition no such error exist. If we compare TEC_{12} measurements directly to the 'true' straight line *TEC*, the difference becomes as large as 10 TECU at day time solar maximum. When correcting for ray path bending, equation (6.3.1.3) below, the difference is less than the threshold of 3 TECU.

The slant path *TEC* is obtained by correcting for the ray path bending as follows,

$$TEC = TEC_{12} - \tfrac{1}{2} C \left(\frac{1}{f_1^2} + \frac{1}{f_2^2}\right) \Gamma_e \tag{6.3.1.3}$$

where

$$G_e = \frac{S_L S_G}{S_0} \left(\frac{dTEC_0}{da_0} \right)^2 + a_0 \frac{dTE^2 C_0}{da_0} \tag{6.3.1.4}$$

When solving equation (6.3.1.4) in practice we replace the straight line TEC_0 with the measured TEC_{12}. The geometric parameters S_L, S_G, S_0, and the straight line impact parameter a_0 are defined in figure 6.3.1.4-1.

The term TE^2C_0 is defined as the integral along the straight line of the square of the electron density,

$$TE^2C_0 = \int_0 N_e^2 ds\,. \tag{6.3.1.5}$$

To compute TE^2C_0 the electron density profile N_e is obtained through inversion of the TEC_{12} measurements. This defines the *TEC* correction scheme we suggest to be applied for the *TEC* data retrieval. It is described in more detail in section 6.3.1.5.

6.3.1.4. Algorithm description and computation

The *TEC* is defined as the integral electron density along the ray path of a radio wave for a given frequency, travelling through the ionosphere from the GPS (or GNSS) satellite to the GPSOS receiver onboard the NPOESS satellite,

$$TEC \equiv \int_{Ray\ path} N_e(s)ds \tag{6.3.1.6}$$

The electron density along the ray path can be evaluated using the equation of the refractive index given with all the physical effects taken into account. As described in chapter 3. Assuming that the magnetic field effects are small and expanding that equation to first order, the refractive index μ becomes,

$$m = 1 - \frac{C}{f^2} N_e \tag{6.3.1.7}$$

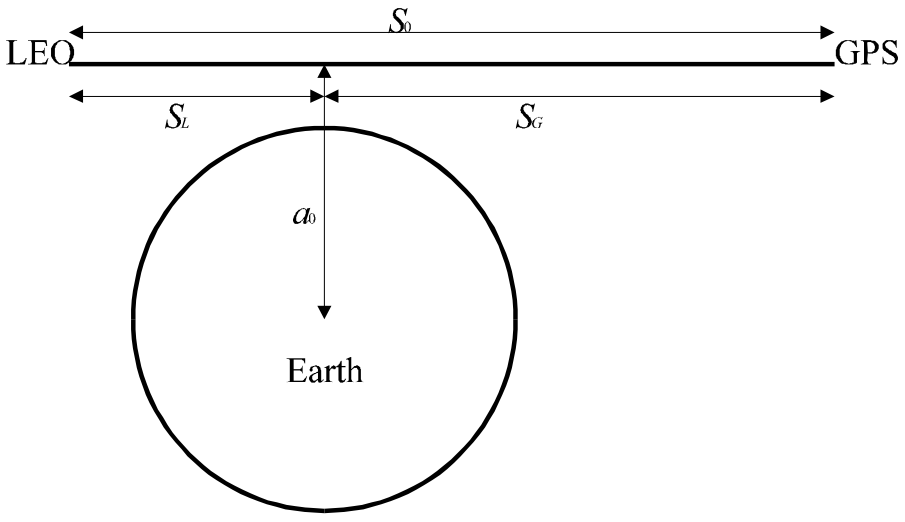

Figure 6.3.1.4-1 Definition of the geometry parameters.

The phase delay L is calculated as the integral of the refractive index along the ray path of the signal. Hence using equation (6.3.1.7) for μ we get,

$$L = \int_{Ray-path} \left[1 - \frac{C}{f^2} N_e(s) \right] ds \qquad (6.3.1.8)$$

Now the dual frequency TEC_{12} measurement is obtained by subtraction of the two phase delays as described in the next derivation,

$$L_1 - L_2 = \int_1 \left[1 - \frac{C}{f_1^2} N_e(s) \right] ds - \int_2 \left[1 - \frac{C}{f_2^2} N_e(s) \right] ds = C \left[\frac{1}{f_1^2} - \frac{1}{f_2^2} \right]_{ray\ path} \int N_e(s) ds \qquad (6.3.1.9)$$

Assuming that both signals follow the same path. Rearranging the equation above the dual frequency TEC_{12} is obtained. But the two signals with different frequencies follow slightly different paths (ray path splitting), which can be threaded as a small error once we have defined the *TEC* measurement by the slant path *TEC* as given in eq. (6.3.1.3).

6.3.1.5. TEC correction

In this subsection we describe the algorithm needed to correct for the systematic error of the satellite to satellite horizontal slant path *TEC* measurements, caused by ray path bending, in order to fulfil the threshold of measuring *TEC* to within an accuracy of 3 TECU. The 'truth' is defined as the *TEC* along the straight line between the transmitter and the receiver. Having the positions of the satellites at each sample, this is a well defined measure of interest to the user. Referring the *TEC* measurement to the ray path, would make the interpretation of the accuracy difficult to use and apply in comparisons with other observations.

In periods of high solar activity, electron densities in the day-time ionosphere may become so large that the traditional *TEC* measurement given by the expression,

$$TEC_{12} = \frac{f_1^2 f_2^2}{C(f_1^2 - f_2^2)} (L_1 - L_2) \qquad (6.3.1.10)$$

fails to give correct results to within the accuracy of this EDR. *L* is the measured phase (including the solution of the phase ambiguity and instrumental biases). The systematic error related to this effect is caused by the fact that both signals travel along slightly bended and different paths. Thus the difference between the traditional measured TEC_{12} and the 'true' slant path TEC_0 along the straight line, have been derived from equation (6.3.1.10) above.

$$TEC_{12} - TEC_0 = \frac{f_1^2 f_2^2}{C(f_1^2 - f_2^2)}\left[\int_1 (1 - \frac{C}{f_1^2} N_e)ds - \int_2 (1 - \frac{C}{f_2^2} N_e)ds\right] - \int_0 N_e ds$$

$$= \frac{f_1^2 f_2^2}{C(f_1^2 - f_2^2)}\left[(\int_1 ds - \int_2 ds) - \frac{C}{f_1^2}(\int_1 N_e ds - \int_0 N_e ds) + \frac{C}{f_2^2}(\int_2 N_e ds - \int_0 N_e ds)\right] \quad (6.3.1.11)$$

The subscripts on the integral symbols refer to the integrals along the respective paths, where the subscript $_0$ refers to the integral along the straight line. N_e is the electron density and *ds* is a small element of length along the ray paths. The second order ionosphere term caused by the Earth's magnetic field has been omitted as it can be dealt with separately and will have no influence on the following derivation. In chapter 7.2 the algorithm errors are assessed and the influence of the Earth's magnetic field terms is seen to be negligible. Analysis results estimates the contribution too less than 0.1 % to the total TEC measurement. It is furthermore assumed that the measurements are taken at altitudes > 100 km, so that the contribution to the delay from the neutral atmosphere can be neglected.

Each of the three terms in parenthesis in the second line of the difference equation (6.3.1.11) can be estimated under the assumption of spherical symmetry. The derivations are lengthy and will not be given here. To second order in C/f^2 we obtain,

$$\int_1 ds - \int_2 ds = \tfrac{1}{2} C^2 (\frac{1}{f_1^4} - \frac{1}{f_2^4})\Gamma_e \quad (6.3.1.12)$$

$$\frac{C}{f_1^2}(\int_1 N_e ds - \int_0 N_e ds) = \frac{C^2}{f_1^4} G_e \quad (6.3.1.13)$$

$$\frac{C}{f_2^2}(\int_2 N_e ds - \int_0 N_e ds) = \frac{C^2}{f_2^4} G_e \quad (6.3.1.14)$$

The difference equation (6.3.1.11) becomes,

$$TEC_{12} - TEC_0 = \tfrac{1}{2} C(\frac{1}{f_1^2} + \frac{1}{f_2^2}) G_e, \quad (6.3.1.15)$$

where the G_e term is defined in (6.3.1.4) and (6.3.1.5). From the *TEC* error correction we see that the error we make if we just apply the TEC_{12} equation is dependent on the square of the vertical derivative of the TEC_{12}.

Numerical simulations show (figure 6.3.1.5-1), that the square of the vertical derivative of the TEC_{12} term constitutes about 80-130 % of the total error in high gradient regions (short-dashed curve), which shows to be almost 10 TEC-units at 200 km. The remaining part (20-30%) comes from the second term in the G_e equation (dotted curve). Therefore

it is expected that a factor of 5 increase/decrease in electron density, representative of night-day ionosphere density differences, would mean about a factor of 25 increase/decrease in G_e. At high electron density concentrations the correction therefore becomes necessary. Applying both terms in equation (6.3.1.4) result in an accurate estimate of the residual (dashed curve). Note also that the G_e equation contains the geometry of the occultation, but that precise (POD) estimates of the geometry factors are not required in order to estimate G_e to within sufficient accuracy.

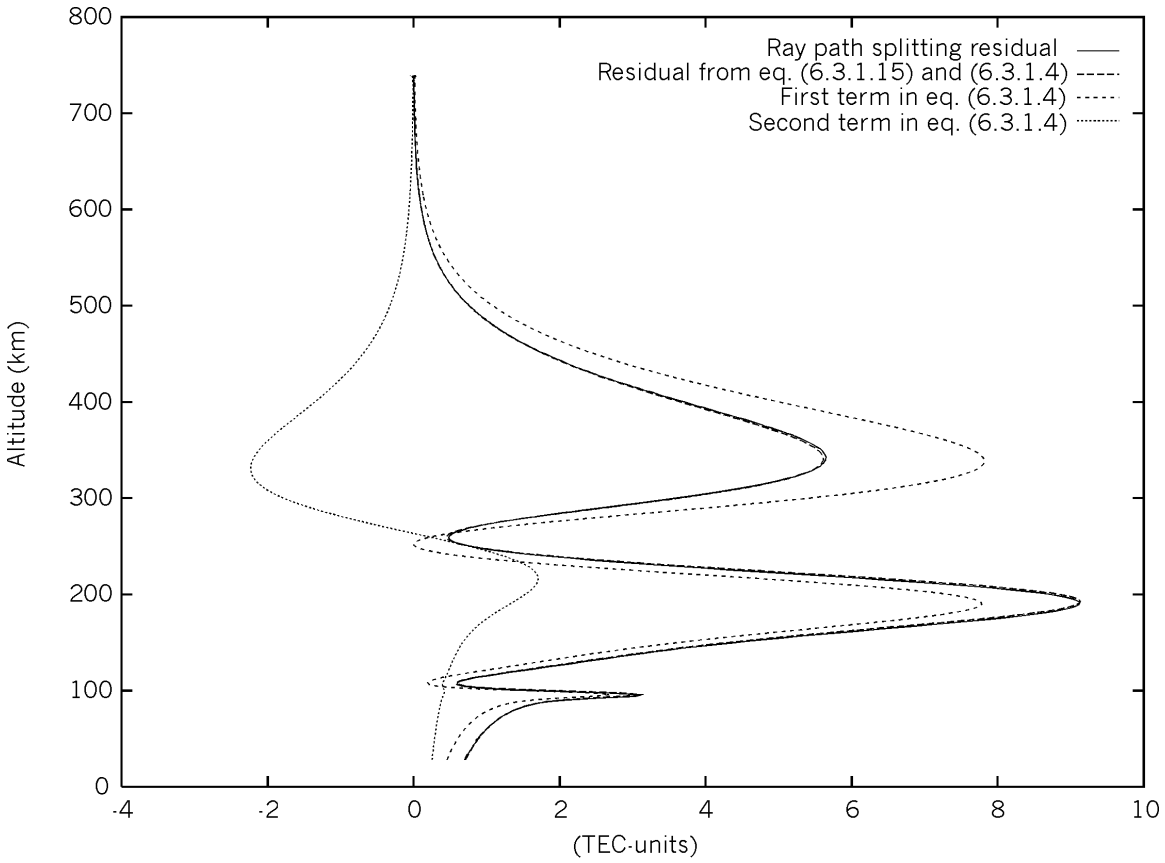

Figure 6.3.1.5-1 The 'true' (solid curve) and estimated ray path splitting residuals. The solid curve has been calculated numerically using ray tracing to estimate the three terms in parenthesis in the second line of eq. (6.3.1.11). The ionosphere model used was a double Chapman model with the following parameters of the ionosphere: E-layer peak density $=2\cdot10^{11}m^{-3}$, peak altitude = 105 km, scale height = 5 km. F-layer peak density = $3\cdot10^{12}$ m^{-3}, peak altitude = 300 km, scale height = 60 km. The maximum TEC for this model occurred about one scale height below the F-layer peak and was about 950 TECU.

In practice the first term in the G_e equation (6.3.1.4) can be easily estimated replacing TEC_0 with the already estimated TEC_{12}. The second term, however, needs to be estimated by other means. The strategy we propose is: First the electron density profile is obtained through inversion of the TEC_{12} measurements and then the TE^2C_0 is obtained assuming spherical symmetry. Preferably the whole procedure can be repeated a number

of times using the new estimate of TEC_0 instead of the previously applied TEC_{12} to estimate G_e. Simulation analysis show that this process converge very fast, so no noticeable improvements are seen by having a complex iterative scheme.

6.3.2. Ionospheric Bending Angle

6.3.2.1. Input Data

The bending angle of the signal ray path when it passes through the ionosphere is computed using the following input.

1. The position vectors of both the LEO and the GNSS satellite $\overline{R}_L$(t) and $\overline{R}_G$(t) for each sample in time (measured in km). Navigation solution is adequate. Thus POD solutions are not necessary.
2. The carrier phases L_1(t) and L_2(t) for each sample (measured in meters).
3. The carrier frequencies f_1 and f_2 (measured in MHz).
4. The sampling rate s (in Hz).

6.3.2.2. Output Data

The output of the ionospheric bending angle algorithm is the bending angle of the ray path as a function of impact parameter.

1. The bending angle α as a function of impact parameter (in radians).
2. The impact parameter a in an array of a fixed number of points (in km).

6.3.2.3. Algorithm

The ray path of a radio wave travelling through the ionosphere suffers a small bending caused by the gradients in the background electron density. Expansion of the appropriate equations to first order results in the following simple and sufficiently accurate expression for the (approximate) bending angle, since the bending angle is very small in the ionosphere, of the order 10^{-2} degree,

$$a \approx \frac{C}{f^2}\frac{dTEC}{da_0} \tag{6.3.2.1}$$

$$a \approx a_0 + a\,\frac{S_0}{S_G S_L} \tag{6.3.2.2}$$

Here $TEC = TEC_{12}$ which is calculated as described in section 6.3.1.3 and $C = 40.3$ m^3s^{-2}. The impact parameter of the straight line a_0 and the distances S_0, S_L and S_G are defined in figure 6.3.1.4-1 above. a is the impact parameter of the bended path connecting the LEO and the GNSS satellites computed to first order. Assuming that $f_1 > f_2$ the bending angle is largest if we use the low frequency f_2 in equation (6.3.2.1). However the differ-

ence between the two choices is negligible, the frequency is just a factor, which cancels out when computing the electron density profile. We choose to set $f = f_1$.

Note that only the position vectors are needed to compute the bending as a function of the impact parameter. The derivative of a_0 with respect to time has a magnitude of the order 3 km/s (assuming 1Hz sampling rate). This implies that only an uncertainty of 30 m/s in the velocity estimates of the satellites is needed to obtain 1% accuracy in bending angle. Thus the algorithm is insensitive to POD errors, and only the navigation solution is needed. This have also been confirmed by EGOPS simulations, which show that adding 1 m/s velocity errors results in less than 0.1 % errors in the derived electron density profiles.

6.3.2.4. Algorithm derivation

The approximate expressions given above have been derived to first order starting with the Abel transform, where the bending angle is given as an integral over the refractive index [Fjeldbo] and [MEL94]:

$$\alpha = -2a_0 \int_{r_0}^{\infty} \frac{(dm/dr)dr}{m\sqrt{m^2 r^2 - a_0^2}} \tag{6.3.2.3}$$

where a_0 is the impact parameter of the straight line ray path, r is the distance from the center of the Earth to the ray path at the tangent point and,

$$\frac{1}{m}\frac{dm}{dr} = \frac{d\ln m}{dr} = -\frac{C}{f^2}\frac{dN_e}{dr} \quad \text{assuming } m = 1 - \frac{CN_e}{f^2} \quad \text{and} \quad m \cong 1 \tag{6.3.2.4}$$

From the geometry in figure 6.3.1.4-1 where s is the distance along the ray from the tangent point towards the GNSS satellite, we determine the relation between ds and dr,

$$r = \sqrt{a_0^2 + s^2} \;\Rightarrow\; \frac{dr}{da_0} = \frac{a_0}{r} \;\Rightarrow\; \frac{dN_e}{dr} = \frac{r}{a_0}\frac{dNe}{da_0} \quad \text{and} \quad ds = \frac{r}{\sqrt{r^2 - a_0^2}}dr \tag{6.3.2.5}$$

Substituting (6.3.2.4) and (6.3.2.5) into equation (6.3.2.3) gives,

$$\alpha \approx 2\frac{C}{f^2}\int_{a_0}^{\infty}\frac{a_0(dN_e/dr)dr}{\sqrt{r^2 - a_0^2}} = \frac{2C}{f^2}\int_0^{\infty}\frac{dN_e}{da_0}ds \approx \frac{C}{f^2}\int_{LEO}^{GPS}\frac{dN_e}{da_0}ds = \frac{C}{f^2}\frac{d\mathrm{TEC}}{da_0} \tag{6.3.2.6}$$

where $TEC = TEC_{12}$ and f is the frequency of the signal, for which we calculate the bending angle.

6.3.2.5. Alternative Algorithm

In this section we summarize the retrieval procedure for the electron density profile. Assuming that the two signal with slightly different frequencies follow the same ray path (limit of small bending) the corrected phase delay L_{1c} is computed using the following equation,

$$L_{1c} \approx \frac{-f_2^2}{f_1^2 - f_2^2}(L_1 - L_2) \tag{6.3.2.7}$$

where we have assumed that the ray path is a straight line. Using the above corrected phase delay both clock and POD errors cancel. If we were to correct for these errors by other means then we could use L_1 or L_2 directly instead. For each data sample the impact parameter a is found by solving the equations below [MEL94],

$$\begin{aligned} &\dot{L}_{1c} + \dot{R}_{LG} - \left(m_i(\bar{R}_L)\left|\dot{\bar{R}}_L\right|\cos j\,(a) - \left|\dot{\bar{R}}_G\right|\cos c\,(a)\right) = 0 \\ &j\,(a) = z\, - \arcsin\left(\frac{a}{\left|\bar{R}_L\right|}\right) \quad , \quad c\,(a) = (p\, - h) - \arcsin\left(\frac{a}{\left|\bar{R}_G\right|}\right) \end{aligned} \tag{6.3.2.8}$$

where $m_i(\bar{R}_L)$ is refractive index at orbit height, which to a close approximation equals unity. Applying this approximation results in a negligible error contribution [Hajj]. is the angle between position and velocity of the GPS satellite, is the angle between position and velocity of the LEO satellite, is the angle between incoming ray and the velocity of the LEO satellite, is the angle between outgoing ray and the velocity of the GPS satellite, R_{LG} is the distance between the GPS and LEO satellite, figure 6.3.2.5-1.

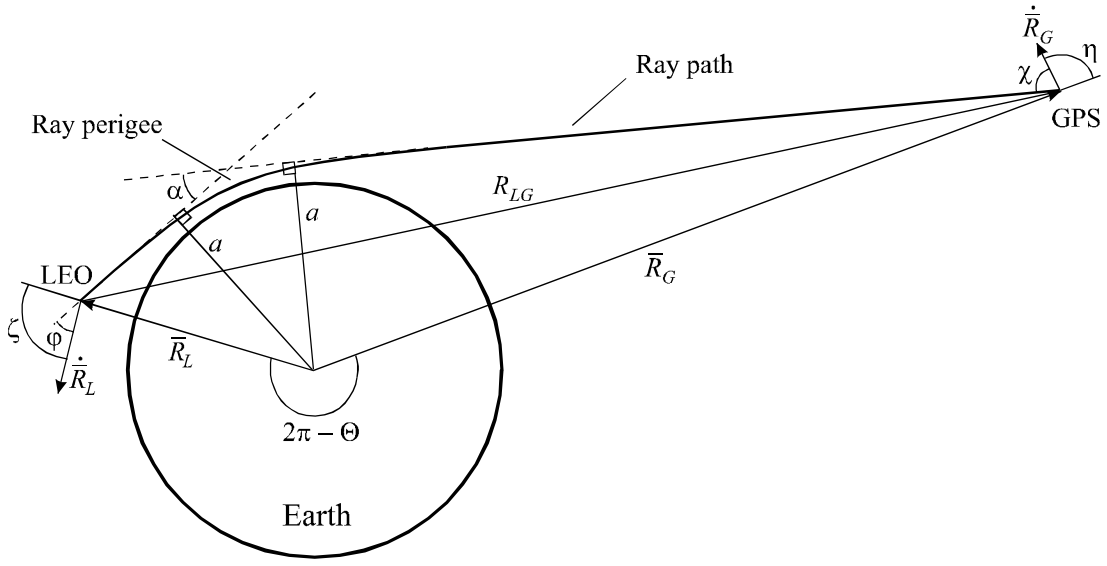

Figure 6.3.2.5-1 Geometry of the occultation.

The ionospheric bending angle can now be found using,

$$a = \Theta - \arccos(\frac{a}{|\overline{R}_L|}) - \arccos(\frac{a}{|\overline{R}_G|}) \qquad (6.3.2.9)$$

where is the angle between the two position vectors. Note that this algorithm is very analog to the calculation of bending angles in the neutral atmosphere, however the insignificance of POD is not as clear as for the baseline bending angle algorithm given in equation (6.3.2.1) and (6.3.2.2). But simulations show that POD is not necessary even using this algorithm, due to the fact that POD errors cancel when applying the correction in equation (6.3.2.7). This method was presented at the SRR. Since then we have refined the argumentation and obtained a more self-consistent set of equations based on the first order approximation, which we present as our baseline algorithm (6.3.2.1) and (6.3.2.2) to compute the ionospheric bending angle.

6.3.2.6. Comparing the two bending angle algorithms

To compare the bending angle algorithm presented at SRR with the new baseline bending angle algorithm, both algorithms were used to invert the same model calculated ionosphere phase delays. A solar maximum double Chapman ionosphere was simulated, with the forward modeling calculated using the ray tracing tool ROSAP developed at DMI. The parameters for the solar maximum ionosphere are given in chapter 7.2, the same ionosphere model as used in figure 6.3.1.5-1. The two bending angle algorithms result in almost identical difference profiles, figure 6.3.2.6-1, which confirms that the approximate bending angle algorithm (6.3.2.1) indeed is a good approximation.

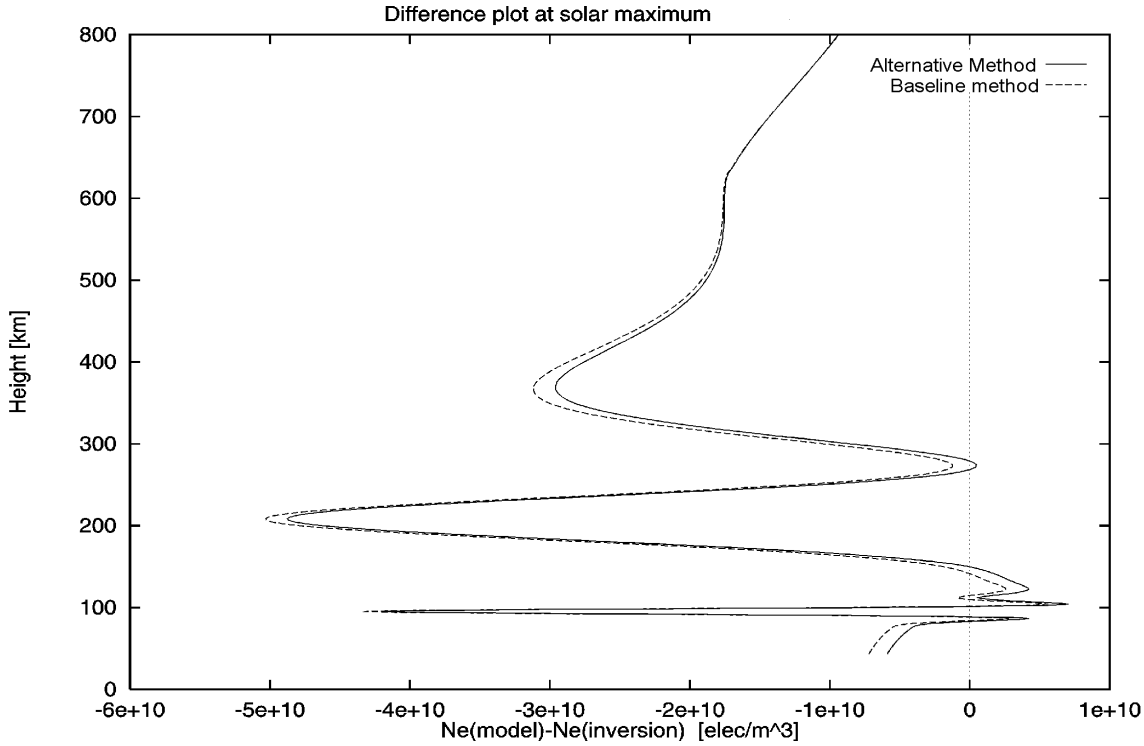

Figure 6.3.2.6-1 The difference between model electron density profile and the inversion result electron density profile plotted as a function of height. Solid curve is the N_e difference using the alternative algorithm (6.3.2.9) and the dashed curve represents baseline bending angle algorithm (6.3.2.1). Same double Chapman ionosphere as used in figure 6.3.1.5-1.

6.3.3. Ionospheric Refractivity Retrieval

6.3.3.1. Input Data

The ionospheric refractivity *N* is calculated using the Abel transform with bending angle and impact parameter computed in 6.3.2 as input.

1. Bending angle α as a function of impact parameter (in radians).
2. Impact parameter *a* (in km).

6.3.3.2. Output Data

The output of the ionospheric refractivity retrieval algorithm will be refractivity profile averaged over the distance traveled by the occultating rays through the ionosphere.

1. The ionospheric refractivity *N(h)* as a function of height (in N units).
2. The height above the surface at the tangent point *h* (in km).

6.3.3.3. Algorithm

The ionospheric index of refraction m_i can be found from the Abel transform [Fjeldbo] and [MEL94] assuming spherical symmetry.

$$m_i(a) = \exp\left(\frac{1}{p}\int_a^{\infty} \frac{a(x)dx}{\sqrt{x^2 - a^2}}\right) \tag{6.3.3.1}$$

The refractivity N as a function of height h can be found by combining the following equations.

$$N = (m_i - 1)10^6, \quad h = \frac{a}{m_i(a)} - R_{curve} \tag{6.3.3.2}$$

where R_{curve} is the curvature radius of the Earth at the tangent point. In the ionosphere the presence of electrons makes the phase travel faster than the signal making the refractivity negative.

6.3.3.4. Algorithm Description and Computation

The Abel transform is computed by (6.3.3.1). Both limits are numerical difficult to handle. In the limit $x \to a$, the integrand becomes infinite (a singularity) and in the limit of $x \to \infty$ it is necessary to extrapolate the measured bending angle.

The singularity problem is resolved by a change of variables:

$$\sqrt{x^2 - a^2} = -a_{ref} \ln(x) \tag{6.3.3.3}$$

where we choose a_{ref} = 2000 km based on performance of the Abel transform algorithm. With this change of variable the Abel integral becomes,

$$\ln(m) = \frac{1}{p} a_{ref} \int_0^1 \frac{a(x)}{x\ x} dx \tag{6.3.3.4}$$

In the limit of $x \to \infty$ ($x \to 0$) the bending angle profile is extrapolated using an exponential fitting method. The following exponential expression is fitted to the bending angle between 600 and 700 km in altitude (i.e. 140 and 40 km below orbit height respectively for GPS/MET data), where p and q are the constants to be determined,

$$a(x) = \exp(p + qx) \tag{6.3.3.5}$$

The fitting is performed twice. First all points are weighted equally. Then using the values of p and q from the first fit, the standard deviation is computed and the fitting is per-

formed with the appropriate weighting. The resulting p and q are used as the constants in equation (6.3.3.5).

The Abel transform assumes spherical symmetry of the region covered by the occultation in the ionosphere. Using only the information of one occultation measurement to calculate an electron density profile, seems to be a useful assumption. Chapter 7.2 treats this case and comes with suggestions to evaluate the problem. When the occulting rays passes through the ionosphere they travel over long distances (several thousand kilometers). Asymmetry in the ionosphere will introduce errors in the derived refractivity and hence in the electron density profile. At mid latitudes (30°- 60°) the ionosphere is fairly symmetric, however the day-night terminator causes an asymmetry. Not accounted for in the above assumptions.

6.3.4. Electron Density Retrieval

6.3.4.1. Input Data

The electron density algorithm needs the following input to compute electron density profiles in the ionosphere.

1. The ionospheric index of refraction $_i(h)$ as a function of height h and the carrier frequency f_1.
2. The height h above the surface (in km).

6.3.4.2. Output Data

The output of the electron density retrieval algorithm will be:

1. The electron density profile $N_e(h)$ (in electrons pr. m^3) as a function of height above the surface h (in km).

6.3.4.3. Algorithm

The electron density profile N_e can be found from the ionospheric index of refraction. A good approximation to the electron density can then be obtained as,

$$N_e(h) = \frac{f_1^2}{C}\left(1 - m_i(h)\right) \qquad (6.3.4.1)$$

This expression applies for the refractive index determined using the Abel transform (6.3.3.1). A fundamentally different algorithm to calculate electron density profiles is presented in section 6.3.5, using the shell method. Here we have assumed spherical symmetry to obtain profiles using only one occultation measurements. But the shell

method technique could be enhanced to a cell method, circumventing the spherical symmetry assumption.

6.3.4.4. Algorithm description and computation

The ionospheric index of refraction with all physical effects taken into account is given by the Appelton-Hartree equation [Budden],

$$m^2 = 1 - \frac{X(U-X)}{U(U-X) - \frac{1}{2}Y^2\sin^2 z \pm \sqrt{\frac{1}{4}Y^4\sin^4 z + Y^2\cos^2 z\,(U-X)^2}} \qquad (6.3.4.2)$$

where U=1–iZ and where X, Y and Z are dimensionless quantities. $X = f_p^2 / f^2$ where f_p is the plasma-frequency, $Y = f_g^2 / f^2$ where f_g is the gyro-frequency and $Z = f_c^2 / f^2$ where f_c is the average collision frequency. ζ represents the angle between the Earth magnetic field and the wave number vector.

This equation can be expanded in a power series, assuming that expansion in power of X and Y is sufficient and that Z is less than order 10^{-5}. For frequencies in the GHz range we obtain,

$$m = 1 - \frac{1}{2}X \pm \frac{1}{2}XY\left|\cos z\right| - \frac{1}{8}X^2 - \frac{1}{4}XY^2(1+\cos^2 z) - i\frac{1}{2}XZ \qquad (6.3.4.3)$$

Comparing the magnitude of the terms on the right hand side of equation (6.3.4.3) using a frequency in the GHz range. The terms relate approximately as 1: 10^{-4}, 10^{-7}, 10^{-9} and smaller. Hence to first order equation (6.3.4.3) becomes,

$$m = 1 - \frac{1}{2}X, \text{ where } X = 2C\frac{N_e}{f^2} \qquad (6.3.4.4)$$

Rearranging (6.3.4.4) we obtain the algorithm for electron density profiles given in equation (6.3.4.1).

6.3.5. Electron Density Retrieval using the Shell Method

6.3.5.1. Input Data

The shell electron density algorithm needs the following input to compute electron density profiles in the ionosphere.

1. TEC measurements (in TECU) corrected to the straight line between the LEO and GPS satellite as a function of height *h*. The corrected TEC measurements are denoted TEC_0 measurements.
2. The height *h* above the surface (in km).

6.3.5.2. Output Data

The output of the electron density retrieval algorithm will be:

1. The electron density profile $N_e(h)$ (in electrons pr. m^3) as a function of height above the surface *h* (in km).

6.3.5.3. Algorithm

In figure 6.3.5.4-1 the atmosphere has been divided into a number of shells. The number of shells is so high that the electron density is nearly constant in each shell. We can in the ionosphere assume that the waves will propagate along straight lines (rays) between the GPS and LEO satellite. In order to assign the correct TEC values to these straight lines, the measured TEC values must be corrected to the straight line TEC_0 values with the use of the TEC correction algorithm described in section 6.3.1.3 and 6.3.1.5. This TEC correction scheme gives only a small change in the TEC values and it can in most cases be neglected. The relationship between the TEC_0 measurements and the electron densities in the shells can be expressed by the following set of equations.

$$\begin{bmatrix} TEC_0 1 \\ TEC_0 2 \\ \\ \\ TEC_0 n \end{bmatrix} = \begin{bmatrix} A_{11} & A_{12} & & A_{1m} \\ A_{21} & A_{22} & & A_{2m} \\ & & & \\ & & & \\ A_{n1} & A_{n1} & & A_{nm} \end{bmatrix} \begin{bmatrix} N_e 1 \\ N_e 2 \\ \\ \\ N_e m \end{bmatrix} \qquad (6.3.5.1)$$

Here *m* is the number of shells and *n* is the number of rays equal to the number of TEC measurements determined by the duration of the occultation and the sampling rate. The matrix element A_{ij} is calculated as the distance traveled by the ray with the number *i* in

the shell with the number *j*. When numbering the shells starting from the innermost shell, this distance is found in one of the following two ways.

1. A_{ij} is twice the distance between the two points where ray number i intersect the two shells numbered j and j-1.
2. A_{ij} is the distance between the two points where ray number i intersect shell number j.

The shells are normally spaced linearly in the altitude range between 40 km and 740 km for measurements based on GPSMET data. Higher resolution and a lower level of the discrete error can be obtained, if the number of shells is increased in the regions of high electron density gradients. The total number of shells can not be chosen to be arbitrarily high. To many shells will just increase the calculation noise level. The correct number of shells is approximate equal to that number for which the shell thickness is approximately equal to the sampling distance. The sampling distance is approximately 3 km in the ionosphere using a 1 Hz sampling rate.

6.3.5.4. Algorithm description and computation

Two different standard techniques to solve the above system of equations have been used. The two techniques are the Algebraic Reconstruction Technique (ART) and the Singular Value Decomposition (SVD) technique.

Algebraic Reconstruction Technique (ART)

The electron density is here found from the TEC measurements by iteration. The iteration scheme can be expressed by the following equation

$$Ne^{k+1} = Ne^{k} + l_k \frac{TEC_i - \sum_{j=1}^{m} A_{ij} Ne_j^k}{\sum_{j=1}^{m} A_{ij} * A_{ij}} A_i \quad where \;\; i = k \mod m \qquad (6.3.5.2)$$

Where l is the relaxation parameter. The best value of the relaxation parameter l is a function of the noise level. It is seen from the equation that the $k+1$th iteration is found from the kth iteration. The iteration process is started with an initial guess on the electron density in the m shells. This guess has been based on a double Chapman ionosphere model or the more precise model, NeUoG, developed by University of Graz. Both these ionosphere models are implemented in the simulation programs EGOPS and ROSAP, which are used for evaluating the error sources, their magnitude and propagation.

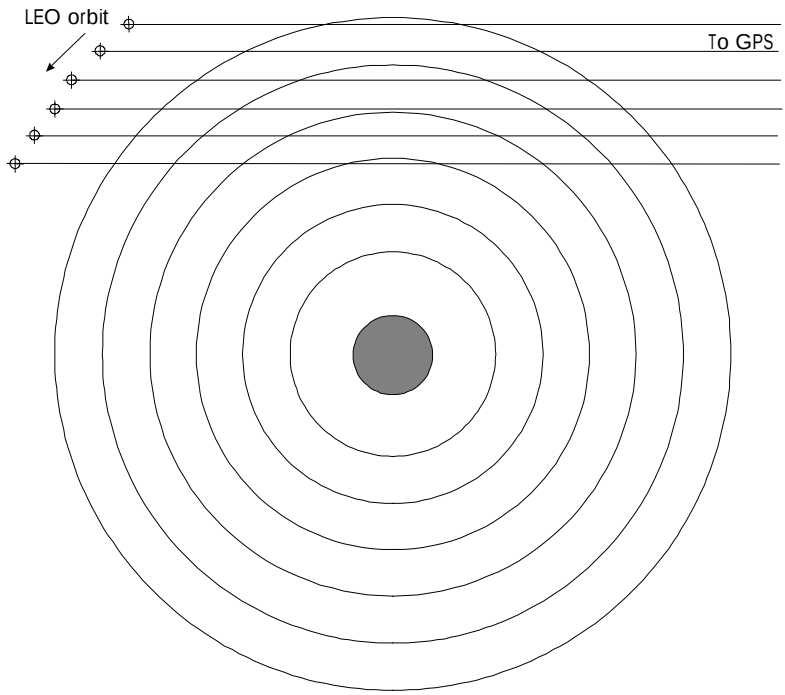

Figure 6.3.5.4-1. An artistic view of the occultating rays passing through the spherical shells surrounding the Earth.

Singular Value Decomposition (SVD)

The Singular Value Decomposition (SVD) method is based on the following theorem from linear algebra. Any $m \acute{} n$ matrix **A** whose number of rows m is greater than or equal to its number of columns n , can be written as the product of an $m \acute{} n$ column-orthogonal matrix **U**, an $n \acute{} n$ diagonal matrix **W** with positive or zero elements, and the transpose of an $n \acute{} n$ orthogonal matrix **V**. This theorem can be used to solve a linear system of equations given by.

$$\mathbf{A}\,\mathbf{x} = \mathbf{b} \tag{6.3.5.3}$$

We here assume that the number of equations is higher than the number of unknowns (more rays than shells). The least-squares solution vector to the over determined set of linear equations is given by

$$\mathbf{x} = \mathbf{V}\left[diag\left(\frac{1}{w_j}\right)\right]\mathbf{U}^T\mathbf{b} \tag{6.3.5.4}$$

where T denotes transposed and w_j is one of the diagonal elements in the matrix **W**. The matrices **U**, **V** and **W** are computed using the singular value decomposition technique. The matrix **W** will in general, for an over determined set of equations, be non-singular.

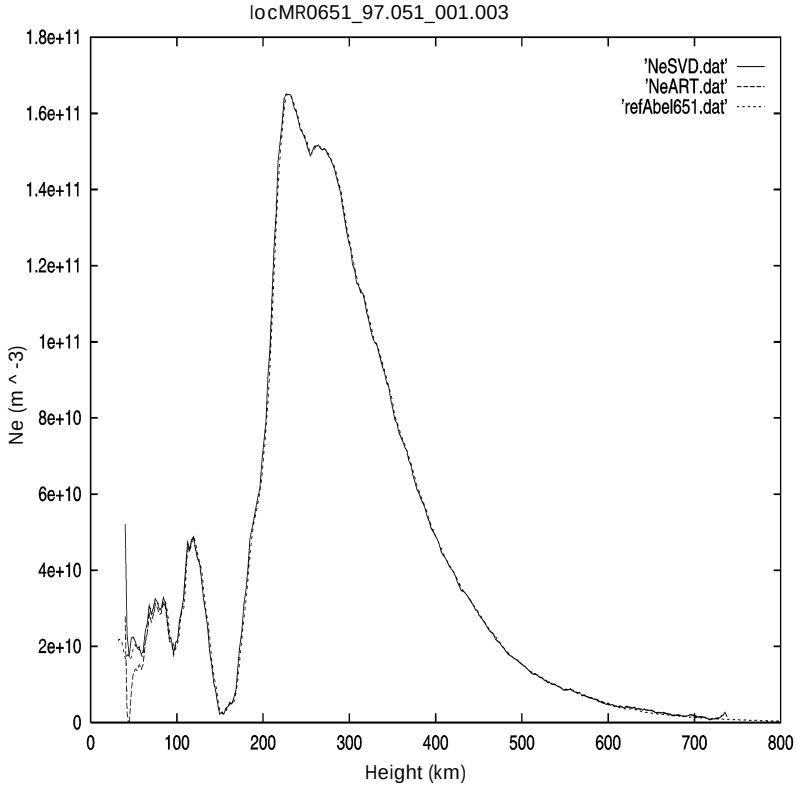

Figure 6.3.5.4-2. This figure shows the electron density as a function of altitude. 3 different algorithms have been used to derive the electron density profile from the GPS/MET measurement on February 20, at 22.10 UT, 1997. The labels are explained in the text bellow. Solid curve represents the SVD algorithm, the ART algorithm result is the dashed curve, and the short-dashed curve is the resulting electron density profile using the bending angle algorithm and Abel transform.

An example of N_e calculated from TEC measurements

Figure 6.3.5.4-2 shows the electron density as a function of altitude for an occultation measured by the GPS/MET instrument. The electron densities have been calculated with the use of 3 different algorithms. The linear set of over determined equations in (6.3.5.1) has been solved using the Singular Value Decomposition (SVD) technique, for the solid curve labeled NeSVD.dat, and the Algebraic Reconstruction Technique (ART) for the dashed curve with the NeART.dat label. The electron density, corresponding to the short-dashed curve labeled refAbel651.dat, has been calculated using the standard Abel transform technique as described in sections 6.3.2-6.3.4. This curve is here used as a reference. The **A** matrix in equation (6.3.5.1) has 643 rows and 300 unknowns, correspond-

ing to 643 rays during the occultation and 300 shells. The 300 shells are placed linearly in the altitude range between 40 km and 740 km.

It is seen from fig. 6.3.5.4-2 that the difference between the results from the 3 algorithms is very small. The result from the SVD algorithm is in this investigation used as the initial guess for the electron density in the ART algorithm. This shows that the ART algorithm converges given that the initial guess is close to the true electron density profile, in this example the SVD algorithm alone have already solved the problem. The ART algorithm can be used as a consistency check on the SVD result. The initial guess based on the double Chapman electron density model is so different from the correct electron density profile that the ART algorithm is unable to converge toward the correct density profile. A model of the ionosphere, which closely resembles the 'truth', is necessary in order to make the ART algorithm capable of retrieving the electron density profile.

The SVD algorithm will in general also require some exponential fitting, although we have not used any form of fitting when calculating the electron density for occultation number 651 in figure 6.3.5.4-2. As an example, assuming maximum solar conditions and a double Chapman model, the calculated TEC (for height>700 km) is shown in figure 6.3.5.4-3. Orbit data from GPS/MET has been used to compute the *TEC* and N_e profiles presented in figure 6.3.5.4-3 and 6.3.5.4-4, for the NPOESS satellites the orbit height is shifted to 833 km, however the same features will be seen.

The rapid decrease in TEC from around 735 km close to orbit height figure 6.3.5.4-3 results in a corresponding increase on the calculated N_e profile in figure 6.3.5.4-4. The sudden increase in the electron density is caused by the sudden decrease in TEC as a function of height, due to the fact that the LEO satellite moves almost only horizontally towards the GNSS satellite close to the orbit height. In order to get the correct electron density profile, it is necessary to extrapolate the electron density profile for altitudes above 700 km using an exponential fit based on the electron density from altitudes between 500 and 650 km. These values should be raised by 100 km to accommodate for the higher NPOESS orbit. Applying this method changes the results of high altitude electron density to become equal to the model profile for the simulation given by the dashed curve in figure 6.3.5.4-4.

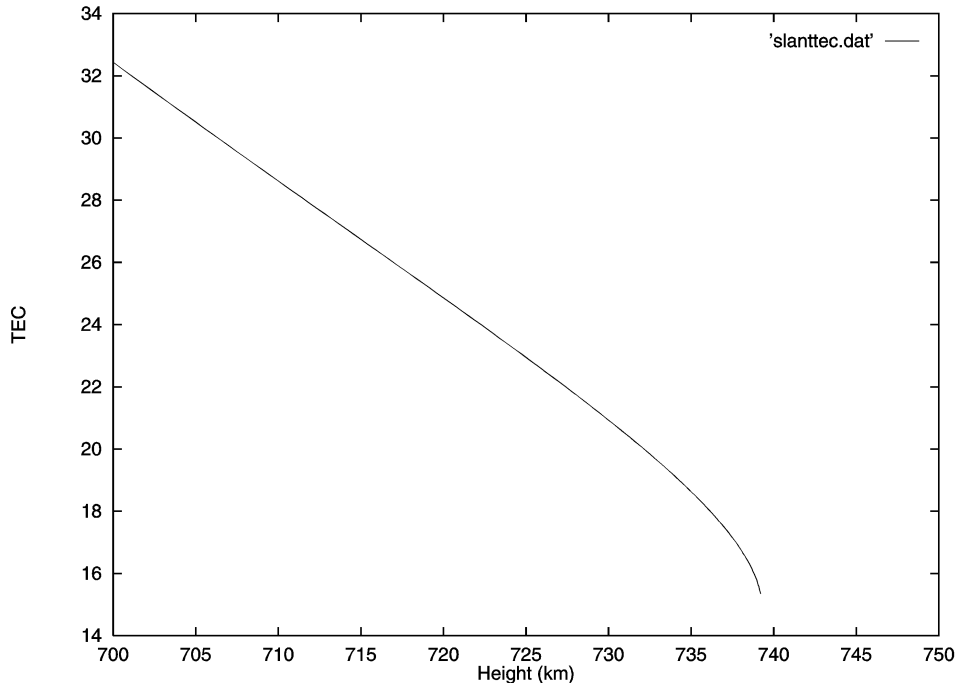

Figure 6.3.5.4-3. TEC profile based on a double Chapman model at daytime solar maximum. The E-peak is at 110 km with density $2 \cdot 10^{11}$ cm^{-3} and the F2-peak at 300 with density $3 \cdot 10^{12}$ cm^{-3}.

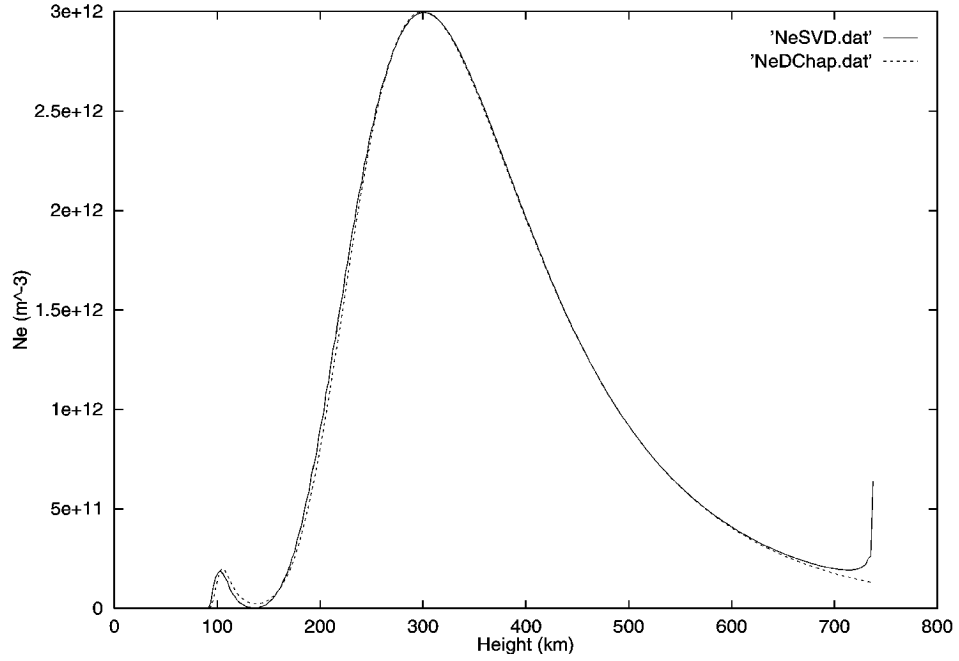

Figure 6.3.5.4-4. Electron density profile corresponding to the TEC profile from figure 6.3.5.4-3. The solid curve labeled NeSVD.dat is obtained using the SVD inversion scheme. While the dashed curve labeled NeDChap.dat is the electron density profile from the double Chapman model.

6.3.5.5. Comparing the Abel transform and the Shell method

The two methods are compared in a difference plot using a double Chapman model ionosphere in the forward modeling simulations. The ionosphere model corresponds to the conditions at daytime solar maximum. The dotted line represent the difference between the electron density calculated with the Shell algorithm and the double Chapman model used in the forward modeling. While the solid curve represent the difference between the electron density calculated from the Abel transform and the ionosphere model.

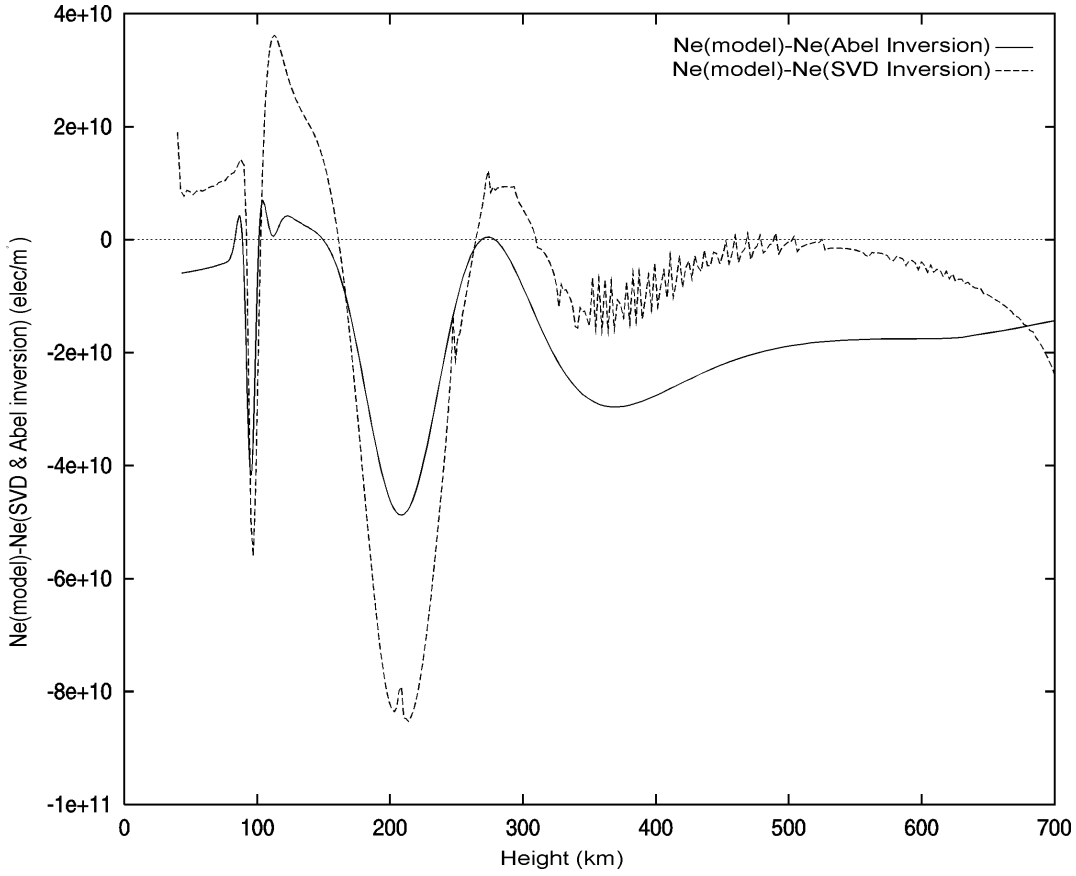

Figure 6.3.5.5-1. Electron density difference plot assuming a solar maximum double Chapman ionosphere model. In this plot a linear selection of shells in three regions have been used in the SVD method (dashed curve). 22 shells in the altitude range 40 to 90 km, 147 shells in the range 90 to 350 km and 167 shells in the range 350 to 740 km. The solid curve represents the difference using the baseline bending angle algorithm. Spherical symmetry of the ionosphere is assumed.

It is seen that the error level for the two algorithms is of the same size. The highest errors for the two algorithms are found around altitudes of 100 km, 200 km and 350 km. This corresponds to the altitudes where the electron density profile has the largest gradients.

The double Chapman ionosphere model used has a F2-layer peak electron density of $3 \cdot 10^{12}$ m^{-3}, hence the relative errors in figure 6.3.5.5-1 is only a few percent. The error level is in general higher for the Shell algorithm than the Abel transform at altitudes below the F2 peak. This means that the Abel transform algorithm is more capable of following the high electron density gradients. For altitudes higher than the F-region the Shell method is more precise than the Abel algorithm. The main reason for this is the exponential fit performed on the bending angle. If the fit is not a close fit, this will introduce an integrated extra contribution to N_e above approximately 500 km. The exponential fitting is however necessary before applying the Abel transform.

The Abel transform algorithm is a faster and easier algorithm to implement. We have therefore chosen this routine as the baseline algorithm for electron density retrieval. Furthermore our studies indicate that the performance in the height range 0-500 km of the Abel transform algorithms is significantly better than SVD for the spherical symmetric climatic ionosphere models used. The Abel transform algorithm takes the bending of the rays into account whereas the SVD algorithm assumes straight line propagation.

6.3.6. The N_e peaks at heights HmE and HmF2

6.3.6.1. Input Data

To determine the peaks in the electron density profile measured during the occultation, the algorithm suggested bellow need the following as input,

1. The electron density profile $N_e(h)$ as a function of height (measured in electrons pr. m^3).
2. The height h (in km) with approximately more than one km spacing between points.

6.3.6.2. Output Data

The output of the HmE and HmF2 algorithm will be the identification of the peaks in the electron density profile,

1. The height of the E-layer HmE (in km).
2. The peak electron density of the E-layer, fmE, (in electrons pr. m^3).
3. The height of the F2-layer HmF2 (in km).
4. The peak electron density of the F2-layer, fmF2, (in electrons pr. m^3).

6.3.6.3. Algorithm

Two layers in the electron density profile are searched for. The most dominant one called the F2-layer, at about 250 km, and a less significant (depending upon solar activity, day/night condition and magnetic latitude) called the E-layer, between 90 km and 130 km. The derivative of the electron density profile is calculated as,

$$\frac{dN_e(h)}{dh} \tag{6.3.6.1}$$

where the peaks are identified by searching where this derivative becomes zero or a minimum in the E-layer region. The F2 peak is determined as the largest peak, while the E-layer is only searched for in the interval between 90 to 130 km in height. If a peak is found outside these limits it is thought of as *not* being the E-layer.

6.3.6.4. Algorithm Description and Computation

The F2 layer is found by searching for the global maximum of the electron density. If this height is coinciding with the minimal height derived in the electron density profile, the F2 layer is per definition not found.

The E layer is searched for only in the mentioned height interval (90-130 km), and it is done in one of two ways. First attempt is to find the maximum within the range. If this fail (in the sense that the maximum is found at the upper height limit) the second method is started, which involves the derivative of the electron density with respect to height. The derivative is denoted $\left|Ne'\right| = |dN_e/dh|$. Searching is then started (from 90km and up to 130 km) for the height with the lowest $\left|Ne'\right|$ combined with a high value of N_e. A new peak height is identified only if both $\left|Ne'\right|$ is lower and N_e is higher than before. If the method states that the E-layer is at 90 km or 130 km (the boundaries) or outside the interval, then the E-layer is per definition not found. Searching for a peak above 130 would lead to situations where the F1-region will be misinterpreted as being the E-region.

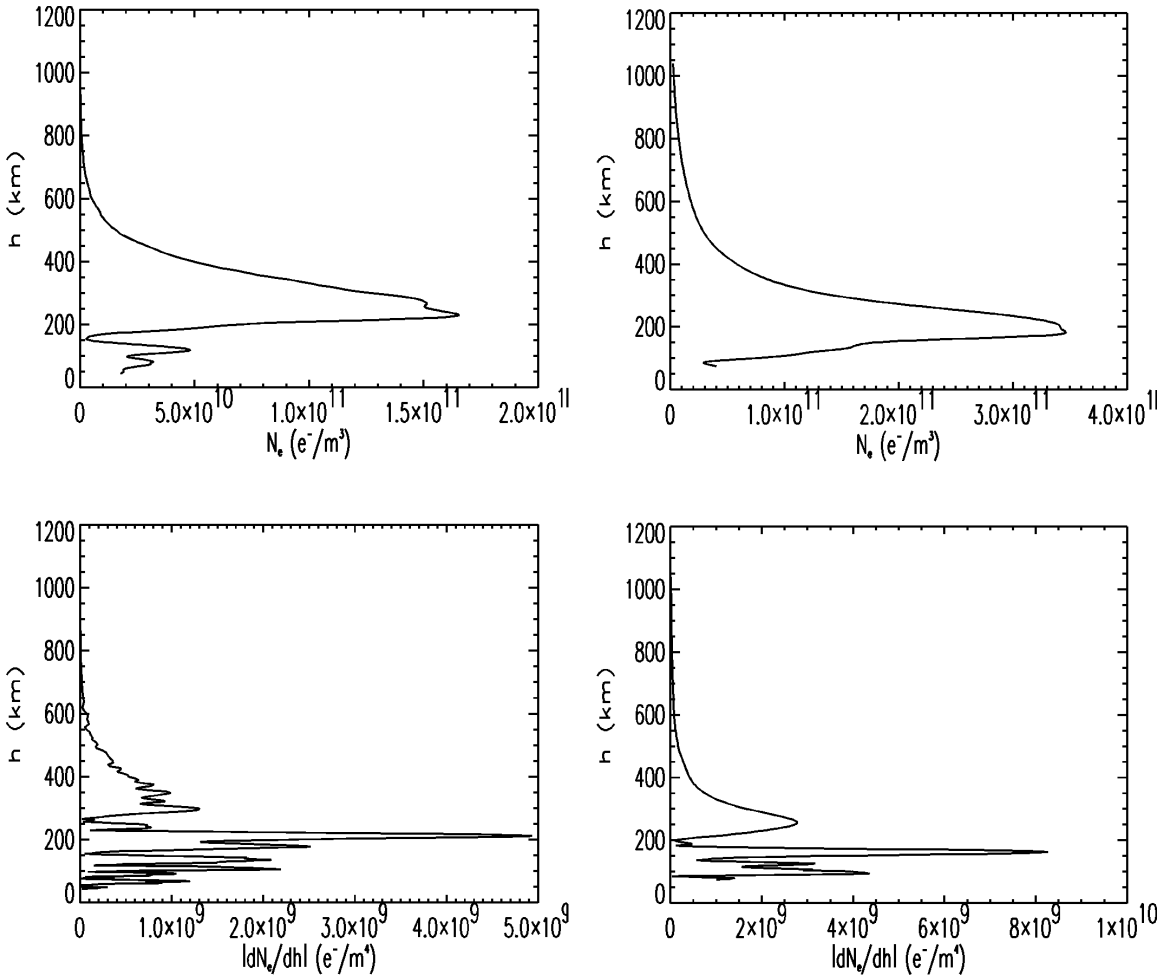

Figure 6.3.6.4-1 Electron density profile and the derivative are shown in two examples taken from February 20, 1997 of the GPS/MET data. The left hand side profile, occultation number 651, shows to distinct peaks. While on the right hand side, occultation number 400 the F1-layer is identified as only the kink on the curve (minimum of the derivative) and no E-layer is identified.

In figure 6.3.6.4-1 above two situations are shown (obtained using GPS/MET occultations summarized in table 6.3.6-1), which are using the two different methods for finding the E layer, the layers are found at (HmF2, HmE)=(230, 119) km and (183, 136) km. The kink at 136 km we identify as a possible F1-layer instead of the E-layer.

The accuracy of the derived heights is corresponding to the resolution in the electron density profile. This applies for both the F2-layer method and the first method for the E-layer. If the second method is used for finding the E-layer, the accuracy is lowered a little due to the differentiation. The above examples in figure 6.3.6.4-1 were obtained from data at 1 Hz sampling rate, the corresponding vertical cell size is about 3 km. The theoretical resolution of about 1.4 km (the diameter of the first Fresnel zone) will be achieved using 5 Hz sampling in the E-region.

Occultation number	UT time	HmF2	HmE
Occ. 651, day 51 20th Feb. 1997	22.10	230 km	119 km
Occ. 400, day 51 20th Feb. 1997	13.40	183 km	None (136 km)

Table 6.3.6-1 Summary of GPS/MET occultation's used in figure 6.3.6.4-1

Very few, only 1-2% of a sample of a little more than 200 occultations, profiles caused problems for the retrieval technique. Most problems occur when the $|Ne'|$ suddenly becomes very small at low altitudes or when the E layer is just outside the selected interval. In all other cases E- and F-region peak altitudes could be determined. In chapter 7.3.6 the F2- and E-layers of the simulated profiles are discussed.

6.3.7. Neutral Atmospheric Bending Angle

6.3.7.1. Input Data

The bending angle of a ray path travelling through the neutral atmosphere is calculated using the following as input:

1. The precise position and velocity vectors of both the LEO (NPOESS) and the GNSS satellite $\overline{R}_L(t)$, $\overline{R}_G(t)$ (measured in km) and $\dot{\overline{R}}_L(t)$, $\dot{\overline{R}}_G(t)$ (measured in km/s) for each sample in time.
2. The two carrier phases $L_1(t)$ and $L_2(t)$ for each sample (measured in meters).
3. The carrier frequencies f_1 and f_2 (in MHz).
4. The sampling rate *s.* (*s* equals from 50 to 100 Hz in the neutral atmosphere).

6.3.7.2. Output Data

The output of the neutral atmospheric bending angle algorithm will be:

1. Bending angle $a(a)$ as a function of impact parameter (in radians).
2. The impact parameter a (in km).

6.3.7.3. Algorithm

For each data sample, phase delay, the impact parameter a is found by solving the equations given below [MEL94].

$$\dot{L}_i + \dot{R}_{LG} - \left(m_i(\overline{R}_L)\left|\dot{\overline{R}}_L\right|\cos j(a) - \left|\dot{\overline{R}}_G\right|\cos c(a)\right) = 0$$
$$j(a) = z - \arcsin\left(\frac{a}{\left|\overline{R}_L\right|}\right) \quad , \quad c(a) = (p - h) - \arcsin\left(\frac{a}{\left|\overline{R}_G\right|}\right) \tag{6.3.7.1}$$

where i=1,2 for the two frequencies received by GPSOS and $m_i(\overline{R}_L)$ is refractive index at orbit height which to a close approximation equals unity. Applying this approximation results in a negligible error contribution [Hajj]. h is the angle between position and velocity of the GPS satellite, z is the angle between position and velocity of the LEO satellite, j is the angle between incoming ray and the velocity of the LEO satellite, c is the angle between outgoing ray and the velocity of the GPS satellite, R_{LG} is the distance between the GPS and LEO satellite, figure 6.3.2.5-1. The bending angle a_{i} can be found using,

$$\alpha_i = \Theta - \arccos\left(\frac{a}{|\overline{R}_L|}\right) - \arccos\left(\frac{a}{|\overline{R}_G|}\right) \qquad (6.3.7.2)$$

where Q is the angle between the two position vectors. The ionosphere corrected bending angle is found from the equation below [Hocke] and [VOR94]

$$\alpha(a) = \frac{f_1^2 \alpha_1(a) - f_2^2 \alpha_2(a)}{f_1^2 - f_2^2} \qquad (6.3.7.3)$$

where $\alpha_1(a)$ is the bending angle of the signal with frequency f_1 and $\alpha_2(a)$ is the bending angle of the signal with frequency f_2.

6.3.7.4. Algorithm Description and Computation

When the occultation is scanning the neutral atmosphere the ray path of the signal passes through the ionosphere twice. This introduces an extra phase delay, which needs to be corrected for before the neutral atmosphere bending can be determined. The simplest possible way to correct for the influence of the ionosphere is the traditional linear correction of phases,

$$L_c(t) = \frac{f_1^2 L_1(t) - f_2^2 L_2(t)}{f_1^2 - f_2^2} \qquad (6.3.7.4)$$

The ionospheric contribution is corrected to first order and $L_c(t)$ is used as input in equation (6.3.7.1) to obtain the impact parameter and bending angle of the neutral atmosphere. This linear correction of phases combines rays at the same time. But due to the ray path splitting between the two signals, the two signals measure different parts of the ionosphere at a given time.

A clearly superior correction scheme is the linear correction of bending angles, where the bending of both signals is computed first and then the bending angle is corrected, comparing the rays at the same impact parameter which better accounts for the ray path splitting. This is the method described in equation (6.3.7.3), which we chose as the algorithm to be used.

Note that since ionosphere correction is essential in the measurement of the neutral atmospheric bending angle, both phase delays need to be corrected for clock errors and POD errors prior to the ionosphere correction.

Neglecting the oblateness of the Earth cause a bias in the resulting temperature profile, which in extreme cases can amount to 6K near the surface [SYN98]. This is corrected for by shifting the center of the curvature radius before applying (6.3.7.1) and (6.3.7.2).

The atmosphere is assumed locally spherical symmetric at the tangent to the ellipsoidal Earth.

6.3.7.5. Statistical Optimization

The general picture is that the bending angle in the neutral atmosphere decreases exponentially as function of height. At heights of approximately 50-60 km the signal drops below the thermal noise level in the receiver. When the bending angle becomes dominated by noise terms we suggest to extrapolate the bending angle using a model. A simple measure for when the noise become dominant is the height for which a becomes negative for the first time. Using an exponential fit turns out to be an efficient approximation. This however introduces a systematic error in the derived temperature profiles due to the fact, that above a given height we assume an isothermal atmosphere.

The method used to extract more information out of the measured bending above a given height is the statistical optimization method [SOK96] and [Hocke], using a model atmosphere to extrapolate the bending angle. The noise on the measured bending angle is obtained by the linear deviation from a model bending angle a_{m} and the expected magnitude of climatological variations of 20% on the signal. This defines s_{noise} and s_{signal} as,

$$s_{noise} = a - a_m \quad \text{and} \quad s_{\mathrm{signal}} = 0.2 a_m \tag{6.3.7.5}$$

Statistical optimization is implemented applying a smooth transition from real measured data to model data by the weighting coefficient *C*, defined as,

$$C = \frac{1}{1 + \left| \frac{s_{noise}}{s_{signal}} \right|} \tag{6.3.7.6}$$

The new bending angle a_{stat} is now computed by the following expression,

$$a_{stat} = a_m + C s_{noise} \tag{6.3.7.7}$$

At initial heights of 100 km the noise dominates completely over the signal, $C \approx 0$ and the bending angle a_{stat} equals the model a_{m} . As the occultation descends through the neutral atmosphere the noise terms decrease with respect to the signal, $C \rightarrow 1$ hence $a_{\mathrm{stat}} \rightarrow a$. Bellow a certain height (determined by the level of noise on the signal) statistical optimization is deactivated and only the measured bending angle α is used to computed the temperature profile. In the analysis studies we have used a height limit of 45 km at approximately 3 mm Gaussian noise, and a slightly higher limit of 50 km when the noise level is corresponding to 0.5 mm or less Gaussian noise.

To constrain the statistical optimization we have used the modified version of the MSIS90 atmosphere model, appendix C, which equals a 1D approximation of the neutral atmosphere. To assign the correct model bending angle to real data (or simulated 3D model data). The model bending angle is adjusted to match the true bending angle profile for the height limit of 45-50 km up to approximately 60 km, figure 6.3.7.5-1. (The 60 km corresponds to 10 km bellow where the bending angle becomes negative due to noise). This can be improved by computing the noise on the bending angle to give a more appropriate value of the limit height.

The model bending angle is re-scaled by computing a c^2 fit to the measured bending between 45 to 60 km weighted according to noise as in equation (6.3.3.5). In figure 6.3.7.5-1 we show an example of how such a re-scaling is performed. Note that statistical optimization (dashed curve) reduce the level of noise and extrapolates the bending angle profile higher above surface. The use of a smooth transition to a model atmosphere reduces the error on a temperature profile by a factor of 5 to 10 compared to the simple exponential extrapolation. See section 7.2 on error assessment.

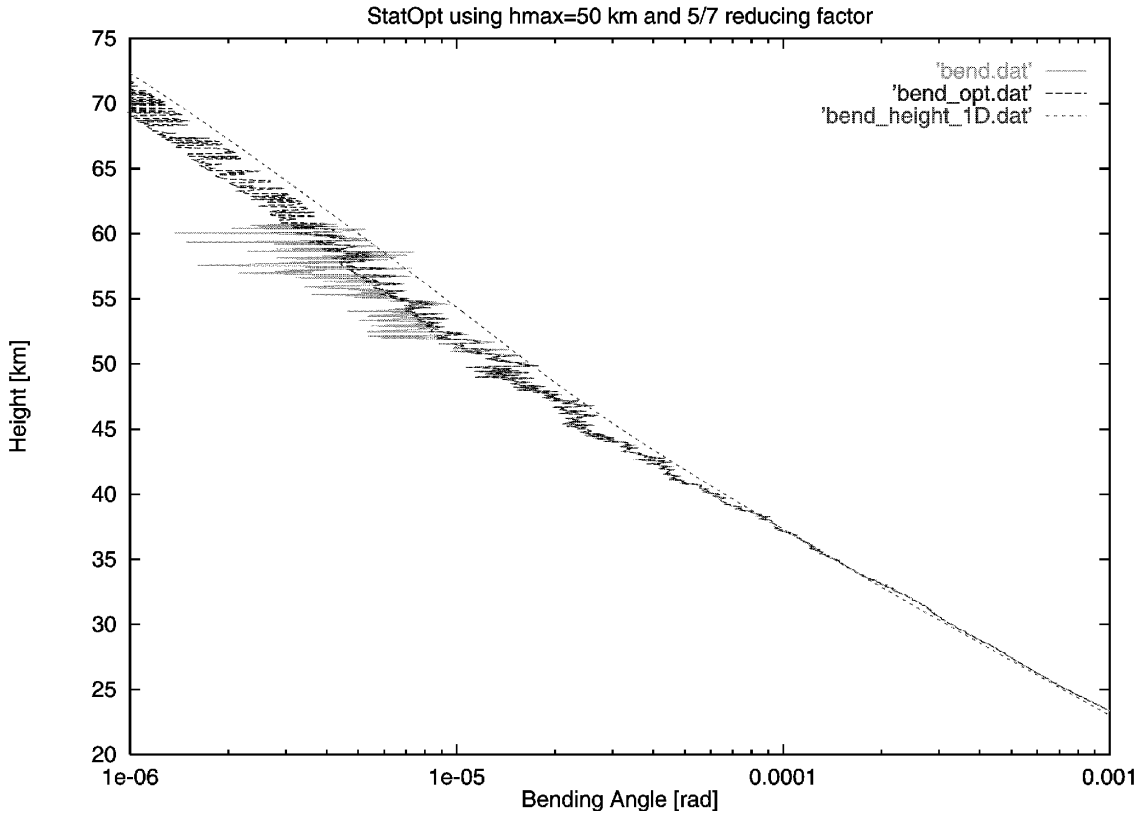

Figure 6.3.7.5-1 Bending angle profile using a GPS/MET observation, occultation number 42 at 1:26 UT on 15th February 1997. The solid curve labeled 'bend.dat' represents the measured bending angle. At a height of 61 km α becomes negative for the first time and data above 61 km are not plotted here. The short dashed curve labeled

'bend_height_1D.dat' is the modified 1D MSIS90 model and the dashed curve labeled 'bend_opt.dat' show the resulting bending angle after applying statistical optimization.

6.3.8. Neutral Atmospheric Refractivity Retrieval

6.3.8.1. Input Data

The neutral atmospheric refractivity *N* is calculated using as input:

1. The ionosphere corrected bending angle of the neutral atmosphere *a(a)* as a function of impact parameter (measured in radians).
2. The impact parameter *a* (in km).

6.3.8.2. Output Data

The output of the neutral atmosphere refractivity algorithm will be:

1. The atmospheric refractivity *N(h)* as a function of height *h*.
2. The height above the surface at the tangent point *h* measured in km.

6.3.8.3. Algorithm

The atmospheric index of refraction m can be found from the Abel transform of the observations [Fjeldbo] and [MEL94].

$$m(a) = \exp\left(\frac{1}{p}\int_a^\infty \frac{a'(x)dx}{\sqrt{x^2 - a^2}}\right) \qquad (6.3.8.1)$$

The refractivity *N* as a function of height *h*, is derived by combining the following equations,

$$N = (m-1)10^6, \quad h = \frac{a}{m(a)} - R_{curve} \qquad (6.3.8.2)$$

R_{curve} is the radius of curvature of the Earth at the tangent point. In the neutral atmosphere the refractivity is always positive and it grows from zero to values of up to 450 N-units near the surface.

6.3.8.4. Algorithm Description and Computation

Equation (6.3.8.1) and (6.3.8.2) are the same equations as (6.3.3.1) and (6.3.3.2) in section 6.3.3.3 where the Abel transform in the ionosphere is discussed. The integral in (6.3.8.1) is computed using the same substitution as in (6.3.3.3) only in the neutral at-

mosphere where a_{ref} = 300 km should be used. Again the limit to infinity is resolved by an exponential fitting as in equation (6.3.3.5).

In the neutral atmosphere the occultation only takes about one minute and the tangent point moves only a few hundred km, much less than for an ionosphere occultation. The assumption of spherical symmetry seems to be a good approximation for most GPS/MET observations and simulations performed in this study.

6.3.9. Temperature, Pressure and Moisture Profile Retrieval

6.3.9.1. Input Data

To determine temperature, pressure and moisture profiles the algorithm need the following input parameters,

1. The refractivity profile of the neutral atmosphere, *N(h)*, as a function of height *z*.
2. The height *z* above the surface at the tangent point measured (in km).
3. The ancillary temperature (in K) of the lower troposphere measured from surface up to 20 km with an uncertainty less than 1 K.

6.3.9.2. Output Data

The output of the temperature, pressure and moisture algorithm will be:

1. The dry pressure, P_{dry} (in hPa), as a function of height.
2. The temperature assuming a dry atmosphere, T_{dry} (in K), as a function of height.
3. The moisture profile, P_W (in hPa), as a function of height between 0-20 km.

6.3.9.3. Algorithm

The secondary EDR parameters of the neutral atmosphere consist of estimates of the temperature, pressure and moisture profile. The retrieval is based on the calculated refractive index profile given above. The refractivity is given as a function of temperature, dry pressure and water vapor pressure as in equation (4.1.4.5), repeated bellow for convenience.

$$N = k_1 \frac{P_d}{T} + k_2 \frac{P_w}{T^2} + k_3 \frac{P_w}{T} \qquad (6.3.9.1)$$

Rearranging equation (6.3.9.1) and assuming a dry ideal gas the density profile can be obtained as,

$$r(z) = \frac{1}{k_1 R_d} N(z) \tag{6.3.9.2}$$

where k_1=77.6 K/hPa and the refractivity is measured in refractivity units (N-units). R_d equals the gas constant of dry air, R_d=0.287 J/(gK). The pressure of the dry atmosphere can now be computed by integration the equation of hydrostatic equilibrium,

$$P_{dry}(z) = \int_z^\infty r(z')g(z')dz' \tag{6.3.9.3}$$

where *g(z)* equals the variation of the gravitational potential as a function of height. From the pressure profile and again using the ideal gas equation the temperature profile becomes,

$$T_{dry}(z) = \frac{k_1 P_{dry}(z)}{N(z)} \tag{6.3.9.4}$$

To estimate the water vapor pressure P_w in equation (6.3.9.1) external input is needed. The ancillary temperature T(z) measured by radiosondes or the temperature profile from Numerical Weather Prediction models (NWP) can be used in this respect. The moisture profile P_w is obtained in an iterative process. First the total pressure is computed using the density profile of dry air,

$$P(z) = \int_z^\infty r(z')g(z')dz' \tag{6.3.9.5}$$

Then the water vapor pressure is estimated using (6.3.9.1) with the k_3 term combined into the k_1 term such that the pressure now is divided into total pressure $P=P_d-P_w$ and water vapor pressure. This introduces an error less than 1% much less than the expected error on the derived moisture profile.

$$P_w(z) = \frac{(N(z)T(z) - k_1 P(z))T(z)}{k_2} \tag{6.3.9.6}$$

With both the total and the wet pressure given it is possible to calculate the new total density of the atmosphere.

$$r(z) = \frac{1}{R_d}\left(\frac{P(z)}{T(z)} - \left[1 - \frac{R_d}{R_w}\right]\frac{P_w(z)}{T(z)}\right) \tag{6.3.9.7}$$

where R_w=0.461 J/(gK). This total density is then used as input in equation (6.3.9.5) and equations (6.3.9.5) to (6.3.9.7) are solved simultaneously by iteration below the altitude

$z=z_0$ converging to a measure of the moisture profile $P_w(z)$. Above initial z_0, the following relations apply $P = P_{dry}$, $T = T_{dry}$, and $P_w = 0$. Rearranging the equations above the wet temperature can be estimated given the moisture profile as input.

6.3.10. Precipitable Water Retrieval (PW)

6.3.10.1. Input data

The precipitable water algorithms need as input:

1. The profiles for temperature T (in K) and water vapor pressure P_w (in hPa) as a function of height.
2. The height above the surface, *h* (in km).

6.3.10.2. Output data

The below relations give as output:

1. The measured Precipitable Water PW (in units of mm) as a function of height in the range from zero up to 20 km.

6.3.10.3. Algorithm

A secondary EDR, which may be provided from the GPSOS system, is the calculated precipitable water defined from the water vapor profile of the troposphere.

In general the GPSOS system is not sensitive to rain or snow particles in the lower troposphere. This is due to the wavelength of the transmitted signals compared to the scale sizes of the particles and the geometry of the observation having the transmitters far away from the probed medium and the receiver. But precipitable water (PW) may also be interpreted as the vertically integrated water vapor profile, at a position on ground, where the water vapor profile from the occultation has its footprint on the surface of the Earth.

From the occultation measurements the wet delay of the refractivity can be mapped onto PW. This is normally calculated at ground GPS sites to monitor the delay caused by the integrated water vapor during a GPS satellite pass over the receiving station.

In other words PW is the integrated water vapor profile mapped onto the precipitable water [Bevis] and [Askne]. The following relations define the mapping function for PW in relation to the zenith wet delay ZWD.

$$PW = \Pi \cdot ZWD \tag{6.3.10.1}$$

$$\Pi = \frac{10^5}{rR_w\left(k_2 \cdot T_m^{-1} + \left(k_3 - m \cdot k_1\right)\right)} \tag{6.3.10.2}$$

where r is the density of liquid water (10^3 kg/m^3), R_w the specific gas constant for water vapor ($R_w = R/M_w = 0.4615$ J/gK), m the ratio between the molar mass of water vapor and dry air ($m = M_w/M_d = 0.6220$), and $k_{i=1,3}$ the constants of the neutral gas given in the expression for the refractivity *N* of the medium (see chapter 4). With these constants of the neutral atmosphere equation (6.3.10.2) defines Π as function of T_m, which is given as a weighted mean temperature of the atmosphere,

$$T_m = \frac{\int_0^\infty \frac{P_w}{T} dz}{\int_0^\infty \frac{P_w}{T^2} dz} \qquad (6.3.10.3)$$

In equation (6.3.10.3) P_w represents the water vapor pressure and *T* the absolute temperature of the troposphere. The values of T_m and Π are known to be in the ranges, 235K< T_m <295K and $6.0 < \frac{1}{\Pi} < 7.5$ with Π depending solely upon T_m.

Table 6.3.10-1 gives the typical values of T_m and Π together with the calculated integrated precipitable water results (PW) from two GPS/MET observations of temperature and humidity profiles. The values have not been compared with other observations of PW. But the magnitudes of the estimates are equivalent to model results for these latitudes at this time of year.

	T_m	$1/\Pi$	ZWD	PW
Typical values	[235 K; 295 K]	[6.0; 7.5]		[1 mm; 70 mm]
Occ. 138, day 284 11 Oct. 1995	292 K	6.02	24.3 cm	40 mm
Occ. 115, day 285 12 Oct. 1995	290 K	6.06	27.1 cm	45 mm

Table 6.3.10-1 Numerical examples of PW calculated using GPS/MET occultations.

An estimation of the terms of the denominator of equation (6.3.10.2) gives that the term $\frac{k_2 \cdot T^{-1}}{k_3 - m \cdot k_1}$ amounts to about 90, indicating that the term containing k_3 contributes only to about 1%.

The ZWD is calculated as,

$$ZWD = \int_0^{\infty} \left(k_2 \frac{P_w}{T^2} + k_3 \frac{P_w}{T} \right) dz \qquad (6.3.10.4)$$

which can be entered into equation (6.3.10.1) for PW. Estimates of the terms in equation (6.3.10.4) shows that the k_3-term contributes to only about 5%.

7. System Error Analysis

7.1. Definition of Atmospheric Conditions

Atmospheric profiling observations based on GPS/GLONASS occultation measurements give an excellent description of a range of parameters in the ionosphere and the stratosphere/troposphere in the lower neutral atmosphere. The total observational system introduces different errors and biases to the retrieved data products. The error sources originate from the GPSOS sensor on the LEO, the GPS and GLONASS transmitting satellites, the medium, the applied data retrieval theories and developed algorithms. All elements of the system contribute to a complex picture of the error sources and the sensitivity of the system. The errors of the retrieved data products can be attributed to four main sources given in table 7.1-1 below.

ERRORS	
Category	*Source*
Geometry	Precise orbit determination errors (position and velocity errors). Earth shape errors. Double differencing errors.
Instrument	Technical limitations of the transmitting system. Carrier frequency drift, SA and AS. The receiver noise level as a function of signal dynamics and receiver electronics. Local multipath errors. Antenna attitude and gain pattern limitations.
Retrieval methods	Ionosphere correction constrains. Bending angle and refractivity retrieval assumptions. EDR retrieval errors and approximations.
Geophysical conditions	Spatial and temporal uniformity of the observables and limitations. Refractivity gradient distribution and medium multipath phenomena.

Table 7.1-1 Error sources.

To identify and quantify the different errors, accuracy and uncertainties of the different parts of the system a set of scenarios for the ionosphere and the troposphere have been chosen for further simulations. They will all present cases of *the best*, *the nominal* and *the worst case conditions* in the atmosphere to test the capabilities of the technique.

These simulations will be performed using the software tool EGOPS and routines developed specifically for this purpose at DMI to monitor the sensitivity and impact of phenomena in the ionized upper atmosphere (ionosphere) as well as the lower dense neutral atmosphere (stratosphere/troposphere).

7.1.1. Ionosphere scenarios

These scenarios will describe ionosphere conditions driven by structures in the electron density distribution in order to observe the predicted 'truth' in the estimated EDR observables. Furthermore these scenarios will demonstrate the influence of external forces originating from the sun on the ionosphere estimates. Two scenarios will center on the conditions in the auroral region as well as the phenomena in the equatorial electrojet.

The simulated scenarios cover the conditions,

- auroral region electron density gradients
- Equatorial electrojet phenomena
- Electron density variations as function of occultation geometry
- Travelling Ionospheric Disturbances (TID)
- Ionosphere high gradient disturbances in the 3D global electron density distribution

7.1.2. Stratosphere/Troposphere scenarios

The scenarios for the lower neutral atmosphere cover conditions, which lead to large gradients in the global spatial refractive index of the medium. They have been chosen to assess some of the most common features determining troposphere termodynamical conditions as well as the dynamical features of the atmosphere. Additionally these scenarios will evaluate the accuracy and the precision of the secondary EDRs. The scenarios cover

- Troposphere frontal systems
- Tropopause foldings
- Troposphere inversion layer conditions
- Gravity waves

7.2. Algorithm Error Assessment

We will in this section perform an assessment on the errors associated with measurements based on the occultation principle. In order to make this error analysis thorough, the accuracies and uncertainties on the measured physical parameters are based on results referenced in the literature (see appendix A and B) and simulations with the EGOPS software tool. Equations for the accuracy and uncertainty on some of the physical parameters have also been derived. The simulation results are based on the current state of the algorithms under development and do not necessarily represent the final performance of all aspects of the EDR algorithms.

The measurement *accuracy* is defined as the difference between the mean estimated value of a parameter and its true value, while the measurement *uncertainty* is given as the root-mean-square of the measurement errors for the estimated parameter. The measurement accuracy and uncertainty is therefore given by the following set of equations

$$\begin{aligned} \text{accuracy} &= \left| \langle x \rangle - x_{true} \right| \\ \text{uncertainty} &= \left[\frac{1}{N} \sum_{i=1}^{N} (x_i - x_{true})^2 \right]^{0.5} \end{aligned} \tag{7.2.1}$$

x_i is an estimate of a parameter with true value x_{true}. The number of estimates in the data set is N. The measurement uncertainty can for large data sets be approximated by the square root of the sum of the squares of the measurement accuracy and precision. Measurement precision is here defined as the standard deviation of the estimated parameter. The measurement precision and the approximate expression for measurement uncertainty is given in the equations below

$$\begin{aligned} \text{precision} &= \left[\frac{1}{N-1} \sum_{i=1}^{N} (x_i - \langle x \rangle)^2 \right]^{0.5} \\ \text{uncertainty} &\approx \sqrt{\text{accuracy}^2 + \text{precision}^2} \end{aligned} \tag{7.2.2}$$

These definitions will be applied in the following sections to describe the results of the error analysis.

7.2.1. Slant Total Electron Content (Slant TEC)

In this section the accuracy and uncertainty on the calculation of the slant total electron content will be found. Equations for the carrier phase L and code phase P has been given in an earlier section. In equation (7.2.1.1) and (7.2.1.2) the index of refraction in the ionosphere has been expressed in a power series expansion that includes terms up to the second order. The effect of the neutral atmosphere has been neglected, since we assume a measurement for which the tangent point is above 100 km.

$\hat{L}$ and $\hat{P}$ are the measured carrier and code phases, including phase ambiguities and clock errors, while L and P gives the theoretical expressions for carrier and code phases.

$$
\begin{aligned}
L_1 &= \int_1 1 - C\frac{N_e}{f_1^2} - K\frac{N_e B_0 \cos(q)}{f_1^3}\,ds \\
\hat{L}_1 &= L_1 + \Delta b_{L1} - B_1 + e_1 \\
L_2 &= \int_2 1 - C\frac{N_e}{f_2^2} - K\frac{N_e B_0 \cos(q)}{f_2^3}\,ds \\
\hat{L}_2 &= L_2 + \Delta b_{L2} - B_2 + e_2
\end{aligned}
\qquad (7.2.1.1)
$$

$$
\begin{aligned}
P_1 &= \int_1 1 + C\frac{N_e}{f_1^2} + 2K\frac{N_e B_0 \cos(q)}{f_1^3}\,ds \\
\hat{P}_1 &= P_1 + \Delta b_{P1} + B_{gr1} + e_{gr1} \\
P_2 &= \int_2 1 + C\frac{N_e}{f_2^2} + 2K\frac{N_e B_0 \cos(q)}{f_2^3}\,ds \\
\hat{P}_2 &= P_2 + \Delta b_{P2} + B_{gr2} + e_{gr2}
\end{aligned}
\qquad (7.2.1.2)
$$

where

$$
\begin{aligned}
C &= \frac{1}{2}e^2 / 4p^2 m e_0 \approx 40.3\,\mathrm{m^3 s^{-2}} \\
K &= \frac{1}{2}e^3 / 8p^3 m^2 e_0 \approx 1.1283 \cdot 10^{12}\,\frac{\mathrm{C}}{\mathrm{kg}}\,\mathrm{m^3 s^{-2}}
\end{aligned}
\qquad (7.2.1.3)
$$

$_j$ is an error term caused by the difference in the GPS and LEO clocks. B_j is the phase ambiguity and bias, B_{gr} is the code phase bias, while and $_{gr}$ are the random errors for the carrier phase L and the code phase P. Bias and random errors are generated in the

receiver electronics on board the LEO and GNSS satellite. N_e is the number density of electrons, and B_0 is the magnitude of the earth's magnetic field. q is the angle between the directions of the ray and the magnetic field. Apart from the ambiguity error, the error on the code phase is in general larger than the corresponding error on the carrier phase, $_{gr} >$. Suffix 1 and 2 in the line integrals represent the paths followed by the two radio waves between the GPS and LEO satellite. Suffix 0 represents the straight line between the two satellites as discussed in chapter 6.

The clock error terms $_j$ will be fully correlated for the two frequencies and will cancel for differential range measurements (L_1–L_2 or P_1–P_2). The terms will not be carried further in the error analysis.

TEC measurements are based on differential carrier and code phase range measurements. From (7.2.1.1) and (7.2.1.2) these difference terms can be written as:

$$\begin{aligned}
\Delta L &= L_1 - L_2 = \Delta L_{TEC} + b_S + b_R + b_{Bo} \\
\Delta \hat{L} &= \Delta L + B_L + e_L \\
\Delta P &= P_1 - P_2 = -\Delta L_{TEC} + b_S - b_R - 2b_{Bo} \\
\Delta \hat{P} &= \Delta P + B_P + e_P
\end{aligned} \tag{7.2.1.4}$$

where

$$\begin{aligned}
b_S &= (\int_1 ds - \int_2 ds) \\
b_R &= -\frac{C}{f_1^2}(\int_1 N_e ds - \int_0 N_e ds) + \frac{C}{f_2^2}(\int_2 N_e ds - \int_0 N_e ds) \\
b_{B_0} &= -\int_1 (K \frac{N_e B_0 \cos(q)}{f_1^3}) ds + \int_2 (K \frac{N_e B_0 \cos(q)}{f_2^3}) ds \\
\Delta L_{TEC} &= C \frac{(f_1^2 - f_2^2)}{f_1^2 f_2^2} \int_0 N_e ds
\end{aligned} \tag{7.2.1.5}$$

where B_L, B_P are bias errors and ε_L, ε_P are random errors from the measurement. B_L and B_P includes differential delay biases in the transmitter and received. In addition, B_L includes a bias due to the unknown ambiguity of the carrier phase measurement.

The equations for measurement of TEC are given in section 6.3.1. This equation is based on a first order expansion of TEC. Further more it is based on both carrier and code phase. Carrier phase is used to record the fine structure and the development of the profile, while the code phase is used to determine the absolute level of the profile. The equations for TEC becomes:

$$\hat{TEC} = \frac{f_1^2 f_2^2 (\hat{L_1} - \hat{L_2} - \hat{B_L})}{C(f_1^2 - f_2^2)} \tag{7.2.1.6}$$

$$\hat{B_L} = \frac{\sum_i w_i (\hat{L_1} - \hat{L_2} + \hat{P_1} - \hat{P_2})_i}{\sum_i w_i}$$

where w_i is a signal quality based weighting factor. For this analysis w_i is assumed to be 1 for some portion of the measurement interval and zero elsewhere. Combining (7.2.1.5) and (7.2.1.6) for $w_i = 1$ gives:

$$\begin{aligned} \hat{B_L} &= \frac{\sum_i (\hat{L_1} - \hat{L_2} + \hat{P_1} - \hat{P_2})_i}{n} \\ &= B_L + B_P + \langle 2b_S - b_{Bo} + e_L + e_P \rangle_{w_i} \end{aligned} \tag{7.2.1.7}$$

Here represent $\langle\ \rangle$ the average over the window w_i. It is seen that $\hat{B_L}$ is an estimate of B_L.

Combining this with the TEC measurement in (7.2.1.6) it is realized that the bias term B_L on L_1 and L_2 can be eliminated. The differential range for TEC can be described as:

$$(\hat{L_1} - \hat{L_2} - \hat{B_L})_j = \Delta L_{TEC} + b_S + b_R + b_{Bo} + e_L - B_P - \langle 2b_S - b_{Bo} + e_L + e_P \rangle_{w_i} \tag{7.2.1.8}$$

The error of the TEC measurement can be evaluated through the range error in (7.2.1.8), where ΔL_{TEC} correspond to the "theoretical length" that the TEC measurement is based on. The error length becomes:

$$e_{L\_TEC} = (\hat{L_1} - \hat{L_2} - \hat{B_L})_j - \Delta L_{TEC} = b_S + b_R + b_{Bo} + e_L - B_P - \langle 2b_S - b_{Bo} + e_L + e_P \rangle_{w_i} \tag{7.2.1.9}$$

and the TEC measurement error is

$$e_{TEC} = \frac{f_1^2 f_2^2}{C(f_1^2 - f_2^2)} e_{L\_TEC} \tag{7.2.1.10}$$

The error length can be separated into measurement errors and algorithm errors.

$$
\begin{aligned}
& e_{L\_TEC} = e^{M}{}_{L\_TEC} + e^{A}{}_{L\_TEC} \\
& \text{where} \\
& e^{M}{}_{L\_TEC} = e_L - B_P - \left\langle e_L + e_P \right\rangle_{w_i} \\
& e^{A}{}_{L\_TEC} = b_S + b_R + b_{Bo} - \left\langle 2b_S - b_{Bo} \right\rangle_{w_i}
\end{aligned}
\qquad (7.2.1.11)
$$

7.2.1.1. TEC differential range measurement errors

From (7.2.1.11) it is seen that the measurement error is represented by three error terms: e_L represented by e_1 and e_2 in (7.2.1.1) above, is the measurement precision of the differential carrier phase range. e_P represented by e_{gr1} and e_{gr2} in (7.2.1.1) above, is the measurement precision of the differential code phase range. B_P represented by B_{gr1} and B_{gr2} in (7.2.1.1) above, is the measurement bias of the differential code phase range. In (7.2.1.11) two terms involving e_L exist. However, the averaged e_L term will be significantly smaller than the not averaged e_L term and the measurement errors can be approximated as:

$$
e^{M}{}_{L\_TEC} = e_L - B_P - \left\langle e_P \right\rangle_{w_i} \qquad (7.2.1.12)
$$

Errors on e_L:

The precision of e_L is illustrated in [SFDA] section 4.4, and is for 1 Hz sampling found to ranging between 0.05 mm and 3 mm. This corresponds to less than 0.03 TEC units. Worst case error for SPS and PPS operation is repeated here, see figure 7.2.1.1-1 and -2:

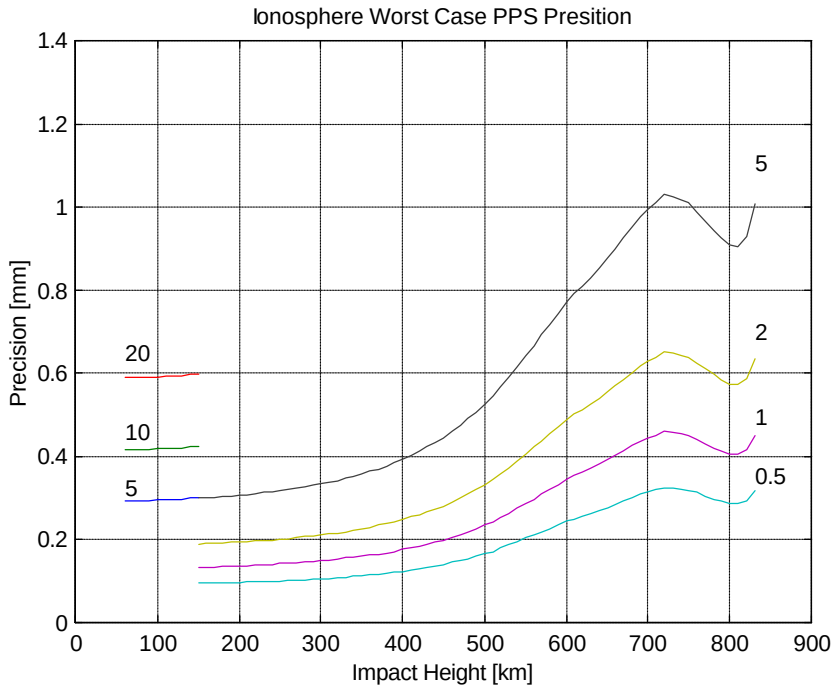

Figure 7.2.1.1-1 PPS worst-case ionosphere measurement precision for indicated sample rates. The number in the plot gives the sample rate in Hz.

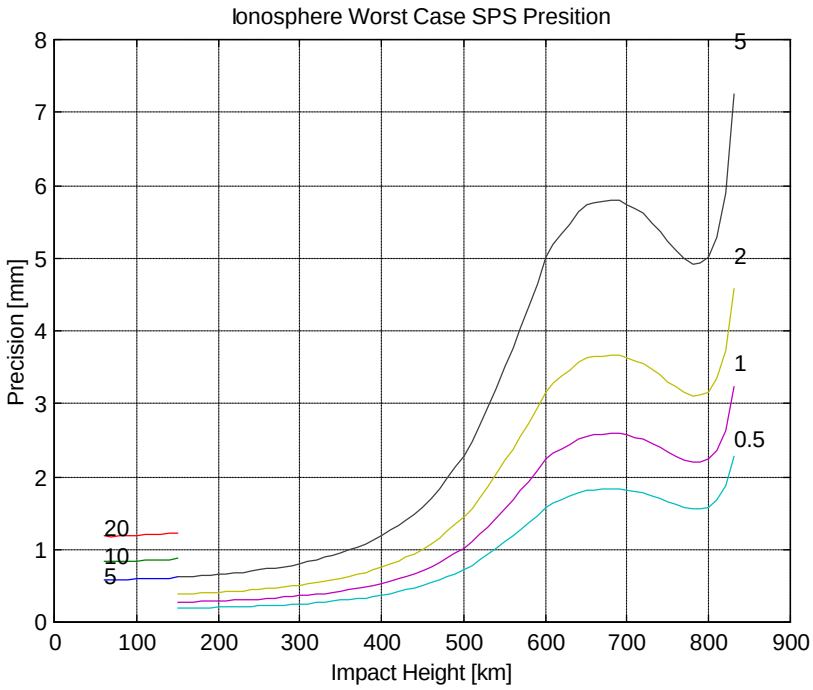

Figure 7.2.1.1-2 SPS with Y code worst-case ionosphere measurement precision for indicated sample rates from 0.5 Hz to 20 Hz.

Errors on $\langle e_P \rangle_{wi}$:

The errors due to the precision of the code phase measurement depend on the carrier to noise density ratio C/No for the P-code measurement channels, the detection loop and the total integration time used to form the average $\langle e_P \rangle_{wi}$. Expected C/No and loop performance is analyzed in [SFDA] section 4.3 and 4.4. Plots for worst case C/No and code loop tracking errors are repeated here, see figure 7.2.1.1-3 and –4.

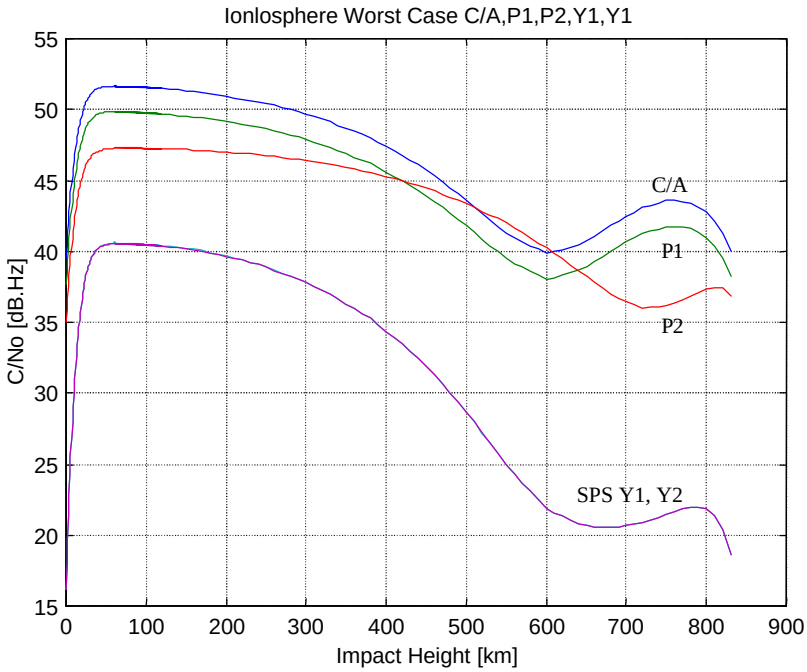

Figure 7.2.1.1-3. Worst case C/No versus impact height for ionosphere.

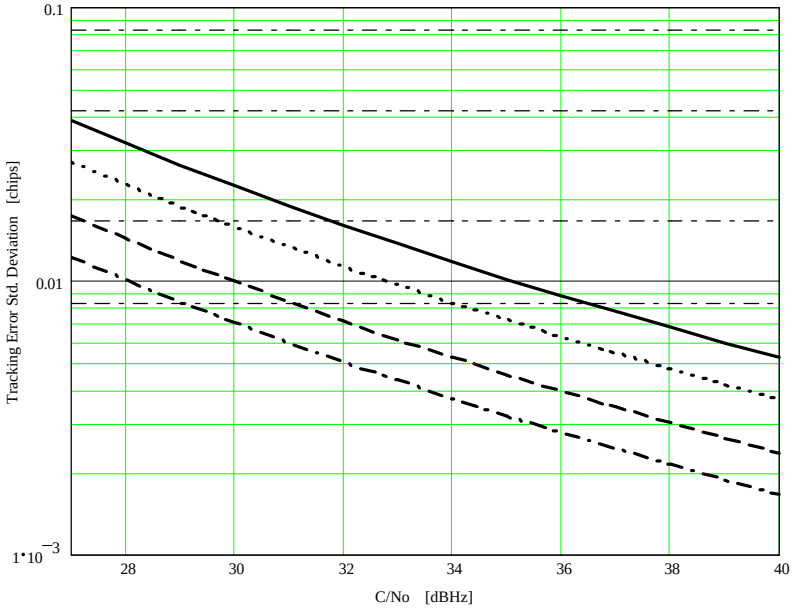

Figure 7.2.1.1-4 Code Tracking Error Standard Deviation and Tracking Thresholds of Dot-Product Loop with B_L = 1 Hz ; Parameter E/L-spacing: 0.5, 0.25, 0.1, 0.05 (top to bottom).

For worst case SPS conditions, the error due to the precision of the code phase measurement for integration between 100 and 300 km altitude can be found by:

- Minimum C/No for P code between 100 and 300 km is 37 dBHz. [SFDA] section 4.4.
- P code measurement precision at 37 dBHz and 1 Hz measurement bandwidth (and 0.25 chip early late chip spacing) is 0.005 chips or 15 cm. [SFDA] section 4.3. 1 Hz measurement bandwidth correspond to 2 Hz sample rate.
- Forming the differential P-code range (P_1-P_2) increase the variance by a factor of 2.
- The occultation time between 100km and 300km is about 2.5 min corresponding to 300 samples at 2 Hz. This reduces the variance by a factor of 300.

Summing the above terms the worst-case one-sigma error of the $\langle e_P \rangle_{wi}$ term in (7.2.1.12) becomes less than 0.15 TEC unit. It should be noted that this is a random error, that for each TEC profile contributes to a fixed bias from a normal distribution with a standard deviation of less than 0.15 TEC units. Table 7.2.1.1-1 below gives measurement errors for three additional worst-case signal conditions.

	SPS 100 < h < 300 km	SPS 500 < h < 700 km	PPS 100 < h < 300 km	PPS 500 < h < 700 km
Worst case C/No [dBHz]	37	23	45	40
One sigma TEC bias [TEC units]	0.13	1.0	0.02	0.09

Table 7.2.1.1-1 Worst-case one-sigma error of the TEC bias arising from code phase measurement precision errors, $\langle e_P \rangle_{wi}$ term in (7.2.1.12).

Errors on B_P:

The last contributing error form the measurement process is the transmitter and receiver group delay biases contributing to B_P. These can be dominating measurement errors.
For GPS the L1/L2 relative group delay bias, is limited to 15 ns with an additional random term of 3ns [GPSNav]. A correction factor (T_{gd}) for the bias term is provided in the navigation message. However, the accuracy of this correction as well as the spectral distribution of the random term, need to be established in order to assess the applicability of directly fixing the absolute TEC level from the code phase measurements. According to [MEL96] bias calibration to 0.3 TEC units (100 ps) is possible.

Group delay uncertainties on the order of 100 to 200 ps are expected to be achievable for GPSOS instrument. This correspond to 0.3 to 0.6 TEC units.

7.2.1.2. Algorithm errors

The algorithmic errors are given in (7.2.1.11), and (7.2.1.13). The errors are seen to depend on β_S, β_R, and β_{Bo}. Normally β_S will be smaller than β_R while β_S and β_R both relate to the fact that we are evaluating the TEC error relative to TEC for the straight line between the satellites without considering the bending of the rays. β_{Bo} is related to the earth magnetic field term. Corrections can be applied to minimize all of these terms, but first we will look at the uncorrected error.

$$e^{A}_{L\_TEC} = b_S + b_R + b_{Bo} - \left\langle 2b_S - b_{Bo} \right\rangle_{w_i} \qquad (7.2.1.13)$$

Uncorrected algorithm errors

The biggest contribution to the line integrals in equation (7.2.1.5) is found when the ray is in the vicinity of its tangent point. For β_{Bo} we have approximated the term $B_0 \cos(\ )$ with B , the along-ray component of the magnetic field at the tangent point. B has been set to 30 T representing the worst case. This value is a representative equatorial value for the magnetic field at an altitude of 100 km.

For β_S and β_R the integrals along path 1 and 2 for the L_1 and L_2 carrier phases, have been calculated for a given occultation with the use of a simulation program called ROSAP, developed at DMI. The line integral of the electron density over the straight line between the LEO and GPS satellite (path 0) can be approximated by the phase delay, calculated at a very high frequency. This frequency was selected to be 100 times the L1 carrier frequency. The ray will at this high frequency very closely follow the straight line between the satellites.

Fig. 7.2.1.2-1 to fig 7.2.1.2-4 show simulation results on the effect of the β–terms, evaluated under the assumption of a symmetric ionosphere in the probed ionosphere region. The three bias terms β_R, β_S and β_{Bo} have been calculated as a function of altitude.

Fig. 7.2.1.2-1 and 7.2.1.2-3 shows the double Chapman ionosphere model used in the simulations corresponding to the conditions in the symmetric case at daytime and night time solar maximum. Fig. 7.2.1.2-2 and 7.2.1.2-4 shows the result of the simulations. These two figures show each of the three bias terms β_R, β_S and β_{Bo} together with the resulting bias as a function of altitude. From fig. 7.2.1.2-2 we deduce the uncorrected TEC accuracy to be around 1 m which equals approximately 10 TECU for worst case conditions, corresponding to a solar maximum daytime situation. The nighttime solar maximum situation presented in figure 7.2.1.2-4 shows that the uncorrected TEC accuracy in this case is around 0.4 TECU. Accumulated numerically errors in the calculations (fig. 7.2.1.2-4) are the reason for the noise seen in the curves especially at low altitudes.

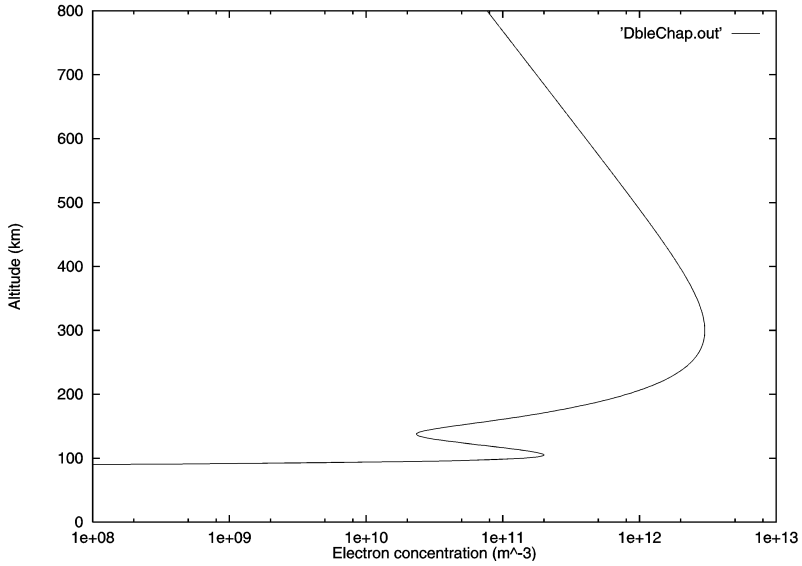

Figure 7.2.1.2-1 Double Chapman ionosphere model corresponding to the conditions at daytime solar maximum. The E layer has a maximum value of $2 \cdot 10^{11}$ electrons/m^3 at an altitude of 105 km. The F layer has a maximum value of $3 \cdot 10^{12}$ electrons/m^3 at an altitude of 300 km.

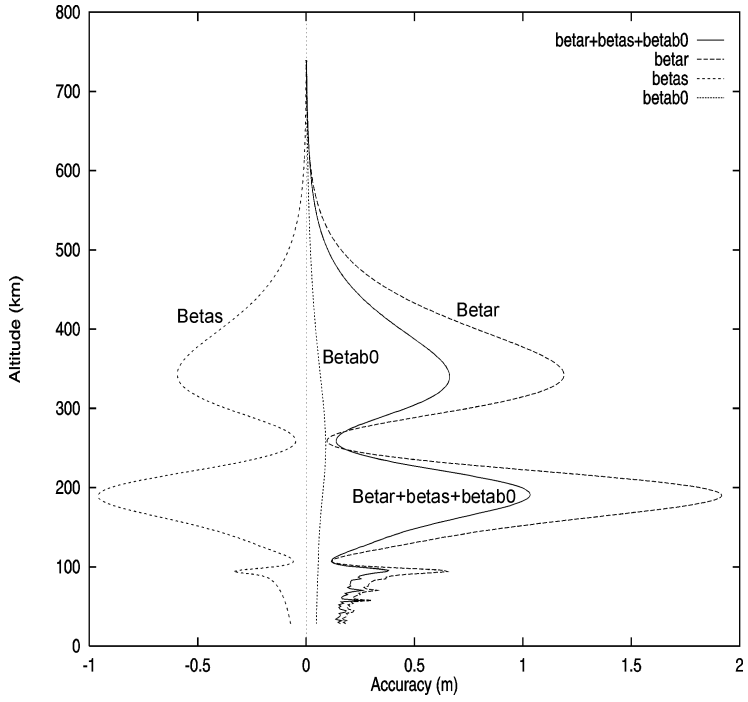

Figure 7.2.1.2-2 Uncorrected TEC measurement accuracy in the symmetric case at daytime solar maximum. The solid line shows the total uncorrected accuracy related to all the bias terms. The accuracy given in meters multiplied by 10 approximates to the accuracy in TECU.

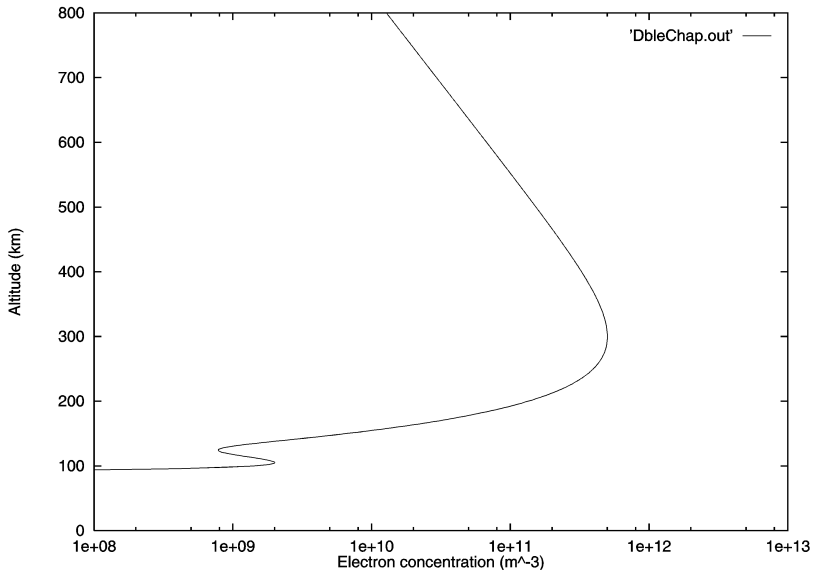

Figure 7.2.1.2-3 Double Chapman ionosphere model corresponding to the conditions at nighttime solar maximum. The E layer has a maximum value of $2 \cdot 10^9$ electrons/m^3 at an altitude of 105 km. The F layer has a maximum value of $5 \cdot 10^{11}$ electrons/m^3 at an altitude of 300 km.

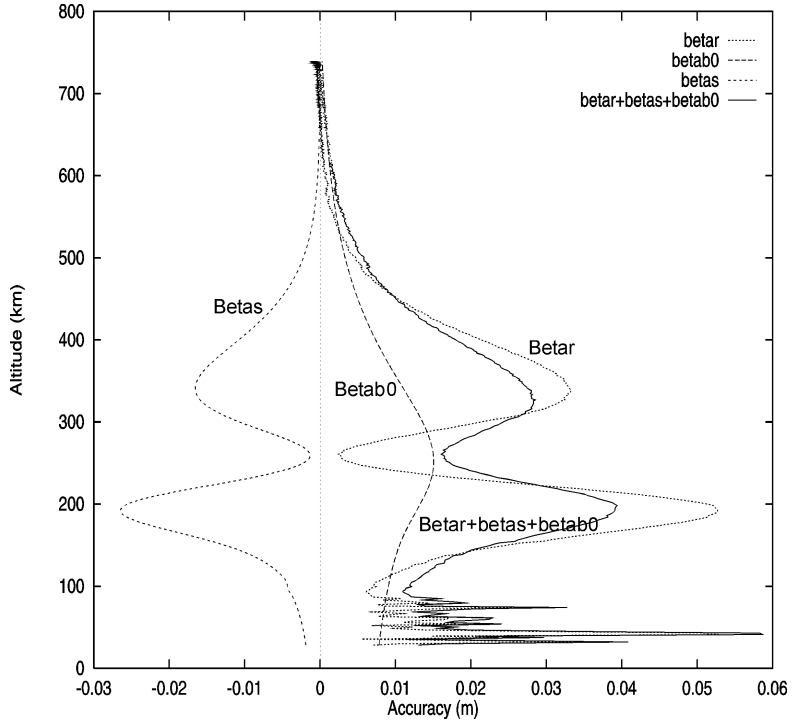

Figure 7.2.1.2-4 Uncorrected TEC measurement accuracy in the symmetric case at nighttime solar maximum. The solid line shows the total uncorrected accuracy related to all the bias terms. The accuracy given in meters multiplied by 10 approximates to the accuracy in TECU.

The error for β_{Bo} is estimated to below 0.1 % and can with the knowledge of the Earth magnetic field be reduced even further. Hence even at worst case condition of 1000 TECU sub TECU levels can be reached for this error as seen in figure 7.2.1.2-5.

Corrected algorithm errors

In this section we show the results of the TEC correction relation (6.3.1.3) and compare the simulation results to the uncorrected data discussed in the previous section. The TEC profiles corresponding to the simulations for day and night time solar maximum conditions are shown in figure 7.2.1.2-5. The four curves show the corrected and uncorrected TEC profile for the two cases. The absolute errors due to the three bias terms are shown in figure 7.2.1.2-6 and figure 7.2.1.2-7 together with the TEC corrections and the residual errors for the daytime and nighttime cases. The TEC correction algorithm estimates the sum of the two bias terms β_R and β_S. The algorithm for performing the TEC correction have been explained in chapter 6.3.1.5. The residual error is found by subtracting the TEC correction from the sum of the three bias terms. It is seen from figure 7.2.1.2-6 that the residual error, corrected accuracy, is less than 0.1 m in the symmetric worst case. By comparing figure 7.2.1.2-6 with figure 7.2.1.2-2 it is seen that the curve for the magnetic bias term β_{Bo} has the same shape as the curve for the residual error. The TEC correction improves the TEC accuracy from 1 m to 0.1 m in the symmetric worst case. Both the corrected and uncorrected TEC profiles for daytime and night time at solar maximum are shown in figure 7.2.1.2-5. It is seen that the TEC correction is small and the relative importance of the correction is highest for high TEC values.

It should be noted that the average part due to the ambiguity estimate in (7.2.1.13) is dependant on $2\beta_{S.}$ Hence, based on the errors introduced by the algorithm this bias should be estimated where β_S is low, i.e. at high altitudes. For bias estimates based on 400 km or higher altitude, the algorithmic part of the error is negligible, since the actual ray paths are almost coincident with the straight line.

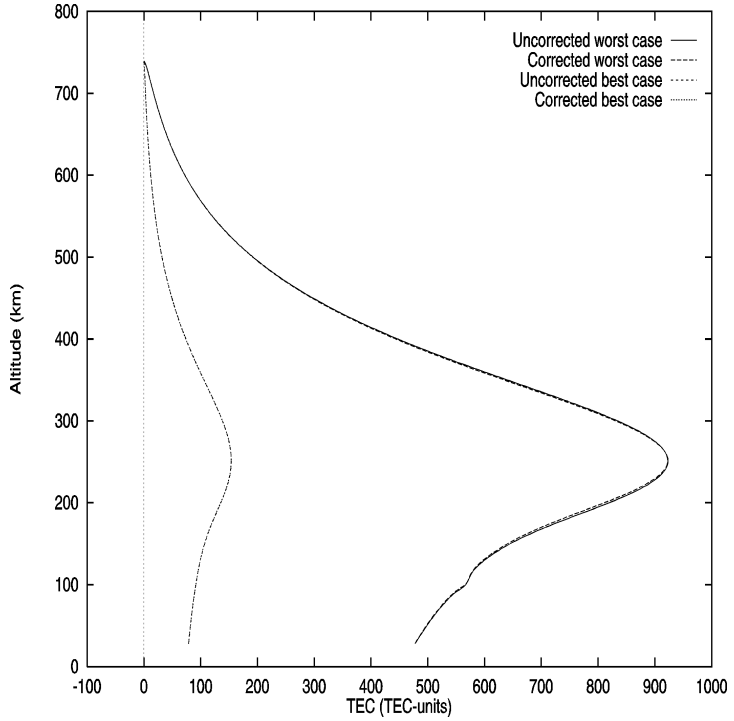

Figure 7.2.1.2-.5. Corrected and uncorrected TEC levels for day and night time simulations in the symmetric case.

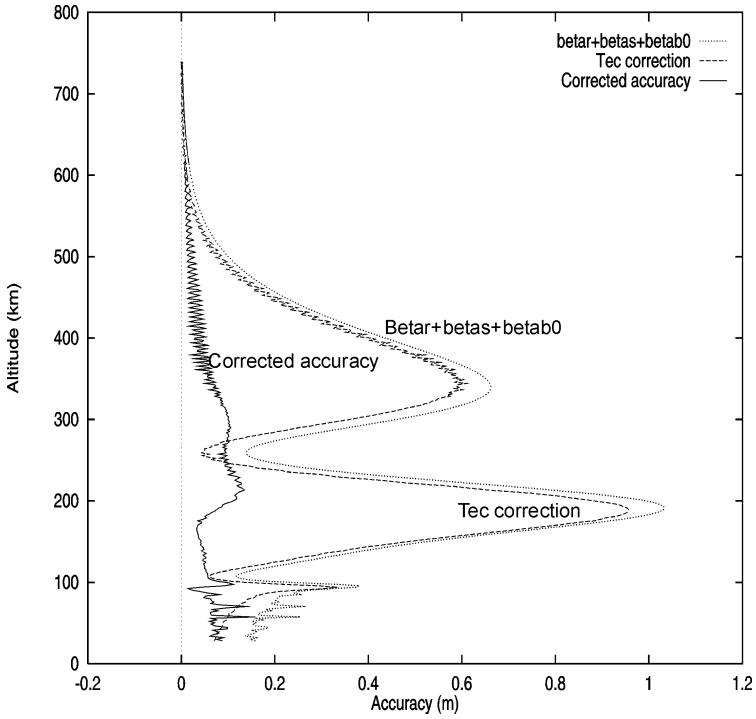

Figure 7.2.1.2-6. TEC error, TEC correction and corrected accuracy in the symmetric case at daytime solar maximum.

From figure 7.2.1.2-6 it is seen that for TEC levels of almost 1000 TECU algorithmic errors are expected to be less than 1 TECU. At worst case TEC levels of 1000 TECU the residual error of 1 TECU, corresponding to an accuracy of 0.1 %, is caused by the magnetic field bias term.

The derivation of the TEC correction was done under the assumption of spherical symmetry. To test the validity of the TEC correction under asymmetric atmosphere conditions a number of numerical simulations have been performed with an asymmetric ionosphere representative of a day-night transition region across the occultation. Several situations with different geometry were studied, and the worst case found was that of a near side-viewing occultation shown in figure 7.2.1.2-8a and 7.2.1.2-8b. The ionosphere model used in this example simulates the ionospheric conditions at a day-night transition. The electron density level is therefore also changed as a function of longitude, which makes the model asymmetric. Figure 7.2.1.2-8a shows in a latitude-longitude plot the positions of the LEO and GPS satellites together with the radio-rays during the occultation projected onto the surface of the Earth. The solid line in figure 7.2.1.2-8b shows the electron density at the lowest impact height of the rays as a function of longitude. Figure 7.2.1.2-9 shows the variation in the electron density for the used day-night transition ionosphere model as a function of longitude and altitude. From the electron density surface it can be seen that the F-layer peak density decreases by a factor of 5 over the longitude span of about 50 degrees, while the E-layer peak density decreases by a factor of 100. This change in magnitudes of the E and F-layer peaks can also be seen in figure 7.2.1.2-8b.

The two broken curves in figure 7.2.1.2-10 shows the TEC correction and the sum of the two bias terms β_R and β_S. The solid curve represents the corrected accuracy, the residual error. The error residual is in this case over-estimated above the F-layer peak, and underestimated below. However, due to the non-spherical symmetry the total electron concentration cannot everywhere be as high as at the daytime situation. This results in a maximum just below the F-layer peak of about 600 TECU compared to the 950 TECU in the symmetric case. Thus, the TEC gradients are reduced similarly, and this again reduces the residual significantly. After applying the TEC correction described above the TEC error in this case is reduced to less than 2 TECU, see figure 7.2.1.2-10. So in general we assess, that the algorithmic errors can be reduced to less than 3 TECU.

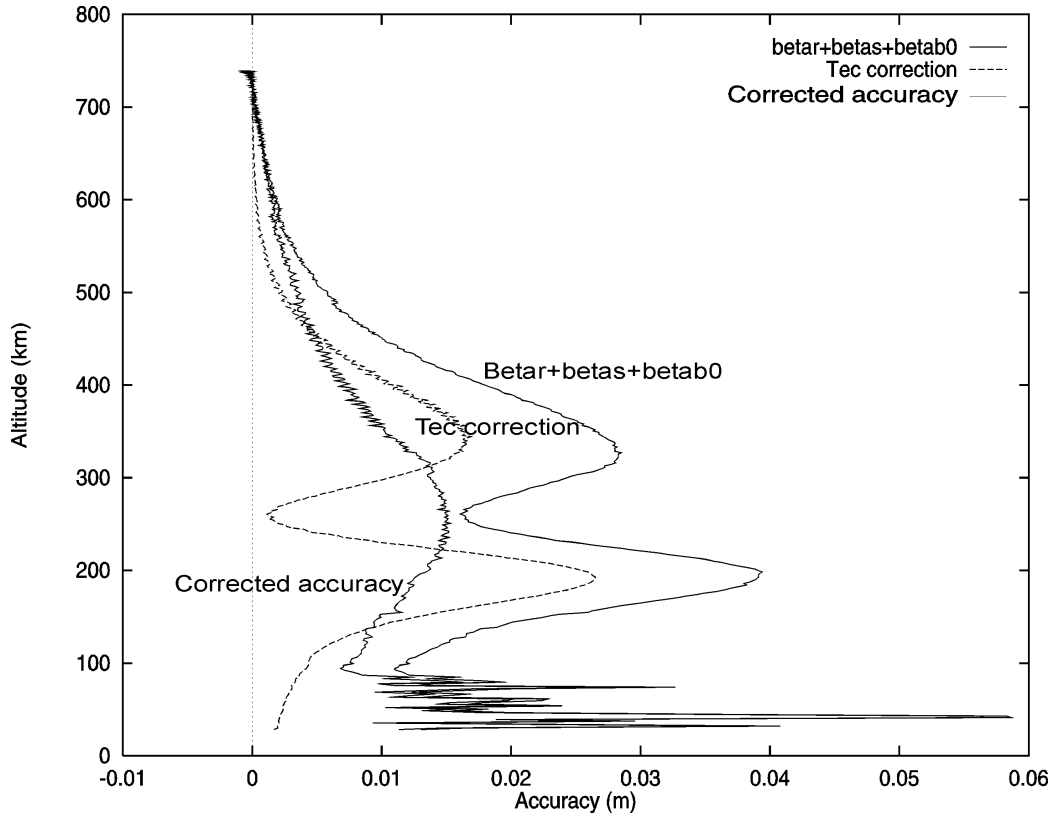

Figure 7.2.1.2-7. TEC error, TEC correction and corrected accuracy in the symmetric case at night time solar maximum.

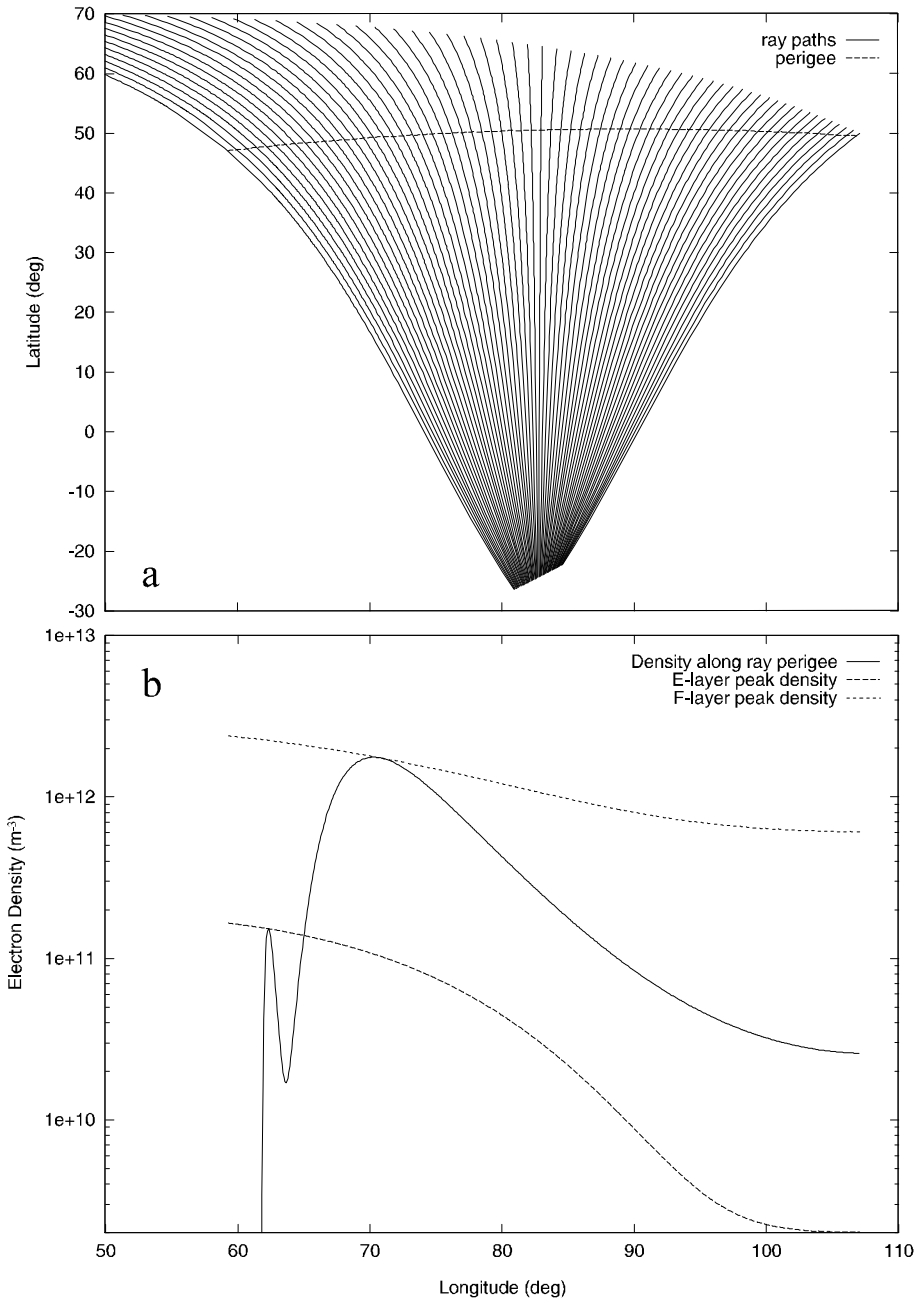

Figure 7.2.1.2-8 a) Ray paths (solid curves) and ray perigee (broken curve) from GPS/MET occultation no. 651, day 51, in a latitude-longitude plot. The LEO satellite longitude-latitude positions are at the top of the ray paths, while the GPS satellite moves along the lower end points of the ray paths. The occultation is a rising one with the perigee going from west to east. b) Electron densities as a function of longitude for the modeled occultation. The solid line gives the change in the electron density at the lowest impact height as function of longitude. The two broken curves shows that the F-layer peak density decreases by a factor of 5 over the longitude span of about 50 degrees, while the E-layer peak density decreases by a factor of 100.

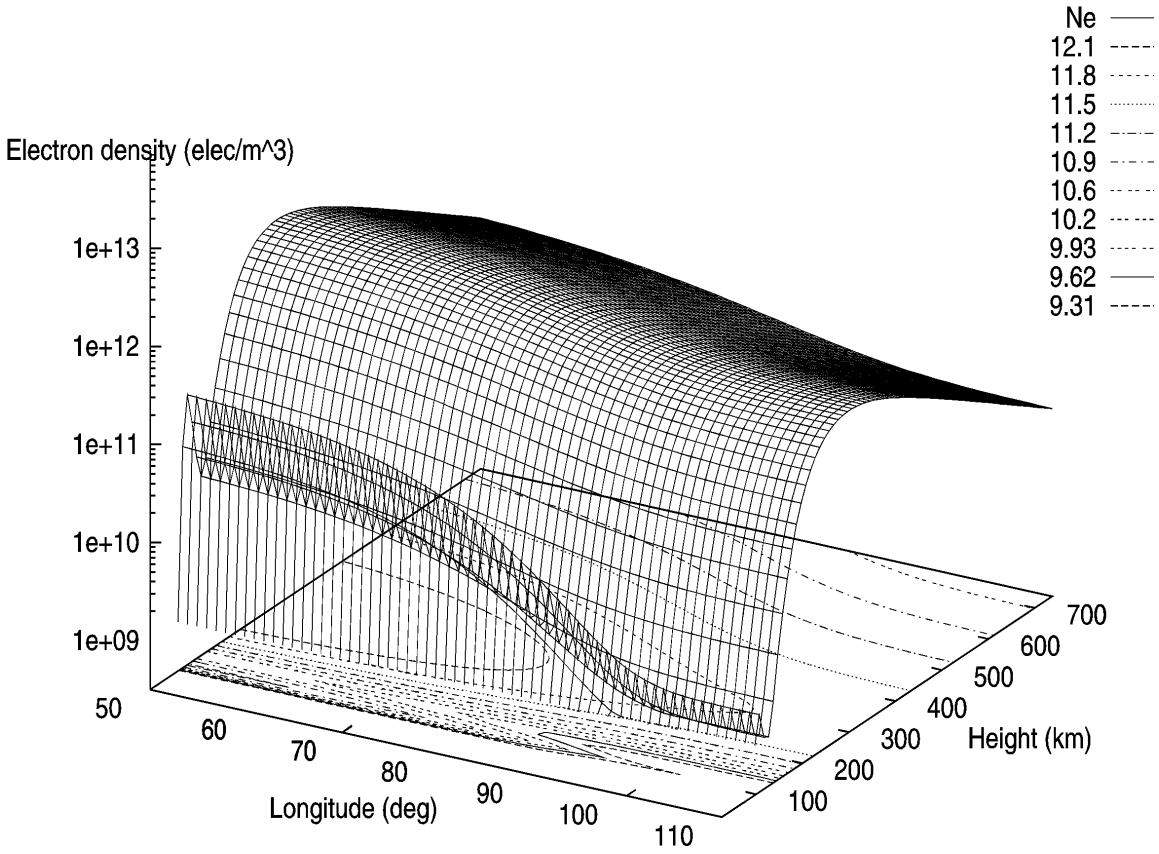

Figure 7.2.1.2-9 The surface and contour plots show the electron density in the ionosphere model for the day-night transition as a function of longitude and altitude. The electron density is presented in a logarithmic scale. The logarithmic scale makes it possible to follow the change in the positions and magnitudes of the E and F peaks with longitude.

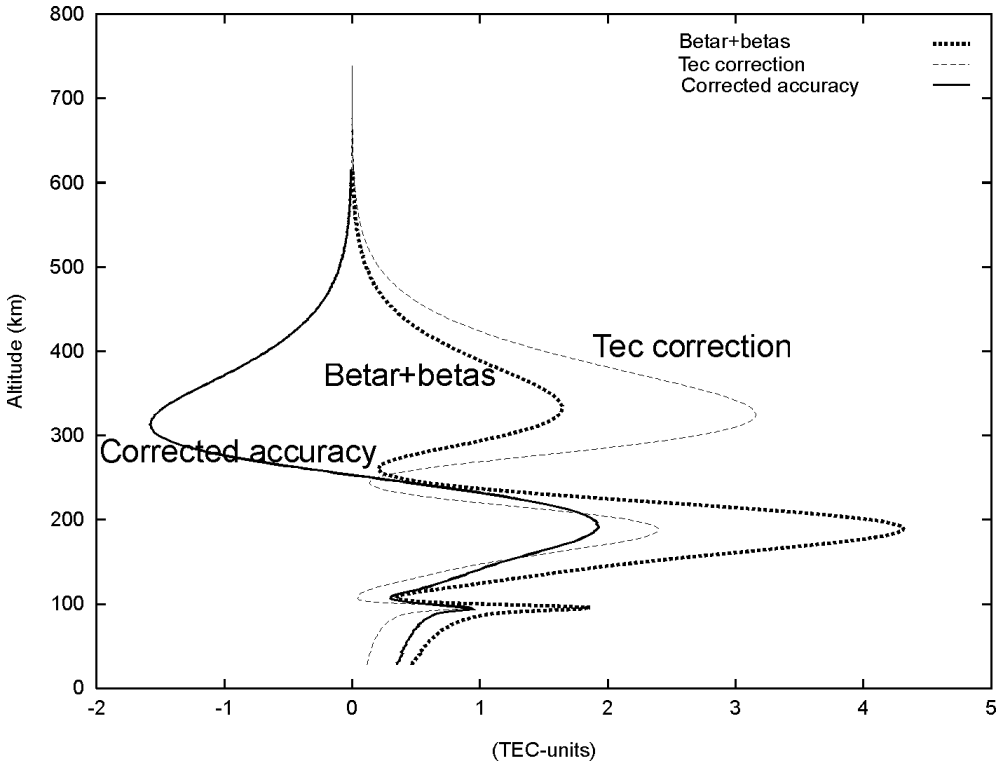

Figure 7.2.1.2-10 The broken curve represent the sum of the two bias terms $_R$ and $_S$ in the non-symmetry case. The TEC correction is represented by the second broken curve. The difference and thereby the resulting error after correction, corrected accuracy is shown as the solid curve.

7.2.2. Summary of TEC errors

In table 7.2.2-1 below the uncertainty on the TEC measurement is estimated based on the analysis above. (SPS refers to standard positioning service, while PPS equals the precise positioning service.)

Error in TEC units	SPS 100-300km bias estimate Med TEC	SPS 100-300km bias estimate Hi TEC	SPS 400-700km bias estimate Med TEC	SPS 400-700km bias estimate Hi TEC	PPS 400-700km bias estimate Med TEC	PPS 400-700km bias estimate Hi TEC	
Carrier phase	0.03	0.03	0.03	0.03	0.00	0.0	Random for each TEC sample
Code Phase	0,1	0,1	0,5	0,5	0,1	0,1	Random for each Profile
Group delay bias	0.4-0.7	0.4-0.7	0.4-0.7	0.4-0.7	0.4-0.7	0.4-0.7	Systematic
Algorithm error	< 1	1-3	<1	~1	<1	~1	For SPS, Hi TEC & low alt. Bias estimate partly systematic.
TOTAL	~1	~3	~1.5	~2	~1	~1.5	

Table 7.2.2-1. Summary of TEC errors.

7.2.3. Electron density

The electron density error assessment can be divided in two different cases, the symmetric and asymmetric case.

Error assessment in the symmetric case

The two different methods for calculating the electron density described in this document have been compared in a difference plot in section 6.3.5.5. The plot corresponds to the conditions at daytime solar maximum. The ionosphere model used is symmetric so figure 6.3.5.5-1 represent a symmetric worst case.

It is seen from figure 6.3.5.5-1 that the error magnitude is less than $5 \cdot 10^4$ elec/cm^3 for the bending angle algorithm. This is the worst case accuracy level that can be expected for occultations under symmetric conditions. At nominal conditions the accuracy is estimated to be below 10^4 elec/cm^3 assuming a spherical symmetric ionosphere. The algorithm error expressed in percentage is less than a few percent in both cases. It is noted that the highest errors are found at altitudes where the electron density profile has the largest gradients. A lower error magnitude for the shell method might be obtained if the resolution of the TEC measurement is increased. This could be done by non-linear interpolation of the LEO, GPS satellite positions and the corresponding TEC measurements. The increased number of measurements would allow us to increase the number of shells

and thereby decrease the error size. The decrease in error magnitude can also be accomplished by an increase in the sampling rate.

Error assessment in the asymmetric case

The ionosphere model presented in figure 7.2.1.2-8 represent an asymmetric worst case ionosphere, corresponding to the conditions at a day-night time transition region. This model together with the near side-viewing occultation showed in figure 7.2.1.2-8a will be used to assess the electron density error in the asymmetric case. The electron density profiles with the label *'Abel inversion'* in figure 7.2.3-1 and figure 7.2.3-2 are calculated with the use of the Abel inversion algorithm. The difference between the two figures is that figure 7.2.3-1 represent the electron density profiles for a occultation that comes from the day-zone and enters into the night zone, while the opposite is true for figure 7.2.3-2. The curves with the labels '*Model lon 60'* and '*Model lon 70*' shows the electron density intrinsic to the ionosphere model at longitudes of 60 and 70 degrees. The curve with the label *'Along ray perigee'* shows the electron density along the ray perigee height of the occultation. This profile is closer to the measured electron density profile than any of the models profiles at high altitudes. When performing the Abel transform the bending angle is integrated from the impact height to infinity, this means that errors caused by the asymmetry will increase with decreasing impact height.

Figure 7.2.3-1 and 7.2.3-2 shows that a worst case occultation, where the tangent point moves from a region of high electron density to a region of lower electron density, can cause a positive bias in the electron density profile. While a occultation from a region with low electron density that enters a region with high density can give a negative bias in the electron density profile. The size of this bias is around $3 \cdot 10^5$ electrons/cm^3 for this worst asymmetric case presented in the figures 7.2.3-1 and 7.2.3-2.

The electron density retrieval algorithms presented in this document are all derived under the assumption of spherical symmetry. The analysis presented above shows that a bias in the calculated electron density profile can be caused by a occultation that has occurred in a region where the assumption of spherical symmetry is not valid. This gives a method to determine if the occultation has occurred under asymmetric conditions in the ionosphere. It can then, during the post processing of the measurements, be decided if the result of the inversion gives a valid estimate of the electron density profile. When multiple simultaneously occultation measurements are available future tomographic algorithms are expected to give a valid electron density profile for measurements taking under asymmetric ionosphere conditions.

A side-viewing occultation normally gives a higher error in the density profile than a straight-on occultation, because the side-viewing occultation is scanned over a much larger area. It is therefore more likely that the assumption of spherical symmetry has been violated.

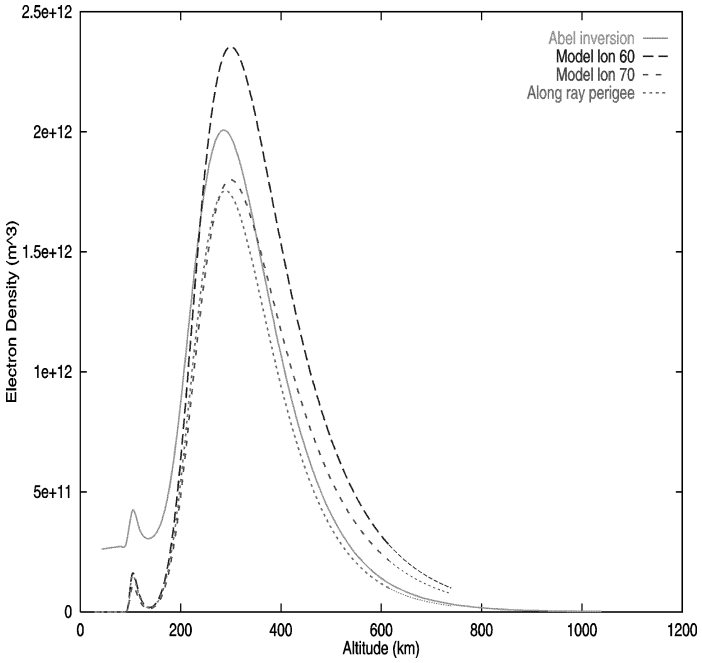

Figure 7.2.3-1. The asymmetric worst case simulation. The electron density profile with the label Abel inversion is calculated for a occultation in the region of a day-night transition. The three other profiles are based on the model presented in figure 7.2.1.2-8 and 7.2.1.2-9.

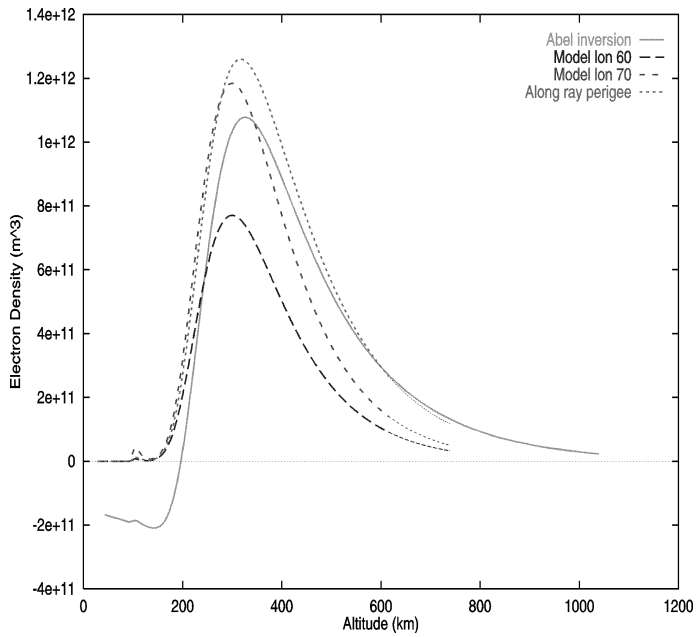

Figure 7.2.3-2. The asymmetric worst case simulation. The electron density profiles are calculated for an occultation in the region of a night-day transition.

Calculation of the electron density profile using the Shell method, described in section 6.3.5, gives the same result as the Abel inversion approach since both methods assume spherical symmetric. The Shell method can however be extended to deal with the asymmetric situation. By dividing each shell into a number of cells (allowing the electron density level to be different in each of the cells) is expected, that the retrieved electron density description becomes a better measure of the ionosphere condition during the asymmetric case.

Measurement resolution

The distance at low sampling rates between the measurement samples will in general limits the measurement resolution in the ionosphere. A 1 Hz sampling corresponds approximately to a vertical resolution of 3 km. This means that the positions of the two peaks HmF2 and HmE in the electron density can be resolved to within a distance of 3 km. The resolution of the measurement can in general not be increased arbitrarily by increasing the sampling rate. If we increase the sampling rate to 2 Hz, this would result in a measurement vertical distance of approximately 1.5 km, which is close to the diameter of the first Fresnel zone in the ionosphere, hence we become limited by diffraction. The diameter of the first Fresnel zone Z_F is in the thin screen approximation given by

$$Z_F = 2\sqrt{lD} \tag{7.2.3.1}$$

The parameters l and D is the wavelength and the distance to the tangent point (thin screen) from the LEO satellite. In the neutral atmosphere the magnitude of D is approximately 3300 km corresponding to Z_F equal to 1.6 km. However in the ionosphere the LEO satellite will approach the tangent point in the upper part of the ionosphere. Hence the value of D is here approximately 2450 km at an altitude of 400 km corresponding to a first Fresnel zone diameter of 1.4 km. This shows that it is a fair approximation to assume that the diameter of the first Fresnel zone is approximately 1.5 km in a large portion of the ionosphere.

7.3. Simulation results for Primaries

For the primary EDRs the errors tested for in the EGOPS simulations are summarized in Table 7.3-1 below. All simulations have been performed for the orbit of the NPOESS satellite, i.e. a circular orbit with an altitude above the ground of 833 km with an inclination of 98.7 degrees. We have simulated occultations in the orbital plane of the NPOESS satellite, as well as occultations with a large angle to the orbit plane of the NPOESS satellite.

Error type	No. of runs	Error size	Abbreviation
Radial position	1	0.5 m	Pos1
	1	15 m	Pos2
Along-ray velocity	1	0.5 mm/s	Vel1
	1	1000 mm/s	Vel2
Navigation solution corresponding to no POD	1	LEO as Vel2 and LEO and GNSS as Pos2	NoPOD
Gaussian noise on phase	50	0.3 mm	Rand1
	50	1.0 mm	Rand2
	50	3.0 mm	Rand3

Table 7.3-1 Errors used in scenarios for primary EDRs.

'Radial position' means that the real position is perturbed radial with the given value as a constant bias (accuracy). The same is then done for the 'Along-ray velocity' where the velocity error is added to the satellite velocity as a bias. The 'Navigation solution' is the sum of errors related to the latter errors. For each of these geometric errors only one run has been performed. For the 'Gaussian noise on Phase' 50 runs have been performed, resulting in both an average result and a standard deviation.

Five different scenarios have been studied, simulating various geophysical phenomena as disturbances on a climatological background ionosphere model. For each geophysical disturbance scenario several cases of ray-path direction or other relevant parameters are varied as listed in Table 7.3-2 below. The abbreviations used in the tables are included in the respective figures associated to the simulation scenarios. Each geophysical disturbance simulation depicted by an abbreviation identifier in Table 7.3-2 have been simulated with all the above error types in Table 7.3-1 giving a total of more than 2800 runs.

Disturbance	Parameters			Abbreviation
auroral region	Latitude 55°	Ray-path direction North-south		AR1
	Latitude 60°	North-south		AR2
	Latitude 65°	North-south		AR3
	Latitude 70°	North-south		AR4
	Latitude 65°	45° to north-south		AR5
	Latitude 65°	east-west		AR6
Electrojet	Ray-paths east-west			EE1
	Ray-paths north-south			EE2
	Ray-paths 45° to north-south			EE3
Day-night termina-tor	Ray-paths east-west			DV1
	Ray-paths north-south			DV2
	Ray-paths 45° to north-south			DV3
Travelling iono-sphere disturbance	Meridional wavelength 500 km	Zonal wavelength 0 km	Relative amplitude 10 %	TI1
	500 km	0 km	30 %	TI2
	2000 km	0 km	30 %	TI3
High gradient	Meridional gradient 20 %/10°	Zonal gra-dient 0 %/10°	Relative disturbance 10 %	HG1
	20 %/10°	0 %/10°	50 %	HG2
	50 %/10°	0 %/10°	10 %	HG3

Table 7.3-2 Parameters used in scenarios for primary EDRs.

The curves in the figures below have different thickness to indicate the different iono-sphere disturbances given in Table 7.3-2. Increasing thickness of the curve corresponds to an increasing number in the abbreviation column. For the auroral region for example scenario AR1 is represented by the very thin line while AR6, as in Figure 7.3.1.3-1, is the simulation result given by the thickest line in the figure.

7.3.1. Auroral Region (AR)

7.3.1.1. Geophysical description

Visible auroras are the most prominent and well-known feature of the auroral region. They occur roughly in an area of the ionosphere, oval in shape, centered 23 degrees from the geomagnetic poles with a width of approximately 10 degrees.

Figure 7.3.1.1-1 pictures the auroral zone as observed by the DE-1 satellite. The dark side of the Earth is the sunlit part of the planet, while the ring-shaped shaded region defines the auroral region. A nighttime phenomena (substorm) is triggered close to the inner edge of the auroral zone, resulting in growing auroral activity (dark areas) and enhanced electron densities in the lower part of the ionosphere. The bottom panel shows a cut through the auroral region with the observed variable electron density profile as function of altitude and magnetic latitude.

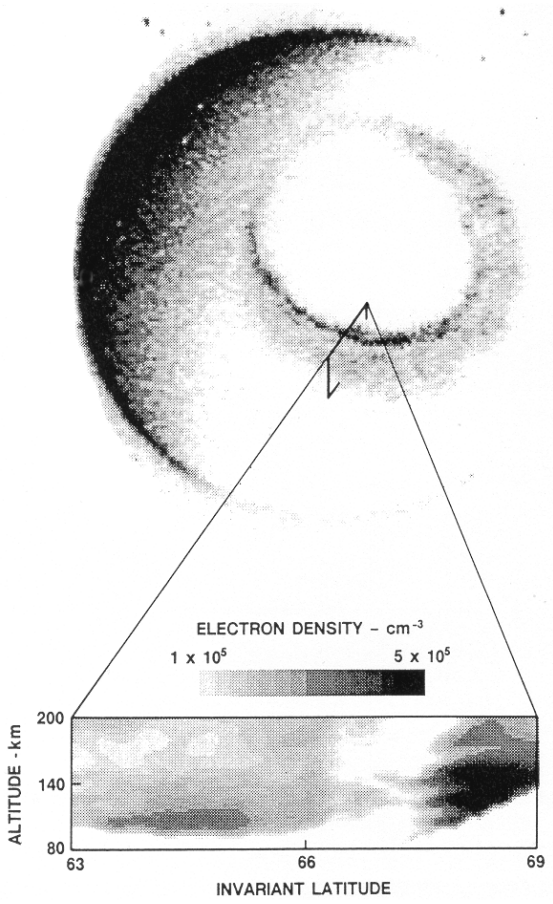

Figure 7.3.1.1-1 Picture of the auroral oval from the DE-1 satellite. The lower inserted contour plot shows the electron density distribution for the indicated meridional rectangular cut through the auroral zone [Robinson89].

The magnetic latitudes from 70° to 80°, comprising of the auroral region, defines a part of the high latitude ionosphere, where the Earth's magnetic field changes configuration from a closed field-line model to an open, having the magnetic field of the solar wind connected directly to the Earth's magnetic field. This leads to particle fluxes of electrons and ions in the energy range for the electrons from 100 eV to 500 keV. Once they pene-

trate into the ionosphere auroras of many forms are seen due to the ionization processes, resulting in large electron density variations giving rise to spatial enhanced and depleted regions.

The horizontal scale sizes of the electron density structures vary from 1 km to several 100 km. The steepness on the edges of the structures is observed to change according to the spatial auroral precipitation strength and the dynamical conditions for the plasma.

The position of these phenomena relates to the solar activity level (sunspot number), direction and magnitude of the solar wind parameters, strength of the perturbation state of the magnetosphere and the condition of the Earth's magnetic field. For strongly disturbed situations the auroral region broadens and moves toward lower latitudes, i.e. larger part of the high latitude Earth magnetic field is in an open magnetic field-line state.

The auroral region is simulated by a geographical circular electron distribution added to the background model, here chosen as the Iono3D model in EGOPS. The major features of the AR electron density distribution are defined through the following relation,

$$N_{e,Auroral} = N_0 \exp\left(-\frac{(q - q_0)^{2n}}{D^{2n}} \right) \cdot Chap(h) \qquad (7.3.1.1)$$

where $Chap(h)$ is a Chapman function as,

$$Chap(h) = \exp\left(0.5 \cdot (1 - z - \exp(z))\right), \qquad z = \frac{h - V}{H} \qquad (7.3.1.2)$$

z reflects the maximum altitude of the ionospheric region and H the scale height of the region. The choice of parameters has been fixed for the AR simulations to the following values: $q_0 = 70°$, $D = 5°$, $N_0 = 10^{11}$ electrons/m^3, $n = 8$, $z = 130$ km and $H = 20$ km. The horizontal scale size D of 5º results in a width of the auroral region of 10 degrees.

7.3.1.2. Parameters

The auroral region simulations listed in table 7.3-2 try to assess the impact of the occultation geometry on the resulting electron density profile of the auroral oval. By choosing different locations in latitude and varying the ray path direction through the auroral region, we try to estimate how sensitive the inversion algorithms are in detecting the extra electron density in the auroral oval. To simulate the auroral oval an extra electron density has been added to the background model in a circular belt around the north pole, as described above in section 7.3.1.1. This circular belt is a fair approximation of the auroral oval locally and can be used in the simulations. The simulations are performed at nighttime, where the influence of the background model is minimal.

The auroral region is in the model centered on 70° latitude with sharp edges at 65° and 75° latitude. The location of the occultation is changed from 55° latitude (AR1) to, 60° (AR2), 65° (AR3), and 70° latitude (AR4). All occultations are simulated as ideal, i.e. the ray paths follow the direction of the LEO orbit causing only a small tangent point drift. The direction of the ray paths is assumed north-south for maximum asymmetry effect.

At the edge of the auroral region (65° latitude) with maximum gradient in electron density we have also performed two simulations with different ray path directions. Ray paths going at an angle of 45° to north-south (AR5), and ray paths going directly east-west (AR6).

7.3.1.3. Results

Figure 7.3.1.3-1 shows the electron density profiles for the cases where no error sources have been applied given in Table 7.3-1. The left panel shows the absolute levels of the electron densities, while the right panel shows the electron density differences between the simulated profiles and the intrinsic model electron density profile including the disturbance.

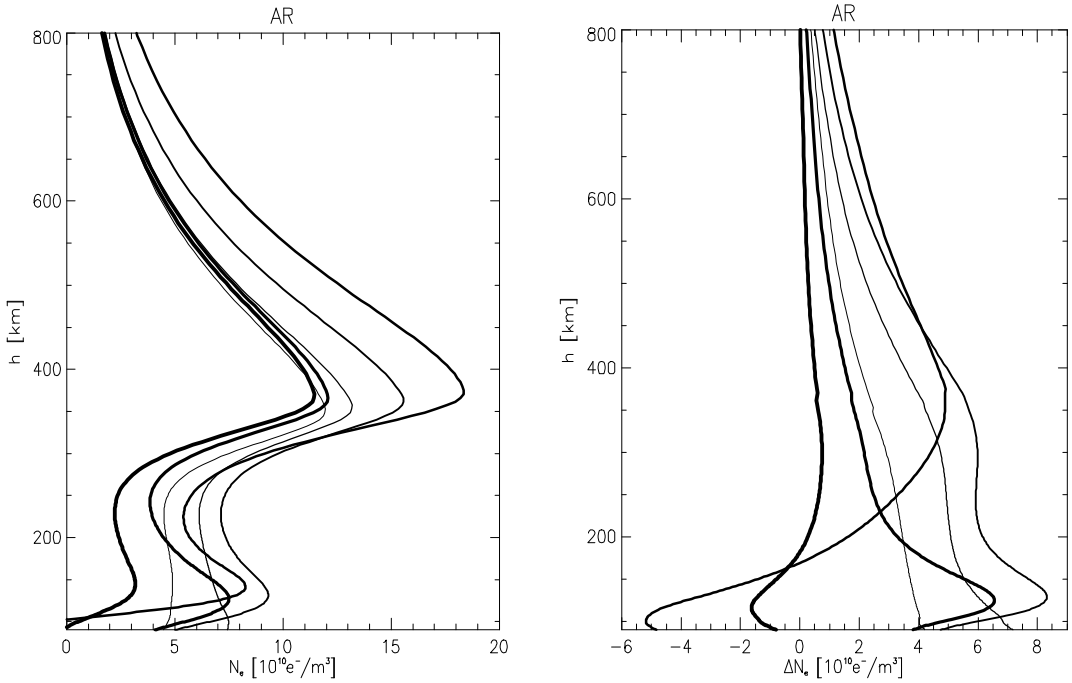

Figure 7.3.1.3-1 Absolute (left panel) and difference (right panel) electron density for auroral region scenarios, where only geometric and algorithm errors contribute to the accuracy of the electron density profile. The curves represent simulations AR1 (thinnest) to AR6 (thickest).

Figure 7.3.1.3-2 represents the received signal amplitude as function of time/height during an occultation.

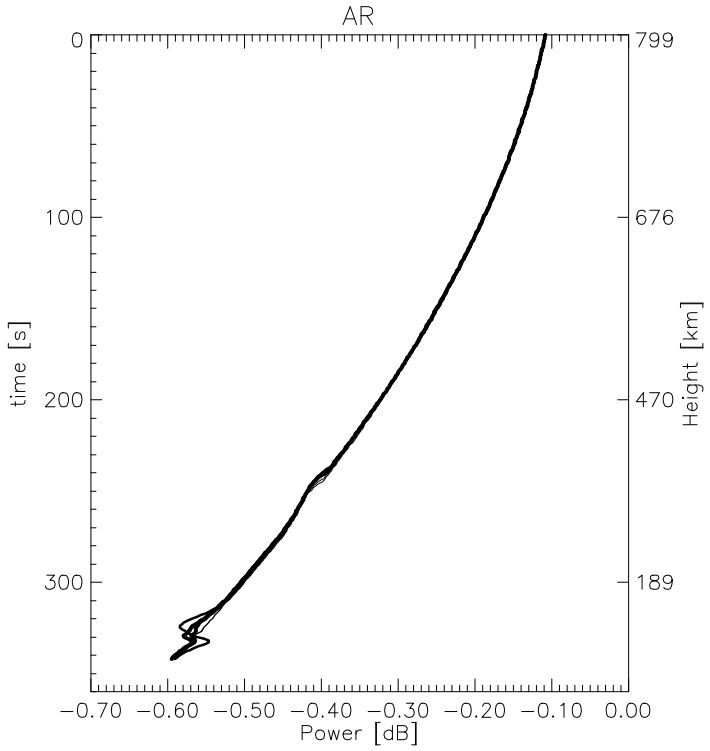

Figure 7.3.1.3-2 The amplitude of the received L1 signal for auroral region scenarios as function of time/height in a descending occultation. All six AR scenarios are plotted. There is, as it can be seen from the two y-axes, a non-linear mapping between occultation height and time.

Figure 7.3.1.3-3 shows the difference between the simulated electron density and the intrinsic model electron density with errors added from Table 7.3-1.

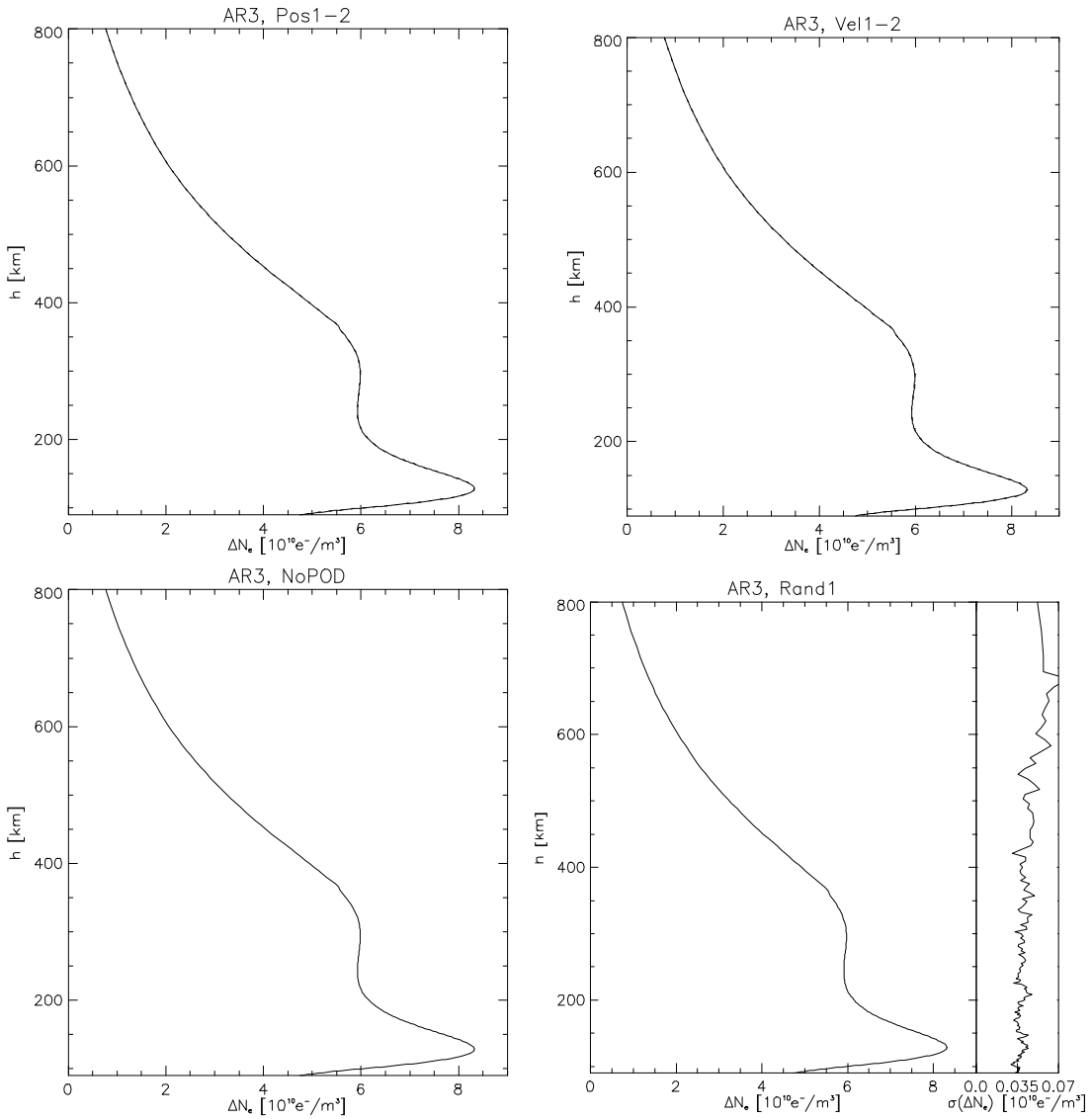

Figure 7.3.1.3-3 Electron density difference plots for the auroral region scenarios. Top left for position errors, top right velocity errors, bottom left no POD and bottom right random error rand1 on phase (where left panel is the mean value and the right the standard deviation). Only curves corresponding to the AR3 disturbance are plotted in this figure.

7.3.1.4. Discussion

Introducing the error types given in Table 7.3-1 in each separate simulation has very little influence on the derived electron density profile, see figure 7.3.1.3-3. This implies that only the geometry of the occultation (ray-path direction) and the ionospheric state are of importance for occultations in and around the auroral region. The same result is deduced from the very small standard deviation of the electron density difference curves when applying random error types to the simulations.

For all the disturbance values, the derived electron density error is below $8.5 \cdot 10^{10}$ electrons/m^3. Above the F2-region peak we see a decrease in the error estimate for the electron density profile. Above 400 km this amounts to half the error in the lower ionosphere.

Figure 7.3.1.3-1 reveals that occultations closer to the southern boundary of the auroral zone leads to increases in the electron density error (AR1-AR3). For occultations that scan the auroral zone (AR4) the error has the larger vertical variations, especially below 400 km. Scanning just south of the auroral zone, but at different angles with respect to the auroral zone (AR4, AR5 and AR6), decreases the error when the rays approach the east-west direction. The AR6 situation exerts the least error of the auroral region simulations totaling $2 \cdot 10^{10}$ electrons/m^3.

The power of the signals is seen to decrease smoothly with time (i.e. with altitude), with only some very minor deviations during the last 10 seconds of the occultation (Figure 7.3.1.3-2). The drop in signal power over the entire occultation is about 0.5 dB.

7.3.2. Equatorial Electrojet (EE)

7.3.2.1. Geophysical description

The eletrodynamical features of the equatorial zone are different from the high latitude auroral oval physics. The auroral electrojet is driven by the dawn-dusk magnetosphere electric field caused by the solar wind interaction with the magnetosphere of the Earth and the particle precipitation. While the equatorial electrojet mostly is driven by the forcing due to the solar heating of the thermosphere and the terminator charge density changes at dawn and dusk. Especially the high wind velocities observed in the post-sunset period are directly linked to the latter, together with the decay of the electron density in the lower part of the ionosphere.

The direction and magnitude of the electric field together with the pressure terms in the equations of motion cause the following morphology for the electrojet.

- The peak eastward electrojet drift at night is twice as large as the peak westward drift during the day.
- Zonal velocities are much larger than the vertical.
- Vertical drift is often strongly enhanced just after sunset (A similar feature is not observed near sunrise).

The zonal component of the electric field of the equatorial electrojet is small but very important since it causes the plasma to move vertically. This motion greatly affects the plasma density and makes the plasma interact with quite different neutral densities as it changes altitude. It strongly inflicts on the recombination rates and in turn the plasma content. The result of this is slowly growing plasma instabilities, which together with the

electron density gradients and shear velocities lead to a highly disturbed F region conditions, causing phenomena as plasma bubbles. Figure 7.3.2.1-1 shows radar and satellite observations during such an event. Rapidly rising plumes of strongly enhanced plasma give radar backscatter echoes all the way down to a few meter wavelength. Wedge-shaped depleted plasma density structures with walls aligned along the magnetic meridian plane cause strong plasma irregularities producing enhanced scintillations from the region [Basu85].

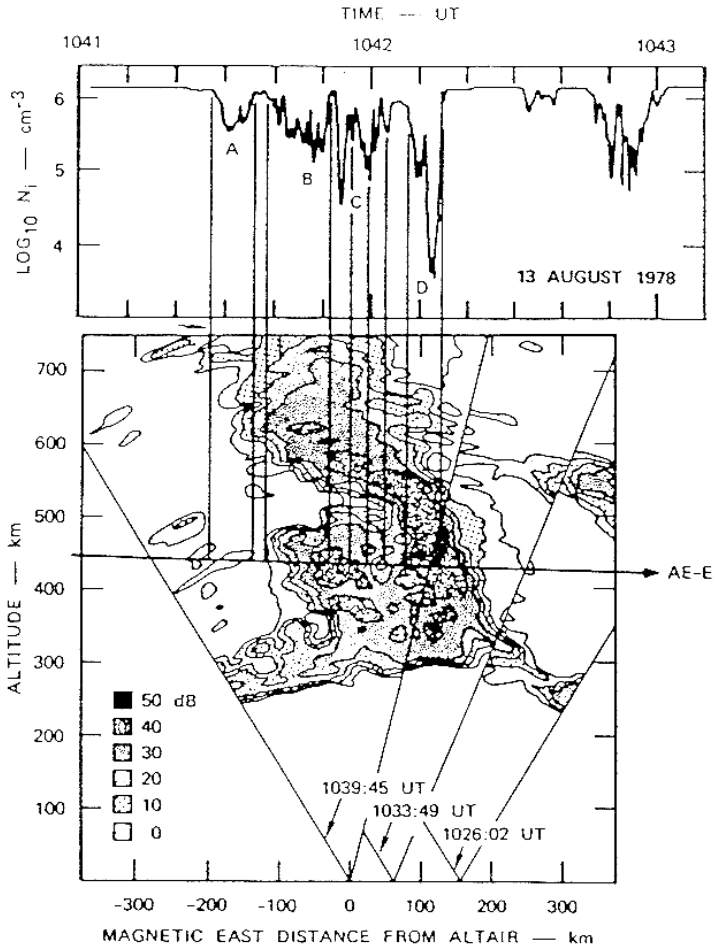

Figure 7.3.2.1-1 Simultaneous backscatter power map of one meter irregularities (lower panel) measured with the ALTAIR radar and AE-E satellite measurements of the equatorial plasma density depletions (top panel) in the 450 km altitude region when traversing the plasma bubble [Tsunoda82].

Another feature of the F region irregularities is the spread-F observed by ionosondes and HF radars. The term is associated with a broad range of plasma irregularities, from the meter scale range of the wavelengths of the irregularities to several hundreds of kilome-

ters. The wave generation processes are generally believed to be related to seed electron density perturbations, upward gradients in the electron density profile and enhanced electric fields. But also the gravity wave breaking could lead to onset of equatorial spread-F phenomena and scintillations [Basu85] [Kohl].

7.3.2.2. Parameters

The large-scale equatorial electrojet phenomena are build into the ionosphere model in our simulation tool EGOPS. By examining regions near the magnetic equator in the solar illuminated sector, we have identified an enhancement of electron density caused by an equatorial electrojet. Three general simulations have been performed, by varying the ray path direction going through this electrojet enhancement.

The tangent point is located at approximately 5° latitude north and 27° longitude, UT time equals 13 hours and the month chosen is April. Solar maximum conditions are assumed $F_{10.7}$ = 200. Ray path directions are assumed east-west (EE1), north-south (EE2) and at an angle of 45° to north-south (EE3). As in the auroral region scenarios ideal occultations have been used.

7.3.2.3. Results

Electron density profiles for the cases without any errors from Table 7.3-1 are seen in Figure 7.3.2.3-1.

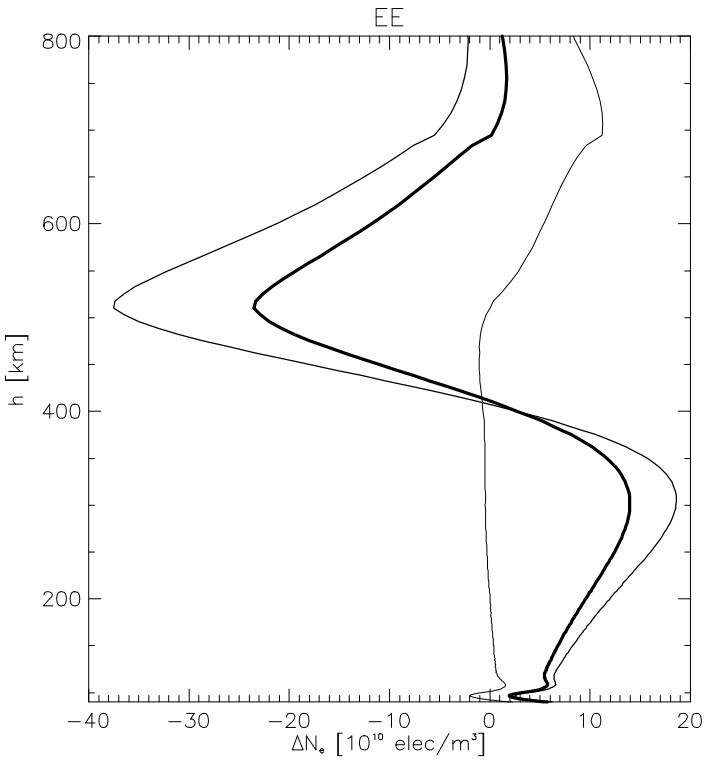

Figure 7.3.2.3-1 Electron density difference for electrojet scenarios. Curves are EE1 (thin) to EE3 (thick).

In Figure 7.3.2.3-2 the power of the received signals is determined as a function of time/height.

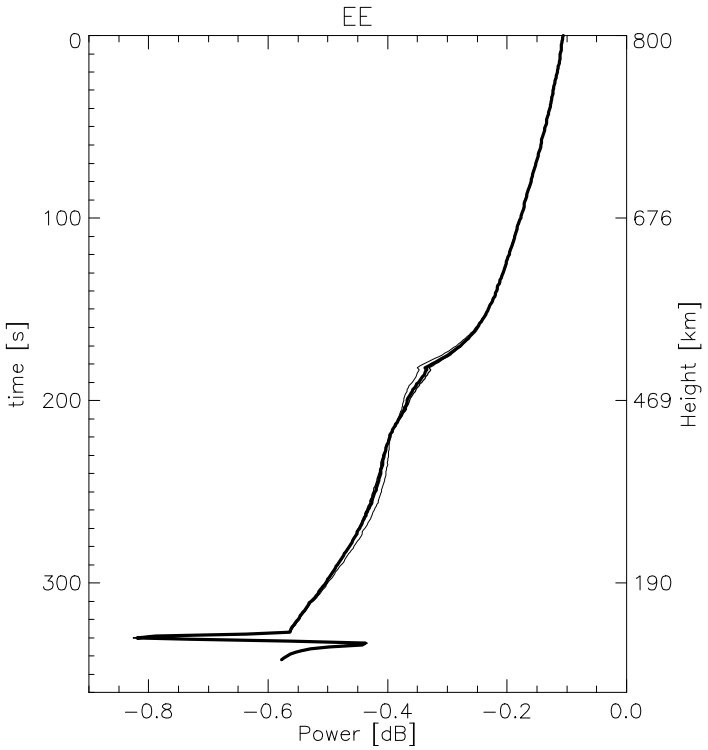

Figure 7.3.2.3-2 Amplitude of received L1 signal as a function of time/height for the electrojet scenarios. EE1 (thin) to EE3 (thick).

In Figure 7.3.2.3-3 the electron density errors are plotted with errors added from Table 7.3-1.

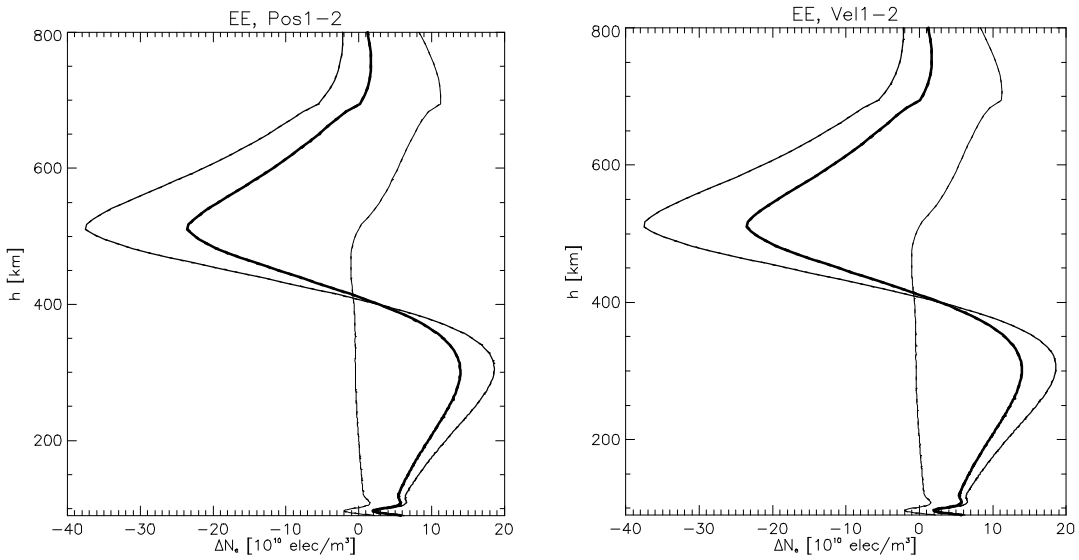

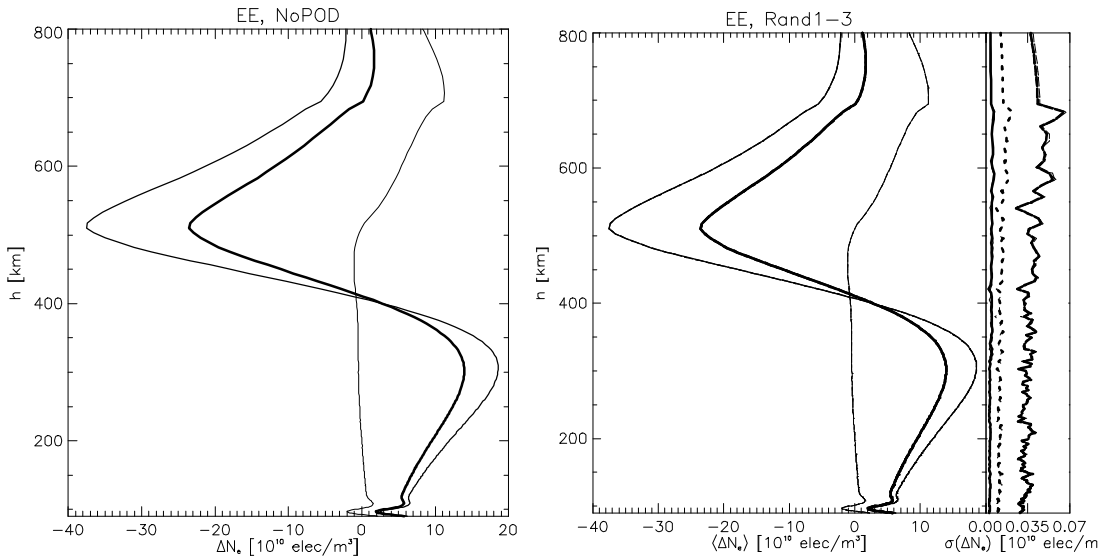

Figure 7.3.2.3-3 Electron density difference plots for the Electrojet scenarios. Top left for position errors, top right velocity errors, bottom left no POD and bottom right random error on phase (where left panel is the mean value and the right the standard deviation). The difference between the mean and standard deviation calculated for each of the three random errors rand1 to rand3 is so small that it can not be seen from the plot in the bottom right panel. Curves are EE1 (thin) to EE3 (thick) and solid line for error one, dotted for error two and dashed for error three.

7.3.2.4. Discussion

For all three disturbances the electron density error stay below $4 \cdot 10^{11}$ electrons/m^3. Especially the disturbance EE1 (thin line) stays very low.

Almost identical electron density difference curves are seen for the four different errors. The standard deviation for the random error runs is very small, but largest for Rand3 (about $0.035 \cdot 10^{10}$ electrons/m^3). A general tendency is observed neither in the error of the electron density difference profile nor in the standard deviation plots.

The geometry of the occultation and the parameters of the disturbance are the governing factors, since applying errors does not change the electron density profiles (Figure 7.3.2.3-3). Ray paths at altitudes above 700 km gives the smallest errors for the EE2 and EE3 situations. While the electron density error is the lowest for the EE1 situation at heights lower than 500 km. The largest error ($3.7 \cdot 10^{11}$ electrons/m^3) are observed for conditions when the direction of the impact height path changes to a more north-south alignment (EE3 to EE2). The error profile for the EE2 and EE3 simulation are very similar. Multiplying EE3 with a scaling factor equal to 0.6 makes the profiles (EE2 and EE3) coincide.

The power of the received signals (see Figure 7.3.2.3-2) decreases rather smoothly for most of the occultation time with about 0.5 dB. During the last 30 s the electrojet feature is clearly seen in the amplitude plot.

7.3.3. Electron density variations (day-night terminator) (DV)

7.3.3.1. Geophysical description

Around the dawn and dusk terminator large spatial variations are observed in the electron density profiles as the result of the presence or absence of solar ionization and motion of the plasma. Figure 7.2.1.2-8 depicts in the lower panel the longitudinal changes of the peak electron densities in the E and F region, taking into account the decrease in the solar radiation in the dusk sector at mid-latitudes and the plasma composition and density.

Two effects enhance each other. The solar flux changes as function of time and latitude due to the rotation of the Earth, giving rise to a gradually changed ionization with respect to height (starting in high altitudes in the F region and terminating in the lower heights of the E region). Together with the different recombination processes of the plasma in the E and F region variable time scales of the electron density decrease as function of altitude are observed.

The most abundant ions of the F region are O^+, H^+ and NO^+. But O^+ dominates the total ionization decay process. The time for the F region to decrease to 0.3 times the original density is of the order of 200 minutes. While the time scale for the E region is about 20 minutes. Here the more dense plasma and the ions O_2^+, N_2^+ and NO^+ dictate the much faster recombination rates. The result is varying gradients in the refraction as function of altitude and horizontal direction. An effect which causes errors in the occultation retrieval estimate of the electron density profile.

7.3.3.2. Parameters

In the variations of electron density scenario we have chosen to simulate the day-night terminator conditions at solar maximum ($F_{10.7}$ = 200), a worst case scenario in order to estimate the retrieval errors. At UT time 18.02 the terminator is identified in the ionosphere model at 90° longitude. Latitude is set to 2° north for maximum electron density in the F-layer, the month is set to April.

Three different ray path directions through this solar maximum day-night terminator have been simulated using ideal occultations as described for the auroral region scenario, sec-

tion 7.3.1.2. Ray path directions are assumed east-west (DV1), north-south (DV2) and at an angle of 45° to north-south (DV3)

7.3.3.3. Results

In Figure 7.3.3.3-1 the electron density difference is seen for the case with no errors from Table 7.3-1 added.

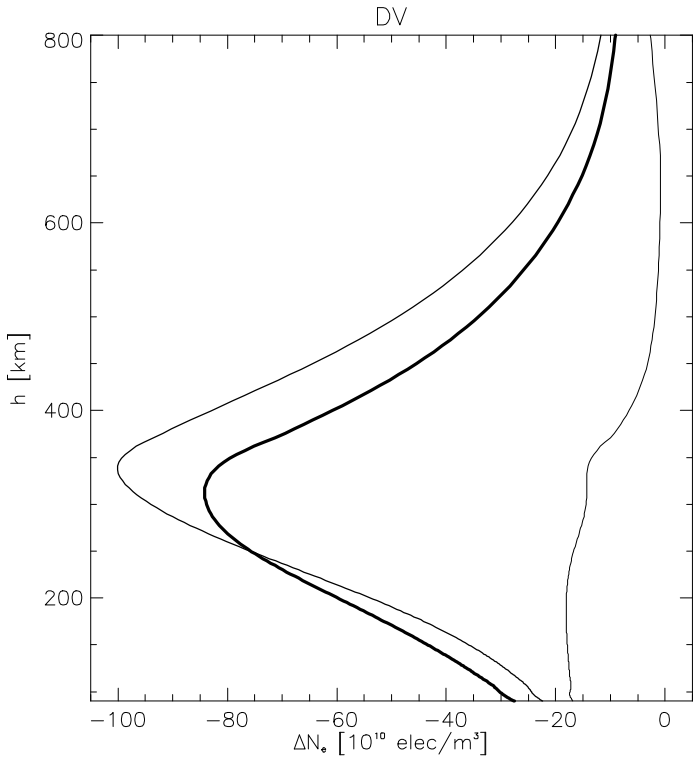

Figure 7.3.3.3-1 Electron density differences for electron density variation scenarios. DV1 (thin) to DV3 (thick).

In Figure 7.3.3.3-2 the received signals are plotted as function of time/height.

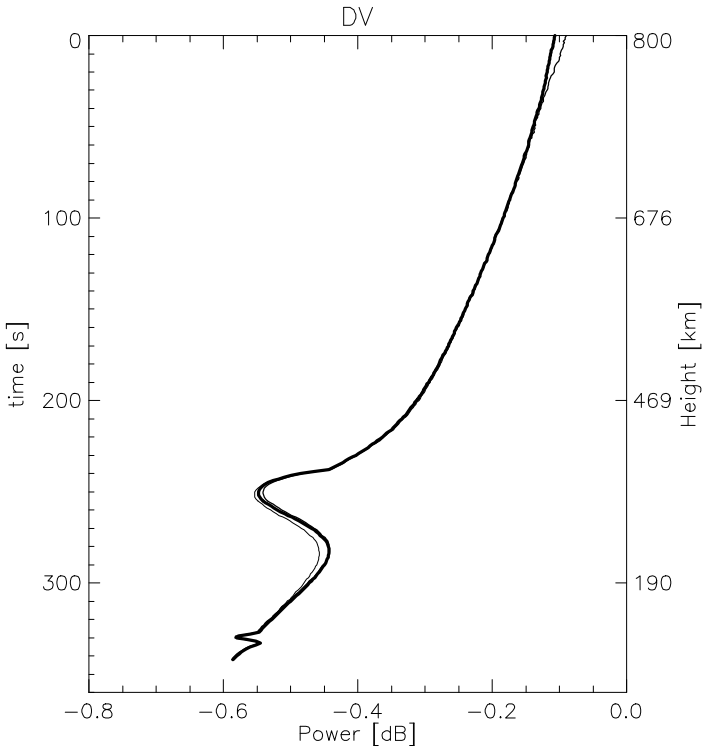

Figure 7.3.3.3-2 Amplitude of received L1 signal for density variation scenarios. Disturbances DV1 (thin) to DV3 (thick).

Figure 7.3.3.3-3 contains electron density error plots for the different error cases (errors from Table 7.3-1).

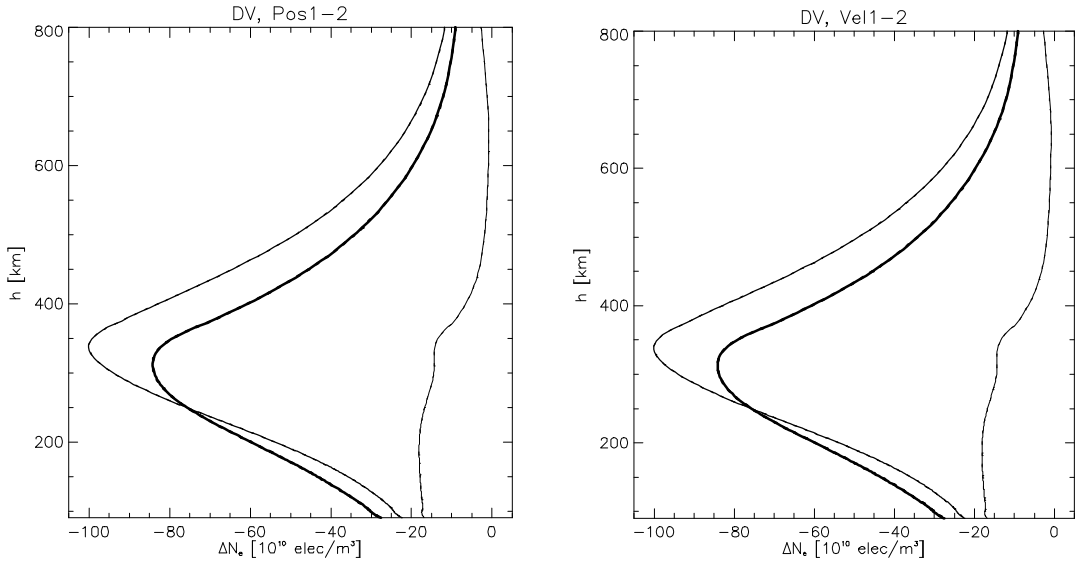

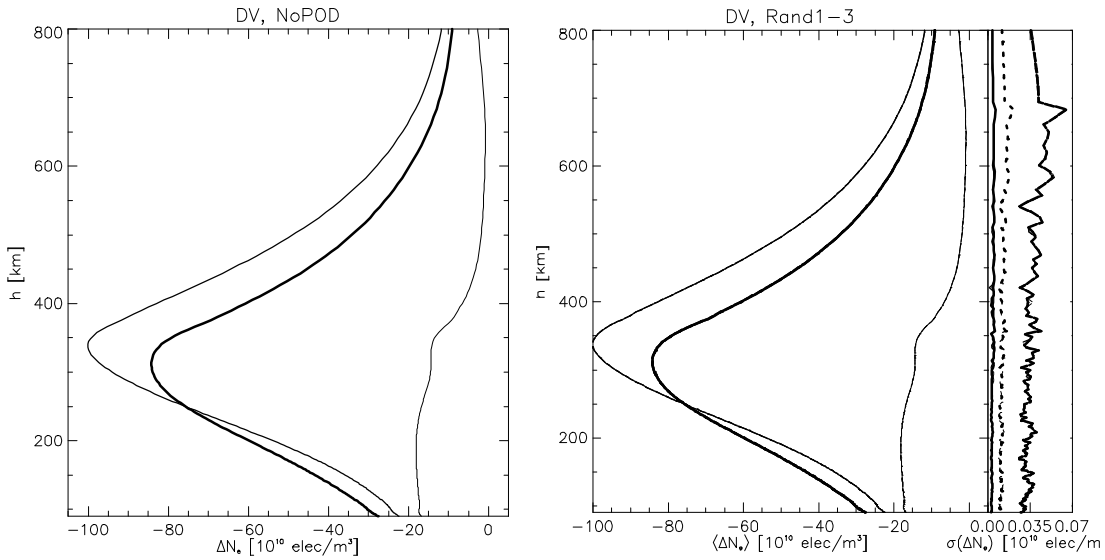

Figure 7.3.3.3-3 Electron density difference plots for the density variation scenarios. Top left for position errors, top right velocity errors, bottom left no POD and bottom right random error on phase (left panel is the average value and right panel the standard deviation). If more different errors are plotted, error one is the solid line, error two dotted and error three dashed.

7.3.3.4. Discussion

In Figure 7.3.3.3-1 a rather large electron density difference is seen for especially DV2, reaching about 10^{12} electrons/m^3 at 350 km. DV1 shows only rather small errors, but this is expected since the rays are perpendicular to the gradient. When the ray paths are parallel to the gradient (DV2) the errors are the largest. DV2 and DV3 are rather similar, just scaled and DV3 having a slightly larger error at low altitudes below 200 km. That DV2 and DV3 are rather similar suggests that a small error is only reached when the rays are close to being perpendicular to the gradient.

Like in the previous scenarios only the geometry is of any importance since all four plots in Figure 7.3.3.3-3 are very similar and the standard deviation for the random noise is very small (at largest $0.07 \cdot 10^{10}$ electrons/m^3).

The power decreases with time, only showing a minor bump about 250 s into the occultation, probably due to defocusing by the density variation.

7.3.4. Travelling Ionosphere Disturbance (TI)

7.3.4.1. Geophysical description

Spatially separated radars and ionosondes have been able to observe wave-like electron density structures in the ionospheric F region. This phenomenon is called a Travelling Ionospheric Disturbance (TID) since the perturbations move with velocities ranging from 100 ms^{-1} to 700 ms^{-1}. The motion for the long horizontal waves is often from polar latitudes towards equator, indicating the source region to be related to the auroral oval and geomagnetic activity at high latitudes. The cause of these large-scale electron density variations is gravity waves in the neutral gas originated from the lower neutral dense troposphere. Gravity waves are primarily a phenomenon of the neutral air. But the motion can be transferred to the ionized gas through the collisions between ions, electrons and neutral particles. At F region altitudes collision frequencies are much smaller than the gyro frequency, which is a function of the Earth's magnetic field intensity. The result of this is an ion and electron motion along the direction of the Earth's magnetic field equal to the gravity wave component along the same direction. Ions and electrons motion across the geomagnetic field is inhibited when no ambient electric field is present (the plasma is magnetized). Thus the ionospheric response to the gravity waves is biased, which not in a simple manner reproduce the motion of the neutral wave.

TIDs are frequently observed at middle and high latitudes with the major horizontal velocity component towards equator.

The wavelengths of TIDs fall into two groups. The *low frequency TIDs* with periods from 30 minutes to a few hours have horizontal wavelengths of a few thousands km. The sources of these waves are related to auroral region phenomena. These waves propagate almost vertically, while the neutral particle motion being nearly horizontal. The *shorter period waves* (15-30 min) have horizontal sizes of 100-500 km. Their wavefronts are tilted at about 30 degrees to 45 degrees to the vertical. The waves leading to these TID phenomena are likely generated by meteorological phenomena as thunderstorms and jet-streams.

7.3.4.2. Parameters

The TID simulations listed in table 7.3-2 try to assess the impact of both the shorter horizontal waves and the long wavelength TIDs (disturbance setup named TI3). The relative amplitude of the TID has been fixed to either 10 %, which is close to a horizontal situation (TI1) or to 30 % variation, representing a worst case condition (TI2 and TI3).

The TID model simulations consist of harmonic waves with meridional and zonal horizontal wave components. The amplitude peak (relative amplitude) is set at 250 km altitude with decreasing amplitudes below and above this height. Steeping of the wavefronts with increasing heights has been included.

Below follow the simulation results for the two situations, 1) applying the TID only and 2) the simulations when both the error scenarios given in table 7.3-1 and the TID are applied.

7.3.4.3. Results

In Figure 7.3.4.3-1 the error on derived electron density profiles is plotted in the case when no errors from Table 7.3-1 are added.

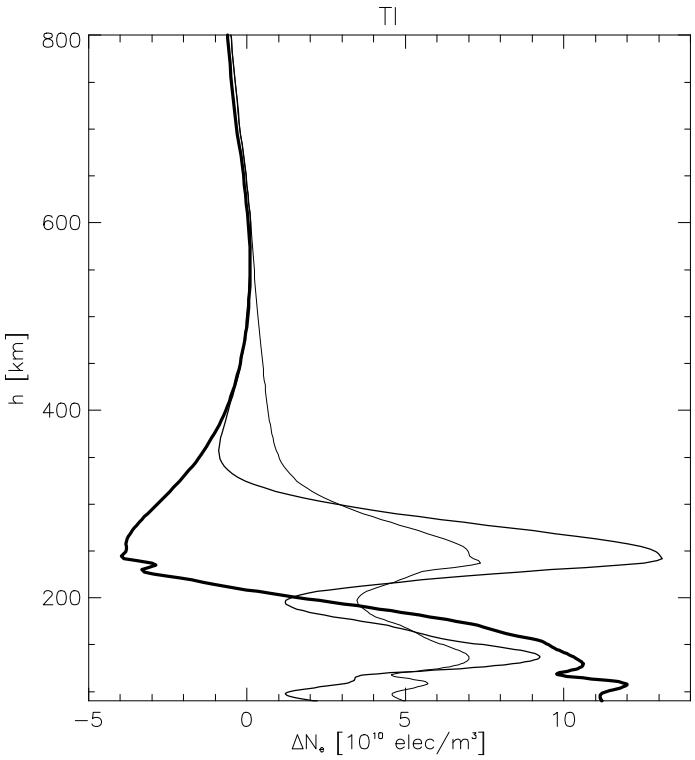

Figure 7.3.4.3-1 Electron density differences for traveling ionosphere disturbance scenarios. Curves are TI1 (thin) to TI3 (thick).

The next graphs (Figure 7.3.4.3-2) show the power of the signal as a function of time/height, plotted for the case with no errors.

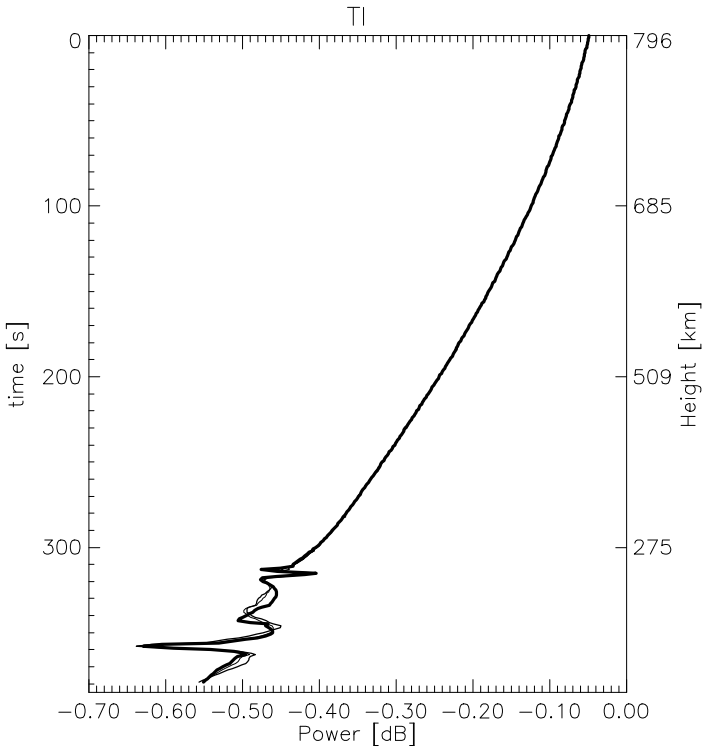

Figure 7.3.4.3-2 Amplitude of received L1 signal for traveling ionosphere disturbance scenarios. TI1 (thin) to TI3 (thick).

Adding the errors given in Table 7.3-1 to the simulations give derived electron density profiles uncertainties as seen in Figure 7.3.4.3-3.

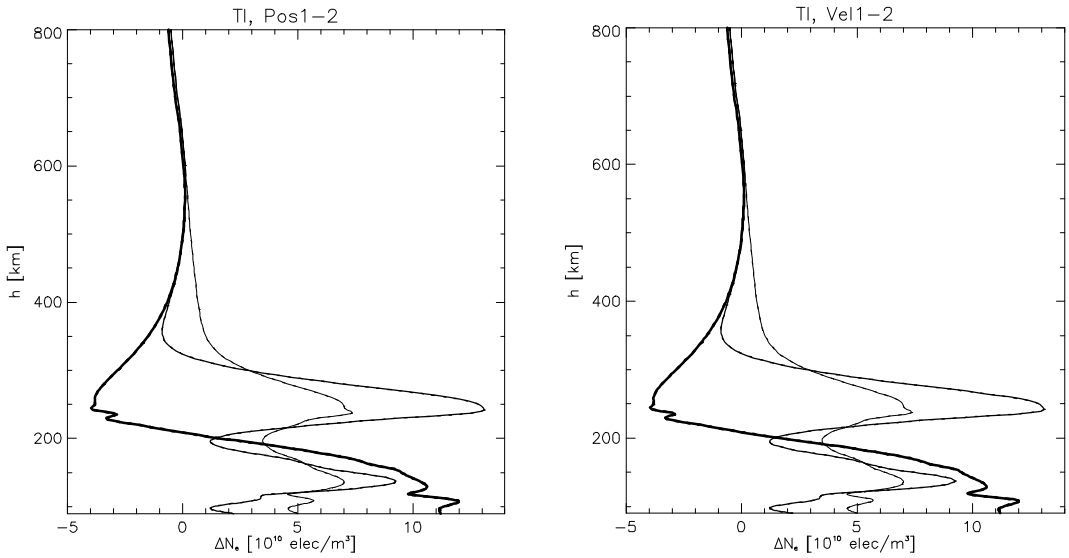

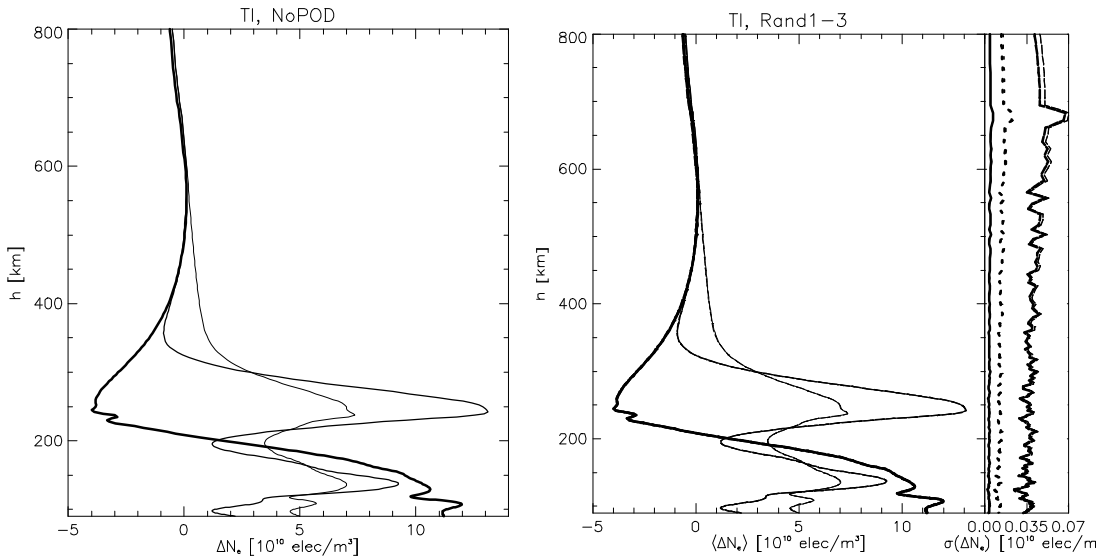

Figure 7.3.4.3-3 Electron density difference plots for the Traveling Ionosphere Disturbance scenarios. Top left for position errors, top right velocity errors, bottom left no POD and bottom right random error on phase (left panel is average value and right panel standard deviation). Error one is solid line, error two dotted and error three dashed.

7.3.4.4. Discussion

No significant differences between the electron density difference profiles derived for the different errors are found. And the standard deviation in the random error case is at the same size as the ones found for the previous disturbances.

Below 400 km large fluctuations in the derived electron density error profile are seen, with errors up to $13 \cdot 10^{10}$ electrons/m^3, but still similar for the different error-types. That adding errors has no influence indicates that only the geometry of the occultation and the magnitude of the disturbance is of any significance. This is further strengthened by the fact that the standard deviation in the random error scenarios is very small, below $0.07 \cdot 10^{10}$ electrons/m^3.

From TI1 to TI2 the relative amplitude is increased and this is reflected in larger amplitudes of the derived errors in the electron density profile. From TI2 to TI3 the meridional wavelength is increased by a factor four, making the error profile have variations over larger scales but keep the large amplitude of the error. In all cases the error is very small (below $1 \cdot 10^{10}$ electrons/m^3) above 400 km.

The power of the received signals shows a rather smooth decrease with about 0.5 dB over the entire occultation. No strong features are seen, but a very small peak at about 310 s and a slightly increased damping at the last 10 s of the occultation.

7.3.5. Ionosphere High Gradient Disturbance (HG)

7.3.5.1. Geophysical description

The high gradient disturbance scenario is meant to be a generic simulation of all the geophysical conditions covering phenomena as, aurora and patches (in the high latitude ionosphere) and bubbles (in the equatorial zone), leading to high horizontal refractivity gradients. The scenario cases mimic various gradients and horizontal features in the ionosphere for a set of selected latitudes and longitudes.

The electron density of the HG model is superimposed onto the climatological ionosphere model.

7.3.5.2. Parameters

The main parameters are as listed in Table 7.3-2, while the simulated error terms are as in Table 7.3-1. The ionosphere high gradient disturbance (HG) simulations try to assess the impact of both low and high meridional gradients. The relative disturbance of the HG has been fixed to either 10 %/10° (HG1 and HG3) or to 30 %/10° variation (HG2). The zonal gradient has been set to 0 %/10° in all of the simulations.

Below follow the simulation results for the two situations when 1) applying the HG only and 2) the simulations when both the error scenarios given in table 7.3-1 and the HG are applied.

7.3.5.3. Results

Results of the simulations are seen in Figure 7.3.5.3-1 when no errors from Table 7.3-1 is added.

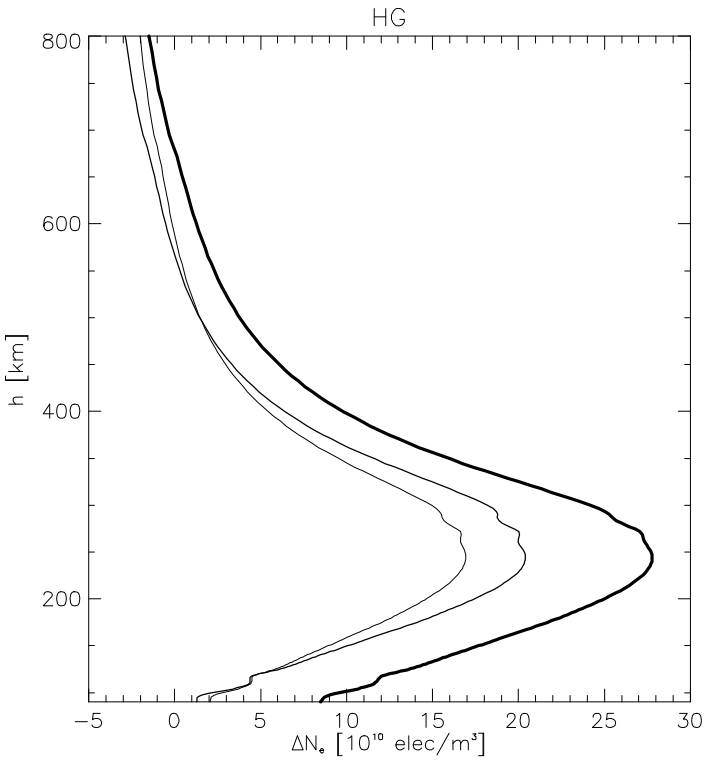

Figure 7.3.5.3-1 Electron density differences for high gradient disturbance scenarios. The curves are for HG1 (thin) to HG3 (thick).

Figure 7.3.5.3-2 shows the amplitudes of the received signals as a function of time/height.

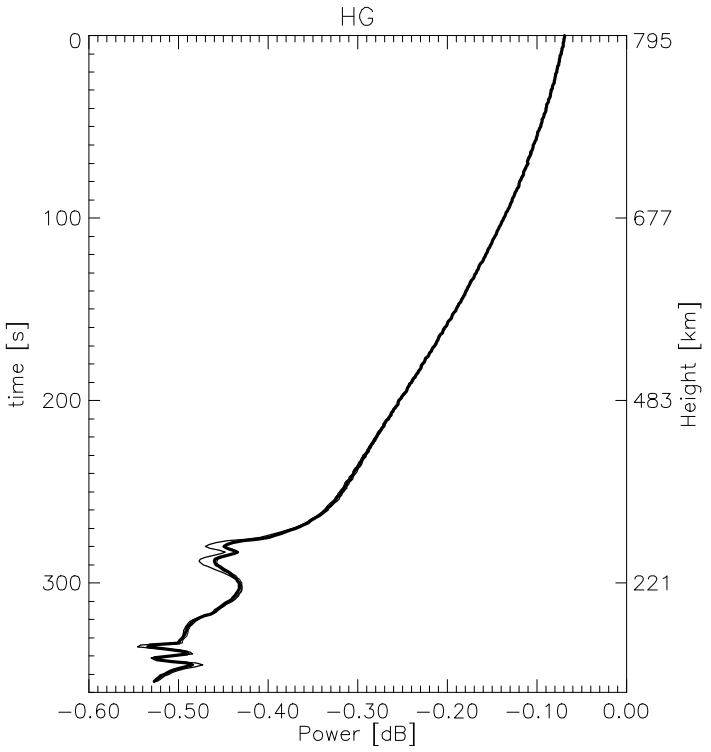

Figure 7.3.5.3-2 Amplitude of received L1 signal for high gradient scenarios. Curves are for HG1 (thin) to HG3 (thick).

Figure 7.3.5.3-3 shows the electron density error for the four different error cases (position, velocity, clock and random error on phase).

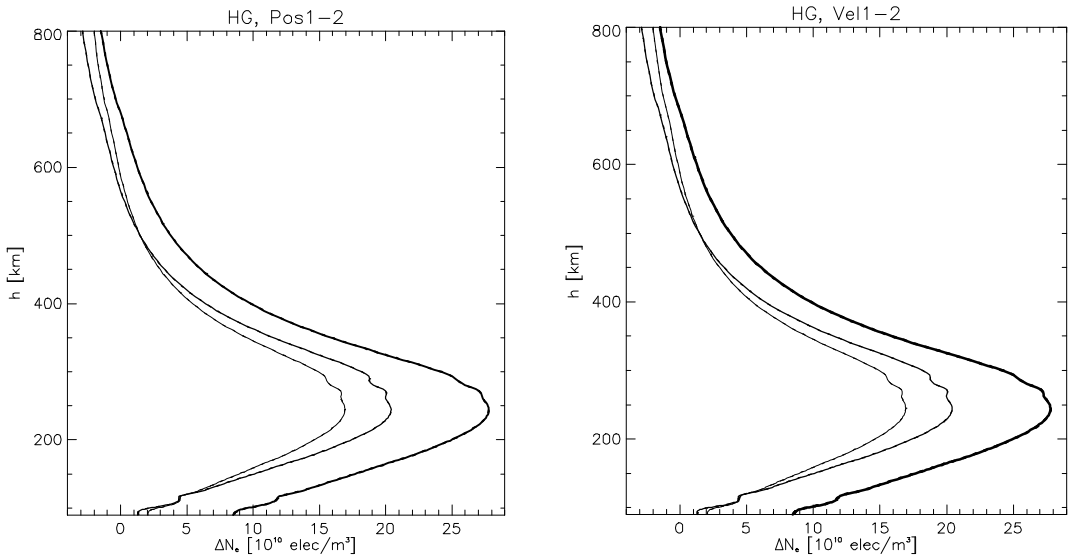

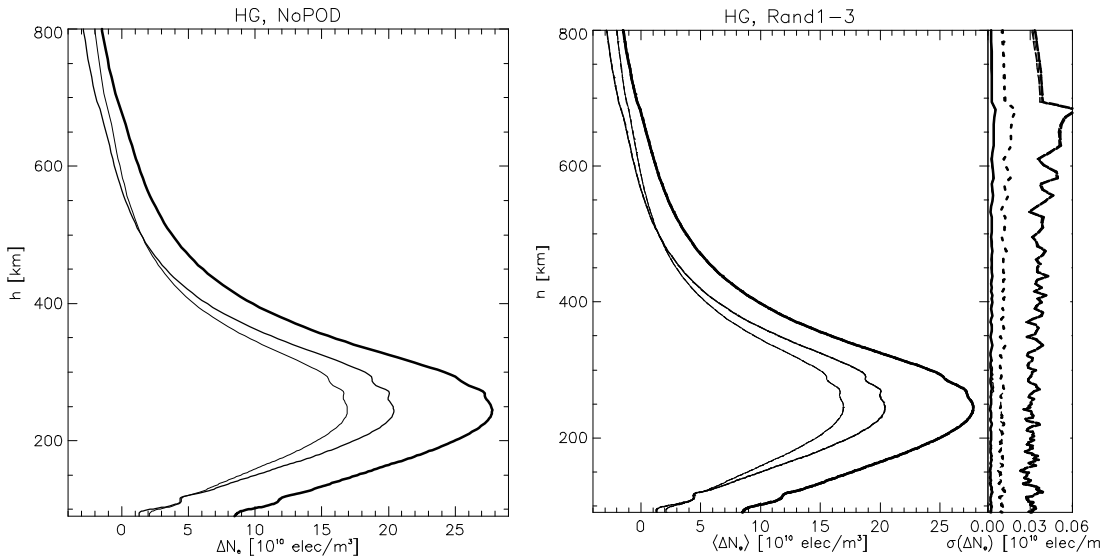

Figure 7.3.5.3-3 Electron density difference plots for the high gradient scenarios. Top left for position errors, top right velocity errors, bottom left no POD and bottom right random error on phase (left panel is average and right panel standard deviation). Error one is solid line, error two dotted and error three dashed.

7.3.5.4. Discussion

Again all the derived electron density difference profiles are all very similar for the different applied errors, implying that the applied errors are of almost no significance. This is further strengthened by the very small standard deviation in the random error scenarios (less than $0.06 \cdot 10^{10}$ electrons/m^3).

For the three disturbances (HG1-HG3) the errors of the derived electron density profiles are rather similar. Enhancing the relative disturbance (comparing HG1 and HG2) only increases the error at the peak value at 250 km from $1.7 \cdot 10^{11}$ electrons/m^3 to $2.0 \cdot 10^{11}$ electrons/m^3. Increasing the meridional gradient (comparing HG1 and HG3) increases the error at all altitudes, but most at the peak value having a maximum error of $2.8 \cdot 10^{11}$ electrons/m^3.

The power of the received signal is dropping smoothly with about 0.5 dB over the time of the occultation, corresponding to about 350 s. Some minor features are seen.

7.3.6. Derived HmF2 and HmE

The derived altitudes and electron densities of the peak value of the F2 layer in the scenarios are plotted in Figure 7.3.6-1. The spread of the derived HmF2 for each set of scenarios leads to a shift of about 15 km of the HmF2 estimate.

The largest changes in HmF2 are observed in the electrojet and high gradient scenarios – the large change seen in the auroral region scenarios is of no real significance since the position of the occultation is moved between the different scenarios while the auroral region is kept fixed. The height and electron density of the F2 layer is seen to increase when the auroral region is approached (+1 to +4). For the electrojet the altitude of the F2 peak is highest when the rays paths are east-west and lowest when they are north-south. For the traveling ionosphere disturbance two scenarios give almost identical results, namely the two with the same meridional wavelength. For the high gradient scenarios almost the same HmF2 is derived, but the electron density is varying. Highest HmF2 the ray paths are east-west and lowest when they are north-south. The same is the case for the density variation scenarios.

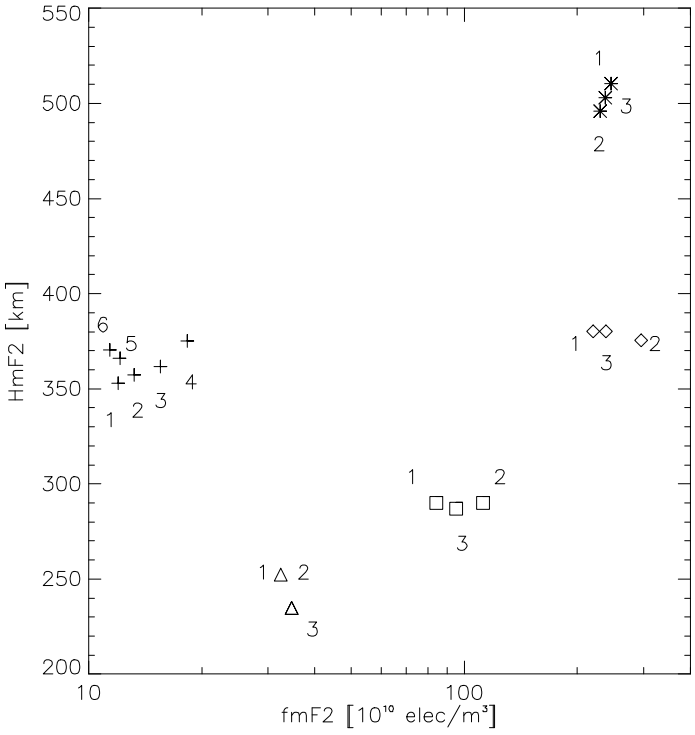

Figure 7.3.6-1 Altitude and electron density for the F2 layer for the different scenarios. + for AR, * for EE, ◊ for DV, Δ for TI and ? for HG. Numbers are corresponding to the numbering in each scenario (Table 7.3-2).

7.3.7. Results of simulations on electron density profiles

We have simulated a total of 5 different geophysical scenarios with error terms added from random fluctuations and from determination of position and velocity for both the LEO and the GNSS satellite. Also the geometry of the occultation have been studied in the simulation runs. In total we have performed more than a 1000 simulations for the

primary EDR evaluation to estimate the uncertainty of the inverted electron density profiles.

All scenario runs show that the derived electron density profiles are insensitive to both expected level of random errors and to POD errors. Indeed the simulations clearly show that the navigation solutions is a sufficient measure of the LEO position and velocity. The strength of the occultation technique when measuring electron density profiles results from the use of the difference between the phase delays of L1 and L2 (N_e is derived by inversion of the occultation *TEC*). In this way almost all errors are subtracted from the measurement. The power of the signal is seen to decrease by only about 0.5 dB when travelling through the ionosphere in the absence of scintillations.

The simulations show that the dominant error contribution on the derived electron density results from the asymmetry of ionosphere coupled with the geometry of the occultation. Our baseline inversion algorithm derives the electron density profile based on the measurement of a single occultation. By coupling the information from several occultations occurring simultaneously using Tomographical techniques will reduce the error in regions with high asymmetry.

7.3.8. Primary EDR table

The error assessment in the presiding sections on the primary EDR values are summarized in the following table. The nominal threshold value is here defined as a representative average value. The conditions, for which the nominal threshold values and worst case threshold values are found, are listed in column 5 and 7 of table 7.3.8-1. These values can also be found in primary tables 1 and 2 in appendix D.

EDR parameter Uncertainty.	Thresholds	Objectives	Nominal Threshold	Nominal condition	Worst case Threshold	Worst case condition
Slant path TEC	3 TECU	1 TECU	<1 TECU	Night time, not solar max.	~3 TECU	Solar max. day time.
Electron density profile	10^5 cm^{-3}	10^3 cm^{-3}	~10^4 cm^{-3}	Mid-latitudes with spherical symmetry, not solar max.	~10^5 cm^{-3}	Large spherical asymmetry (terminator), solar max.
HmF2 (height of the F2 peak)	20 km	5 km	~5 km	Mid-latitudes with spherical symmetry with 1 Hz sampling	~20 km	Large spherical asymmetry
HmE (height of the E layer peak)	10 km	5 km	~5 km	Mid-latitudes with spherical symmetry with 1 Hz sampling	~10 km	Large spherical asymmetry
Scintillation index S_4	0.1			Equator at local time 20-24		Auroral region, magnetic storm
Scintillation index σ_φ	0.1 radian			Equator at local time 20-24		Auroral region, magnetic storm

Table 7.3.8-1 Primary EDR values.

7.4. Simulation results for secondary EDRs

The influence of different error types on the retrieved temperature profiles have been investigated. All the simulations are dry air simulations using the modified MSIS90 atmosphere model. Most of the profiles show the difference between the retrieved parameter and the originally used MSIS90 parameter. The bending angle retrieval and Abel Transform described earlier has been used in all simulations to retrieve EDRs. The error type, sampling rate and other parameters are summarized in Table 7.4-1 below.

Error type	No. of runs	Error size	Sampling rate	Abbreviation
Position	1	0.1 m	50 Hz	Pos1
	1	0.3 m	50 Hz	Pos2
	1	1.0 m	50 Hz	Pos3
Velocity	1	0.1 mm/s	50 Hz	Vel1
	1	0.3 mm/s	50 Hz	Vel2
	1	1.0 mm/s	50 Hz	Vel3
Clock error, 1 sec Allan dev.	50	10^{-12}	50 Hz	Clock1
	50	10^{-13}	50 Hz	Clock2
Gaussian noise on phase	50	0.3 mm	10 Hz	Rand1
	50	1.0 mm	10 Hz	Rand2
	50	0.7 mm	50 Hz	Rand3
	50	2.2 mm	50 Hz	Rand4

Table 7.4-1 Errors used in scenarios for secondary EDRs.

The retrieved temperature profiles in these simulations are in general found with a relative high error ($\Delta T \geq 1$ K) at altitudes above 20 km. Applying a statistical optimization algorithm, currently under development and described in chapter 6, will improve the retrieved temperature profile substantially. Preliminary results indicate the improvement to be varying with a factor from 5 to 10.

In chapter 7.4.5 the method has been tested for the tropopause disturbance scenario with a small vertical extent perturbation for nominal amplitude (TD3). This tropopause disturbance is the most critical for accurate temperature retrievals. The results of the simulations applying statistical optimization confirm the above quoted improvement factors.

The errors above are in the simulations applied to the different scenarios where a physical state of the atmosphere/troposphere is set up for the neutral lower atmosphere. The parameters and abbreviations (used in all tables and figures) are found in Table 7.4-2. The total number of simulations amount to more than 4000 runs describing different occultations. The simulated occultations are all based on a NPOESS-like satellite at 833 km

in altitude, in a circular orbit, and with a 98.7° inclination. Both GPS and GLONASS satellites are used to compute a range of useful occultations.

Disturbance	Parameters				Abbreviation
Tropopause disturbance	Center height 11 km	Vertical width 5 km	Amplitude 4 %		TD1
	11 km	2 km	4 %		TD2
	11 km	0.5 km	0.7 %		TD3
Inversion layers	Center height 4 km	Vertical width 5 km	Gradient 3.5 %/km		IL1
	3 km	2 km	4 %/km		IL2
	6 km	0.8 km	3 %/km		IL3
Frontal systems	Meridional gradient 5 K/100km	Zonal gradient 0 K/100km	Slope 5 %	Tangent path 1° south of frontal base	FS1
	5 K/100km	0 K/100km	1 %	5° S	FS2
	10 K/100km	0 K/100km	1 %	5° S	FS3
Gravity waves	Meridional wavelength 50 km	Zonal wavelength 0 km	Relative amplitude 4 %		GW1
	50 km	0 km	2 %		GW2
	200 km	0 km	2 %		GW3

Table 7.4-2 Parameters used in the scenarios for secondary EDRs.

7.4.1. Tropopause disturbances (TD)

7.4.1.1. Geophysical description

The tropopause region between the troposphere and the stratosphere is a spatial sloping discontinuity surface, separating two air masses of markedly different lapse rate and composition. The standard rate of temperature change with altitude for a dry adiabatic atmosphere is negative in the troposphere and of the order of -10°/km. While the lapse rate in the stratosphere is positive and normally less than 3°/km.

From the dynamic boundary condition the density must be continuos across the tropopause. From the equation of state and the hydrodynamic equation the first order differential terms of pressure become continuos across the boundary region, but not the second order derivatives. This implies, that the first order discontinuity in temperature leads to an abrupt change at the height of the tropopause, as seen in the observations presented in this document.

The height of the tropopause varies with latitude, season and in response to various disturbances. In general, the tropopause is said to be about 17 km above the Earth in the tropics and 8 to 10 km in the polar regions.

Normally the tropopause is defined by the thermodynamic properties of an air column. But close to for example jets, cut-off lows or folding phenomena large uncertainties in the determination results in wrong specifications of the boundary layer due to the physics of the problem as well as the observational capabilities.

To model tropopause disturbances for high density gradients it is important that the intensity of the gradients is limited by the stability requirement for the air mass, as dense and cold air overlaying warmer and less dense air leads to instability. The adiabatic equilibrium defining the upper limit of the gradients is a condition, which the air masses should obey. Thus for this particular tropopause parameterization, we have assumed an isothermal atmosphere with an exponential density profile $r(z)$, where H is defined as the atmosphere scale height.

$$r(z) = r_0 e^{-\frac{z}{H}} \tag{7.4.1.1}$$

The density perturbation with the following form has been superimposed to the above profile at the tropopause height z_t.

$$dr = A\arctan(z - z_t) e^{-\frac{(z-z_t)^2}{s^2}} \tag{7.4.1.2}$$

A is a constant amplitude coefficient and s a parameter defining the vertical extent of the perturbation. The combination of the magnitudes of A and s have been constrained to satisfy the adiabatic equilibrium condition, which requires,

$$\frac{1}{r}\frac{dr}{dz} < 4\% \left[\text{km}^{-1}\right] \tag{7.4.1.3}$$

The main features of this tropopause perturbation algorithm is:

- it is centered at the tropopause with an asymmetric form around z_t ,
- the magnitude of the perturbation, as well as its first derivative, vanishes to zero away from z_t ,
- the shape of the perturbation is similar to the faults and the foldings usually observed at the tropopause altitude.

7.4.1.2. Parameters

Two main aspects of tropopause disturbance phenomena have been simulated (the vertical width and amplitude of the disturbance) to assess the importance of spatial structures in relation to the thermodynamical conditions. Amplitudes vary in the simulations from 0.7% to 4% for the stable conditions simulated here with vertical extents ranging from 0.5 km to 5 km (see Table 7.4-2).

7.4.1.3. Results

Results are mainly plots of the described temperature difference from original disturbed MSIS90 atmosphere model to the simulation retrieved temperature profile with or without the errors listed in Table 7.4-1. All the shown plots have increasing disturbance number corresponding to increasing line thickness. Solid line corresponds to error 1, dotted to error 2, dashed to error 3 and dot-dashed to error 4.

Figure 7.4.1.3-1 shows in the left panel the absolute temperature levels, while the right panel shows the temperature differences between the simulated profiles and the intrinsic model temperature profile.

Figure 7.4.1.3-2 and Figure 7.4.1.3-3 presents the relative pressure differences and the relative refractivity differences. The signatures for the graphs are like mentioned above with increasing line thickness with increasing disturbance number.

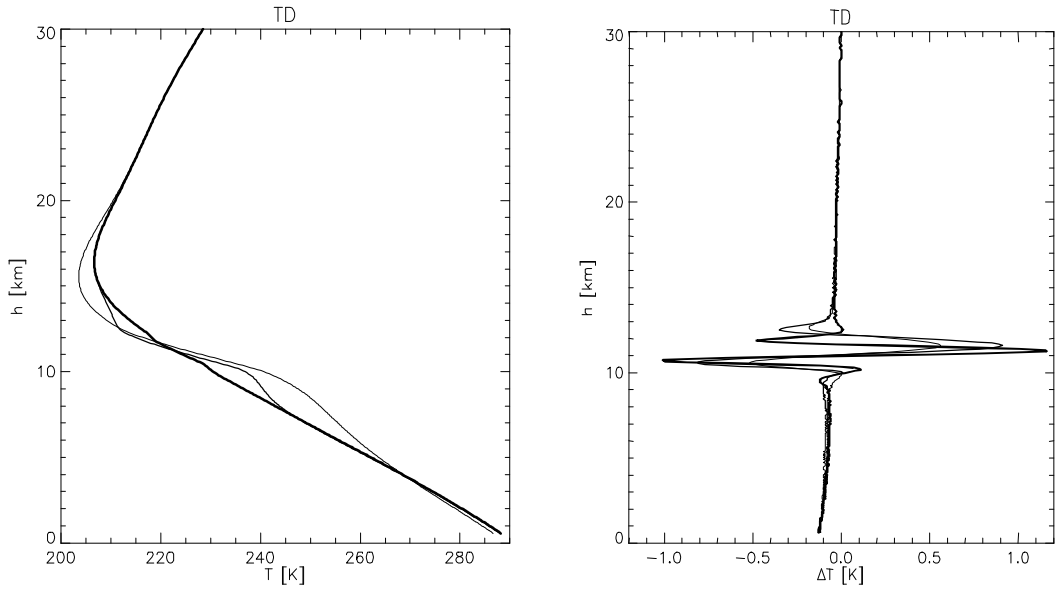

Figure 7.4.1.3-1 Absolute and difference temperature plots for the tropopause disturbance without any errors added from Table 7.4-1. The difference temperature plots are calculated as the difference between the simulated temperature profile and the original disturbed MSIS90 atmosphere model.

In Figure 7.4.1.3-4 the amplitude and phase of the received signal are plotted together with the phase derivative as a function of time and height of the occultation. Figure 7.4.1.3-5 shows the temperature difference plots in the cases with errors from Table 7.4-1 added.

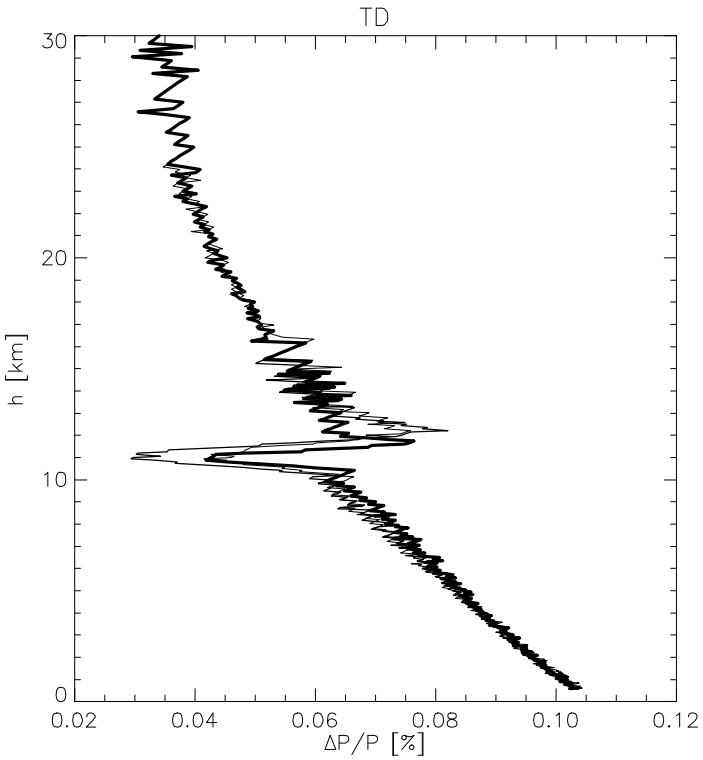

Figure 7.4.1.3-2 Relative pressure difference plot for the tropopause disturbance.

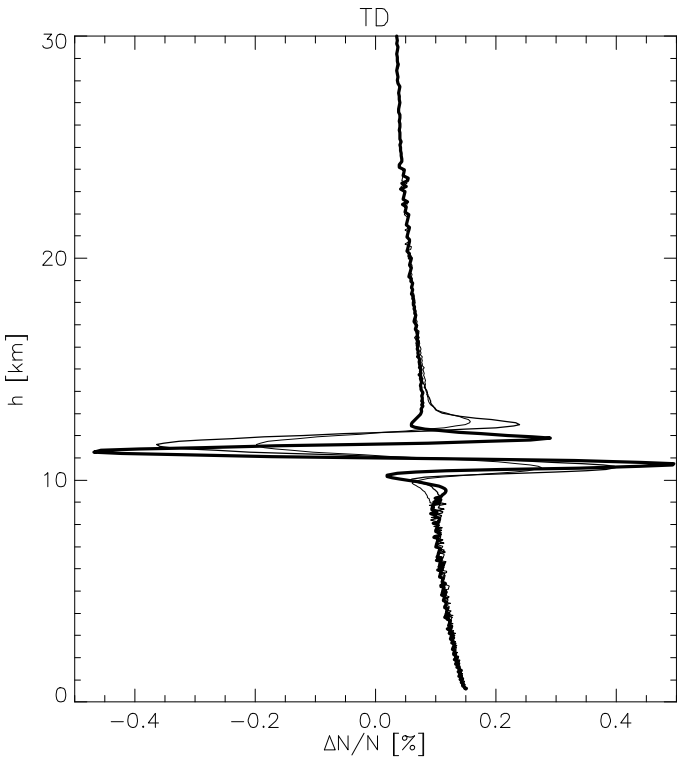

Figure 7.4.1.3-3 Relative refractivity difference plots for the tropopause disturbance.

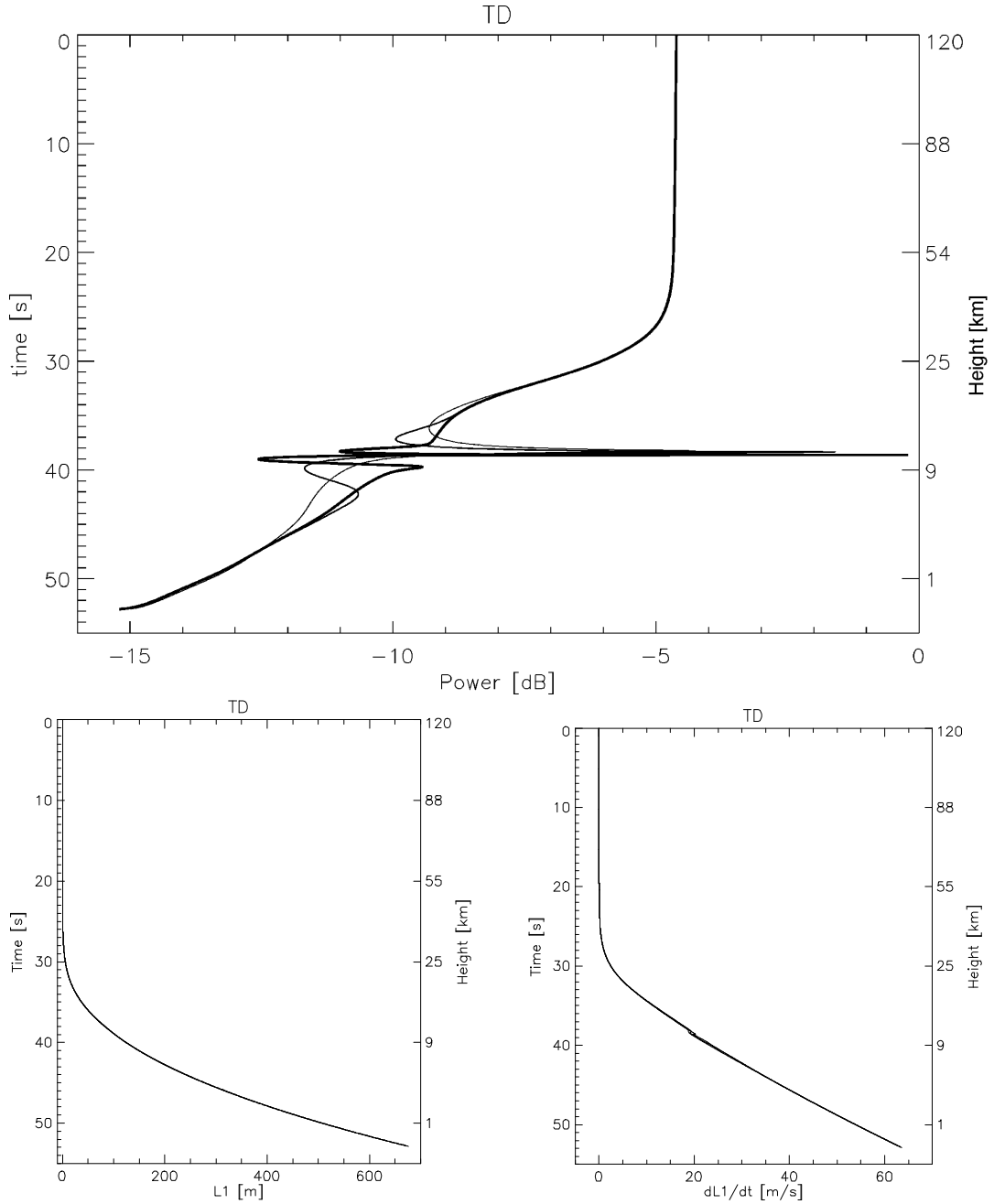

Figure 7.4.1.3-4 Amplitude, phase and the derivative of the phase for the received L1 signal calculated for the tropopause disturbance scenarios. Curves corresponding to the three disturbances scenarios TD1 (thin) to TD3 (thick) are showed in each of the three panels. The y-axis on the left side shows the time during the occultation while the y-axis on the right side shows the corresponding impact height. There is a non-linear mapping between occultation time and height.

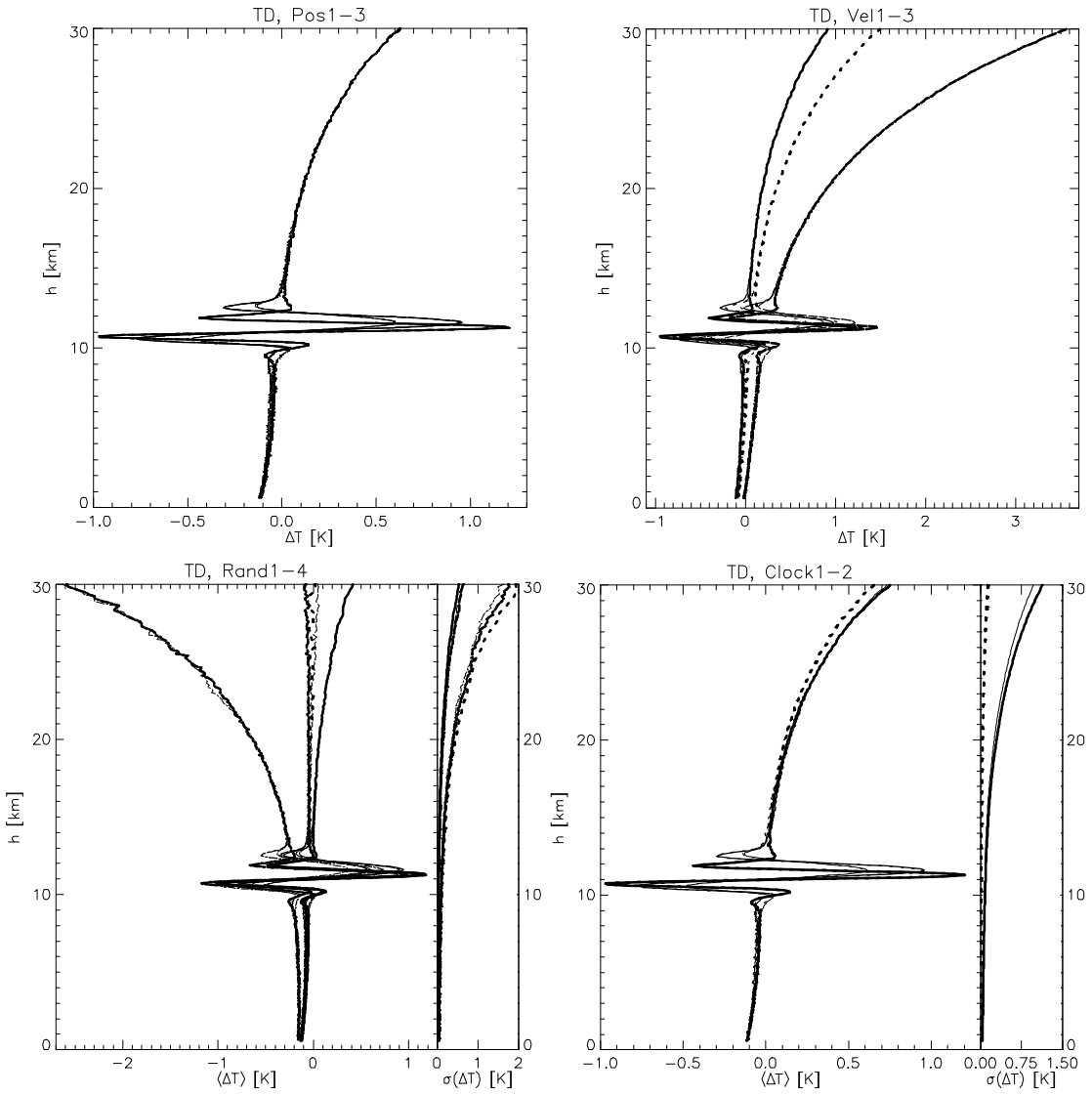

Figure 7.4.1.3-5 Temperature difference plots for the tropopause disturbance scenarios. Top left for position errors, top right velocity errors, bottom left random error on phase and bottom right clock errors. When there are two panels (for Rand and Clock) the left panel is the average and the right panel the standard deviation. Curves are TD1 (thin) to TD3 (thick).

7.4.1.4. Statistical presentation

Calculating the maximal accepted error value to numerically stay below 1 K error in the temperature profile results in an indication of the impact of the applied error type for that scenario. It is done by making a numerical differentiation of the error with respect to ΔT and multiplying with the desired ΔT limit. Hence we have assumed a linear dependency of ΔT on the total error. The result for the velocity error is seen in Figure 7.4.1.4-1. The

1 K limit being solid line, the 0.2 K limit dotted, the 0.5 K limit dashed and the 2.0 K limit being dot-dashed.

The figure reveals that if 1 K is desired all the way to 30 km, the maximal velocity error that can be tolerated is about 0.3 mm/s (corresponding to Vel2), and if 0.2 K is desired a velocity error level corresponding to Vel1 is needed. If a 0.2 K level is desired below 20 km then errors corresponding to Vel2 is the goal. These conclusions, along with many of the others, will be modified when statistical optimization is implemented. The same type of plot for position errors shows no dependency, which is also expected since all the ΔT -curves for position errors are giving similar results.

With a 50 Hz sampling for random errors (Figure 7.4.1.4-2) ΔT <1 K can be achieved almost all the way up to 30 km with errors corresponding to Rand3. At 20 km ΔT <1 K can be achieved with a random error of 2.4 mm, a little more than Rand4.

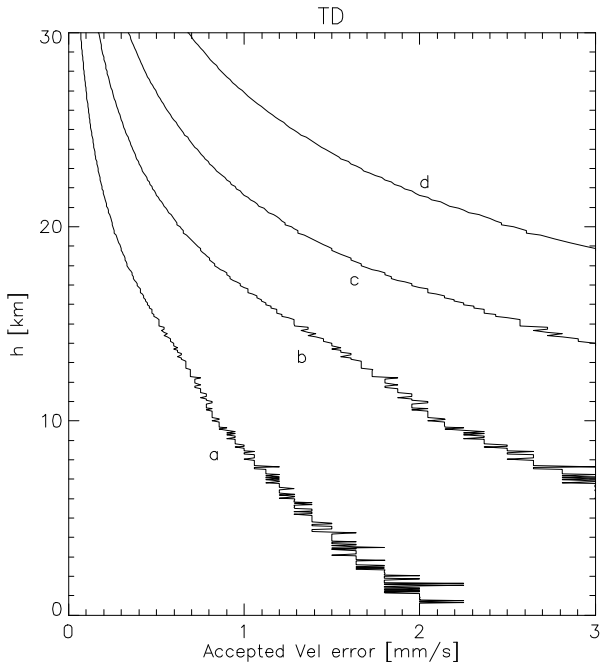

Figure 7.4.1.4-1 Limits of the velocity error for the tropopause disturbance scenarios in order to stay below 0.2 K (a), 0.5 K (b), 1 K (c) and 2.0 K (d).

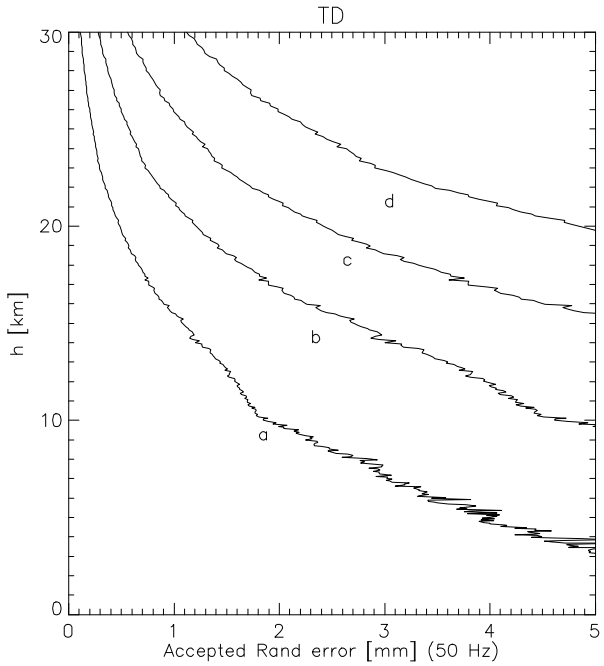

Figure 7.4.1.4-2 The limits of the random errors (sampled at 50 Hz) in order to stay below 0.2K (a), 0.5K (b), 1.0 K (c) and 2.0K (d).

7.4.1.5. Discussion

In the Figure 7.4.1.3-1 where no errors are included in the simulations for TD a kind of 'ringing' is seen around the disturbance. The 'ringing' seems to have no error exactly at the disturbance altitude, just like the disturbance is defined to have. In general ΔT for the case without any errors added is very small, indicating a high numerical stability of the algorithm for tropopause disturbances.

For the position-errors (Figure 7.4.1.3-5), no difference is seen between Pos1, 2 and 3. The systematic increase of ΔT with height is below 0.6 K for all heights below 30 km. Adding a velocity error gives larger ΔT than when adding a position error (Pos1-Pos3). Especially errors the size of Vel3 gives ΔT above 1 K from 20 km. Errors the size of Vel1 keeps the error below 1 K all the way to 30 km and Vel2 makes the error pass 1 K at 27 km.

For the Gaussian noise Rand4 is too strong for the algorithms to keep the average ΔT below 1 K below 30 km, and also the scatter of the simulation result profiles is rather large, only the scatter for Rand2 is larger.

Clock errors give much the same impact on all disturbances. Errors of the size of Clock2 makes ΔT stay rather low. It gives at the same time a standard deviation less than 0.2 K

for heights below 30 km. Errors the size of Clock 1 gives a standard deviation of 1 K below 30 km.

In Figure 7.4.1.3-4 the power of the received signal is varying very rapidly at the disturbance height, about 12 dB in 5 s, which is a great challenge for the receiver. This feature is on top of a general decrease in the signal power of about 10-11 dB over the last 25 s of the occultation. It is interesting to see that the phase of the signal is smooth during the occultation. There is only a small dip, see the curve for the derivative of the phase in figure 7.4.1.3-4, at the tropopause disturbance height at 11 km.

In section 7.4.5 the results of implementing statistical optimization on the TD3 disturbance with random noise is treated.

7.4.2. Inversion layers (IL)

7.4.2.1. Geophysical description

The inversion layer is a phenomenon of the troposphere well below the tropopause. It is defined as a layer within which the temperature increases with elevation. Quite frequently a layer of clouds is present at the base of the inversion, if the positive lapse rate does not reach the ground, as is the case frequently at our latitudes during summer situations.

The inversion layer form when the air is cooled from below by for example a cold Earth surface. If the wind is sufficiently strong to mix the boundary layer at the surface an inversion layer occurs. The lapse rate of the air column is normal just above the surface until an altitude, where the derivative of the temperature profile as function of height changes abruptly from negative to positive values defining the bottom part of the inversion layer.

If the wind is light, so there is not much turbulent mixing, a positive lapse rate is created for the whole air mass leading during calm and clear nights to fog. This is also frequently observed over polar ice fields in all seasons and over cold continents during winter.

7.4.2.2. Parameters

The simulation of the inversion layer conditions describes rather narrow layers with varying gradients, as given in the Table 7.4-2, to assess the geometric aspects of the phenomena on the occultation retrievals. The center height is between 3–6 km with a vertical width ranging from 0.8 km to 5 km.

7.4.2.3. Results

The results for the inversion layer disturbance without any errors from Table 7.4-1. can be seen in Figure 7.4.2.3-1.

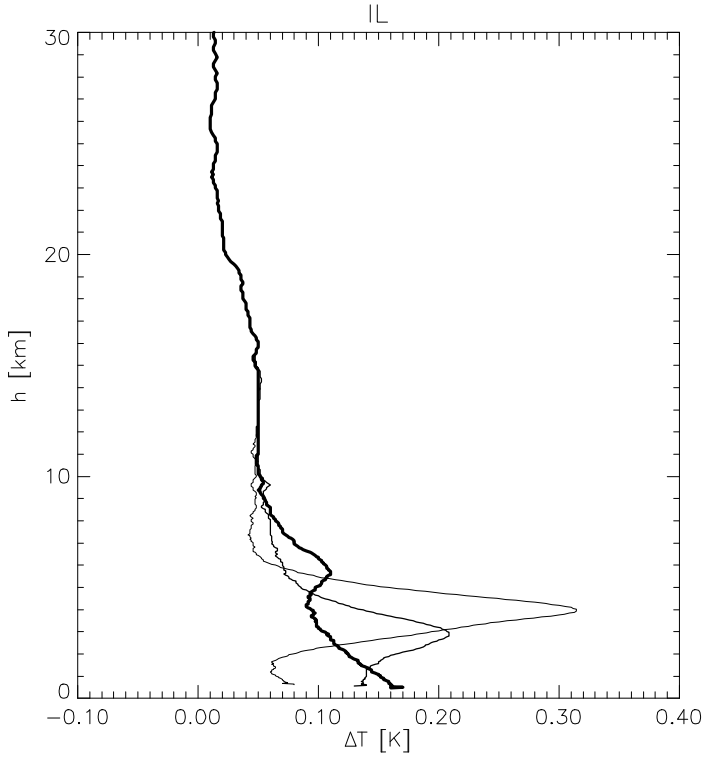

Figure 7.4.2.3-1 Temperature difference plots for inversion layer disturbance, without errors from Table 7.4-1. added.

Corresponding plots with added errors with values listed in Table 7.4-1. (for position, velocity, clock and random noise on phase) are found in Figure 7.4.2.3-3, and the amplitudes of the received signals as function of time in Figure 7.4.2.3-2.

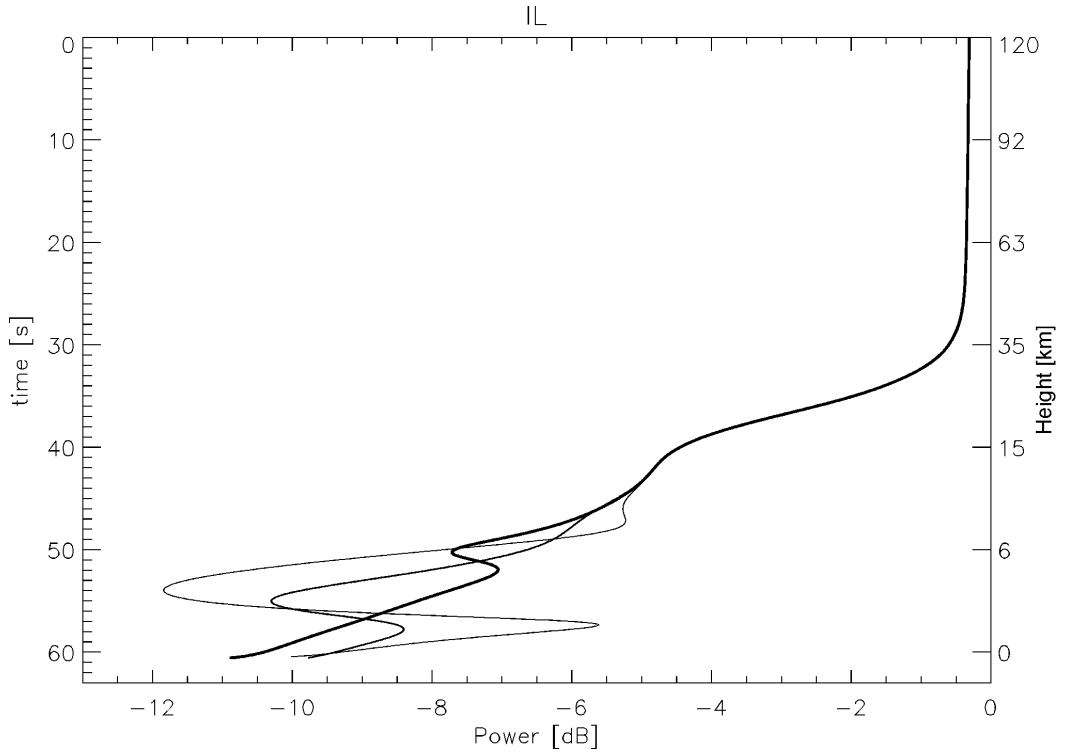

Figure 7.4.2.3-2 Amplitudes of received L1 signals for inversion layer scenarios, no error case, with only geometric and algorithmic errors contributing. All disturbances IL1-IL3 are plotted with different thickness.

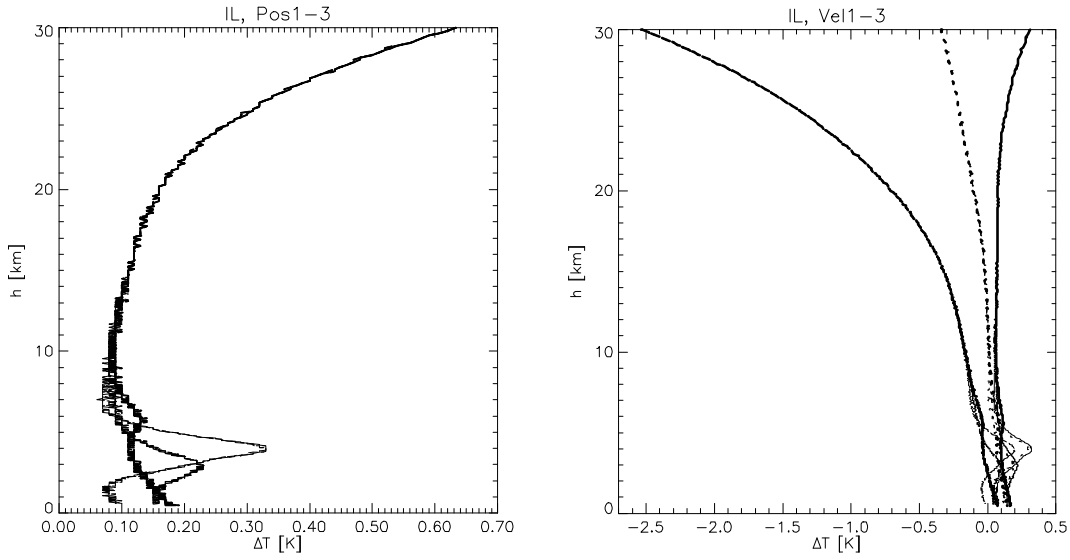

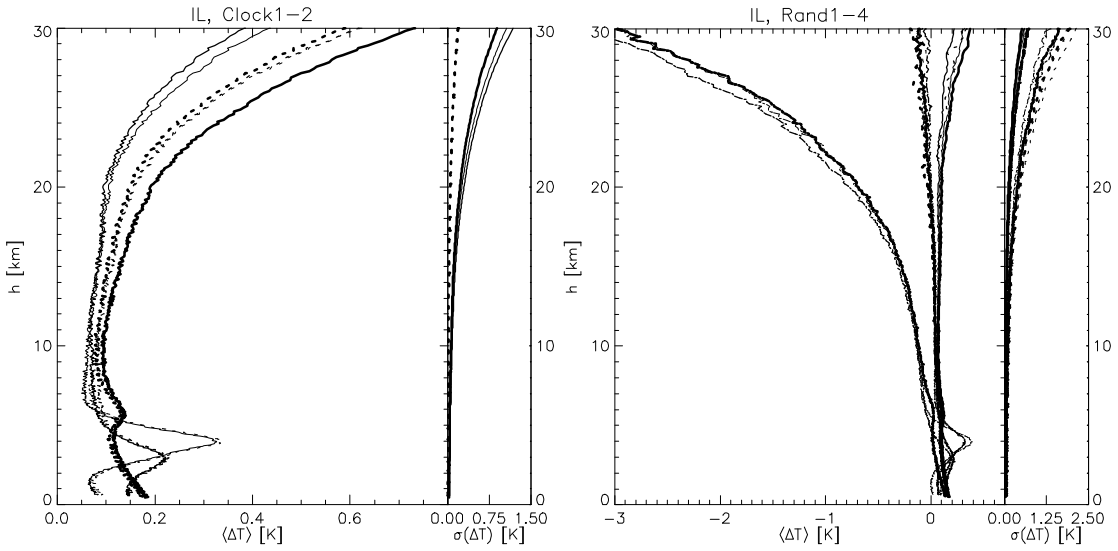

Figure 7.4.2.3-3 Temperature difference plots for the inversion layer scenarios. Top left for position errors, top right velocity errors, bottom left clock errors and bottom right random error on phase. In the Clock and Rand figures (bottom) the left panels are for the average temperature difference and the right panels for the standard deviations.

7.4.2.4. Statistical presentation

In Figure 7.4.2.4-1 the estimated limits on the velocity and random noise on phase types are plotted.

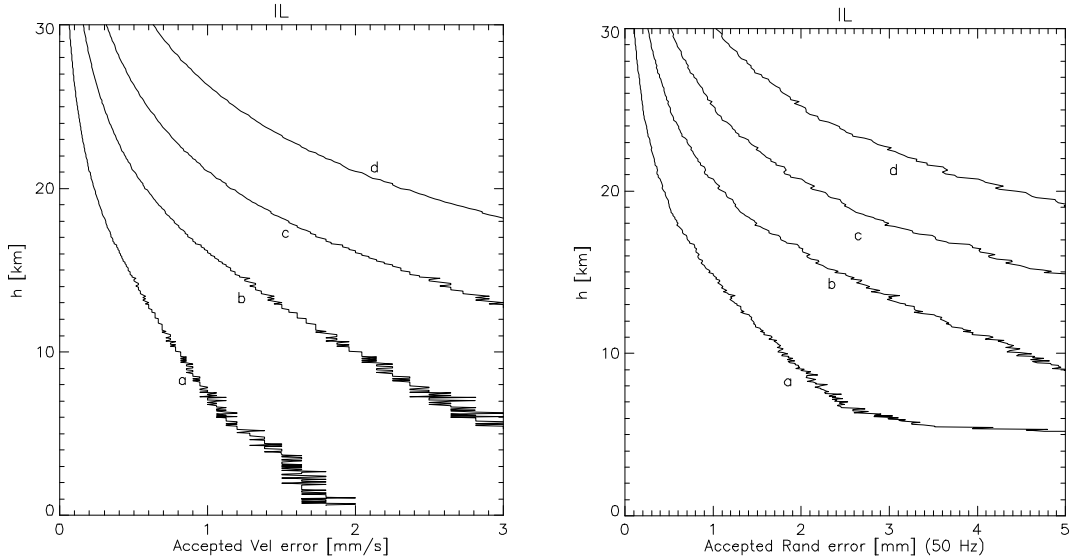

Figure 7.4.2.4-1 Limits of the velocity error (left) and random error on phase (right) in order to stay below 0.2 K (a), 0.5 K (b), 1.0 K (c) and 2.0 K (d).

Many of the same results are derived from Figure 7.4.2.4-1 as for the other secondary EDRs. In order to stay below 1 K up to 30 km a velocity error of about 0.3 mm/s can be accepted, corresponding to Vel2, and this at the same time keeps the temperature error below 0.5 K below 25 km and below 0.2 K below 18 km.
For random noise about 0.5 mm at 50 Hz (a little worse than Rand3) can keep the temperature error below 1 K below 30 km, and this would keep the temperature error below 0.5 K below 26 km and below 0.2 K below 19 km.

Below about 10 km the results get rather noisy because of the small difference between the temperature errors, and at the same time the temperature determination gets uncertain because of water vapor.

7.4.2.5. Discussion

For the three different position errors the ΔT s merges to the same just above the disturbances (at about 10 km) and from then only the systematic ΔT -increase is seen. For velocity errors Vel3 results in a ΔT above 1 K from 20 km and up. The three velocity errors all show the same behavior for the different disturbances, indicating that the algorithm is more sensitive to the error than the disturbance. For the random errors only Rand4 'shoots of' already below 20 km (see Figure 7.4.2.3-3). This is expected to be improved with statistical optimization. Clock errors give a systematic increasing ΔT but below 0.75 K below 30 km. Clock1 also induces a standard deviation of about 1 K at 30 km.

The power of the signal is decreasing 11-12 dB in the last 30 s of the occultation, and in the final 10 s, below 7 km, some rather rapid variations are emerging of about 6 dB within 7 s but with no sharp peaks.

7.4.3. Frontal systems (FS)

7.4.3.1. Geophysical description

Warm and cold fronts form the frontal weather systems govern most of the weather situations at our latitudes. They originate from the encounter of relatively warm moist air from the south with polar colder air masses. The shear velocity between the different air types form the cyclone or cyclone systems, consisting of several whirls. The separation between the two air masses is normally sharp, since it in many cases represents the border of the polar air mass. Along the front the temperature and the wind change suddenly, as also is the case for the state of the cloud cover.

The definition of a warm front is the situation where warm air displaces colder air. The slope of the separation region is normally less steep compared to the cold front, defined

by the reverse characteristics. A cross section just to the south of the low-pressure center of the cyclone shows a wedge of gentle sloping cold air under the rising warmer air mass at the right side of the vertical cut (warm front). The rising warm air leads to extensive cloud formation and gentle precipitation over a large region. At the left hand side the cold air mass with the sharper gradient lifts the warm air faster resulting in a narrower belt of clouds and rain showers (cold front).

The largest temperature variation is observed in the border region between the cold and the warm air masses. In the same zone, thermal winds will be strong, which at the upper level will be the position of the jetstream.

The model of the frontal system consists of a sloping change in the refractivity of the atmosphere as function of altitude, where the meridional and zonal gradients of the front also are variables. Figure 7.4.3.1-1 gives the temperature changes from one of the simulations performed for the frontal system studies.

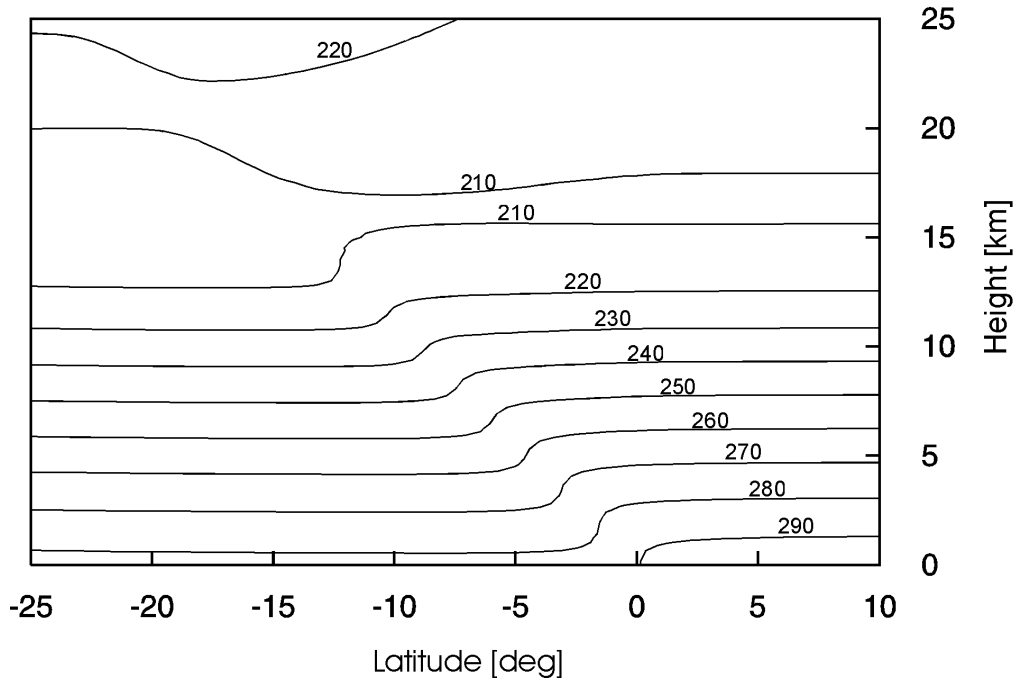

Figure 7.4.3.1-1 Contour plot of the temperature changes around a frontal system.

7.4.3.2. Parameters

The frontal system phenomena are studied by simulating three different frontal disturbances. Both the meridional gradient and the slope of the front is varied, the zonal gradi-

ent is set equal to zero and the occultation is chosen such that the ray paths are going approximately from north to south. The tangent point of the occultation is centered south of the frontal base for maximum impact on the phase delays. The meridional gradient is varied from 5K/100km to 10K/100km and the slope is changed from 1% to 5%.

7.4.3.3. Results

Figure 7.4.3.3-1 and Figure 7.4.3.3-3 contains temperature difference plots without and with errors from table 7.4-1 added. The amplitude of the received signals as function of time can be seen in Figure 7.4.3.3-2.

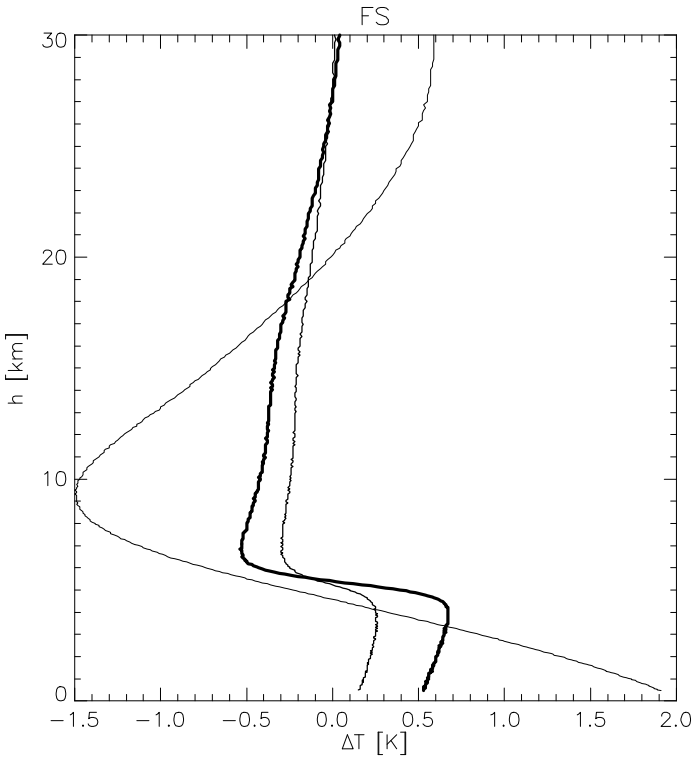

Figure 7.4.3.3-1 Temperature difference plots for the frontal system disturbance. Curves are FS1 (thin) to FS3 (thick).

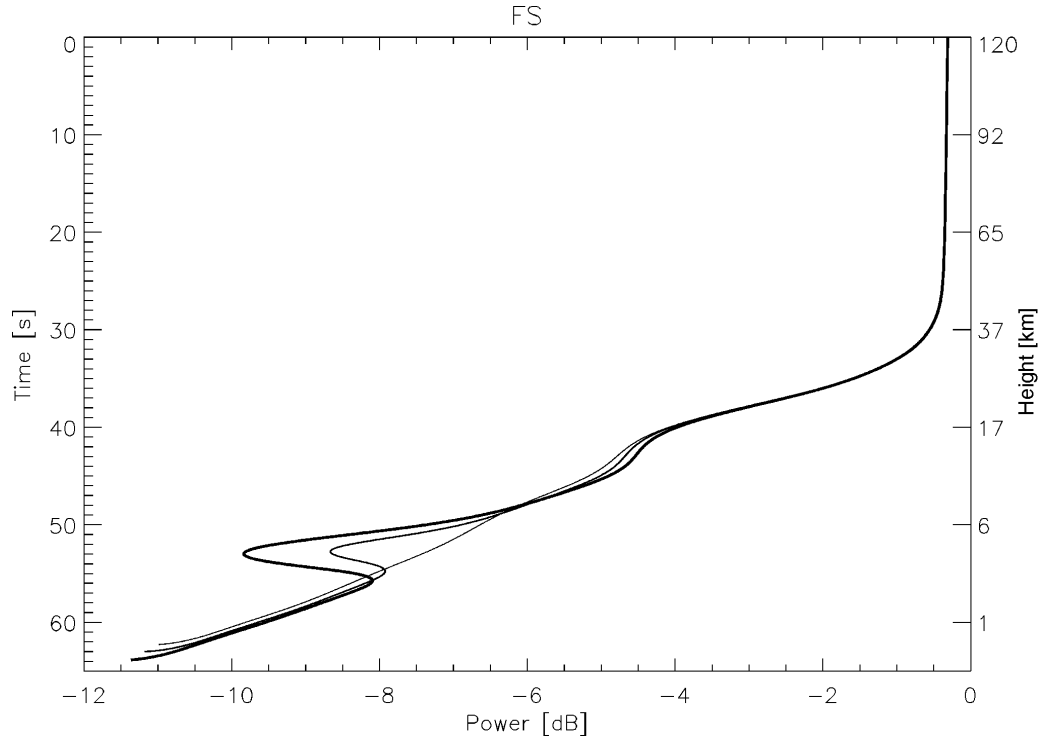

Figure 7.4.3.3-2 Amplitudes of received L1 signals for frontal system scenarios. FS1 thin line, FS2 medium line and FS3 thick line.

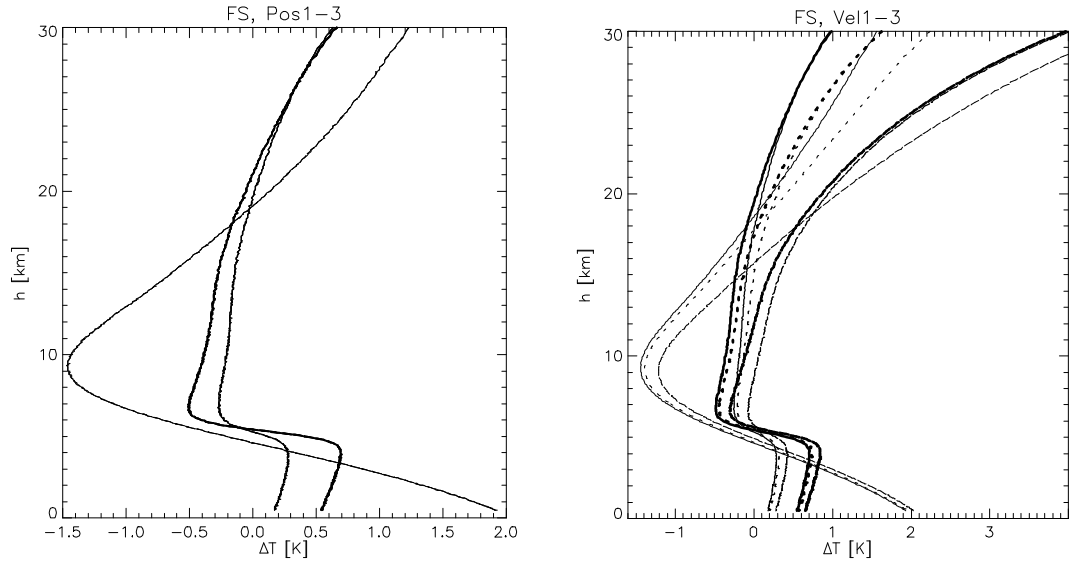

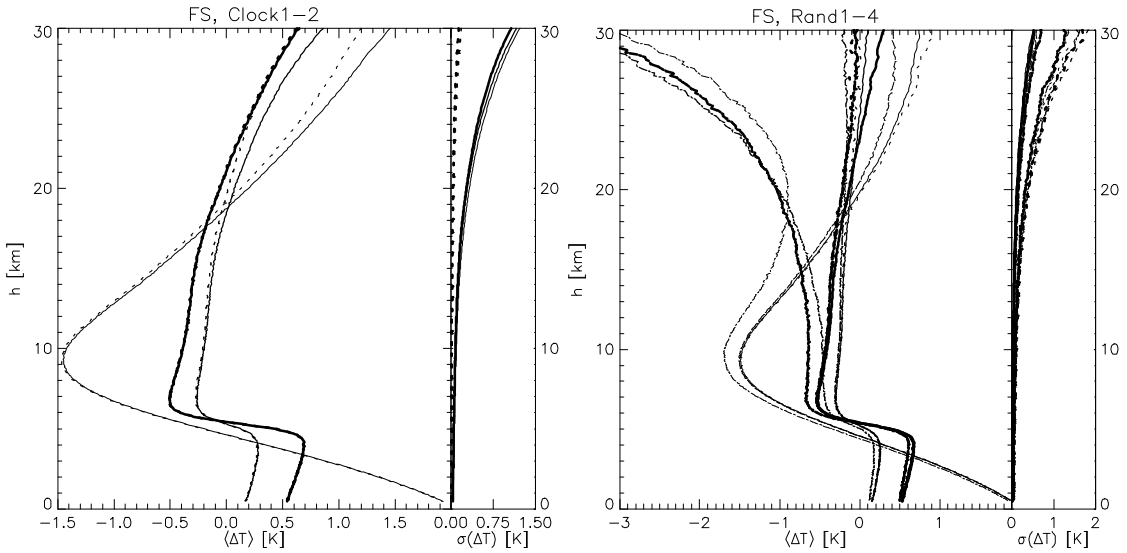

Figure 7.4.3.3-3 Temperature difference plots for the frontal system scenarios. Top left for position errors, top right velocity errors, bottom left clock errors and bottom right random error on phase. In the bottom plots the right panels are for the average temperature difference and the right panels for the standard deviations.

7.4.3.4. Statistical presentation

From Figure 7.4.3.4-1 it is derived that the in order to keep the temperature error below 1 K the velocity error has to be below 0.3 mm/s, corresponding to Vel2. This would further keep the temperature error below 0.5 K below 24 km and below 0.2 K below 17 km.
For the random error the maximal accepted error when reaching for 1 K below 30 km is 0.4 mm, corresponding to about half the value of Rand3. A random error of 0.7 mm, corresponding to Rand3, would only fulfil the 1 K demand below 26 km.

These results are improved when implementing statistical optimization, see e.g. section 7.4.5.

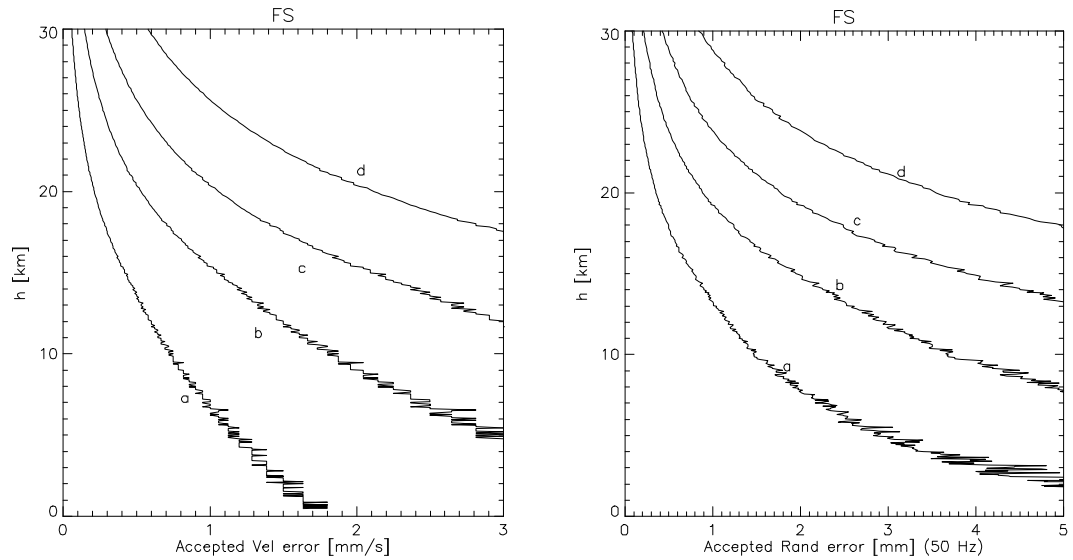

Figure 7.4.3.4-1 Limits of the velocity error (left) and random error on phase (right) in order to stay below 0.2 K (a), 0.5 K (b), 1.0 K (c) and 2.0 K (d).

7.4.3.5. Discussion

In the case without errors from Table 7.4-1 both FS2 and FS3 give ΔT below 1 K all the way to 30 km altitude. This is in accordance with other findings quoted in the literature [Hardy]. FS1 causes ΔT to be large in a small region below 10 km. The effect is further enhanced if a position error is added (Pos1-Pos3), making ΔT for FS1 go above 1 K from about 25 km too. No difference is seen between Pos1, Pos2 and Pos3, indicating that this error is not very important. The increase in ΔT relative to the no-error case is caused by a change in the upper bound in the Abel transform from 70 km in the error case to 110 km in the non-error case. The velocity errors (Vel1-Vel3) cause ΔT to further increase, especially for FS1 and Vel3. The increase in ΔT mainly is seen above 10-15 km. The four random noise errors in general have not much effect, except for Rand4. Rand2 causes a large standard deviation in the derived ΔT, but the average is not much affected.
Clock errors does not affect the derived temperature differences much. The standard deviation of Clock2 stays below 0.2 K and of Clock1 below 1.2 K.

The power of the received signal is decreasing smoothly 11 dB over the last 30 s of the occultations. But FS2 and FS3 show bumps of about 1.5 dB and 3 dB at 10 s before the ending of the occultation, lasting for 5 s. These bumps do not cause any problems to the temperature retrieval.

7.4.4. Gravity waves (GW)

7.4.4.1. Geophysical description

Gravity waves of the neutral lower atmosphere are a very common feature, which generation mechanism is related to a range of meteorological phenomena. Tropospheric weather fronts, tornadoes, thunderstorms, heating events and mountain ridges are some of the known causes resulting in gravity wave activity. Gravity waves play a major role in the global atmospheric circulation processes and the energy transport, which may be seen as an intrinsic part of the atmospheric structure.

The periods of the waves range from minutes up to an hour with vertical wavelengths from 1 km to 15 km. The horizontal gradients generated by gravity waves can be comparable to the horizontal distance traveled by the occulted ray. Thus an effect on the propagation path of the probing signal will be inevitable due to the spectrum of gravity waves.

The dispersion relation for gravity waves is established for an exponential varying atmosphere with constant scale height H through the equation of motion, retaining only terms due to gravity, pressure gradients and inertia. This leads to an expression for the growth of the waves, direction and amplitude as function of the specific heat ratio of the atmospheric gas, the sound velocity and the gravitational acceleration term.

The model for the gravity waves for small wave disturbances relates the density variations caused by the above mentioned terms about a basic state of rest to the wavelength and amplitude of the waves.

$$\frac{dr}{r} = (A_1(z) + A_2(z))e^{-i\vec{k}\cdot\vec{x}} \qquad (7.4.4.1.1)$$

The $A(z)$ functions express the variation of the wave amplitude with altitude. They are separated into two parts. $A_1(z)$, an exponential increase due to the decrease in molecular density with a typical scale height of $2H$, and $A_2(z)$, a damping factor preventing the gravity wave from breaking. The second term acts also as a constraining function, keeping the atmosphere in adiabatic equilibrium and satisfying boundary conditions.

7.4.4.2. Parameters

Only single frequency plane waves are simulated, even though gravity waves normally are observed as a spectrum of wavelengths. But the simulated results can easily be generalized to the situation, where whole spectrums of monochromatic waves are simulated. The conclusions though will be similar to the below results and conclusions.

The simulations cover cases for short horizontal meridional wavelengths having a scale length of 20 km. Another case of this scenario represents the results of varying the wave amplitude. The last case covers the situation of a longer wavelength of 200 km.

7.4.4.3. Results

Figure 7.4.4.3-1 contains the temperature profiles for the gravity wave scenarios with no error sources given is Table 7.4-1.

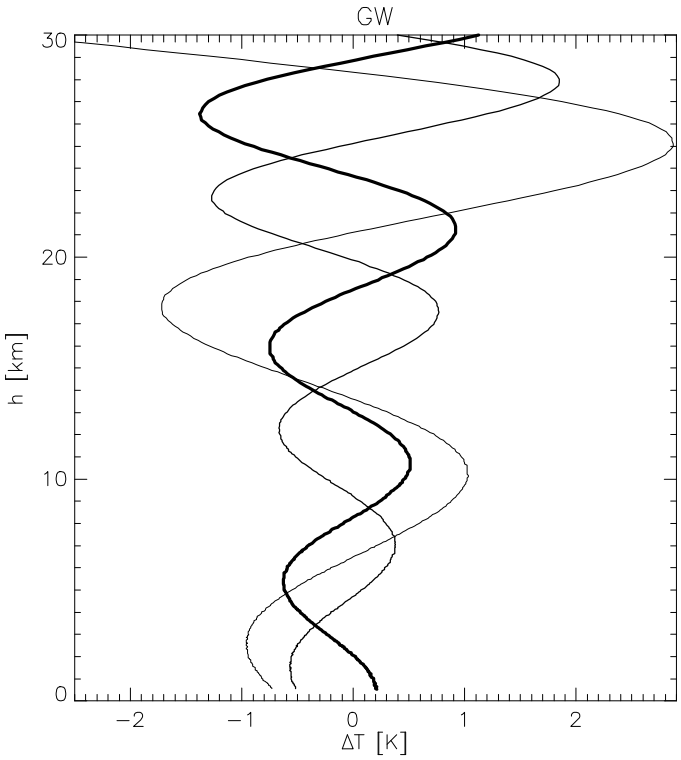

Figure 7.4.4.3-1 Temperature difference plots for the gravity wave disturbance scenarios.

In Figure 7.4.4.3-3 are the temperature difference profiles when the errors listed in Table 7.4-1 are added. Figure 7.4.4.3-2 contains the amplitudes of the received signals as function of time and height.

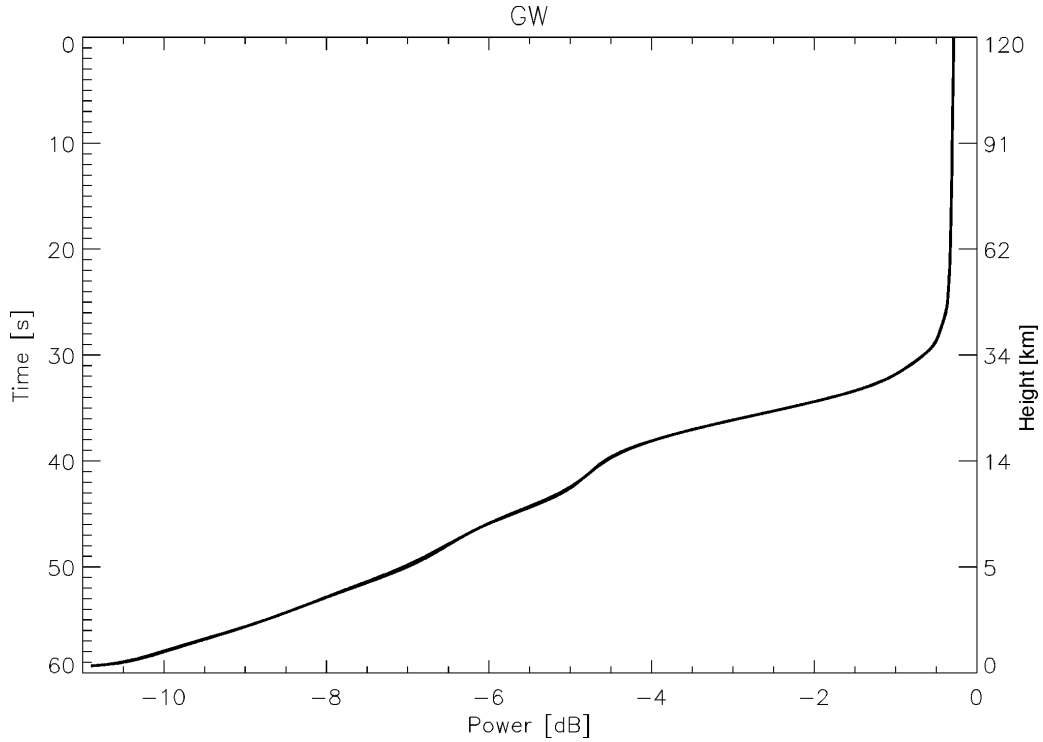

Figure 7.4.4.3-2 Amplitudes of received L1 signals for gravity wave scenarios. All three scenarios GW1-GW3 are plotted with different line thickness but they all overlap.

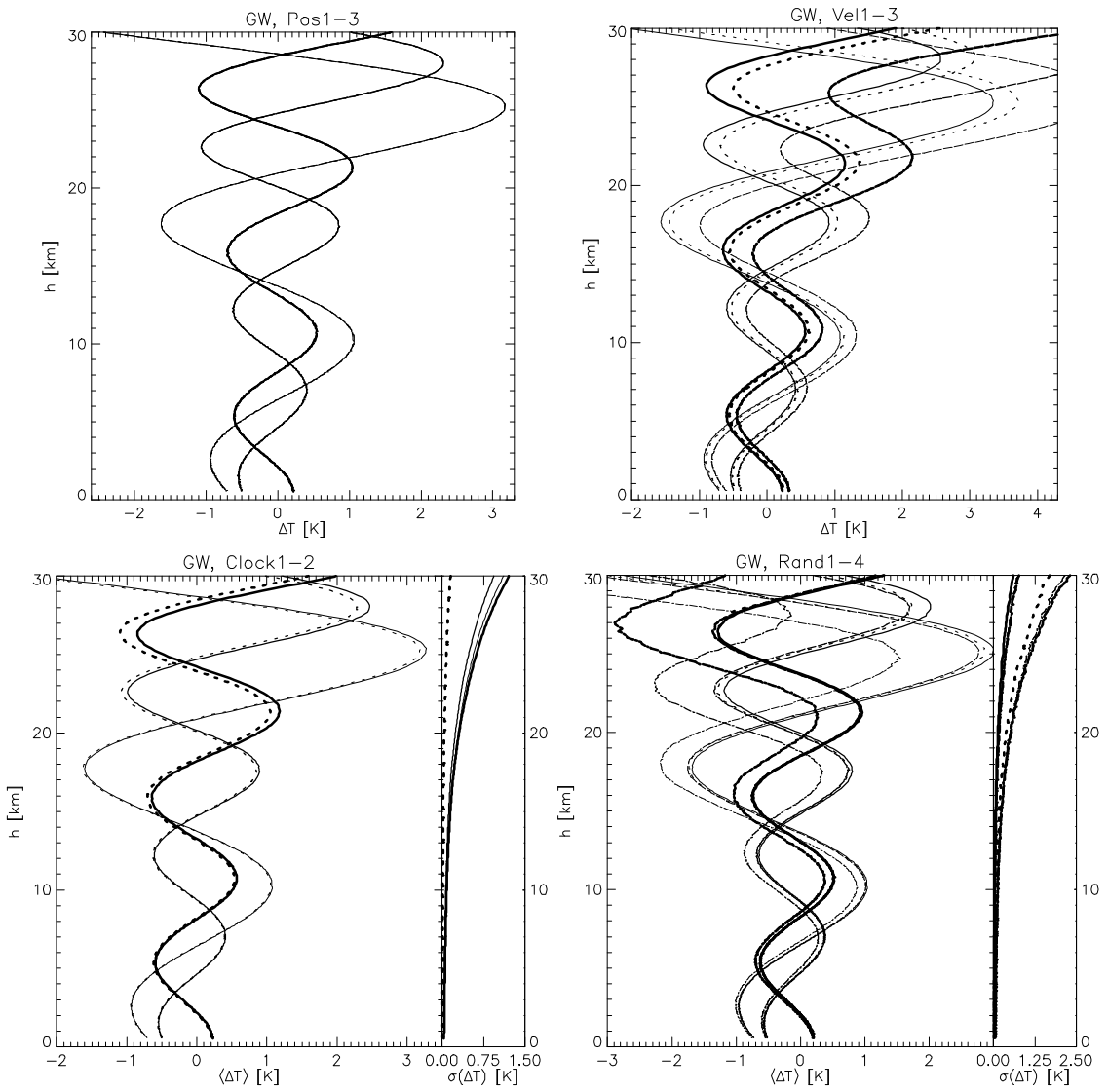

Figure 7.4.4.3-3 Temperature difference plots for the gravity wave scenarios. Top left for position errors, top right velocity errors, bottom left clock errors and bottom right random error on phase. In the two bottom plots (Rand and Clock) the left panels are for the average temperature difference and the right panels for the standard deviation.

7.4.4.4. Statistical presentation

Figure 7.4.4.4-1 illustrates the temperature limits at 0.2 K, 0.5 K, 1.0 K and 2.0 K for velocity and random errors as function of height. The left figure illustrates that a 1 K error can be achieved all the way up to 30 km with a Vel2-like velocity error, but 0.5 K requires velocity errors less than Vel1, unless 0.5 K is only required below 20 km, then about 5.5 mm/s is the velocity-error requirement.

The right figure illustrates that 0.5 K below 20 km requires 1.3 mm random phase-error at 50 Hz (corresponding to two times Rand3) and 1 K at 30 km requires 0.6 mm random

noise, corresponding to a little less than Rand3. This would at the same time give 0.5 K below 25 km and below 0.2 K below 19 km.

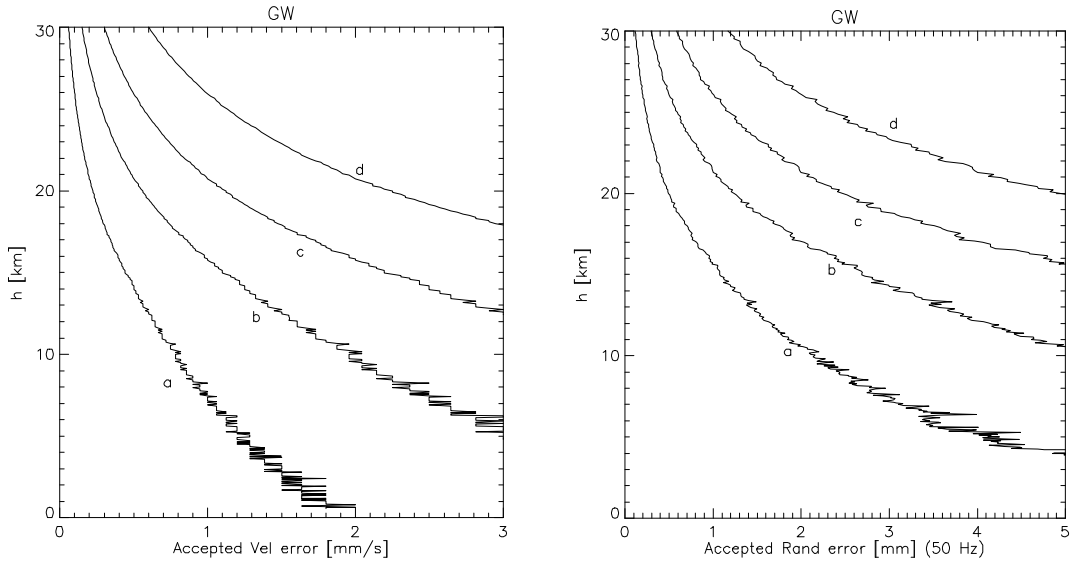

Figure 7.4.4.4-1 Limits of the velocity error (left) and random error on phase (right) in order to stay below 0.2 K (a), 0.5 K (b), 1.0 K (c) and 2.0 K (d).

7.4.4.5. Discussion

Below 30 km GW2 and GW3 stays close to or below 1K in ΔT, but GW1 is causing ΔT above 1 K already at about 15-20 km, and further increasing with height. This indicates that the algorithm is more sensitive to gravity waves with small wavelength than large amplitude waves.

As for all the other cases no effect is seen when applying a radial position error.

Increasing velocity error tends to shift ΔT to higher values (and hence shift the direct temperature profiles to higher temperatures). The effect seems to be almost linear with the size of the radial velocity error.

The random noise on phase tends to make a shift downward of $\langle \Delta T \rangle$ for increasing error-value. The derived standard deviation of ΔT is increasing with height, but it is for Rand1 and Rand3 staying below 1 K all the way up to 30 km.

Adding a clock-error also shifts $\langle \Delta T \rangle$ downwards. The standard deviation of ΔT increases to about 1.2 K at 30 km for Clock1, where as it for Clock2 stays below 0.2 K.

The power of the received signal decreases in the last 30 s with about 10 dB of which 5 dB damping is seen within less than 10 s around the tropopause.

7.4.5. Statistical Optimization

For the tropopause disturbance scenario TD3 with Gaussian noise added as an error (Rand1-Rand4), a statistical optimization algorithm has been tested. The height limit (refers to chapter 6) for Rand1 and Rand2 (e.g. the 10 Hz sampling rate cases) is set to 50 km, and for Rand3 and Rand4 (e.g. the 50 Hz sampling rate cases) to 45 km. The results are summarized in Figure 7.4.5-1.
As can be seen the error on the average temperature profile is now very low, below 0.3 K for all cases, with the standard deviation below 0.5 K, in all keeping the error well below 1K.

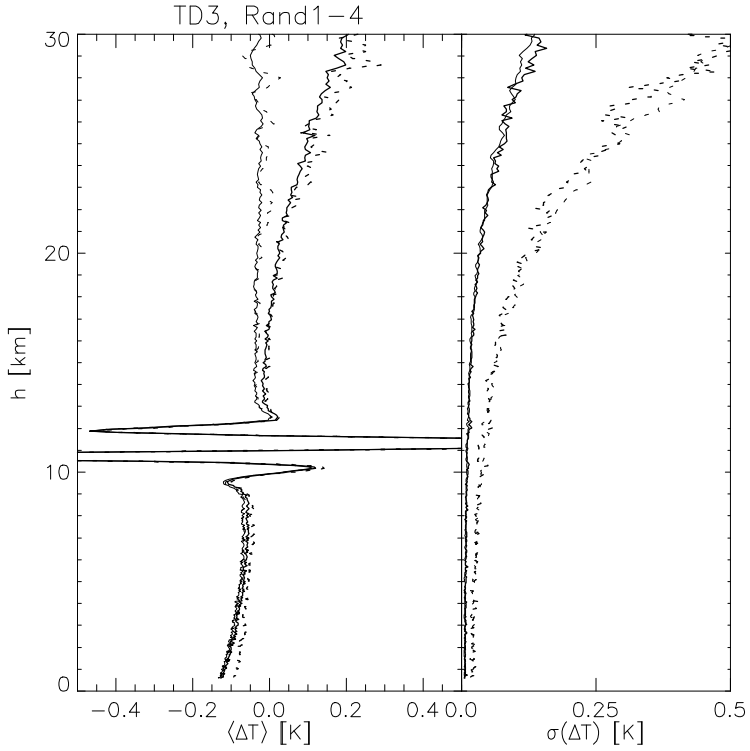

Figure 7.4.5-1 The result of statistical optimization on TD3 with random errors. Left panel gives the average temperature difference and right panel the standard deviation. Thin: 10 Hz, thick: 50 Hz, solid line: little noise and dotted line: most noise.

In Figure 7.4.5-1 two interesting features can be identified. First the two high-noise cases for 10 Hz and 50 Hz (Rand2 and Rand4) coincide in standard deviation and so does the low-noise cases (Rand1 and Rand3), even though the noise in the 50 Hz case is larger than in the 10 Hz case (see Table 7.4-1). The factor between the 10 Hz and 50 Hz high-noise noise levels is $\sqrt{50Hz/10Hz} = \sqrt{5}$ and so it is for the low-noise cases. Using this factor should in theory lead to the same noise in the derived temperature profile if the temperature profile is retrieved in the optimal way. Since the standard deviations are found to coincide as mentioned the temperature retrieval is close to optimal.

The other interesting feature is that the temperature profile derived at high sample rate (50 Hz) seems to cause larger errors than the lower sampling rate. This might be explained by the fact that a high sample rate causes the statistical optimization to begin at a lower altitude because the bending angle a becomes negative at lower altitudes when sampling faster (see chapter 6.3.7.5). This is also reflected in the characteristic height mentioned above, which is 45 km in the 50 Hz cases and 50 km in the 10 Hz cases.

Directly comparing Figure 7.4.5-1 with Figure 7.4.1.3-5 (bottom left) it can be seen that the standard deviation is decreased by a factor four to five for all random errors and the average temperature difference with a factor of up to 10 for Rand4.

7.4.6. Summary of Secondary simulations

For all the scenarios the algorithms are found to be stable, but a general tendency of increased ΔT with height is seen. This problem is decreased in the tested case when statistical optimization is implemented in the algorithms.
All the disturbances can be seen as ΔT-irregularities which in most cases are below 1K. Worst problems are encountered in two of the scenarios. For small gravity waves, which tend to give ΔT-profiles a wave-like structure with large amplitudes (especially for heights above 20 km) and steep frontal systems.
Most of the errors are giving acceptable ΔT-profiles for all disturbances. Worst are Clock1, Rand4 and Vel3, all causing temperature errors of more than 1K from about 20 km. These errors correspond respective to 10^{-12} Allen deviation, 2.2 mm random phase error sampled at 50 Hz and 1.0 mm/s radial velocity error.
Most of the disturbances stay within the 1 K limit in the no-error case, even though the disturbances are mainly 'worst case'. Problems are seen for the FS1 and GW1 scenarios only, indicating that frontal systems with a high slope and gravity waves with short wavelengths can cause problems – or that these kinds of geophysical phenomena can be identified from the temperature profiles due to their strong signatures. It must be remembered that most of the plots shown are temperature differences and hence are only a fractional change on the direct temperature curves.
A preliminary version of statistical optimization has shown to be able to reduce the general increase of the temperature error with altitude by a factor of up to 10, and at the same time reduce the standard deviation by a factor of four to five.

The power of the received signal is in most cases smooth, but in the tropopause disturbance scenarios, resembling a worst case situation, phase lock might be difficult to maintain because of the very fast and large variations of the power.

7.4.7. Secondary EDR simulations without geophysical disturbances

Fig. 7.4.7-1 to 7.4.7-5 show the results of secondary EDR simulations performed with the EGOPS simulation tool package. The influences of different error types on the retrieved temperature profiles have been investigated. All the simulations are dry air simulations using the modified MSIS90 atmosphere model. The figures show the statistics of the difference between the simulated temperature profiles and the MSIS90 model based temperature profile. The grey curves representing measurement accuracy is the mean temperature difference while the black curves representing measurement precision is the standard deviation of the temperature differences.

The bending angle retrieval, Abel transform and the statistical optimization algorithm applied to the bending angle retrieval process have been used to calculate all the temperature profiles in the simulations. The starting height for the statistical optimization algorithm was set to 40 km in these simulations. The error type, sampling rate and the corresponding figures are summarized in the two tables below. In table 7.4.7-1 only one error type is applied to the signal, while four different error types are applied to the signal at the same time in table 7.4.7-2. Fifty different runs have been made for each of the entries in two tables and the corresponding figures. The measurement accuracy, precision and uncertainty stated in the two tables are the worse case values in the height interval up to an altitude of 30 km. The uncertainty in table 7.4.7-1 and 7.4.7-2 has been calculated from the accuracy and the precision with the use of equation (7.2.2).

Error type	*Error size*	*Sampling rate*	*Figure*	*Accuracy (H < 30 km)*	*Precision (H < 30 km)*	*Uncertainty (H<30 km)*
Clock error, White noise, 1 sec. Allan dev.	10^{-12}	50 Hz	7.2.6-1	<0.15 K	<0.25 K	<0.29 K
Clock error, Flicker noise, 1 sec. Allan dev.	10^{-12}	50 Hz	7.2.6-2	<0.25 K	<0.55K	<0.60 K
Gaussian phase noise	2.2 mm	50 Hz	7.2.6-3	<0.25K	<0.45 K	<0.51 K

Table 7.4.7-1 Simulations with one introduced error. The uncertainty is derived from the accuracy and the precision with the use of equation (7.2.2).

It is seen from the figures and the numbers in table 7.4.7-1 that the temperature retrieval process is in general more sensitive to flicker clock noise than white noise and Gaussian noise. The bias, measurement accuracy, is for all of the errors quite small. The bias seen in the curves for altitudes close to the surface of the earth is a residual error from the

earth oblateness correction scheme mentioned in chapter 6. This correction scheme is developed and described in detail by [SYN98]. The uncertainties are all within the threshold value of 1 K for altitudes up to 30 km.

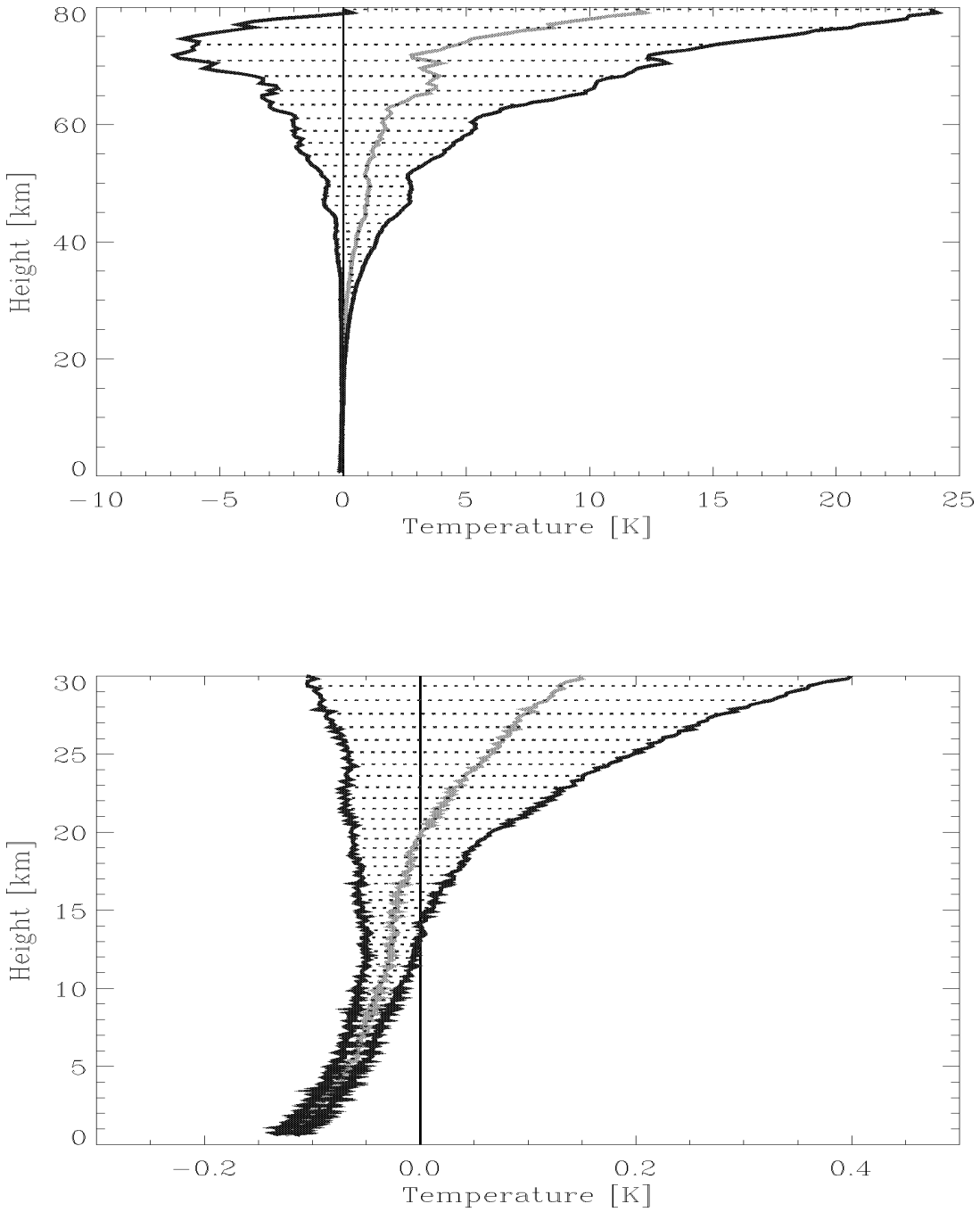

Figure 7.4.7-1 Simulation of temperature profiles, with white noise clock error. The two figures show for two different height scales the statistics of the difference between the simulated temperature profiles and the model based temperature profile. The grey curve represents the mean temperature difference while the black curves represent the corresponding standard deviations. The statistics is based on 50 simulation runs.

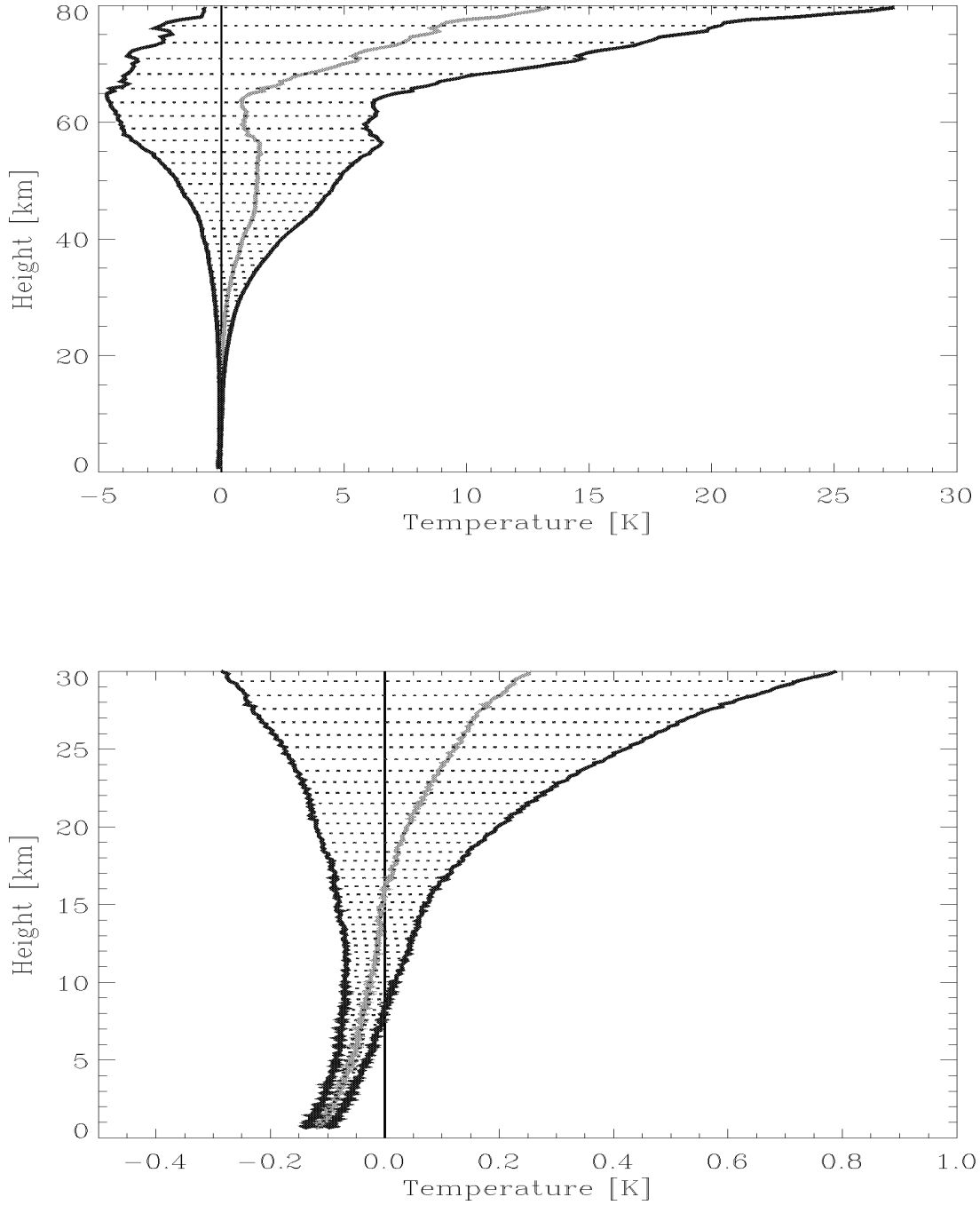

Figure 7.4.7-2 Simulation of temperature profiles, with flicker noise clock error. The two figures show for two different height scales the statistics of the difference between the simulated temperature profiles and the model based temperature profile. The grey curve represents the mean temperature difference while the black curves represent the corresponding standard deviations. The statistics is based on 50 simulation runs.

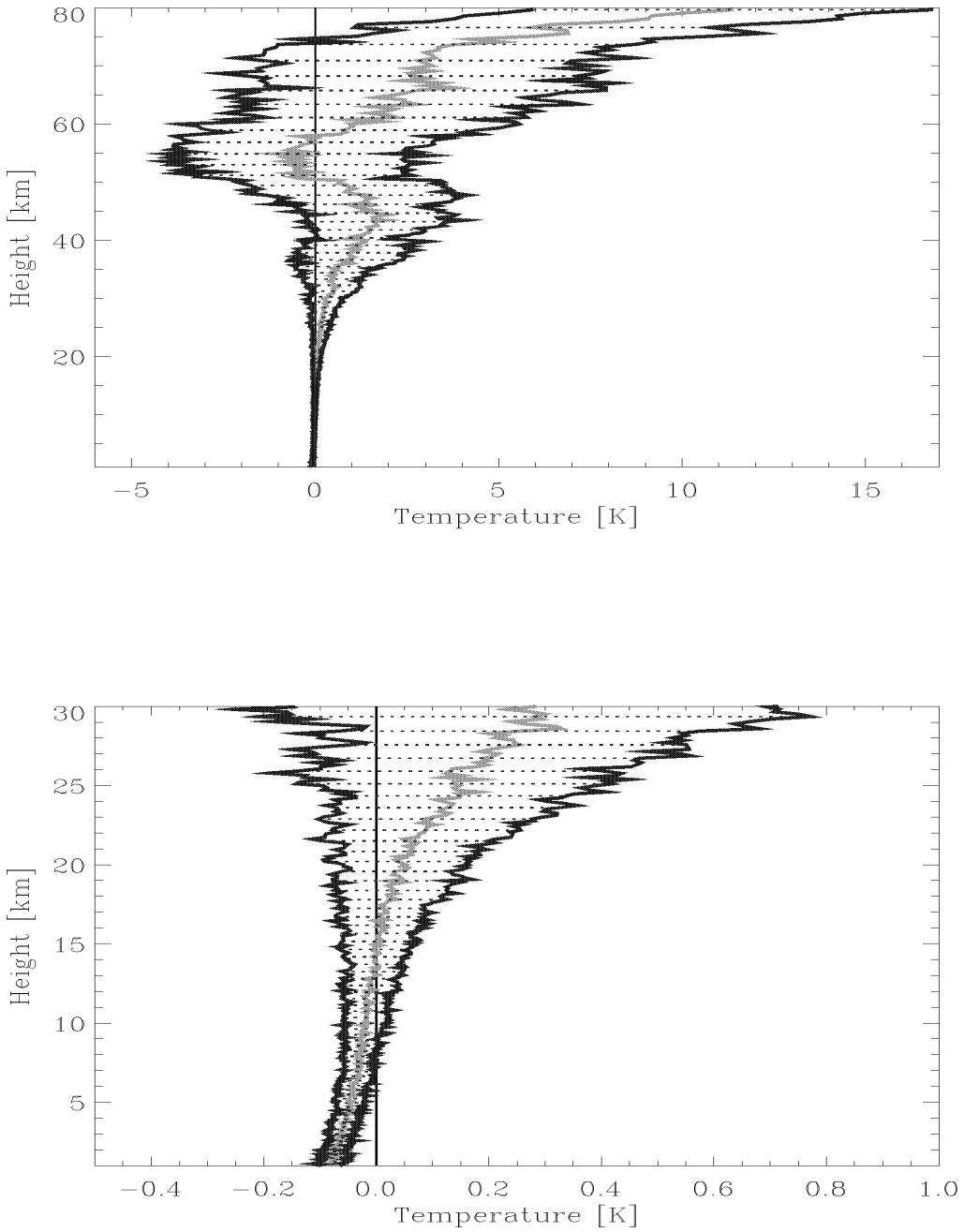

Figure 7.4.7-3 Simulation of temperature profiles, with a Gaussian random error of 2.2 mm on the phases. The two figures show for two different height scales the statistics of the difference between the simulated temperature profiles and the model based temperature profile. The grey curve represents the mean temperature difference while the black curves represent the corresponding standard deviations. The statistics is based on 50 simulation runs.

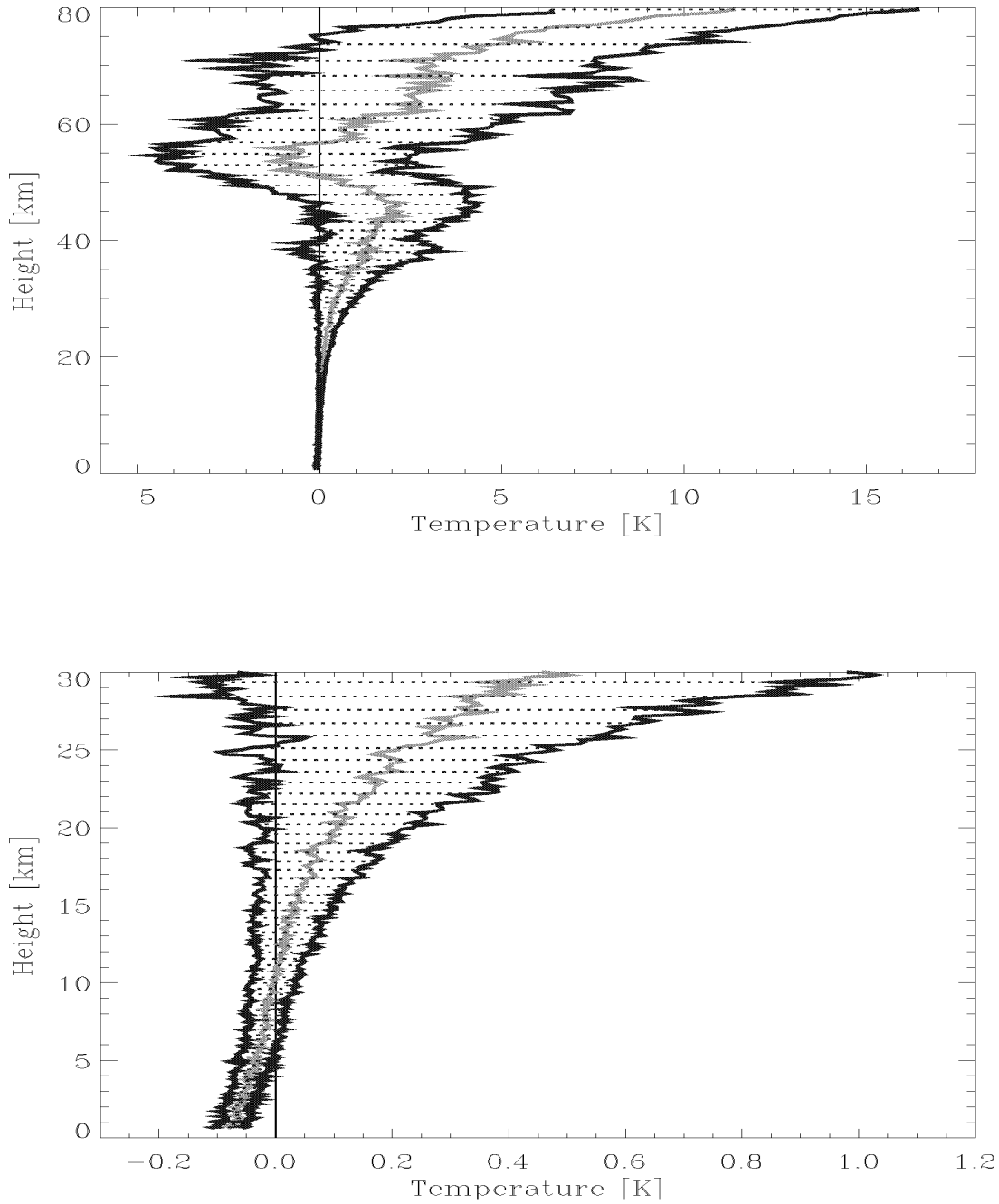

Figure 7.4.7-4 Simulation of temperature profiles. The following four error sources have been included in the simulations white clock noise, local multi path, velocity error and Gaussian random error on the phases. The two figures show for two different height scales the statistics of the difference between the simulated temperature profiles and the model based temperature profile. The grey curve represents the mean temperature difference while the black curves represent the corresponding standard deviations. The statistics is based on 50 simulation runs.

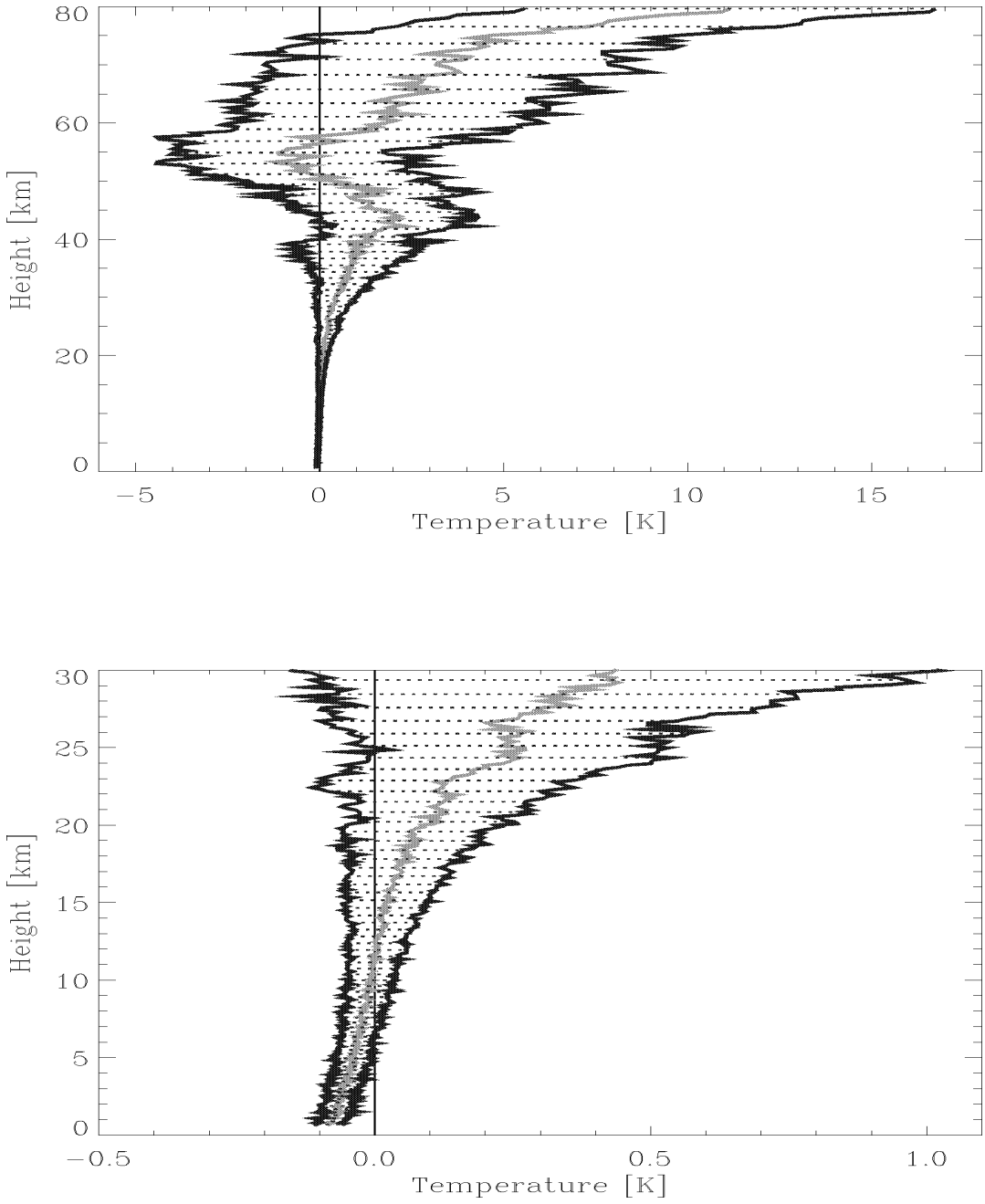

Figure 7.4.7-5 Simulation of temperature profiles. The following four error sources have been included in the simulations flicker clock noise, local multi path, velocity error and Gaussian random error on the phases. The two figures show for two different height scales the statistics of the difference between the simulated temperature profiles and the model based temperature profile. The grey curve represents the mean temperature difference while the black curves represent the corresponding standard deviations. The statistics is based on 50 simulation runs.

Error type and size 1	Error type and size 2	Error type and size 3	Error type and size 4	Sam-pling rate	Figure	Accuracy H<30 km	Precision H<30km	Uncertainty H<30km
Clock error, White noise, 1 sec Allan dev. 10^{-12}	Gaussian noise on phase 2.2 mm	Velocity error 0.1 mm/s	Local multipath Direct to multipath signal ratio in the order of 10 %	50 Hz	7.2.6-4	<0.5 K	<0.5 K	<0.71 K
Clock error, flicker noise, 1 sec Allan dev. 10^{-12}	Gaussian noise on phase 2.2 mm	Velocity error 0.1 mm/s	Local multipath Direct to multipath signal ratio in the order of 10 %	50 Hz	7.2.6-5	<0.4 K	<0.55K	<0.68 K

Table 7.4.7-2 Simulations with four introduced errors. The uncertainty is derived from the accuracy and the precision with the use of equation (7.2.2).

Table 7.4.7-2 above shows the magnitudes of the four error sources used in the simulations corresponding to the curves in figure 7.4.7-4 to 7.4.7-5. (A direct signal to multipath signal ratio of the order of 10 % is normally considered to be a worst case situation). By comparing the figures applying one and four error sources it can be deduces that the contribution from the two error sources, local multi path and velocity error, to the total measurement accuracy and uncertainty is relatively low. The measurement accuracy and uncertainty are not dramatically changed when all of the 4 error sources are applied in the simulations. The uncertainties are still within the threshold values for the secondary EDR temperature parameter.

7.4.8. Secondary EDR table

The error assessment in the presiding sections on the secondary EDR values are summarized in the following table. The nominal threshold value is here defined as a representative average value. The conditions, for which the nominal threshold values and worst case threshold values are found, are listed in column 5 and 7 of table 7.4.8-1. These values can also be found in the table for secondary values in appendix D.

EDR parameter Uncertainty.	Thresholds	Objectives	Nominal Threshold	Nominal condition	Worst case Threshold	Worst case condition
Refractivity Profile	0.3 %	0.05 %	< 0.3 %	High SNR, not solar max.	~ 1 %	Low SNR, solar max. day time.
Pressure profile	0.3 %	0.05 %	< 0.3 %	High SNR, not solar max, high latitude.	~ 1 %	Low SNR, solar max. day time, low latitude.
Temperature profile	1 K	0.2 K	< 1 K	High SNR, not solar max, high latitude.	~ 3 K	Low SNR, solar max. day time, low latitude.
Moisture profile	20 %	5 %	~ 20 %	High SNR, not solar max. External temperature well determined.		Low SNR, solar max. day time. Poor external temperature.

Table 7.4.8-1 Secondary EDR table

7.5. External Data Error Assessment and Sensitivity Analysis

External data sources for most algorithms are clock correction data and POD data. Furthermore, in two specific cases in-situ N_e and troposphere temperature can be input to algorithms for ionosphere and troposphere EDRs.

The electron density profile algorithm may use in-situ N_e as input. However, it is not required as an input in order to meet the requirements and the current assumption is not to use this observation. Theoretically the in-situ N_e should be used as input. However, the impact of not using this input it is small as quoted in [Hajj].

The secondary algorithm for the water vapor profile requires troposphere temperature data as input. The accuracy that can be provided for the water vapor profiles is about

20% for low latitudes up to an altitude of 8 km, given independent temperature observations of an accuracy of about 1.5 Kelvin. At high latitudes, where the water vapor content is low the above mentioned accuracy is only fulfilled up to 5 km during summer and 3 km during the winter season [KUR95], [KUR97].

Radiosonde observations may lead to absolute errors of 2-5% depending on the brand of the instrument. So in a NWP model errors a worst case scenario may become up to 10%. Thus an error of up to 20% for the water vapor profile can be acceptable in a worst case. For most of the time the error is less than 10%.

7.5.1. Results of POD Simulations

The POD solution serves two purposes in relation to the EDRs. The result is used to remove the effect of the GNSS and LEO satellite movement from the carrier phase measurements, i.e. to remove the Doppler contribution from satellite geometry. The result is used to calculate the ray-path bending and thus to estimate the reference locations for the tangent point.

For the primary EDR algorithms Doppler contribution due to satellite movement has no impact on the retrieved EDRs. This is due to that the Doppler contribution is the same on both the L1 and the L2 frequency. The primary EDR algorithms use only the difference between the two phases, so a contribution that is identical on both phases will be completely removed in the retrieval process.

The primary EDR algorithms will thus only be affected by errors in the POD solution during the estimation of ray-path bending. We know from the literature [KUR96] that this usually has no significant influence on the retrieved profiles. Here we will verify it through our EGOPS scenario simulations.

POD errors are in EGOPS applied as worst-case absolute values. For position errors the radial position are usually considered the most critical during occultations. Position errors for the LEO or the GNSS satellite are therefore treated as radial position errors.

For velocity errors the most critical component are the along-ray velocity error. This is due to its direct contribution to the Doppler frequency and thus its direct impact on the secondary EDRs. Velocity errors are applied to the LEO satellite to simulate the well-known fact that drag perturbations makes POD for the LEO significantly more difficult than for the GNSS satellites.

EGOPS addresses the velocity errors and position errors independently. EGOPS is therefore well suited to analyze whether the driving requirement for POD precision is the position or the velocity.

To analyze the effect of POD error on the primary EDR algorithms we have made simulations with 0.5 mm/s along-ray velocity error and simulations with 0.5 m LEO radial position errors.

If POD is unnecessary for the primary EDR algorithms, the navigation solutions could be used instead. We have therefore made simulations with 15 m LEO radial position error and simulations with 1000 mm/s along-ray velocity error.

Finally, to address the combined situation where we don't use the POD solution for the primary EDRs, we have made simulations with 15 m LEO radial position error, 15 m GNSS radial position error and 1000 mm/s along-ray velocity error.

Tables 7.5.1-1 and 7.5.1-2 shows the maximum difference between retrieved electron density profiles where POD errors have been added to the simulated measurements and retrieved electron density profiles where ideal error free simulated measurements have been used. The height where the maximum difference occurs is also listed.

	Position Error 0.5 m		Position Error 15 m	
	Max. Electron Density Diff. (10^{10} e/m^3)	Height (km)	Max. Electron Density Diff. (10^{10} e/m^3)	Height (km)
HG1	< 0.005	-	0.01	252.2
HG2	< 0.005	-	0.01	247.1
HG3	< 0.005	-	0.01	244.5
TI1	< 0.005	-	0.01	113.0
TI2	< 0.005	-	0.01	115.6
TI3	< 0.005	-	0.01	107.3
DV1	0.01	348.9	0.04	296.54
DV2	0.01	328.7	0.04	310.19
DV3	0.01	340.6	0.04	303.22
EE1	0.01	361.6	0.02	394.7
EE2	0.01	344.6	0.02	574.2
EE3	0.01	399.8	0.02	105.0
AR3	< 0.005	-	< 0.005	-

Table 7.5.1-1 Maximum electron density profile difference for POD position errors.

	Velocity Error 0.5 mm/s	Velocity Error 1000 mm/s	No POD

	Max. Electron Density Diff. (10^{10} e/m^3)	Height (km)	Max. Electron Density Diff. (10^{10} e/m^3)	Height (km)	Max. Electron Density Diff. (10^{10} e/m^3)	Height (km)
HG1	< 0.005	-	< 0.005	-	0.01	249.6
HG2	< 0.005	-	< 0.005	-	0.01	247.1
HG3	< 0.005	-	< 0.005	-	0.01	249.6
TI1	< 0.005	-	< 0.005	-	0.01	113.84
TI2	< 0.005	-	< 0.005	-	0.01	115.56
TI3	< 0.005	-	< 0.005	-	0.01	107.3
DV1	< 0.005	-	0.01	348.9	0.04	306.8
DV2	< 0.005	-	0.01	415.6	0.04	328.7
DV3	< 0.005	-	0.01	548.8	0.04	313.8
EE1	< 0.005	-	0.01	574.2	0.02	432.4
EE2	< 0.005	-	0.01	389.7	0.02	574.2
EE3	< 0.005	-	0.01	469.0	0.02	105.0
AR3	< 0.005	-	< 0.005	-	< 0.005	-

Table 7.5.1-2 Maximum electron density profile difference for POD velocity errors and combined velocity/position errors (no POD).

It is clear that the electron density algorithms are practically insensitive to velocity errors. Position errors have a measurable but small impact on the retrieved profiles. Even if we look at the combined No POD situation, we have a worst case electron density difference of $4 \cdot 10^8$ electrons/m^3. This is several magnitudes smaller than the $3 \cdot 10^{11}$ electrons/m^3 threshold uncertainty value for electron density profiles and also significantly smaller than the $1 \cdot 10^{10}$ electrons/m^3 objective.

Table 7.5.1-3 shows the maximum difference for the retrieved slant path TEC profiles, together with the impact parameter where the maximum occurs. The slant path TEC routine does not take the velocities as input, so we consider only the position errors and the combined No POD error situation.

	Position Error 0.5 m		Position Error 15 m		No POD	
	Max. TEC Difference (10^{-3} TEC Units)	Impact Parameter (km)	Max. TEC Difference (10^{-3} TEC Units)	Impact Parameter (km)	Max. TEC Difference (10^{-3} TEC Units)	Impact Parameter (km)

HG1	0.6	6693.0	16.6	6682.0	17.2	6682.0
HG2	0.9	6695.7	22.1	6682.0	22.9	6682.0
HG3	0.7	6698.4	18.6	6682.0	19.3	6682.0
TI1	0.3	6642.9	6.5	6635.1	6.7	6635.1
TI2	0.3	6472.4	8.0	6472.4	8.4	6472.4
TI3	0.2	6648.1	6.0	6640.3	6.3	6642.9
DV1	2.3	6913.3	48.7	6793.3	50.5	6793.3
DV2	1.7	6913.3	36.9	6637.4	37.6	6631.4
DV3	1.9	6913.3	40.3	6637.4	41.7	6631.4
EE1	3.3	6913.3	45.8	6924.3	47.3	6924.3
EE2	3.1	6913.3	43.0	6913.4	43.6	6924.3
EE3	3.2	6913.3	44.3	6911.1	45.3	6924.3
AR3	0.1	6913.3	0.2	6764.4	2.4	6793.3

Table 7.5.1-3 Maximum slant path TEC difference for POD position errors and combined velocity/position errors (no POD).

The maximum difference of the TEC profiles amounts to $4.73 \cdot 10^{-2}$ TECU. It is significantly less than the 3 TECU threshold and the 1 TECU objective. So the situation is the same as for the electron density profiles. From this it is reasonable to conclude that POD will not be required for the primary EDRs, unless the requirement for the on-board generated NPOESS navigation solution is significantly relaxed.

As previously mentioned the situation is different for the secondary EDRs. While position errors still are expected to give little or no influence, velocity errors could become a major problem due to its impact on the Doppler frequency. The values used to simulate the effect of POD position and velocity errors on the secondary EDRs are selected around the following uncertainties, 0.5 m for position, 0.5 mm/s for velocity.

Table 7.5.1-4 shows the absolute difference between the retrieved temperature profiles and the originally used disturbed atmosphere model for an error free simulation and for three different LEO radial position errors. The difference is taken at 30 km height, which is the highest point at which the 1 K threshold is required as maximum temperature uncertainty.

	No Error	Position Error 0.1 m	Position Error 0.3 m	Position Error 1.0 m
	Temperature Error (K)	Temperature Error (K)	Temperature Error (K)	Temperature Error (K)
TD1	0.63	0.63	0.63	0.62

TD2	0.63	0.63	0.63	0.62
TD3	0.63	0.63	0.63	0.62
IL1	0.63	0.63	0.63	0.63
IL2	0.63	0.63	0.63	0.63
IL3	0.63	0.63	0.63	0.63
FS1	1.23	1.23	1.23	1.23
FS2	0.63	0.63	0.63	0.63
FS3	0.66	0.66	0.66	0.66
GW1	-2.38	-2.38	-2.38	-2.39
GW2	1.05	1.05	1.05	1.05
GW3	1.56	1.56	1.56	1.56

Table 7.5.1-4 Temperature error for different POD position errors at 30 km height.

As it can be seen from the Tropopause Disturbances and the Inversion Layers No Error simulation results, there is a significant bias in the retrieved temperature profiles. This is due to the low maximum upper bound height used in the Abel transform (70 km). This bias will be eliminated when methods of statistical optimization are used in the bending angle retrieval and the maximum upper bound height thus can be raised as explained elsewhere in this report. For the Frontal Systems and the Gravity waves scenario we can see that the disturbance has a great influence on the retrieved profile at 30 km height.

The interesting issue however for the POD analysis is the difference between the No Error situation and the profiles where position error has been added to the simulated measurements. This difference is nearly always zero except for a few of the 1.0 m position error simulations where a 0.01 K error difference is identified. We can thus, as expected, conclude that POD position errors has little or no influence on the retrieved temperature profiles.

Table 7.5.1-5 shows the absolute temperature error at 30 km for different POD velocity errors.

	No Error	Velocity Error 0.1 mm/s	Velocity Error 0.3 mm/s	Velocity Error 1.0 mm/s
	Temperature Error (K)	Temperature Error (K)	Temperature Error (K)	Temperature Error (K)
TD1	0.63	0.91	1.49	3.55
TD2	0.63	0.91	1.49	3.55
TD3	0.63	0.91	1.49	3.55
IL1	0.63	0.31	-0.33	-2.53
IL2	0.63	0.31	-0.34	-2.53
IL3	0.63	0.31	-0.34	-2.53
FS1	1.23	1.56	2.23	4.66

FS2	0.63	0.96	1.62	4.00
FS3	0.66	0.98	1.62	3.95
GW1	-2.38	-2.06	-1.41	0.92
GW2	1.05	1.37	2.02	4.36
GW3	1.56	1.88	2.52	4.81

Table 7.5.1-5 Temperature error for different POD velocity errors at 30 km height.

As it can be seen from Table 7.5.1-5 POD velocity errors has a major impact on the retrieved profiles. Approximately 0.3 K for 0.1 mm/s error, 1 K for 0.3 mm/s, and 3 K for 1.0 mm/s. From this it is clear that the original 0.5 mm/s requirement is insufficient to reach the 1 K threshold for temperature error at 30 km height. A 0.3 mm/s requirement would at least be necessary, but that would allocate the entire error budget for POD velocity errors and leave no room for Gaussian noise, clock errors, local multipath etc.

A number of tests using combinations of different error types have showed that it is possible to reach the 1 K threshold if the POD along-ray velocity error is kept below a 0.1 mm/s requirements. In Volume 2 of this document it is described how a 0.1 mm/s POD along-ray velocity error maps into a 0.2 m POD radial position error. As we saw in the radial POD position error simulations above, that is far better than required for the secondary EDR's. It is thus recommended that the uncertainty on the POD along-ray velocity shall be less than 0.1 mm/s for the secondary EDR's.

7.5.2. Results of Local Multipath Simulations

For the estimation of local multipath's impact on the primary EDR's, the instrument designer has calculated the expected local multipath contribution to the simulated residual phases during an occultation. Using the EGOPS simulation tool these contributions have been added to simulated occultations. Two different cases were considered, a typical case and a worst case. The used occultations was an undisturbed version of the occultations from the High Gradient scenario HG0 and one of the disturbed occultations (HG3 was randomly selected, see also Section 7.3).

Figure 7.5.2-1 shows the range error and the corresponding velocity error which was added to the simulated occultation.

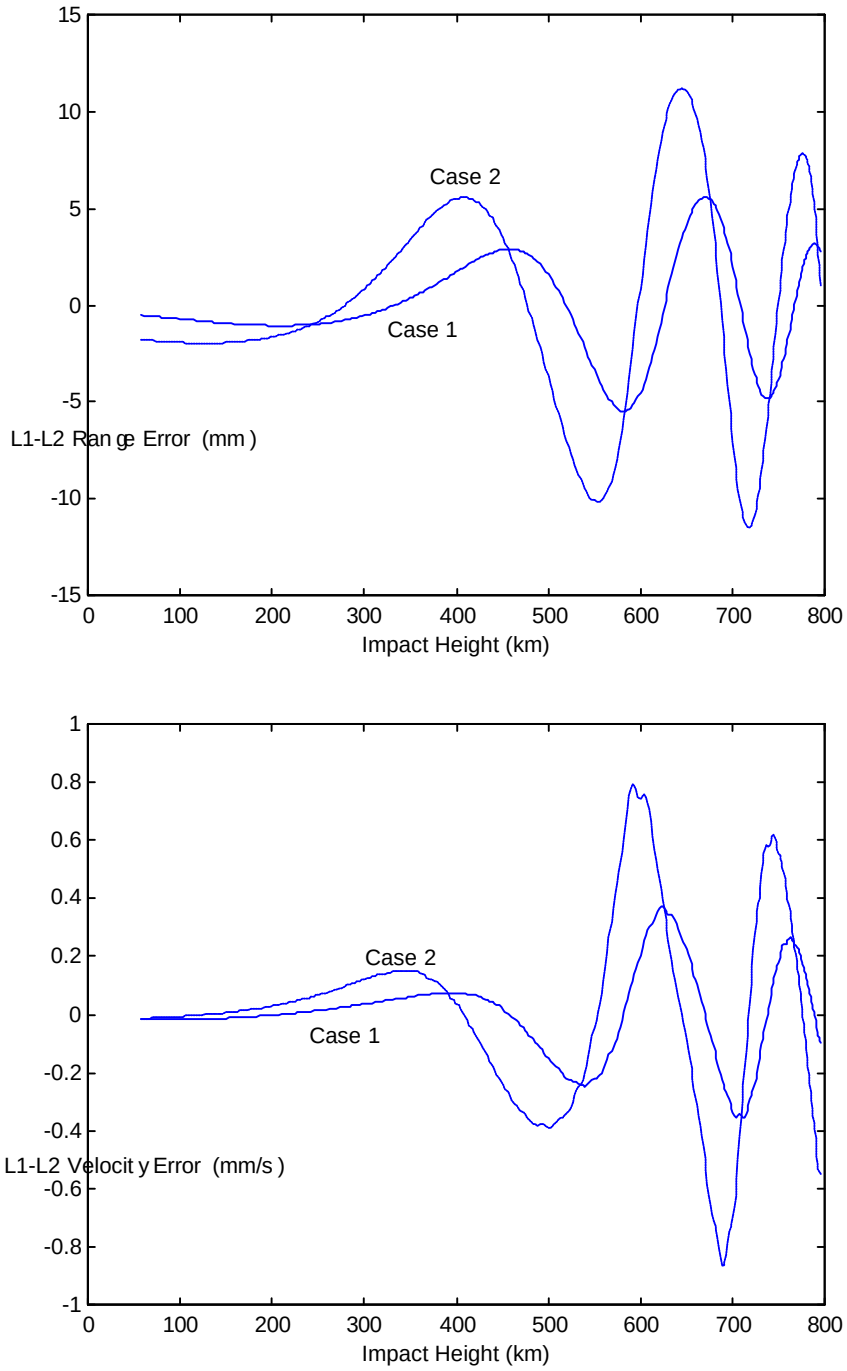

Figure 7.5.2-1 Range and velocity error applied to the simulated occultations. Case 1 is the typical case and Case 2 is the worst case situation.

Table 7.5.2-1 summarizes the maximum difference between the retrieved electron density profiles when local multipath is added and the retrieved electron density profiles without local multipath. Table 7.5.2-2 shows the same for slant path TEC profiles.

	Typical Case		Worst Case	
	Max. Electron Density Diff. (10^{10} e/m^3)	Height (km)	Max. Electron Density Diff. (10^{10} e/m^3)	Height (km)
HG0	0.127	610.5	0.205	672.0
HG3	0.131	610.5	0.217	672.0

Table 7.5.2-1 Maximum electron density profile difference when realistic local multipath is added.

	Typical Case		Worst Case	
	Max. TEC Difference (TEC Units)	Impact Parameter (km)	Max. TEC Difference (TEC Units)	Impact Parameter (km)
HG0	0.053	7038.6	0.109	7092.1
HG3	0.060	6950.2	0.109	7092.1

Table 7.5.2-2 Maximum slant path TEC difference when realistic local multipath is added.

The maximum electron density error of $2.2 \cdot 10^9$ e/m^3 is below the 10^{10} e/m^3 objective and well below the $3 \cdot 10^{11}$ e/m^3 threshold value. The same can be observed for the TEC error where the 0.11 TEC Unit error is below the 1 TEC Unit objective and significantly below the 3 TEC Units threshold.

Even though no final conclusion can be made from this first assessment of local multipath impact on the primary EDR's, the results clearly imply that local multipath will have little effect on the retrieved profiles.

7.6. End to End Error Assessment

7.6.1 Sensitivity and assumptions for occultation data retrieval

The occultations data, observed with the GPSOS instrument, can be categorized by, 1) their physical spatial extent in the atmosphere, 2) coverage in the sky with respect to the receiving antenna, and 3) time for the total occultation spanning either the ionosphere (I) or the stratosphere/troposphere region (SS/TS).

Four criteria may be defined to estimate the usefulness of EDR occultations based on the assumptions for the suggested retrieval methods and algorithms in chapter 6.

Characterization of the occultation trace
The straight-line correlation coefficients to the actual movements of the GPS/GLONASS and NPOESS satellite in the reference frame of the receiving antenna describes the goodness of the linear approximation for the satellite-to-satellite trace. The retrieval technique for obtaining the EDRs does not require that the observations follow a straight line. But the parameter helps in establishing the geophysical correlation between the single observations in the full occultation. Thus observations, which follows a straight line, will shorten the time of a full occultation and will have a significant impact on the quality of the inverted data product. The goodness of an occultation is therefore described by how well the movements of the transmitting satellite approximate a straight line, and thereby minimizing the changes in the location of the tangent point, taking place during the occultation**.**

For the tomographic representation of TEC and the spatial electron density distribution the definition will have no importance, since the quality of this retrieval technique will be governed by the time criteria given below. A stringent time criterion will omit dynamical features to interplay with the data imaging results.

Out-of-track angle of an occultation
The tilt angle of an occultation a with respect to the vertical direction defines how well the total set of measurements in an occultation are able to represent the reality for that parameter. Vertical is here defined as the perpendicular direction to the horizon of the Earth with respect to the coordinate system centered in the LEO. The tilt angle a is the angle between the LEO velocity vector and the raypath projected onto the plane, defined by the LEO radius vector as the normal to this plane. The larger the tilt angle becomes, the less the criteria for retrieving the profile satisfy the assumption, that no temporal effects will influence the data profile reconstruction. Our analysis concludes, that $a < 45$ degrees results in reliable EDRs. While larger a introduces a spatial (impact point

movements) and temporal (long occultations) smearing giving rise to higher order term errors in the EDRs.

Altitude coverage
To be able to perform the retrieval of the EDRs by applying occultation theory it is crucial to have the observations span certain parts of the atmosphere. The height intervals for the regions defined by the primary and secondary EDRs cover:

Region	Height region
(I)	[90km; 600km]
(SS/TS)	[0km; 100km]

Temporal coverage
Dynamical phenomena perturb the data retrieval in the full occultation observation when the time for obtaining the occultation data set becomes too long. This again relates to the above spatial considerations that fulfill the requirement, to have coherence in the geophysical conditions during the measurement period. Our evaluation results in the following time constraints:

Region	Time requirement
(I)	$t < 600$ sec
(SS/TS)	$t < 100$ sec

7.6.2 Summary of errors for retrieved EDRs

The major conclusions from the previous sections in chapter 7 are summerized below for both primary and secondary EDRs. These conclusions are mapped into the primary and secondary EDR tables found in appendix D.

TEC
After applying the TEC correction described in chapter 6, the TEC error even in the asymmetric worst case is reduced to less than 2 TEC. So in general we assess, that the algorithmic errors can be reduced to less than 3 TECU. These conclusions are obtained for the electron density TEC0 along the straight line between the two satellites. The TEC0 (and TEC12) accuracy is limited by the magnetic field term (less than 1 TECU) in the expression for the index of refraction.

Electron density
With a spherical symmetric ionosphere at solar maximum conditions the error magnitude is less than $5 \cdot 10^4$ elec/cm^3 on electron density using the bending angle algorithm. This is the accuracy level that can be expected for occultations under symmetric conditions. It is noted that the highest errors are found at altitudes where the electron density profile has the largest gradients.

The electron density retrieval algorithms presented in this document are all derived under the assumption of spherical symmetry. A bias in the calculated electron density profile can be caused by a occultation that has occurred in a region where the assumption of spherical symmetry is not valid. The size of this bias is around $3 \cdot 10^5$ electrons/cm^3 for the worst asymmetric case assuming a side-viewing occultation geometry.

Since the electron density difference profiles for each type of errors within each scenario are very similar, the applied errors is of minor significance, and the geometry of the occultation and the ionospheric state (deviation from spherical assumption made in the Abel transform) are the governing factors. In all scenarios for primary EDRs the power of the received signal decreases smoothly with 0.5 dB over the occultation.

HmE and HmF2
The distance at low sampling rates between the measurement samples will in general limit the measurement resolution in the ionosphere. A 1 Hz sampling corresponds approximately to a vertical resolution of 3 km. This means that the positions of the two peaks HmF2 and HmE in the electron density can be resolved to within a distance of 3 km.

The spread of the derived HmF2 for each set of scenarios leads to a shift of about 15 km of the HmF2 estimate.

Refractivity
The accuracy of the refractivity measurement is limited by the thermal noise error for altitudes higher than 30 km, while horizontal variation in the refractivity limits the accuracy of the measurements for altitudes less than 25 km. The error in the refractivity measurement is less than 0.4 % for altitudes between 5 and 30 km.

Temperature
The accuracy of the temperature measurement is limited by the thermal noise and the Abel transform boundary value problem for altitudes higher than 40 km. At equatorial latitudes the high concentration of the water vapor limits the temperature accuracy for altitudes less than 8 km, while the temperature at high latitudes can be found with an error less than 2.5K for altitudes near the earth surface. The temperature accuracy is limited by horizontal variation in the refractivity for altitudes between 9 and 17 km. For altitudes between 17 and 40 km the accuracy is limited by contributions from thermal noise, local multipath and residual ionosphere. The residual ionosphere error term gives a significant error in the worst case, but it has little impact in the best case.

It is seen from the figures and the numbers in table 7.2.6.1 that the temperature retrieval process is in general more sensitive to flicker clock noise than white noise and Gaussian noise. The bias, measurement accuracy, is for all of the errors quite small. The uncertainties are all within the threshold value for altitudes up to 30 km.

For the three different position errors the ΔT s merges to the same just above the disturbances (at about 10 km) and from then only the systematic ΔT -increase is seen. For velocity errors Vel3 in section 7.4.2.5 results in a ΔT above 1 K from 20 km and up. The three velocity errors all show the same behavior for the different disturbances, indicating that the algorithm is more sensitive to the error than the disturbance.

Four different values of random errors have been tested with the simulation runs, 0.1 mm and 0.3mm using 10 Hz sampling, and 0.7 and 2.2 mm using a 50 Hz sampling rate. As can be seen the error on the average temperature profile is very low (using statistical optimization), below 0.3 K for all cases, with the standard deviation below 0.5 K, in all keeping the error well below 1K.

Appendix A

A1 Secondary EDRs

The uncertainties on the measured secondary EDRs are summarized in the tables below. The uncertainties are calculated as the square root of the sum of the squares of all the contributing errors. The uncertainties for most of the secondary EDRs are calculated for two different extreme conditions. The first number, representing worse case conditions, includes conditions representative of daytime solar maximum conditions, relatively low SNR and low latitude. The low latitude means that the contribution to the refractivity from the water vapor is at a maximum. The second number, best case conditions, represent conditions with a night time solar maximum, a relatively high SNR, and high latitude troposphere conditions where the influence of water vapor is at a minimum. h represents the altitude in the tables. Most of the table numbers are extracted from studies in the literature [KUR97]. In figure A1-1 to A1-4 some of the interesting plots in this context have been attached from this paper [KUR97].

The five main error sources, with the summarized effect showed in the tables, are:

- *Thermal noise caused by receiver noise in the front end*. This error type will increase with altitude. The measurement method becomes more sensitive to thermal errors at increasing altitude, since thermal errors dominate relatively to the magnitude of the signal related to the atmosphere refraction.

- *Local multipath*. This occurs when multiple images of the signal arrive at the antenna after scattering off structures in the vicinity of the antenna.

- *Upper integration limit for the Abel transform and the hydrostatic integral*. At high altitudes when the signal disappears into the noise floor the density and bending angle structures have to be estimated by models and a set of assumptions.

- *Horizontal variation in the refractivity profile*. This error relates to the spherical symmetry assumption in the retrieval process.

- *Residual ionosphere error*. The presently used calibration scheme removes most of this ionospheric effect. The error type is only significant during the daytime solar maximum.

Secondary EDR	Uncertainty, fractional error, worst conditions	Uncertainty, fractional error, best conditions
Vertical Refractivity Profiles	< 0.4% [5km < h < 30km]	< 0.4% [5km < h < 40km]

Secondary EDR	Temperature error, worst conditions	Temperature error, best conditions
Vertical Temperature Profiles	< 1.0 K [8km < h < 30km] < 0.5 K [10km < h < 20km]	< 0.6 K [8km < h < 30km] < 0.4 K [10km < h < 20km]

Secondary EDR	Temperature error	Error in vertical moisture profiles (Water Vapor)
Troposphere	0.3/1.0/3.0 K	0.075/0.25/0.75 mb

Refractivity
The accuracy of the refractivity measurement is limited by the thermal noise error for altitudes higher than 30 km, while horizontal variation in the refractivity limits the accuracy of the measurements for altitudes less than 25 km. The error in the refractivity measurement is less than 0.4 % for altitudes between 5 and 30 km.

Temperature
The accuracy of the temperature measurement is limited by the thermal noise and the Abel transform boundary value problem for altitudes higher than 40 km. At equatorial latitudes the high concentration of the water vapor limits the temperature accuracy for altitudes less than 8 km, while the temperature at high latitudes can be found with an error less than 2.5K for altitudes near the earth surface. The temperature accuracy is limited by horizontal variation in the refractivity for altitudes between 9 and 17 km. For altitudes between 17 and 40 km the accuracy is limited by contributions from thermal noise, local multipath and residual ionosphere. The residual ionosphere error term gives a significant error in the worst case, but it has little impact in the best case.

Moisture profiles
The table above shows the relation between an error in temperature and the corresponding error in the vertical moisture profile, so an error of 1.0 K gives an error of approximate 0.25 mbar. The best humidity data will be obtained in the middle and lower troposphere at low latitudes where profiles are expected to have a relative accuracy of 20 % for altitudes of up to 6 and 7 km, given independent temperature at accuracies of 1.5 K.

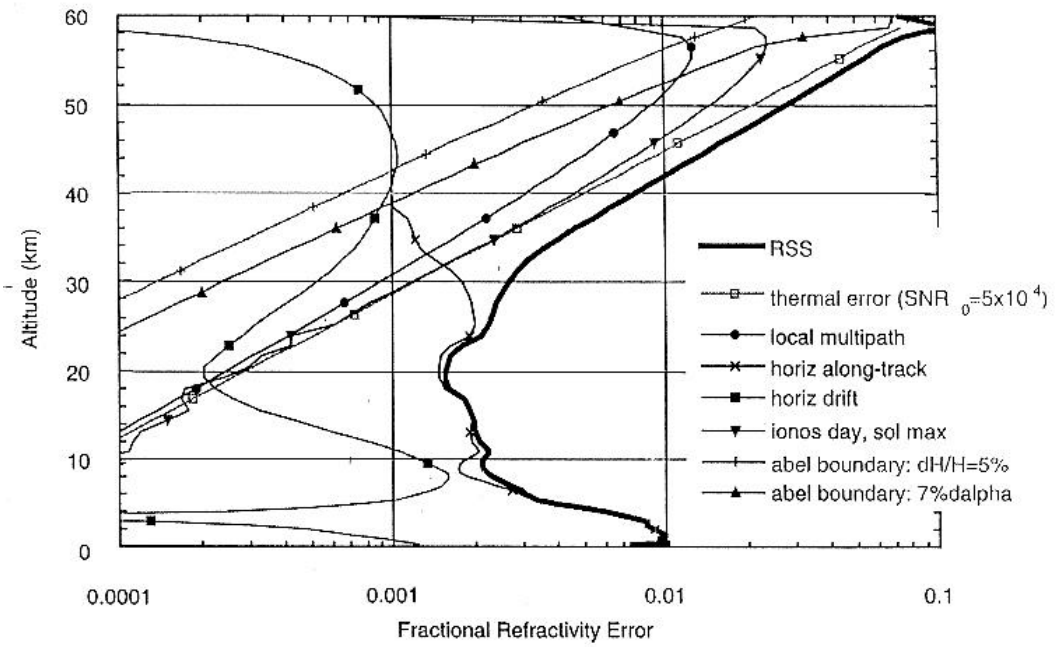

Figure A1-1 Refractivity error, worst case [KUR97].

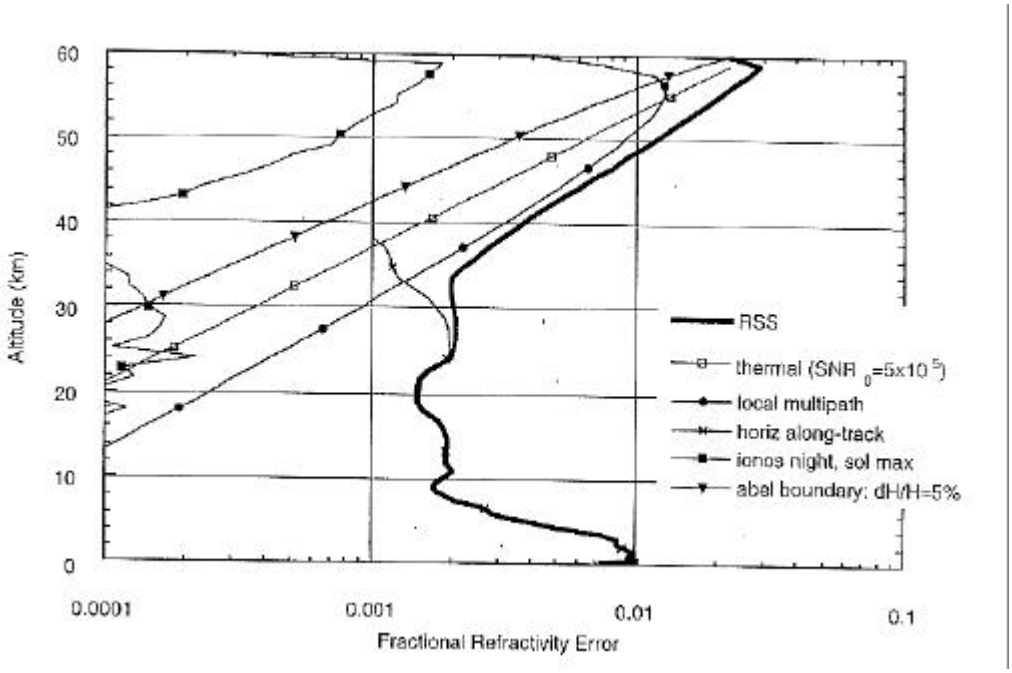

Figure A1-2 Refractivity error, best case [KUR97].

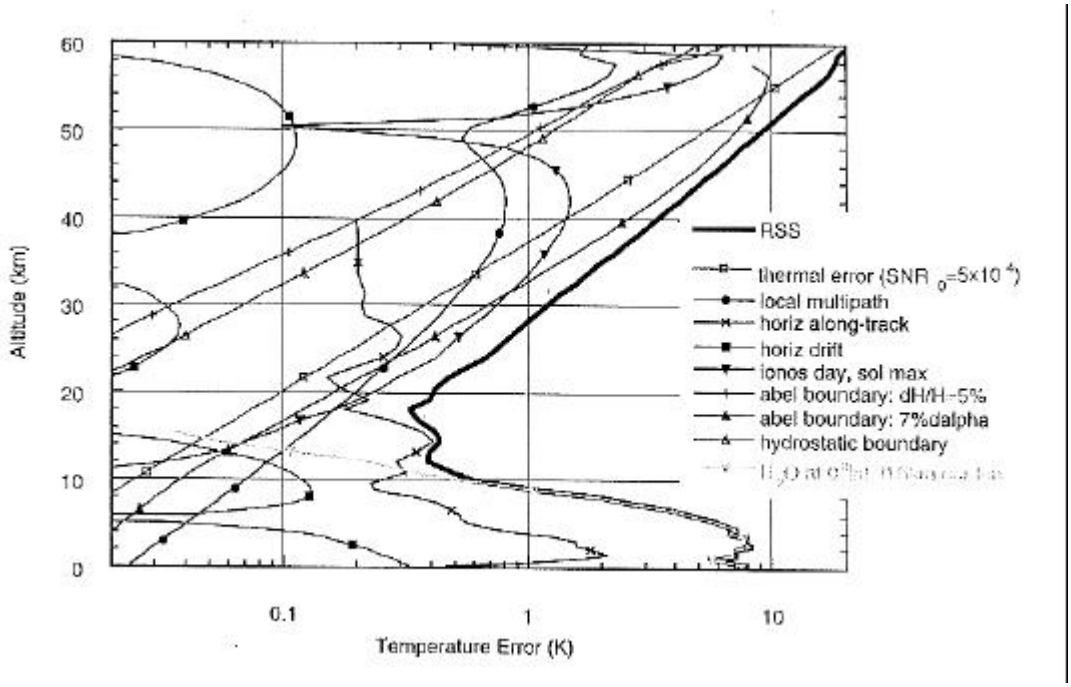

Figure A1-3 Temperature error, worst case [KUR97].

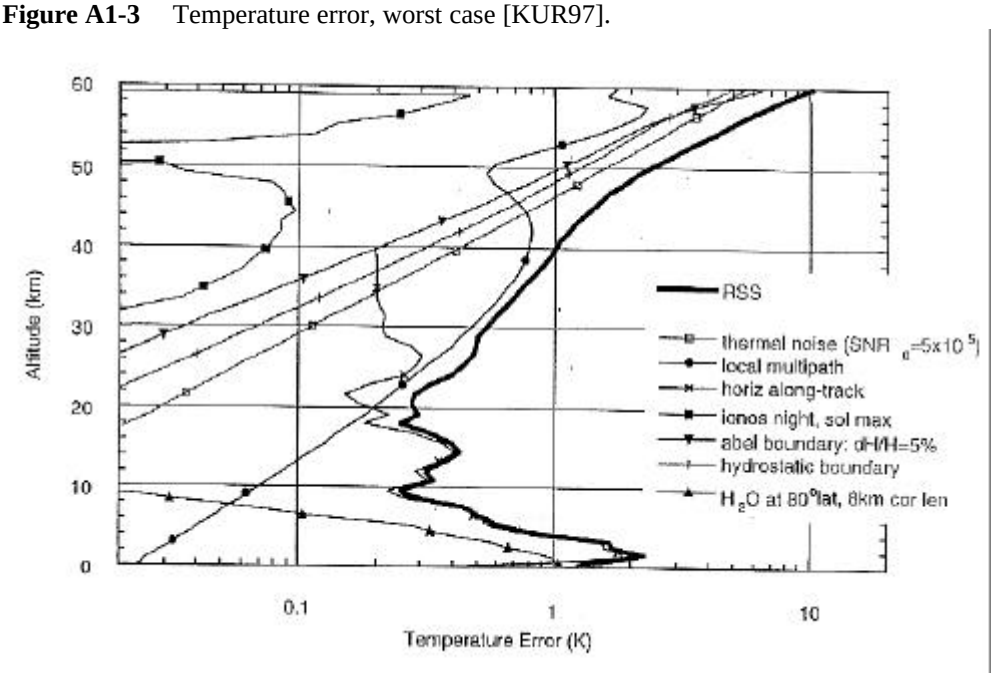

Figure A1-4 Temperature error, best case [KUR97].

Appendix B

B1 Ionosphere correction

As the radio signal travels from the GNSS satellite to the NPOESS receiver scanning the neutral atmosphere it passes through the ionosphere twice. This introduces an extra phase delay, which must be corrected for before an accurate temperature profile can be measured. In chapter 6 we discussed two different correction methods, the traditional linear correction of phases and the bending angle correction method [Hocke].

In figure B-1 below we show how both method apply on simulated data. The bending angle correction method A) is clearly superior to the traditional linear correction of phase delays B). The background ionosphere model NeUoG [LEI96] was assumed at solar maximum, $F_{10.7}$ = 200, during the forward simulation. The resulting phase delays appear noisy due to numerical noise caused by discontinuities in the second order derivatives of the NeUoG model. This level of noise corresponds to approximately 1 mm uncorrelated Gaussian noise on both phase delays. By applying the ionosphere correction and inversion algorithms the temperature profiles are obtained.

From figure B-1 panel A) we note that the bending angle correction (our baseline algorithm) method result in an *unbiased* temperature measurement up to 60 km (the random error is a numerical error observed due to the discontinuity in the ionosphere model). Hence we estimate that ionosphere correction can be performed to high accuracy, even at around 60 km where the limiting random noise (SNR), clock and local multipath errors are the cause of the inaccurate estimates. This is also the result from the detailed error study [KUR97], from where we have obtained the figures presented in appendix A1.

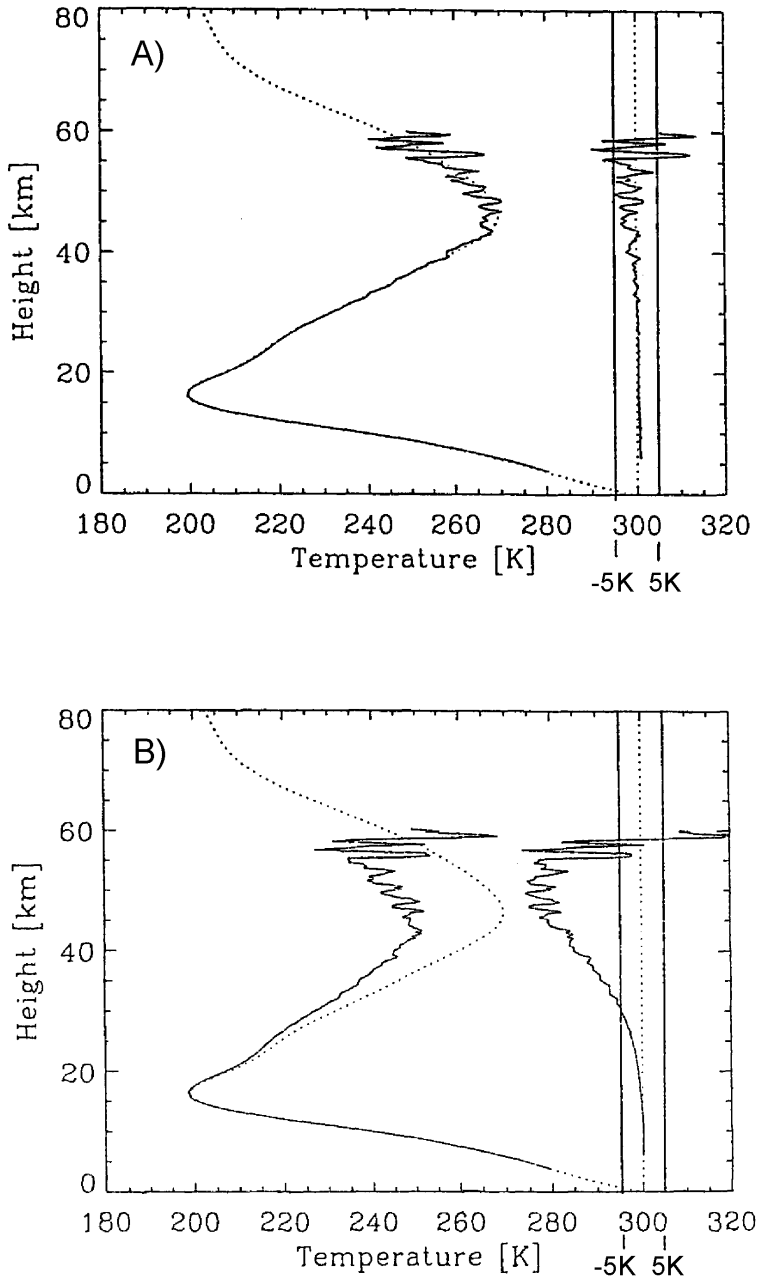

Figure B-1 The dotted curve show a model atmosphere temperature profile using the MSIS90 model [Hedin] on orbit data from GPS/MET occultation no. 31 on Oct. 11, 1996. From a forward model simulation including the NeUoG model for the ionosphere at solar maximum and subsequent inversion the resulting temperature profiles are shown as the solid curves. In A) the bending angle correction scheme was applied, where as in B) the traditional linear correction of phases was used [Hocke].

Appendix C

This appendix contains a description of some of the models used in the report.

C1 The MSIS90 atmosphere model

MSIS90 is an empirical model describing the climatological features of the atmosphere. It is based on temperature, density and composition data from a comprehensive summary of rocket flights, satellites and incoherent scatter radar, including data from high solar activity. This model was first designed in 1977 and subsequently improved and revised in 1983, 1986 and 1991. See [Hedin].

The latest version of MSIS (MSIS90) now extends into the mesosphere and lower atmosphere to provide a single analytic model for calculating temperature and density profiles representative of the climatological average for various geophysical conditions. It includes a longitudinal variability linked to the planetary waves activity, and a time dependence from the solar activity. While months to month details are not completely represented, lower atmosphere temperature data are fit to an overall standard deviation of 3K and pressure to 2%. Comparisons with measured data indicate that the model represents reasonably well current knowledge of the climatological average.

A discontinuity near the mesopause inherent to the early version of MSIS90 has now been removed by introducing a correction term at an altitude of 72.5 km smoothing out the density discontinuity.

The model used in this study is a parametrization of the MSIS90 model using Chebyshef polynominals and spherical harmonics. The modified 1D MSIS90 model corresponds to only keeping the zero order spherical harmonic.

Appendix D

Primary EDR table no. 1

Para. No.		Thresholds	Objectives
G40.8.5-1	a. Horizontal Reporting Interval (Not applicable to slant path TEC)	500 km	500 km
G40.8.5-2	b. Vertical Reporting Interval (Applicable to profile only)	10 km within 100 km of E/F peaks, 20 km elsewhere	3 km
	c. Horizontal Cell Size (Not applicable to slant path TEC)		
G40.8.5-3	1. 0-30° latitude	400 km	100 km
G40.8.5-4	2. 30-50° latitude	400 km	250 km
G40.8.5-5	3. 50-90° latitude	400 km	50 km
G40.8.5-6	d. Vertical Cell Size (Applicable to profile only)	10 km within 100 km of E/F peaks, 20 km elsewhere	3 km
G40.8.5-7	e. Horizontal Coverage	Global	Global
G40.8.5-8	f. Vertical Coverage (Not applicable to slant path TEC)	90-600 km	80-833 km
	g. Measurement Range		
G40.8.5-9	1. Density profile	10^4-10^7 cm^{-3}	10^3-10^7 cm^{-3}
G40.8.5-10	2. Slant Path TEC	3-1000 TEC units	1-1000 TEC units
	h. Measurement Uncertainty		
G40.8.5-11	1. Density profile	Greater of 20 % or $3 \cdot 10^5$ cm^{-3}	10^3 cm^{-3}
G40.8.5-12	2. HmF2	20 km	5 km
G40.8.5-13	3. HmE	10 km	5 km
G40.8.5-14	4. Slant path TEC	3 TEC units	1 TEC unit
G40.8.5-15	i. Average Maximum Local Average Revisit Time (Not applicable to slant path TEC)	24 hrs	3 hrs

G40.8.5-1 The Horizontal Reporting Interval is here taken as the average over 24 hours of the horizontal spacing between profile locations for one satellite orbit.

G40.8.5-3,4,5 Thresholds is based on the formula relating the horizontal and vertical resolution [KUR97], the vertical resolution being determined by a 1 Hz sampling rate in the ionosphere.

G40.8.5-8 The objective upper level for vertical coverage is determined by the NPOESS LEO orbit, the lower level corresponds to the possible D-layer, this corresponds to the size of the ionosphere below the NPOESS LEO orbit.

G40.8.5-10 The TEC used in the table refers to the TEC0 described in chapter 6 and 7. TEC0 is the electron content along the straight line between the LEO and GPS satellite. TEC is defined as the electron content along the radio ray path between the two satellites. This value of TEC is approximately equal to TEC12, see section 4.1.4. The measured value TEC12 is corrected to the straight line TEC0 by the TEC correction algorithm described in chapter 6. The measurement range of slant path TEC is based on simulated performance under solar maximum daytime conditions. This corresponds to a maximum electron density of $3 \cdot 10^{12}$ m^{-3}. The lower limit is determined by the TEC measurement uncertainty.

G40.8.5-11 Threshold uncertainty interval is based on preliminary nominal value simulations for conditions at the solar maximum.

G40.8.5-12,13 Thresholds based on the vertical cell size and the fact that the E-layer peak is sharper than the F2-layer peak.

G40.8.5-14 The TEC used in the table refers to the TEC0 described in chapter 6 and 7. TEC0 is the electron content along the straight line between the LEO and GPS satellite. TEC is defined as the electron content along the radio ray path between the two satellites. This value of TEC is approximately equal to TEC12, see section 4.1.4. The measured value TEC12 is corrected to the straight line TEC0 by the TEC correction algorithm described in chapter 6. The uncertainty on the TEC12 value is approximately equal to the magnetic field term described in section 7.2.1.2. This value is around 1 TECU under the worst case situation. Threshold measurement uncertainty of slant path TEC is a combination of instrument and algorithm errors. Algorithm errors dominate at solar maximum conditions.

G40.8.5-15 Average maximum based on the horizontal cell size and the number of useful occultations (about 3200 per day) produced by 3 satellites.

Primary EDR table no. 2

Para. No.		Threshold	Objectives
G40.8.11-1	a. Horizontal Cell Size	N/A	N/A
G40.8.11-2	b. Horizontal Coverage	Global	Global
	c. Measurement Range		
G40.8.11-3	1. S_4	0.1-1.5	(TBD)
G40.8.11-4	2.	0.1-20 radians	(TBD)
	d. Measurement Uncertainty		
G40.8.11-5	1. S_4	0.1	(TBD)
G40.8.11-6	2.	0.1 radian	(TBD)
G40.8.11-7	e. Local Time Range	17-04 hrs[1] 0-24 hrs[2]	0-24 hrs

G40.8.11-7 The threshold is based on observations by [Basu88]. [1)] refers to the equatorial region. [2)] refers to auroral latitudes. Measurements all day and night has been chosen as the objective. At the equator scintillations can be measured in the time range 8:00 pm to 0:00 am, while scintillations can be measured all day at the pole.

Secondary EDR table

Para. No.		Threshold	Objectives
G40.x.x-1	a. Horizontal Reporting Interval	500 km	500 km
	b. Vertical Reporting Interval		
G40.x.x-2	1. Troposphere	3-25 m	3-25 m
G40.x.x-3	2. Stratosphere	10-25 m	10-25 m
G40.x.x-4	c. Horizontal Cell Size	200 km-300 km	100 km
	d. Vertical Cell Size		
G40.x.x-5	1. Troposphere	0.2-1.0 km	200 m
G40.x.x-6	2. Stratosphere	1.0-1.5 km	200 m
G40.x.x-7	e. Horizontal Coverage	Global	Global
G40.x.x-8	f. Vertical Coverage	0.5-30 km	0.1-50 km
	g. Measurement Range		
G40.x.x-9	1. Refractivity profile	4-450 N unit	0.2-450 N unit
G40.x.x-10	2. Pressure profile	10-1100 mb	0.5-1100 mb
G40.x.x-11	3. Temperature profile	180-335 K	180-335 K
G40.x.x-12	4. Moisture profile	1-45 mb	0.1-50 mb
	h. Measurement Uncertainty		
G40.x.x-13	1. Refractivity profile	0.3 %	0.05 %
G40.x.x-14	2. Pressure profile	0.3 %	0.05 %
G40.x.x-15	3. Temperature profile	1 K	0.2 K
G40.x.x-16	4. Moisture profile	20 %	5 %
G40.x.x-17	i. Maximum Local Average Revisit Time	4 days	12 hrs

G40.x.x-1 The Horizontal Reporting Interval is here taken as the average of the horizontal spacing between profile locations for one satellite orbit.

G40.x.x-2,3 Based on a 100 Hz sampling rate in the neutral atmosphere, and simulation studies in a multipath region.

G40.x.x-4,5,6 Thresholds is based on the formula relating the horizontal and vertical resolution [KUR97], the vertical resolution being determined by the first Fresnel diameter. For high sampling rates the vertical resolution can be decreased by applying Fresnel diffraction inversion of the oversamplied information of phase and amplitude.

G40.x.x-4,5,6 Objective is based on the horizontal drift of the tangent piont. Objectives

is based on the formula relating the horizontal and vertical resolution [KUR97], the vertical resolution being determined by a 100 Hz sampling rate in the neutral atmosphere.

G40.x.x-8 The lower altitude level depends on latitude and the moisture and surface conditions.

G40.x.x-9,10 Based on model parameters in the vertical coverage ranges.

G40.x.x-13,14,15 Threshold values are based on the paper, Observing Earth's atmosphere with radio occultation measurements using the Global Positioning by [KUR97]. This is also consistent with our own simulation runs. Objectives are based on the algorithm uncertainty introduced by the algorithms presently used. The objective uncertainty values are the difference between the intrinsic model value of the physical parameter and the corresponding value of the parameter after the inversion process.

G40.x.x-16 Threshold and objective values are based on the paper Observing Earth's atmosphere with radio occultation measurements using the Global Positioning by [KUR97].

G40.x.x-17 Average maximum based on the horizontal cell size and the number of useful occultations (about 3200 per day) produced by 3 satellites.